

UNIVERSITY OF BIRMINGHAM

**A Global Analysis Of Igneous Sill
Dimensions And Their Effect On
Sedimentary Basins And Petroleum
System - Statistics And Modelling Of
Seismic Observations.**

by

Murray Hoggett

A thesis submitted in partial fulfillment for the
degree of Doctor of Philosophy

in the
College of Life and Environmental Sciences
School of Geography, Earth and Environmental Science

May 2019

UNIVERSITY OF
BIRMINGHAM

University of Birmingham Research Archive

e-theses repository

This unpublished thesis/dissertation is copyright of the author and/or third parties. The intellectual property rights of the author or third parties in respect of this work are as defined by The Copyright Designs and Patents Act 1988 or as modified by any successor legislation.

Any use made of information contained in this thesis/dissertation must be in accordance with that legislation and must be properly acknowledged. Further distribution or reproduction in any format is prohibited without the permission of the copyright holder.

Declaration of Authorship

I, Murray Hoggett, declare that this thesis titled, ‘A Global Analysis Of Igneous Sill Dimensions And Their Effect On Sedimentary Basins And Petroleum System - Statistics And Modelling Of Seismic Observations.’ and the work presented in it are my own. I confirm that:

- This work was done wholly or mainly while in candidature for a research degree at this University.
- Where any part of this thesis has previously been submitted for a degree or any other qualification at this University or any other institution, this has been clearly stated.
- Where I have consulted the published work of others, this is always clearly attributed.
- Where I have quoted from the work of others, the source is always given. With the exception of such quotations, this thesis is entirely my own work.
- I have acknowledged all main sources of help.
- Where the thesis is based on work done by myself jointly with others, I have made clear exactly what was done by others and what I have contributed myself.

Signed:

Date:

“Science never solves a problem without creating ten more.”

George Bernard Shaw

UNIVERSITY OF BIRMINGHAM

Abstract

College of Life and Environmental Sciences
School of Geography, Earth and Environmental Science

Doctor of Philosophy

by Murray Hoggett

Igneous sill intrusion majorly impacts sedimentary basins, causing forced folding of host rocks, thermal maturation of source rocks, and basinal fluid flow changes. However, the detail of these effects has received little study. Similarly, the mechanisms by which sills are emplaced in basins are poorly understood, and emplacement mechanism may influence the aforementioned basinal impacts. The key that ties impacts and mechanisms together is that models explaining both have not been tested due to a lack of data on sill dimensions. Seismic reflection data presents a unique opportunity to collect detailed measurements on sill dimensions. Work presented in this thesis suggests that the number, shape and dimensions of sills have significant differences between sedimentary basins, having major implications for palaeoclimate modelling. Comparing theoretical sill models with measurements of actual sills undermines many models based around linear elastic fracture mechanics. However, intrusion models which incorporate an overlying elastic plate predict far more accurate sill geometries in comparison with seismic measurements. Additionally, several authors have noted that there is a discrepancy between the amplitude of forced folds and the thickness of their underlying sills. This thesis shows that a large proportion of this discrepancy can be explained by compaction of the fold after sill emplacement. While collecting data on forced folds, a seismic reflector in the Northeast Rockall Trough was mapped which displays undulose topography. Multiple observations point to this reflector being an opal A – opal CT transition. Numerical modelling and kinetic parameterization of the opal A–CT indicates that this topography can arise from local lateral temperature variations. Finally, a recently published model for hydrocarbon prospectivity based on fluid flow arising from sill tips is investigated. It is demonstrated that the original study shows no evidence for the validity of the model, prompting new questions on the scale at which intrusions could affect fluid flow. This thesis therefore shows that current paradigms of sill intrusion mechanisms, palaeoclimate model parameterizations, opal A–CT formation mechanisms and intrusion related fluid flow all need to be reexamined.

Acknowledgements

I would like to thank Dr. Steve Jones and Dr. Carl Stevenson for supervision, ideas, support and the occasional spot of troubleshooting over the years. Thanks also to Dr. Craig Magee and Prof. Chris Jackson at Imperial College London for external supervision, data and tough questions on the more controversial ideas. Thanks to Prof. Tim Reston, who has acted like a supervisor despite having plenty of students of his own to supervise. Thanks to Spectrum Geophysical (particularly Karyna Rodriguez) and the Irish government's Petroleum Affairs Division (PAD) for data. IHS and Midland Valley are gratefully thanked for licenses for commercial software. The developers of R, Python, QGIS, Seismic Unix (SU) and Generic Mapping Tools (GMT) ([Wessel et al., 2013](#)) are also thanked for making brilliant open source software which has been used for the majority of this thesis. The departmental administration team of Gretchel Coldicott and Aruna Mistry deserve special thanks for solving many problems before and as they arose. Gina Wright and Joanne Murray are thanked for providing data and interpretations which were used and modelled in this thesis. Thanks to the staff, PhD students and undergraduates at Birmingham for many good times. Finally, thanks to my housemates, close friends and family for listening to much grumbling over the years.

Contents

Declaration of Authorship	i
Abstract	iii
Acknowledgements	iv
List of Figures	ix
List of Tables	xxiii
Abbreviations	xxiv
Symbols	xxv
1 Introduction	1
1.1 A global analysis of sill size distributions	4
1.1.1 Sill size distributions	4
1.1.2 Sill emplacement models	6
1.2 Impacts of sills on petroleum systems	9
1.2.1 Forced folds and the amplitude/thickness discrepancy	9
1.2.2 The search for a new fluid flow proxy	10
1.2.3 Statistically testing fluid flow around sills	12
1.3 Thesis outline and research questions	12
1.4 Study areas	14
1.4.1 Atlantic margin basins	14
1.4.2 Bight Basin	17
1.4.3 Canterbury Basin	18
1.4.4 Carnarvon Basin	20
1.4.5 Karoo Basin	22
2 Datasets	23
2.1 Introduction	23
2.2 2D seismic data	23
2.2.1 UK Oil and Gas Authority (OGA) survey	23
2.2.2 Petroleum Affairs Division (PAD) survey	26

2.2.3	Spectrum INROCK (reprocessed) survey	29
2.2.4	Spectrum ISROCK (reprocessed) survey	32
2.2.5	Spectrum DGER96 (reprocessed) survey	35
2.2.6	Spectrum DGSRT96 (reprocessed) survey	38
2.2.7	Spectrum DGWH96 (reprocessed) survey	41
2.2.8	Spectrum PORC96 (reprocessed) survey	44
2.2.9	Hatton Basin survey	47
2.2.10	Bight Basin	50
2.3	3D seismic data	53
2.3.1	NE Rockall survey	53
2.3.2	Judd survey	56
2.3.3	TGS FSB Megasurvey Plus survey	58
2.3.4	Carnarvon survey	58
2.4	Well data	58
2.5	Remote sensing data	60
2.6	Literature data	61
2.7	Implications of different surveys on measurement resolution	61
3	A global analysis of sill dimensions	63
3.1	Introduction	63
3.2	Methods and definitions	64
3.2.1	Seismic resolution of sills	68
3.2.2	The difference in statistics between 2D and 3D seismic data	73
3.3	Sill statistics	78
3.3.1	Sill shape	78
3.3.2	Sill diameter	80
3.3.3	Sill thickness	84
3.3.4	Sill transgressive height	88
3.3.5	Sill emplacement depth	90
3.3.6	Implications of sill statistics	93
3.3.6.1	Sill shape	93
3.3.6.2	Sill diameters implications	94
3.3.6.3	Transgressive height implications	95
3.3.6.4	Sill thickness implications	95
3.3.6.5	Sill emplacement depth implications	97
3.4	The missing sills test	97
3.4.1	Parameterizing the missing sills test	98
3.4.2	North Atlantic Igneous Province results	100
3.5	Using the sill database to test emplacement models	111
3.5.1	Intrusion modelling context	111
3.5.2	Intrusion modelling parameters	113
3.5.3	Order of magnitude intrusion estimates	114
3.5.4	2D Linear Elastic Fracture Mechanics (LEFM) model	122
3.5.5	Elastic plate flexure models	124
3.5.5.1	Modelling sill profiles	124
3.5.5.2	Dimensionless sill profiles	129
3.6	Summary	132

4	Forced folds and the amplitude / thickness discrepancy	135
4.1	Introduction	135
4.2	The amplitude/thickness discrepancy in the Rockall and Bight Basins . .	139
4.2.1	Data and methods	139
4.2.2	Results	155
4.3	Case study: the Resolution-1 Amplitude/thickness discrepancy	160
4.3.1	Data and methods	160
4.3.2	Results	165
4.3.2.1	Forward problem	165
4.3.2.2	Inverse problem	166
4.3.2.3	Inversion of matrix velocities	166
4.4	Discussion	168
4.5	Summary	170
5	Does the Opal A–CT transition in Rockall document the influence of sills on fluid flow?	171
5.1	Introduction	171
5.2	Reflector A in Rockall	172
5.3	Is Reflector A an opal A–CT transition?	180
5.4	Evidence for opal A–CT fossilisation	186
5.5	Relation to sills	191
5.6	Towards a model for the Rockall opal A–CT transition	192
5.7	Opal A–CT kinetic parameterization	195
5.8	Summary	203
6	The influence of sills on hydrocarbon migration and fluid flow	204
6.1	Introduction	204
6.2	Data and methods	206
6.2.1	Seismic data	206
6.2.2	Well data	207
6.2.3	Statistical analysis	211
6.3	Results	215
6.3.1	Method 1 of 3: distribution analysis	215
6.3.2	Method 2 of 3: statistics of “close” and “not close” subsets.	215
6.3.3	Method 3 of 3: Monte Carlo modelling	216
6.4	Discussion	218
6.5	The importance of sills in petroliferous basins	221
6.6	Summary	223
7	Discussion and Further Work	225
7.1	Large Igneous Province plumbing systems	225
7.1.1	Magma pressure implications	225
7.1.2	Volumetric implications	226
7.2	Emplacement mechanisms of sills	228
7.2.1	Magma fingers and smaller scale structures	230
7.3	Forced folds as hydrocarbon traps	230
7.3.1	Influence of sills on fluid flow	236

7.4	Sills outside sedimentary basins — magmatic margins and oceanic crust .	238
7.5	Towards an integrated understanding of opal A-CT transitions	241
8	Conclusions	244
A	Sills database	247
B	Sill thickness database (well data)	248
C	Opal A-CT database	260
	Bibliography	267

List of Figures

1.1	An example of a sill at Kilt Rock on the Isle of Skye, Scotland. The sill, which makes up a famous landmark, is Paleocene in age and intrudes a Jurassic clastic succession.	2
1.2	Sill intrusion recorded by different data types for the 2010 Eyjafjallajökull eruption. Left: Tarasewicz et al.'s (2014) figure 9, showing microseismicity tracking the intrusion of a sill. Right: Sigmundsson et al.'s (2010) figure 4 showing inSAR data of the same intrusion event.	3
1.3	The PETM, shown in oxygen isotope records (after Zachos, 2001, (upper panel)), and the possible cause of it: the emplacement of the NAIP (lower panel, after Saunders et al. (1997), from http://earthwise.bgs.ac.uk/index.php/Igneous_geology:_regional_setting,_Palaeogene_volcanic_districts_of_Scotland , accessed 5/10/2017)	5
1.4	Spacapan et al.'s (2017) figure 1, showing common models for sill intrusion. a to d represent variations on the fluid filled crack model. e represents the fluidization model, and f represents the viscous indenter model. See text for details.	7
1.5	A typical seismic section from the Rockall basin. Seismic data allows the full sill extent to be imaged. [Redacted]	8
1.6	A forced fold and shallowly emplaced sills imaged on seismic data in the Rockall basin. [Redacted]	11
1.7	Datasets used in the Atlantic margin basins. Base map show shows bathymetry (data: ETOPO1 (Amante, 2009)).	15
1.8	Datasets used in the Atlantic margin basins. Base map shows FA gravity anomaly (data: WGM2012 (Bonvalot et al., 2012)).	16
1.9	Datasets used in the Atlantic margin basins. Base map shows magnetic anomaly (data: GGM02 (Tapley et al., 2005)).	16
1.10	Datasets used in the Bight Basin. Top left shows bathymetry (data: ETOPO1 (Amante, 2009)), top right panel shows FA gravity anomaly (data: WGM2012 (Bonvalot et al., 2012)), and bottom left shows magnetic anomaly (data: GGM02 (Tapley et al., 2005)).	18
1.11	Datasets used in the Canterbury Basin. Top left shows bathymetry (data: ETOPO1 (Amante, 2009)), top right panel shows FA gravity anomaly (data: WGM2012 (Bonvalot et al., 2012)), and bottom left shows magnetic anomaly (data: GGM02 (Tapley et al., 2005)).	20
1.12	Datasets used in the Canarvon Basin. Top left shows bathymetry (data: ETOPO1 (Amante, 2009)), top right panel shows FA gravity anomaly (data: WGM2012 (Bonvalot et al., 2012)), and bottom left shows magnetic anomaly (data: GGM02 (Tapley et al., 2005)).	21

1.13	Geological map of the Karoo Basin and outcropping intrusions. After De Kock et al. (2017).	22
2.1	Example seismic line from the OGA survey, with interpretation	25
2.2	Power spectral density estimates for the OGA survey. Individual black lines are power spectral density estimates for individual seismic lines in the survey, while green curve is the mean of the individual lines.	26
2.3	Power spectral density estimates for the PAD survey. Individual black lines are power spectral density estimates for individual seismic lines in the survey, while green curve is the mean of the individual lines.	27
2.4	Example seismic line from the PAD survey, with interpretation	28
2.5	Power spectral density estimates for the INROCK96 survey. Individual black lines are power spectral density estimates for individual seismic lines in the survey, while green curve is the mean of the individual lines.	30
2.6	Example seismic line from the INROCK96 survey, with interpretation. [Redacted]	31
2.7	Power spectral density estimates for the ISROCK96 survey. Individual black lines are power spectral density estimates for individual seismic lines in the survey, while green curve is the mean of the individual lines.	33
2.8	Example seismic line from the ISROCK survey, with interpretation. [Redacted]	34
2.9	Power spectral density estimates for the DGER96 survey. Individual black lines are power spectral density estimates for individual seismic lines in the survey, while green curve is the mean of the individual lines.	36
2.10	Example seismic line from the DGER96 survey, with interpretation. [Redacted]	37
2.11	Power spectral density estimates for the DGSRT96 survey. Individual black lines are power spectral density estimates for individual seismic lines in the survey, while green curve is the mean of the individual lines.	39
2.12	Example seismic line from the DGSRT96 survey, with interpretation. [Redacted]	40
2.13	Power spectral density estimates for the DGWH96 survey. Individual black lines are power spectral density estimates for individual seismic lines in the survey, while green curve is the mean of the individual lines.	42
2.14	Example seismic line from the DGWH96 survey, with interpretation. [Redacted]	43
2.15	Power spectral density estimates for the PORC97 survey. Individual black lines are power spectral density estimates for individual seismic lines in the survey, while green curve is the mean of the individual lines.	45
2.16	Example seismic line from the PORC97 survey, with interpretation. [Redacted]	46
2.17	Power spectral density estimates for the Hatton survey. Individual black lines are power spectral density estimates for individual seismic lines in the survey, while green curve is the mean of the individual lines.	48
2.18	Example seismic line from the Hatton survey, with interpretation	49
2.19	Power spectral density estimates for the Bight survey. Individual black lines are power spectral density estimates for individual seismic lines in the survey, while green curve is the mean of the individual lines.	51
2.20	Example seismic line from the Bight survey, with interpretation	52
2.21	Power spectral density estimates for the Rockall 3D survey. Individual black lines are power spectral density estimates for individual inlines in the survey, while green curve is the mean of the individual lines.	54

2.22	Example seismic line from the Rockall 3D survey, with interpretation. [Redacted]	55
2.23	Power spectral density estimates for the Judd 3D survey. Individual black lines are power spectral density estimates for individual inlines in the survey, while green curve is the mean of the individual lines.	56
2.24	Example seismic line from the Judd 3D survey, with interpretation. [Redacted]	57
2.25	Example of a sill on the remotely sensed data. Data is from Google Earth, accessed October — May 2013.	60
3.1	Definitions of measurements taken on each sill in the sills database.	65
3.2	Definition of sill diameter, as measured for the sill database. Measurement A was made on each sill instead of measurement B. See text for discussion.	66
3.3	Checkshot surveys for the Rockall (left panel) and Bight (right panel) Basins, used for depth conversion of seismic data. Second order polynomial regression lines are in blue, with pale blue envelope representing a 95% confidence interval.	67
3.4	Definitions of sill shapes. Sill shapes are used to subset data in later analysis	68
3.5	An example of a sill above and below tuning thickness in the Rockall basin. [Redacted]	70
3.6	Setup for the synthetic wedge model without noise, used to study the importance of seismic resolution on measurements. Top left is P-wave velocity. Top right is density. Bottom left is the acoustic impedance, which is the product of P-wave velocity and density. Bottom right is the reflection coefficient, the depth derivative of the acoustic impedance.	71
3.7	Results of the noise free synthetic wedge experiment. Actual amplitude is measured along the true location of the sediment-sill interface. Apparent amplitude is the maximum amplitude in a window of 20 milliseconds around the true location of the sediment-sill interface.	72
3.8	Results of the synthetic wedge experiment with added Gaussian noise, simulating the random component of seismic noise.	73
3.9	Box and whisker plot of sill diameter data, coloured by whether the seismic data measurements were collected from 2D or 3D data. Points represent outliers, defined as less than the lower quartile (LQ) plus 1.5 times the interquartile range (IQR) or the upper quartile (UQ) plus 1.5 times the IQR. The box extents represents the upper and lower quartiles, hence the IQR is the UQ - the LQ. The horizontal line through the box is the median. The upper and lower whiskers represent the LQ plus 1.5 times the IQR, and the UQ plus 1.5 times the IQR, respectively. Karoo Basin data is marked NA due to it being measured from satellite data. Porcupine Basin data is marked NA as it has close to equal proportions of 2D and 3D data, however the 2D and 3D data in Porcupine is from different spatial regions within the basin and so is not fair to split and directly compare.	74
3.10	Setup for the Monte Carlo model investigating random intersection of a 2D seismic line with a sill.	76
3.11	Monte Carlo modelling of random intersections of a seismic line with a sill. Black line is the median value. Purple envelope represents the interquartile range.	76
3.12	Histogram of the Monte Carlo run results for a 100000 m diameter sill	77

3.13 Monte Carlo modelling results for simulated random samples of circular sills of increasing mean diameter taken from a normal distribution.	78
3.14 Stacked bar graph of proportions of sill shapes inside the study basins . . .	79
3.15 Sill diameter data, split by basin. For how to read box and whisker plots, see figure 3.9 caption.	81
3.16 Sill diameter data, split by sill shape. For how to read box and whisker plots, see figure 3.9 caption.	81
3.17 Results of the Tukey HSD multiple comparisons test. This shows the differences in means of the log of sill diameter between different pairs of datasets. For each pair of datasets compared, an estimate of the difference between the means of the populations is shown as a point, with error bars showing the 95% confidence intervals for these estimates. If the error bars overlap 0, then there is evidence that there could be no difference between means of the datasets, and hence there is no statistical evidence that the means of the log sill diameters from those datasets are different.	83
3.18 Fractal plot for sill diameter data. A linear section on the data would imply a fractal relationship. The data appears to curve smoothly, arguing against a fractal relationship.	84
3.19 Histogram of sill thickness measured from seismic data, depth converted with values of 4500 m s^{-1} (min) and 6000 m s^{-1} (max) (after Smallwood and Maresh, 2002).	85
3.20 Histogram of sill thicknesses from well and field data	86
3.21 Box and whisker plot of sill thicknesses split by basin, for basins with more than 10 datapoints. For how to read box and whisker plots, see figure 3.9 caption.	86
3.22 Left: Sill diameter vs sill thickness scatter plot and regression line. Right: Sill diameter vs sill thickness scatter plot, with regression line forced through the origin. Note no R^2 value for the right hand panel, as the intercept is used in the equation for calculating R^2 , so comparison of R^2 values is not valid.	87
3.23 Fractal plot for sill thickness. A linear section on the data would imply a fractal relationship. The data appears to curve smoothly, arguing against a fractal relationship.	88
3.24 Fractal plot for sill volume. A linear section on the data would imply a fractal relationship. The data appears to curve smoothly, arguing against a fractal relationship.	89
3.25 Box and whisker plot of transgressive height measurements, split by basin. For how to read box and whisker plots, see figure 3.9 caption.	90
3.26 Box and whisker plot of transgressive height, split by sill shape. For how to read box and whisker plots, see figure 3.9 caption.	91
3.27 Semi transparent histograms showing the comparison between data presented here before and after decompaction for sills in the sills database. Note purple corresponds to overlapping semitransparent red and blue bars.	93
3.28 Model of Jamtveit et al. (2004) for hydrothermal venting associated with sill intrusions. Red bars on the depth axes represent the intrusion depth of a sill where an associated hydrothermal vent has been interpreted on seismic.	94

3.29	Stacked proportional bar graph for sills intruding faults verses sills intruding sediments, in a selection of basins. The highest proportion of fault intrusion is in the Coverack dataset, which images sills likely to have been intruded synrift.	96
3.30	Cullen and Frey plot, showing the theoretical probability distributions that can be used to model sill lengths. Blue point shows the square of skewness and kurtosis for the sill diameter sample being investigated. Yellow points show bootstrapped samples, indicating a confidence region for the blue point.	100
3.31	Results of fitting uniform, normal and lognormal distributions to the Rockall sill diameter samples.	101
3.32	One run (out of 1200) of the Monte Carlo missing sills test	102
3.33	Results of applying the missing sills test to different 2D seismic surveys. The number of sills observed, and the corresponding minimum and maximum bounds for the number of sills predicted is shown for each survey.	105
3.34	Curves of observed sills against actual sills within seismic survey footprint, from the missing sills test. Envelopes are two standard deviations wide.	106
3.35	Great circle distances from palaeo-plume centres of White and McKenzie (1989) and Nisbet et al. (2009) to mid points of 2D seismic surveys. Bathymetry data from ETOPO1 (Amante, 2009).	107
3.36	Scatter graph of distance of the mid point of each survey from the centre of the palaeo-plume head models of White and McKenzie (1989) and Nisbet et al. (2009), against sill area-density.	108
3.37	Histograms of bathymetry extracted from each survey. Red line is mean, while green envelope is two standard deviations.	109
3.38	Scatter graph of sill area density against mean survey bathymetry, extracted from ETOPO1 (Amante, 2009).	110
3.39	Measured sill data (crosses) against theoretical predictions using equation 3.15	116
3.40	Measured sill data (crosses) against theoretical predictions using equation 3.17	117
3.41	Comparison between equation 3.15 and 3.17	117
3.42	Comparison of real data (crosses) with inequality 3.19	118
3.43	Histograms of sill lengths and thicknesses. Coloured lines represent the predicted maximum lengths and widths for different parameter combinations from equations 3.20 and 3.21	119
3.44	Measured sills (red crosses) plotted against the right hand side of equation 3.22 (green lines). The blue line shows the parameter values of Lister (1990)	120
3.45	Left: Parameter fitting for equation 3.15. Right: Parameter fitting for equation 3.17. For both equations blue regions show the bounds of parameters in sedimentary basins for the parameter on the horizontal axis, while green regions show the bounds for parameters on the vertical axis. Where the two regions cross shows the parameters space in sedimentary basins. Both plots show modelled values fall outside of the normal parameter space for sedimentary basins, by several orders of magnitude.	121

3.46	Results of modelling equation 3.23 using 3D seismic data, and parameters from table 3.5. Black bars are modelled values, while coloured bars are measured data points from the Faeroe-Shetland Basin (FSB), Judd Basin, Rockall Basin and Slyne-Erris Basins. Error bars on measured data points show variation due to depth conversion velocities. Depth conversion uses values in Smallwood and Maresh (2002).	123
3.47	Modelling as in figure 3.46, but using both 2D and 3D seismic observations. Colours represent whether data is from a 3D seismic survey (blue) or 2D seismic survey (red).	123
3.48	Model estimates versus seismic measurements for the maximum thickness of sills using the Johnson and Pollard (1973)'s model. Measurements are in red, with error bars reflecting uncertainty in sill V_p . Black bars are modelled values using parameters in table 3.5 and the emplacement depth and sill length measured from each sill to predict the maximum sill thickness.	126
3.49	Johnson and Pollard (1973) model applied to sill profiles, using parameter ranges from table 3.5, for Rockall Trough data.	127
3.50	Johnson and Pollard (1973) model applied to sill profiles, using parameter ranges from table 3.5, for Bight Basin data.	128
3.51	Non-dimensionalized measured sill profiles, plotted against equation 3.26 (the dimensionless form of the Johnson and Pollard (1973) model).	131
3.52	Relationship between A_0 , B and y , see equations 3.30 and 3.31	132
3.53	The dimensionless model of Spence and Turcotte (1985), plotted against non-dimensionalized sill profiles	132
4.1	An example of a sill and it's overlying forced fold from the DGSRT96 survey	136
4.2	Reproduction of Hansen's (2006) figure 5, with regions where there is a discrepancy between the forced fold and the sill thickness highlighted in red. Modified after Hansen and Cartwright (2006a).	137
4.3	Reproduction of Jackson et al.'s (2013) figure 7 (upper four panels) and Magee et al.'s (2013a) figure 3 (bottom panel), with regions where there is a discrepancy between the forced fold and the sill thickness highlighted in red. Modified after Jackson et al. (2013) and Magee et al. (2013a).	138
4.4	Schematic cartoon of measurements taken on sills and forced folds. Note arrows are offset for visual clarity, but in reality all measurements are taken at the same horizontal position, such that the shafts of the arrows would overlap.	140
4.5	Seismic line DGER96-26, used in forced fold amplitude / sill thickness modelling. Yellow is top forced fold. Red is top sill. Orange is base sill. Sill is identified by (1) high amplitude, (2) positive polarity reflection forming the top of the sill, and (3) a corresponding negative reflection forming the base of the sill. The reflection is (4) laterally discontinuous, and (5) locally transgresses stratigraphy, especially to the left of the figure. The base reflection is difficult to follow, but is observed as the negative reflection with a different dip to the surrounding stratigraphy. [Redacted]	141

- 4.6 Seismic line INROCK-96-06, used in forced fold amplitude / sill thickness modelling. Yellow is top forced fold. Red is top sill. Orange is base sill. Sill is identified by (1) high amplitude, (2) positive polarity reflection forming the top of the sill, and (3) a corresponding negative reflection forming the base of the sill. The reflection is (4) laterally discontinuous, and (5) locally transgresses stratigraphy. The base reflection is easy to observe as the only high amplitude negative polarity reflection under the sill. Lower frequency "ringing" reverberations are seen for up to three seismic loops under the sill, corresponding to inter-bed multiples generated within the sill. [Redacted] 142
- 4.7 Seismic line 9003m_1-new2, used in forced fold amplitude / sill thickness modelling. Yellow is top forced fold. Red is top sill. Orange is base sill. Sill is identified by (1) high amplitude, (2) positive polarity reflection forming the top of the sill, and (3) a corresponding negative reflection forming the base of the sill. The reflection is (4) laterally discontinuous, and (5) locally transgresses stratigraphy. The base reflection is easy to follow, as the only continuous negative polarity reflection with a different dip to the surrounding stratigraphy. Seismic "ringing" is also observed under the sill, but is of lower amplitude and frequency making it easy to distinguish from the base reflection. 143
- 4.8 Seismic line PORC-97-06, used in forced fold amplitude / sill thickness modelling. Yellow is top forced fold. Red is top sill. Orange is base sill. Sill is identified by (1) high amplitude, (2) positive polarity reflection forming the top of the sill, and (3) a corresponding negative reflection forming the base of the sill. The reflection is (4) laterally discontinuous, and (5) locally transgresses stratigraphy. The base reflection is easy to follow due to its differing dip to the surrounding stratigraphy, especially on the right hand side of the image. Seismic "ringing" is also observed under the sill, but is of lower amplitude and frequency making it easy to distinguish from the base reflection. [Redacted] 144
- 4.9 Seismic line ISROCK-96-18, used in forced fold amplitude / sill thickness modelling. Yellow is top forced fold. Red is top sill. Orange is base sill. Sill is identified by (1) high amplitude, (2) positive polarity reflection forming the top of the sill, and (3) a corresponding negative reflection forming the base of the sill. The reflection is (4) laterally discontinuous, and (5) locally transgresses stratigraphy. The base reflection is easy to follow on the left hand side, as the only continuous negative polarity reflection with a different dip to the surrounding stratigraphy. In the middle and on the right hand side the reflection becomes difficult to follow as it goes below tuning thickness, introducing uncertainty to the measurement. Seismic "ringing" is also observed under the sill, but is of lower amplitude and frequency making it easy to distinguish from the base reflection. [Redacted] 145

- 4.10 Seismic inline 20722 from the Rockall 3D survey, used in forced fold amplitude / sill thickness modelling. Yellow is top forced fold. Red is top sill. Orange is base sill. Sill is identified by (1) high amplitude, (2) positive polarity reflection forming the top of the sill, and (3) a corresponding negative reflection forming the base of the sill. The reflection is (4) laterally discontinuous, and (5) locally transgresses stratigraphy. The base reflection is easy to follow, as the only continuous negative polarity reflection with a different dip to the surrounding stratigraphy. Seismic "ringing" is also observed under the sill, but is of significantly lower amplitude and frequency making it easy to distinguish from the base reflection. [Redacted] 146
- 4.11 Seismic inline 20934 from the Rockall 3D survey, used in forced fold amplitude / sill thickness modelling. Yellow is top forced fold. Red is top sill. Orange is base sill. Sill is identified by (1) high amplitude, (2) positive polarity reflection forming the top of the sill, and (3) a corresponding negative reflection forming the base of the sill. The reflection is (4) laterally discontinuous, and (5) locally transgresses stratigraphy. The base reflection is easy to follow, as the only continuous negative polarity reflection with a different dip to the surrounding stratigraphy, especially on the left hand side of the figure. [Redacted] 147
- 4.12 Seismic line WOOFDWO091, used in forced fold amplitude / sill thickness modelling. Yellow is top forced fold. Red is top sill. Orange is base sill. Sill is identified by (1) high amplitude, (2) positive polarity reflection forming the top of the sill, and (3) a corresponding negative reflection forming the base of the sill. The reflection is (4) laterally discontinuous, and (5) locally transgresses stratigraphy. 148
- 4.13 Seismic line WOOFDWO089, used in forced fold amplitude / sill thickness modelling. Yellow is top forced fold. Red is top sill. Orange is base sill. Sill is identified by (1) high amplitude, (2) positive polarity reflection forming the top of the sill, and (3) a corresponding negative reflection forming the base of the sill. The reflection is (4) laterally discontinuous, and (5) locally transgresses stratigraphy. The base reflection is easy to follow in the centre as the only continuous negative polarity reflection with a different dip to the surrounding stratigraphy. It becomes difficult on the limbs of the sill as it approaches tuning thickness, introducing some uncertainty to the interpretation. 149
- 4.14 Seismic line WOOFDWO060, used in forced fold amplitude / sill thickness modelling. Yellow is top forced fold. Red is top sill. Orange is base sill. Sill is identified by (1) high amplitude, (2) positive polarity reflection forming the top of the sill, and (3) a corresponding negative reflection forming the base of the sill. The reflection is (4) laterally discontinuous, and (5) locally transgresses stratigraphy. The base reflection is easy to follow, as the only continuous negative polarity reflection with a different dip to the surrounding stratigraphy. 150

4.15	Seismic line WOOFDWO085, used in forced fold amplitude / sill thickness modelling. Yellow is top forced fold. Red is top sill. Orange is base sill. Sill is identified by (1) high amplitude, (2) positive polarity reflection forming the top of the sill, and (3) a corresponding negative reflection forming the base of the sill. The reflection is (4) laterally discontinuous, and (5) locally transgresses stratigraphy. The base reflection is easy to follow, as the only continuous negative polarity reflection with a different dip to the surrounding stratigraphy.	151
4.16	Seismic line WOOFDWO080, used in forced fold amplitude / sill thickness modelling. Yellow is top forced fold. Red is top sill. Orange is base sill. Sill is identified by (1) high amplitude, (2) positive polarity reflection forming the top of the sill, and (3) a corresponding negative reflection forming the base of the sill. The reflection is (4) laterally discontinuous, and (5) locally transgresses stratigraphy. The base reflection is easy to follow, as the only continuous negative polarity reflection with a different dip to the surrounding stratigraphy.	152
4.17	Seismic line WOOFDWO057, used in forced fold amplitude / sill thickness modelling. Yellow is top forced fold. Red is top sill. Orange is base sill. Sill is identified by (1) high amplitude, (2) positive polarity reflection forming the top of the sill, and (3) a corresponding negative reflection forming the base of the sill. The reflection is (4) laterally discontinuous, and (5) locally transgresses stratigraphy. The base reflection is easy to follow, as the only continuous negative polarity reflection with a different dip to the surrounding stratigraphy.	153
4.18	Seismic line WOOFDWO070, used in forced fold amplitude / sill thickness modelling. Yellow is top forced fold. Red is top sill. Orange is base sill. Sill is identified by (1) high amplitude, (2) positive polarity reflection forming the top of the sill, and (3) a corresponding negative reflection forming the base of the sill. The reflection is (4) laterally discontinuous, and (5) locally transgresses stratigraphy. The base reflection is easy to follow, as the only continuous negative polarity reflection with a different dip to the surrounding stratigraphy.	154
4.19	The first eight forced folds extracted horizons from seismic interpretations, used in the backstripping modelling. Blue is seafloor, orange is top forced fold, green is top sill, and red is base sill.	156
4.20	The final six forced folds extracted horizons from seismic interpretations, used in the backstripping modelling. Blue is seafloor, orange is top forced fold, green is top sill, and red is base sill.	157
4.21	First eight examples of backstripping modelling. Sill thickness (red envelope) against a range of modelled original fold amplitudes. The green shaded area is the envelope of values covered by different backstripping parameters for the forced fold amplitude.	158
4.22	The final six examples of backstripping modelling. Sill thickness (red envelope) against a range of modelled original fold amplitudes. The green shaded area is the envelope of values covered by different backstripping parameters for the forced fold amplitude.	159
4.23	New Zealand, with Resolution-1 well and seismic line shown. DEM data is from ETOPO1 (Amante, 2009).	161

4.24	Seismic data crossing the Resolution-1 well and forced fold. Yellow horizon is slightly below the top of the forced fold (chosen as the top of the forced fold shows slight erosion on a crossing line), red is the top sill reflection and orange is the base sill reflection.	162
4.25	Wireline log data for Resolution-1 wells. Tracks are Caliper log, Sonic log (DT, $\mu\text{s ft}^{-1}$), Gamma log (API), Deep and Shallow resistivity (RES-D and RESS, Ωm) and Spontaneous potential log (SP, mV). Blue vertical line denotes the top of the forced fold, while red vertical line denotes the top of the sill.	163
4.26	Time depth curve for Resolution-1, from the cumulative integration of the sonic log. This function was used to depth convert the Resolution-1 seismic data.	164
4.27	Resolution-1 forward model, comparing modelled forced fold amplitude to sill thickness. Overlap of the ranges for the majority of the fold gives support to the model of the forced fold amplitude / sill thickness discrepancy being compaction related.	165
4.28	Parameter sweep of decompaction parameters for forced fold/sill thickness RMS misfit minimization. Black points show the optimum parameters. . .	167
4.29	Best fitting inversion model for the Resolution fold-sill pair	167
4.30	Left panel: misfit curve for inversion of matrix velocity from sonic logs in the Resolution-1 well. Right panel: Porosity log using the inverted matrix velocities.	168
4.31	Summary of compaction model for the forced fold amplitude / sill thickness discrepancy. 1. Sediments are deposited, but as yet are not compacted or lithified. 2. a igneous sill intrudes by deforming the overburden into a forced fold. The sill cools and solidifies. 3. Sediment is continuously deposited, compacting the underlying sediment. The whole sediment pile compacts, leading to the amplitude of the forced fold being reduced. . . .	169
5.1	Seismic inline 20690 from the Rockall 3D seismic survey, and interpretation. Reflector A is shown in bright green. Black arrows show a possible fluid flow mechanism after Rateau et al. (2013). [Redacted]	173
5.2	Map showing the three surveys where reflector A was mapped in the North Rockall basin. See text for details.	175
5.3	Seismic inline 20670 from the Rockall 3D survey, showing the interpreted stratigraphy of the basin. [Redacted]	176
5.4	The same section on three different seismic surveys, showing that reflector A (delimited by arrows) is unlikely to be a seismic artefact. Reflector A is present on three different seismic surveys collected over a 20 year time span, with different seismic acquisition and processing for each survey. . .	177
5.5	Stratigraphic column for NE Rockall, showing context for reflector A. Bulk lithology based on well 164/28-1.	178
5.6	Time map of reflector A across the Rockall 3D seismic survey.	179
5.7	Map of reflector A across one of the 3D seismic surveys, with colours representing seismic amplitude.	181
5.8	Maps of Reflector A. Clockwise from top left: Time structure map, Amplitude (time) map, Time-Semblance co-blend map, Amplitude-Semblance co-blended map.	182

5.9	DSDP leg 48 hole 406 well logs, showing signatures which may imply an opal CT boundary. Zone where opal CT is found in cores is marked in red.	184
5.10	Map of depth below seafloor of reflector A in the NE Rockall seismic survey. Depth conversion used velocity information from well 164/27-1. Inset shows histogram of the depths.	185
5.11	Reflector A to underlying Balder isopach.	186
5.12	Sea floor to Balder isopack.	188
5.13	The depth below sea level of the top Horda horizon, interpreted on the Rockall 3D seismic survey.	189
5.14	Isopack map showing distance between the top Horda horizon and reflector A.	190
5.15	Topography of the opal A–CT boundary, with underlying sill outlines. The shallowest level of sills are coloured red. Under the model of Rateau et al. (2013), the highs should correlate with the edges of the shallowest sills or the outermost sills. This does not appear to be the case.	191
5.16	Similarity between the topography on the opal A–CT and a convective planform. a. Jones et al.'s (2012) figure 1a, showing the long wavelength gravity anomaly over Africa as a proxy for the mantle convective planform, modified to show sites of upwelling (green stars) and downwelling (orange dotted lines). b. Time structure map of the opal A–CT boundary in Rockall, with sites of upwelling (green stars) and downwelling (white dotted lines).	192
5.17	Radiometric derived ages for intrusion and extrusive magmatism in the NAIP, after Egbeni et al. (2014b). The dominant period of volcanic activity stretches from the mid Danian to the late Thanetian, a period of around 4 Ma.	193
5.18	Conceptual model for the formation of topography on opal A–CT boundary in Rockall. Many sills intrude close together spatially in a short period of time, leading to the intruded stratigraphic sequence heating up. This layer stays hot through much of the Eocene, driving a convective system of pore fluids. During this time, opal rich sediments are deposited, and the opal A–CT boundary develops topography as a result of the perturbations in lateral geothermal gradients caused by the convective system.	194
5.19	Scatter plot matrix for opal A–CT transitions less than 1 km deep. Plots on the lower left are scatter plots, the middle diagonal shows density polygons, and the upper right shows the Pearson correlation coefficient. See text for discussion.	196
5.20	Comparison of data with published model results for opal CT-quartz kinetic parameterization. a) shows measured opal A to CT transition depths in DSDP, ODP and IODP wells around the world (grey bars), and modelled opal CT to quartz depths (white fill). Inactive opal A to CT depths are in blue. b) shows cumulative frequency plots of the active opal A to CT transitions, along with best fitting kinetic parameterization, and published models. Of the published models, EC69 refers to Ernst and Calvert (1969), while D13 refers to Dralus (2013). c) shows the importance of burial rate and depth — an indicator of a strong thermal control on the reaction.	198

5.21	Inversion results for opal A–CT kinetic parameterization, model created by Jones, SM. Left panel is RMS misfit for frequency factor and activation energy. Right hand panel is best fit parameterization to all data.	200
5.22	Sedimentation rate for the three closest wells to the opal A–CT boundary in NE Rockall.	202
5.23	Model based predictions for the depth of the opal transition for different geotherms and burial rates, by Jones SM. Different lines correspond to different geothermal gradients ranging from $70^{\circ} \text{ km}^{-1}$ (top line) to $20^{\circ} \text{ km}^{-1}$ (bottom line) in steps of $10^{\circ} \text{ km}^{-1}$. bold line is $40^{\circ} \text{ km}^{-1}$, the present day geothermal gradient in the Faeroe-Shetland basin.	202
6.1	Schematic diagram showing the two potential modes of the sill-focused fluid flow model. a shows one possible mechanism, that the thermal aureole induces compaction and cementation in the host rock, decreasing porosity and permeability in the surrounding sediments and thus focusing fluid through sediments just outside of the aureole. b represents that the opposite can also occur, that the sill can cause development of a fracture network in the host rock, which may be higher permeability than the surrounding sediments and hence focus fluid flow.	206
6.2	Panel A shows all three datasets, the 2D OGA seismic data set, and the NE Rockall and Judd basin 3D seismic datasets. Panel B shows the Judd 3D dataset, while Panel C shows the NE Rockall 3D dataset. Bathymetry is ETOPO1 satellite derived bathymetry (Amante, 2009).	207
6.3	Locations of sills and major structural features in the Faeroe-Shetland Basin, and the presence/absence of shows in exploration wells. Modified after Rateau et al., 2013	208
6.4	A selection of seismic data and interpretations from the OGA Rockall survey. Measurements from the well to the nearest sill edge are given in red.	209
6.5	Schematic showing measurements made on the various datasets. Measurement 1 shows a well outside of the sill complex, where the measurement to the nearest sill equates to measuring to the edge of the sill complex. Measurement 2 is for a well in the middle of the sill complex. In this situation the measurement is made to the nearest sill tip which is not overlain by another sill vertically above. This method works for all sill complexes with randomly distributed, similar diameter sills without intervening dikes, as shown in this figure. However the method breaks down where large diameter, regionally extensive sills exist at depth, which would focus fluid to the edge of the sill complex and leave all other sills in a migration “shadow zone”. However, for the study datasets this should not introduce errors, as all wells happen to be drilled near the edge of the sill complex anyway.	211
6.6	Model set up for Monte Carlo models. Note the lack of scales on the y axis — $P(A)$ and $P(C)$ were systematically varied throughout the modelling.	214
6.7	The distribution of distances from sill edges for wells with and without shows. Upper panel shows a histogram of wells with and without shows. The lower panel is a box and whisker plot of the same data, where the edges of the box show the lower and upper quartiles and the central line of the box shows the median. For detail on how to interpret box and whisker plots, see caption on figure 3.9.	216

6.8	P-value as a function of the threshold value used to define a sill as close or not close to a sill edge. Black points are the calculated p-values. Blue line is a loess smooth trend line of the black points. Red line is the significance level of 0.05. If black points are below the red line, they are statistically significant and therefore there is a relationship between the chance of observing a show in a well and the distance from the sill. If the points are above the red line, the set of wells “close” to sills are statistically indistinguishable from the set of wells “not close” to sills, which would imply no effect of sills on the chance of observing a show in a well.	217
6.9	Monte Carlo models with real data plotted as points. Curves are Monte Carlo models, where $P(C)$ is held at 0.5, and red, yellow, blue and purple curves correspond to $P(A)$ s of 0.9, 0.8, 0.7 and 0.6 respectively. Model curves show that the bigger the difference in probability in observing a show in well “close” and “not close” to a sill, the larger the value of $\frac{A/(A+B)}{C/(C+D)}$. Points have values very close to 1, indicating no difference in proportions close to and far from sill edges.	218
6.10	The sample size needed to observe different effect sizes, assuming the standard (in the statistical literature) power values of 0.8 and significance level of 0.05. In the case of this chapter, effect size corresponds to the increase in likelihood of observing a show, and the sample size is the number of wells in the basin before the effect could be observed.	221
6.11	Conceptual model of how sills might influence fluid flow in sedimentary basins. The key factors are how close the sill is to the exploration target (labelled target), and whether other more permeable pathways (e.g. faults, carrier beds) exist in between. See text for discussion.	222
7.1	Polygons of sill extent, modified after White and Mckenzie (1989), Eldholm and Grue (1994), Geissler et al. (2017) and Horni et al. (2017). Projection is Albers conic equal-area projection.	228
7.2	Schofield et al.’s (2012) figure 9, showing a sill intruding without deforming its overburden, at least at the scale of the field outcrop.	231
7.3	Model of a conductively cooling intrusion with latent heat, from equation 7.4. Parameters are $a = 20$ m, $T_m = 1200$, $T_0 = 30$, $C_p = 1480 \text{ J K}^{-1}$, $\rho = 2830 \text{ kg m}^{-3}$, $k = 1 \text{ m}^2 \text{ s}^{-1}$ and $L = 4e5 \text{ J kg}^{-1}$. A future research target may be relating such temperature models to zones of diagenetic alteration inside thermal aureoles, to predict aureole fluid flow properties.	234
7.4	Forced fold horizon (top Balder) in the Rockall 3D dataset. Field of view is the same in each image.	235
7.5	Pollard’s (1973) figure 15, showing vectors visualising the calculated deformation in an ideal forced fold.	236
7.6	Seismic line of the Dooish discovery, showing a sill (labelled “Tertiary intrusive”) climbing the flank of the structure. Other seismic lines show the sill to transgress almost to the top of the structure. Accessed on the 22/12/2017 from http://www.serica-energy.com/downloads/farmouts/Serica_Rockall_APPEX2013_Presentation_March2013.pdf	237
7.7	White et al.’s (2008) figure 2, showing wide angle data from the Hatton margin (a), the Faeroe-Shetland margin (b) and seismic reflection data with an overlaid velocity model from the Faeroe-Shetland margin (c). For full caption, see White et al. (2008).	240

-
- 7.8 Figure 3.1 from Dralus (2013), showing the trapping mechanism (via permeability decrease) for the opal transition play in the San Joaquin basin, USA. 242
- 7.9 Basin floor fan play in NE Rockall. Upper left is seismic section in TWT. Horizons from top are Horda (pink), opal A-CT (green), basin floor fan (purple), Balder (orange), Flett (green), Lambda (brown), Vaila (blue), Cretaceous undifferentiated (beige) (see figure 5.5 for stratigraphy). Upper right is time structure map of the basin floor fan horizon. Lower left is dominant frequency, and lower right is Envelope. Blue and red line shows the seismic line. 243

List of Tables

2.1	Wells used in this thesis, and seismic lines each well intersects.	59
2.2	Summary of resolution parameters for datasets used in this thesis.	62
3.1	Differences in sample statistics when using decompation routines on sill emplacement depth data. Measurements are in km.	93
3.2	Results of the missing sills test for 2D seismic surveys.	103
3.3	Multiple linear regression model coefficients to predict sill area density from distance to the palaeo-plume centre and the water depth (a proxy for crustal thickness).	110
3.4	Polynomial multiple linear regression model coefficients to predict sill area density from distance to the palaeo-plume centre and the water depth (a proxy for crustal thickness).	111
3.5	Parameters used in LEFM models	113
5.1	Rate constant units for different reaction orders	199
6.1	Summary statistics for the distances from wells with and without shows to the nearest sill edge	215

Abbreviations

LIP	L arge I gneous P rovince
NAIP	N orth A tlantic I gneous P rovince
PETM	P aleocene- E ocene T hermal M aximum
TWT	S eismic T wo W ay T ravel time
RMS	R oot M ean S quared
PD	P robability D istribution
DHI	D irect H ydrocarbon I ndicator

Symbols

V_p	P-wave velocity	m s^{-1}
V_{sill}	P-wave velocity of a sill	m s^{-1}
d	Distance	m
d_T	Tuning thickness	m
F_d	Dominant frequency	Hz
A	Amplitude	m
N	Number	
Z	Depth	m
m	Solid grain proportion	
w	Sill width	m
W	Nondimensionalized sill width	
l	Sill length	m
h	Sill height (= 1 for 2d case)	m
a	Sill horizontal coordinate	
A	Maximum diameter of a sill	m
G	Shear modulus	Pa
P_e	Elastic crack closing pressure	Pa
P_h	hydrostatic pressure	Pa
P_v	Viscous resistance force	Pa
P_c	Crack extension pressure	Pa
V	Volume	m^3
t	Time	s
E	Young's modulus	Pa
A_0	Dimensionless variable from Spence and Turcotte (1985)	
B	Dimensionless variable from Spence and Turcotte (1985)	

ai	Acoustic impedance	Pa s m^{-3}
RC	Reflection coefficient	
g	Acceleration due to gravity, 9.81	m s^{-2}
u	Velocity	m s^{-1}
m	$G/(1 - \mu)$	
λ	Wavelength	m
ϕ	Porosity	
ϕ_0	Initial porosity	
ν	Poisson's ratio	
ΔP	Magma overpressure	Pa
ρ	Density	kg m^{-3}
μ	Viscosity	Pa s

To my friends and family

Chapter 1

Introduction

Igneous sills are horizontal or subhorizontal intrusions which are common in many sedimentary basins around the world (e.g. [Airoidi et al., 2011](#); [Burgess et al., 2017](#); [Fernandes, 2011](#); [George, 1993](#); [Hansen et al., 2004](#); [Jackson et al., 2013](#); [Magee et al., 2016](#); [Spacapan et al., 2017](#); [Svensen et al., 2004](#); [Walker et al., 2017](#)). Interconnected sills (sill complexes) form part of the magmatic plumbing system, which allows magma transport through the brittle crust to sites of emplacement or eruption (Figure 1.1) (e.g. [Jerram and Bryan, 2015](#)). Sills are found in greatest numbers in large igneous provinces (LIPs) (see [Bryan and Ernst, 2008](#), for a review of definitions). In LIPs, intrusion of a large number of discrete sills form high velocity lower crustal bodies ([White et al., 2008](#)), making them a volumetrically important part of an LIP. The emplacement of LIPs are often associated with some of the most cataclysmic events in earth history, involving continental splitting, magmatic outpouring, and mass extinctions ([Bond and Grasby, 2017](#); [Ernst and Youbi, 2017](#); [White and Mckenzie, 1989](#); [Wignall, 2001](#)). However, as yet the volumetric component of shallowly intruded sills has not been properly quantified in LIPs; this will be addressed in this study. Furthermore, neither volcanic eruptions nor magmatic intrusions are continuous events, they are discrete and punctuated events. By studying the sizes of sills we can get closer to an understanding of the average size of a magma batch, which may shed light on the fundamental process changing continuous magma production at depth into punctuated eruption or intrusion in the upper crust.

Sill intrusion is the dominant process for building two thirds of the Earth's crust — oceanic crust makes up two thirds of the Earth's crust at the present day, and it is now accepted that a significant proportion of oceanic crustal accretion takes place by intrusion of sills across the depth range between the base of the sheeted dykes and the Moho ([Henstock et al., 1993](#); [Marjanović et al., 2014](#); [Singh et al., 2006](#)). However, limited worldwide outcrop of these sills exists, and geophysical imaging of these sills is



FIGURE 1.1: An example of a sill at Kilt Rock on the Isle of Skye, Scotland. The sill, which makes up a famous landmark, is Paleocene in age and intrudes a Jurassic clastic succession.

extremely difficult. Studying sills on the continents, however, is much easier, allowing knowledge of such an important process to be gained in a simpler setting provided sill intrusion in the two environments shares characteristics.

Sills are important for their implications for petroleum systems and exploration for oil, gas, and unconventional hydrocarbons. The process of deformation at the surface above a sill is termed forced folding. Sills can form traps in forced folds which can reservoir hydrocarbons (e.g. the Tulipan discovery, see [Schmiedel et al., 2017](#)). Furthermore, at the time of emplacement mafic sills can be in excess of 1100°C ; easily hot enough to cause thermal maturation of organic rich shales and thus hydrocarbon production (e.g. [Aarnes et al., 2011](#)). This mechanism is one of the leading hypotheses for the rapid generation of large volumes of greenhouse gasses during, for example, the Paleocene-Eocene thermal maximum ([Svensen et al., 2004](#)), the end Triassic mass extinction ([Davies et al., 2017](#); [Heimdal et al., 2018](#)) and the end Permian mass extinction ([Jamtveit et al., 2008](#)). However, palaeoclimatic change is difficult to model quantitatively without robust statistics to feed into models. Much of this thesis describes measurement of various sill dimensions, both for study in their own right, and for input into such models. The measurements this thesis is mainly focused around are fundamental dimensions such as the diameter and thickness of sills. Knowing accurate values for these feed directly into thermal models for sill cooling which can allow prediction of the mass of greenhouse gasses emitted from intrusion into different host rocks.

Sills are also important because present day sill intrusion and emplacement events are often found to precede volcanic eruptions and can instigate ground deformation, thus making understanding them of importance for hazard prediction and forecasting (Figure 1.2) (e.g. [Castro et al., 2016](#); [Sigmundsson et al., 2010](#); [Tarasewicz et al., 2014](#)). Models of magmatic intrusion are important for understanding observations from GPS base stations at actively deforming volcanoes, which can form part of eruption early warning systems (e.g. [D’Auria et al., 2015](#)). However, recent work by [Magee et al. \(2013a\)](#) has highlighted that ground deformation is not necessarily equated to the size of a magmatic

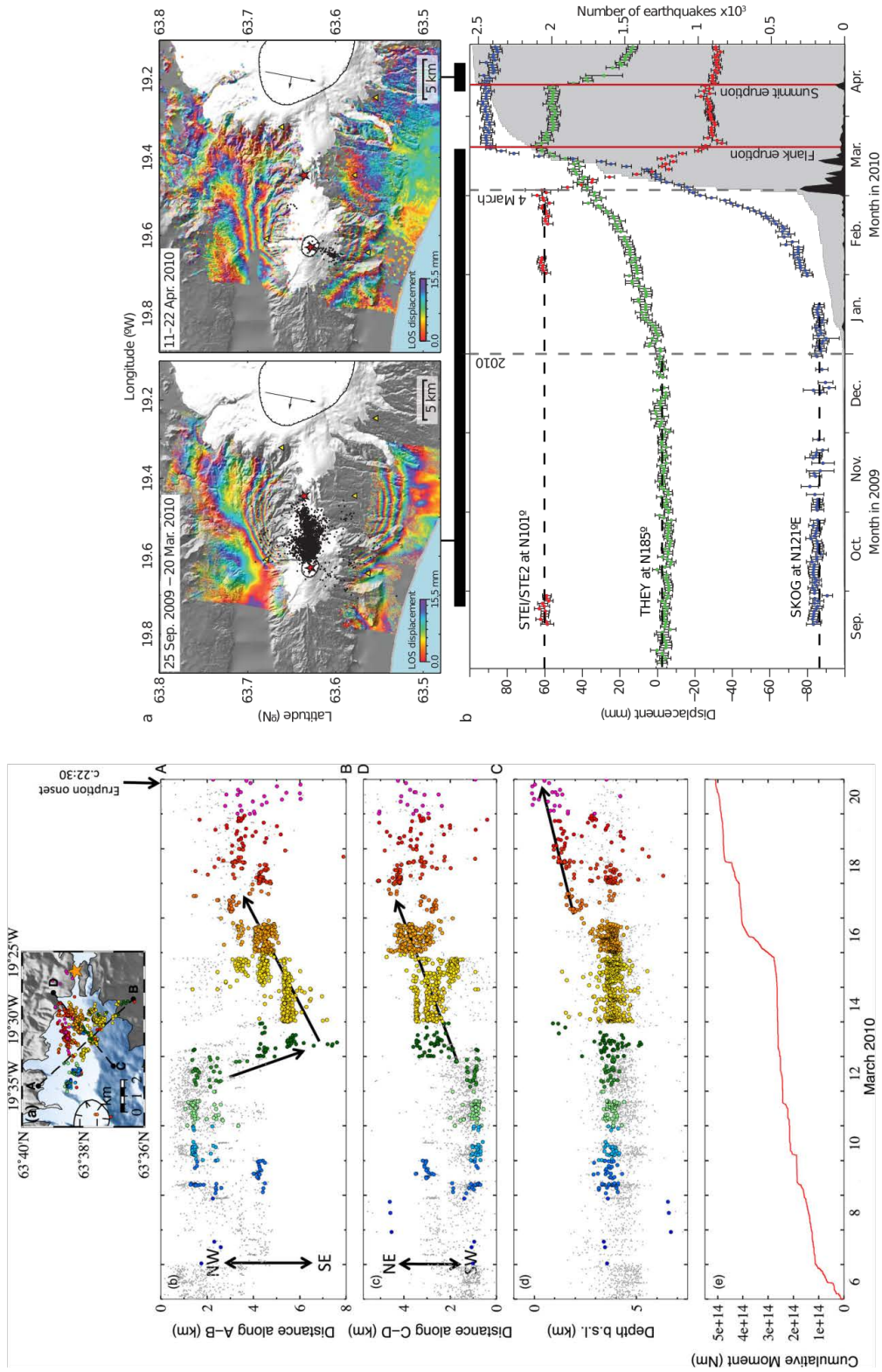


FIGURE 1.2: Sill intrusion recorded by different data types for the 2010 Eyjafjallajökull eruption. Left: Tarasewicz et al.'s (2014) figure 9, showing microseismicity tracking the intrusion of a sill. Right: Sigmundsson et al.'s (2010) figure 4 showing inSAR data of the same intrusion event.

intrusion at depth. Unravelling this discrepancy is thus important for understanding how observed ground deformation can feed into hazard forecasting. This thesis will not directly study how ground deformation leads to hazard prediction and forecasting, but will study discrepancies between the amount of magma intruded and the amount of deformation observed at the surface, which may feed into forecasting models in the future.

In the following sections the past understanding and present state of research on sills in a number of situations of interest is described.

1.1 A global analysis of sill size distributions

1.1.1 Sill size distributions

The Paleocene–Eocene Thermal Maximum (PETM) was a time of rapid carbon input to the atmosphere around 56 Ma (Dunkley Jones et al., 2017). The PETM has been proposed to be the closest geological analogy to present day anthropogenic climatic warming (Bowen et al., 2006; Zachos et al., 2008). Svensen et al. (2004) suggested that sills intruding organic-rich source rock sequences during emplacement of the North Atlantic Igneous Province (NAIP) LIP may be responsible for production of large amounts of methane and carbon dioxide which are expelled through hydrothermal vents, which could drive ancient warming (Figure 1.3).

A number of sill intrusion features control whether venting of greenhouse gasses to the atmosphere is a viable mechanism to drive palaeoclimatic warming: 1. The number of sills intruding organic rich source rock, 2. the surface area and thickness relationships of the sills (which control the thermal aureole size), 3. the number of hydrothermal vents available to transport hydrocarbons to the atmosphere, 4. the duration of the magmatic emplacement event (which controls the regional gas flux), 5. the emplacement depth of the sills (as the source rock sequences are not expected to be uniformly distributed with depth, and the background temperature influences final aureole size) and 6. the source rock richness.

Previous estimates of these parameters have been based on sparse datasets (e.g. Jackson et al., 2013; Magee et al., 2014a; Svensen et al., 2004, 2006, 2012b). Svensen et al. (2004) mapped 735 vents emanating from sill tips in an area of 85,000 km², but modelled them as $0.9 - 2.5 \times 10^4$ km² magma volume on the basis of an average vertical accumulated sill thickness of 100 – 300 m in the Vøring and Møre basins, rather than mapping and modelling the sills in detail. Similarly Svensen et al. (2006) and Svensen et al. (2012a)

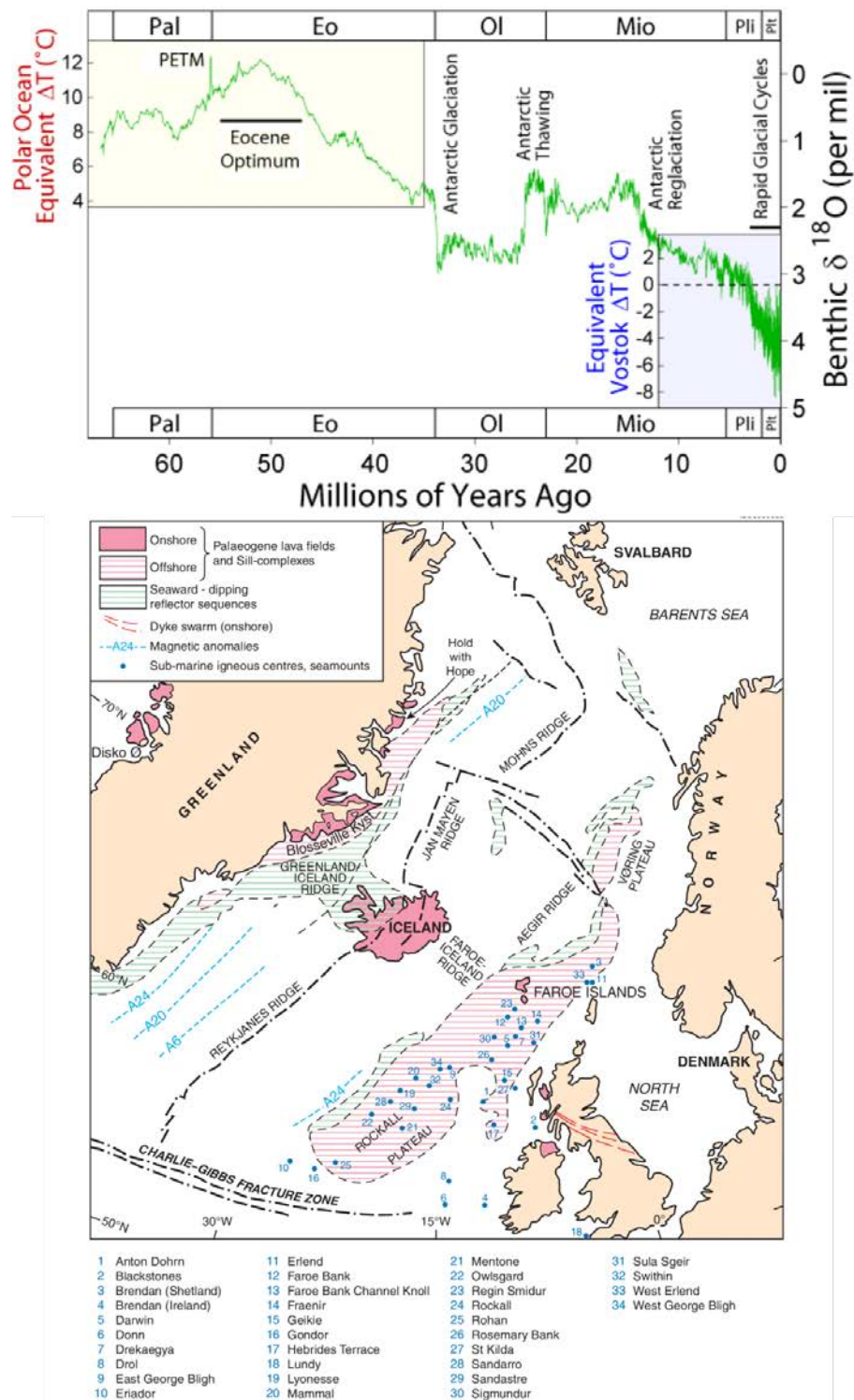


FIGURE 1.3: The PETM, shown in oxygen isotope records (after Zachos, 2001, (upper panel)), and the possible cause of it: the emplacement of the NAIP (lower panel, after Saunders et al. (1997), from http://earthwise.bgs.ac.uk/index.php/Igneous_geology:_regional_setting,_Palaeogene_volcanic_districts_of_Scotland, accessed 5/10/2017)

linked the Karoo-Ferrar LIP to rapid warming in the Toarcian, and found a volume of $340,000 \text{ km}^3$ of sills in an area of $5.5 \times 10^5 \text{ km}^2$ in the Karoo basin. However, as these authors do not describe the average sizes of these sills, more useful modelling parameters such as sill area-density (number of sills per kilometre), sill radius or diameter and sill thickness are difficult to derive. Luckily, in some publications these statistics can be derived. For example, [Magee et al. \(2014a\)](#) found 82 sills in a 2400 km area ($\sim 0.03 \text{ sills km}^{-2}$) near the middle of the eastern flank of the Rockall Basin, and those sills were 5.6 km diameter on average. [Jackson et al. \(2013\)](#) found 33 sills in an area of $4.4 \times 10^4 \text{ km}^2$ ($\sim 0.0008 \text{ sills km}^{-2}$) in the Bight Basin, with an average diameter of 7.4 km. From these examples it can immediately be seen that the number and dimensions of sill vary from basin to basin significantly. Thus to test the influence of the NAIP on the PETM, there is a real need for hard statistical data with which to parameterize and model the influence of sills on climatic processes.

1.1.2 Sill emplacement models

Measurements of the average size, thickness and profile shape of sills can also be used to constrain different models of sill emplacement. Currently sill emplacement models can be classified into one of three essential types:

- A fluid filled crack (e.g. [Johnson and Pollard, 1973](#); [Lister, 1990](#); [Lister and Kerr, 1991](#); [Rubin, 1995](#); [Spence and Turcotte, 1985](#))
- A partially ductile viscous indenter (e.g. [Scheibert et al., 2017](#); [Spacapan et al., 2017](#))
- Thermally triggered fluidization model (e.g. [Schofield et al., 2010, 2012](#))

Figure 1.4 summarises these models, where panels a – d represent variations on a fluid filled crack model, panel e shows a fluidization model and panel f shows the viscous indenter model. These models have proved difficult to test against real sills because only seismic data allows the measurement of the whole sill, as opposed to a 2D section at field outcrop. A 2D field outcrop is unlikely to represent the true dimensions of the sill (e.g. compare figure 1.1 to figure 1.5), and the main (and arguably most important, given that many models are two dimensional) prediction of many of the numerical models is the thickness versus diameter profile of the intrusion. In Chapter 3, use is made of rare examples of sills where both the top and base of the sill are imaged on seismic data, allowing measurement of the whole sill, to test published analytical models against seismic observations of sills. This novel approach, which has not been tried before, makes advances in testing these models by improving the resolution of sill geometrical measurements (uncertainty of which is discussed in chapter 3), offering the first chances

to test many of the models, and also offering insight into the underlying parameters representing host rock properties (section 3.5).

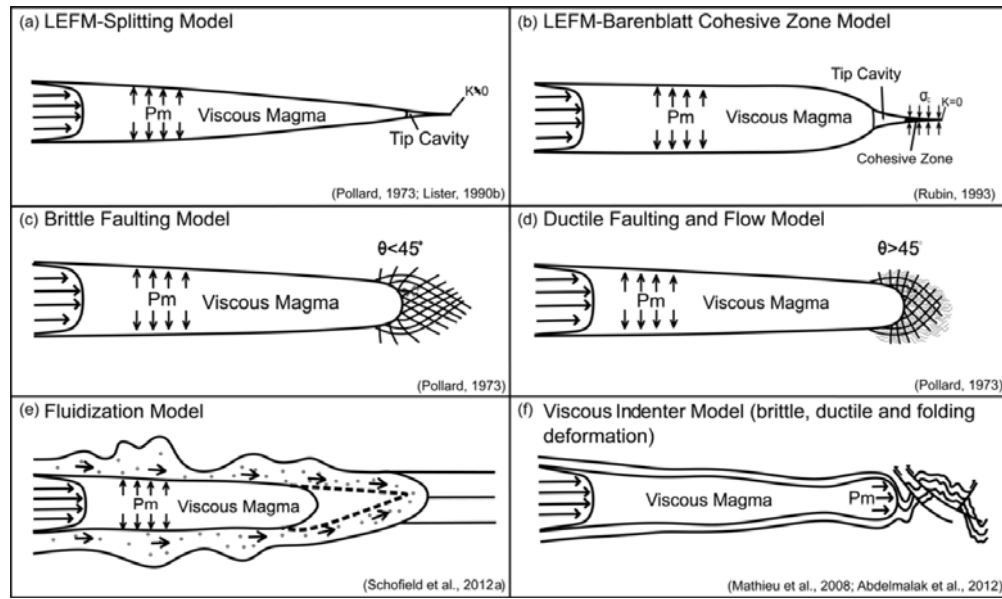
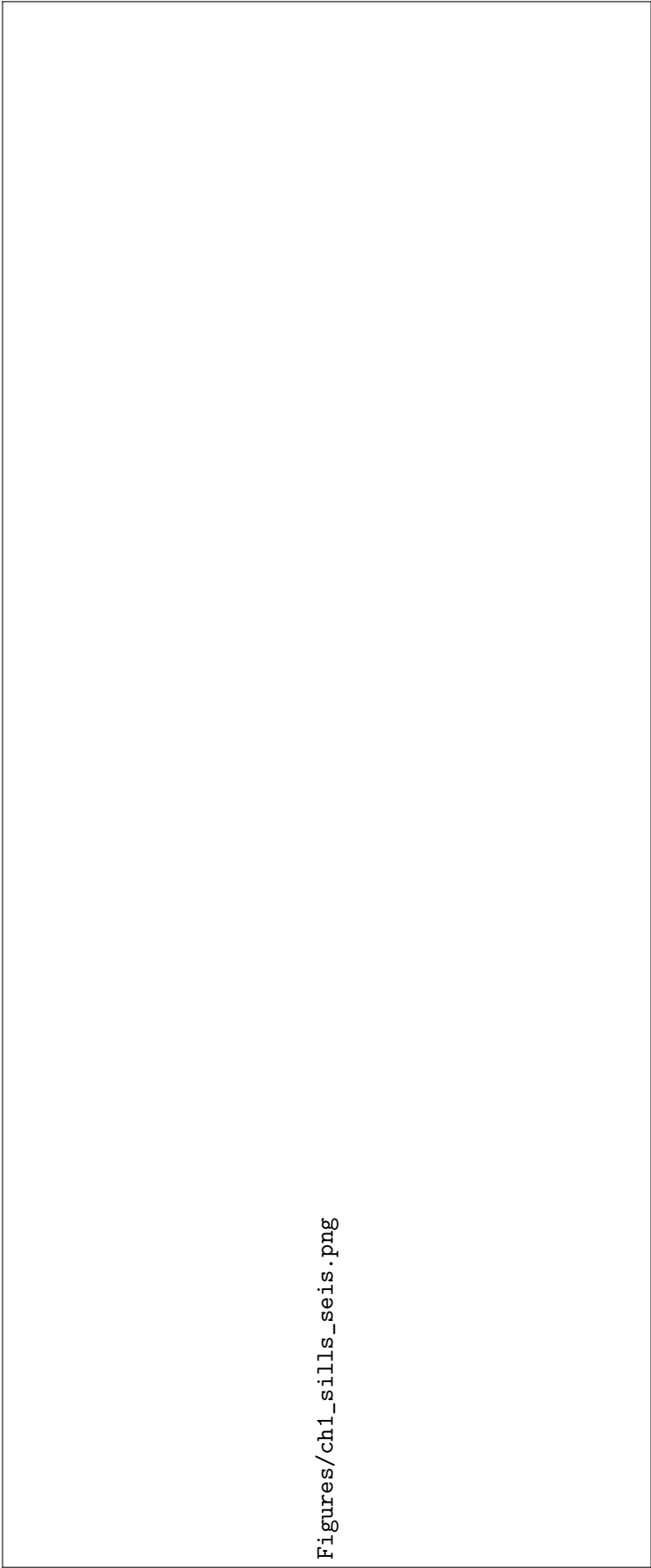


FIGURE 1.4: Spacapan et al.'s (2017) figure 1, showing common models for sill intrusion. a to d represent variations on the fluid filled crack model. e represents the fluidization model, and f represents the viscous indenter model. See text for details.



Figures/ch1_sills_seis.png

FIGURE 1.5: A typical seismic section from the Rockall basin. Seismic data allows the full sill extent to be imaged. [Redacted]

1.2 Impacts of sills on petroleum systems

Sills can have potentially significant impacts on sedimentary basins, having the potential to alter the conditions for each of the factors needed for a working petroleum system. A “working” petroleum system is one where: a source rock is present and at high enough temperatures for maturation to occur; a reservoir sequence exists; a migration pathway connects the source rock to the reservoir; and a trap exists consisting of a permeable and porous reservoir and low permeability cap rock sequence such that hydrocarbons migrating into the trap cannot migration out again; and that the timing of these elements to be in place is such that a petroleum accumulation can occur (e.g. [Gluyas and Swarbrick, 2013](#)).

At the time of intrusion, sills are hot enough to cause maturation in the thermal aureole around them, should they intrude source rock sequences (e.g. [Bishop and Abbott, 1995](#)). Sills also cause fracturing and development of joint networks in their host rocks, thus potentially having a positive impact on primary migration from the source rock sequence into faults or carrier beds which may make up a migration pathway. Sills themselves can be permeable due to well developed columnar joint networks, thus they may act as migration pathways if in a favourable configuration (e.g. [Cartwright et al., 2007](#); [Rateau et al., 2013](#)). If emplaced shallowly, sills can cause appreciable folding above them to accommodate the intruded magma volume, and thus can form traps for hydrocarbon accumulations ([Schmiedel et al., 2017](#)). Chapter 4 of this thesis will focus on the effect of sills on forming potential traps, while Chapter 6 will focus on testing evidence that sills have a significant effect on migration and fluid flow at a basin scale.

1.2.1 Forced folds and the amplitude/thickness discrepancy

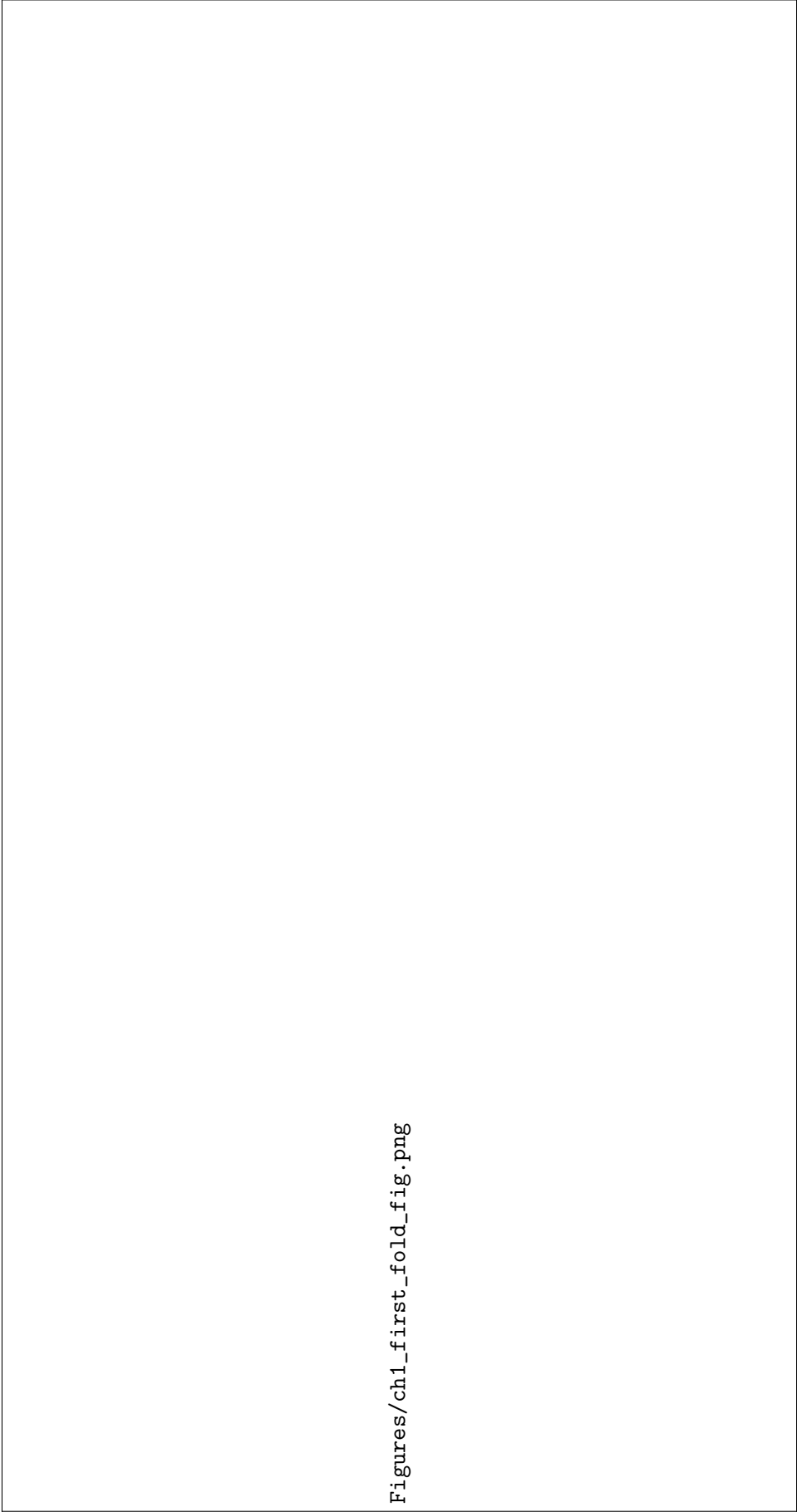
When intruded shallowly, sills deform the overburden into a structure commonly termed a forced fold ([Hansen and Cartwright, 2006a](#)) (e.g. figure 1.6). This is formed by hydraulic-like jacking-up of the overburden ([Gilbert, 1877](#)). Such folds may form an ideal 4 way dip closed structure, should suitable reservoir and seal sequences exist above the level of sill emplacement, or should seal sequences be deposited immediately above the forced fold. Obviously the main challenge for exploiting such a structure as a viable hydrocarbon field is the presence of a hydrocarbon charge; however, should this be in place a number of potential challenges still exist in exploitation of such structures. [Hansen and Cartwright \(2006a\)](#) and [Magee et al. \(2013a\)](#) show that crestal normal faults are commonly found in such structures due to outer-arc extension during folding, which could easily compartmentalise reservoir sequences. If intra-reservoir seals are required to make the play work, these same faults could also lead to seal breach and hydrocarbon

leakage. Similarly, the edges of the fold have been predicted to be the highest strain zones (e.g. [Gudmundsson and Lotveit, 2014](#); [Malthe-Sørenssen et al., 2004](#)), which would predict faulting in these zones. Such faulting could move the spill-point for forced fold hosted reservoirs, reducing volumes of hydrocarbons in-place. [Hansen and Cartwright's \(2006a\)](#) figure 4 and [Magee et al.'s \(2013a\)](#) figure 2 support that this can indeed occur, as do a number of examples from seismic datasets used in this thesis. However, one of the most interesting, but poorly understood, observations is that the amplitude of the forced fold often does not equal the thickness of the sill. This observation was found by [Magee et al. \(2013a\)](#) and [Jackson et al. \(2013\)](#), and is seen in [Hansen and Cartwright's \(2006a\)](#) figure 4b and 4c. This thesis explores whether post emplacement compaction is a sensible model to explain the observed differences in fold amplitude and sill thickness, and what this implies for any reservoir sequences present in forced folds.

1.2.2 The search for a new fluid flow proxy

Fluid flow is difficult to observe and quantify on seismic data. Most methods involve observation of amplitude blooms (increases) and fades (decreases), polarity changes, or seismic chimneys (see [Cartwright \(2007\)](#) and [Ligtenberg \(2005\)](#) for reviews, and [Simm and Bacon \(2014\)](#) for background). Such methods rely on the fact that changes in fluid content can affect the bulk density and p-wave velocity of the rocks, which causes them to be imaged differently on seismic data. Whether any of these amplitude based proxies are or are not observable on real seismic data is controlled by the seismic amplitude of the reflection of such a feature compared to the background amplitude — if the difference in amplitude is small, the feature is less likely to be correctly interpreted. A potential proxy for fluid flow could be diagenetic boundaries. Some diagenetic boundaries may represent isothermal boundaries in sedimentary basins, and thus changes in their depth could show changes in geothermal gradients, which in turn could show passage of hotter fluids from the depth of the basin to shallower regions.

In Chapter 5 the evidence for one such diagenetic boundary — an opal A to opal CT transition, is described in the Rockall Trough. Opal A is a silicious sediment, formed mainly from the remains of phytoplanktonic organisms such as diatoms and radiolarians, as well as sponge spicules, clay and detrital quartz. Deposition of such sediment is often thus correlated with times of high organic productivity ([Ireland et al., 2011](#)). The “A” in opal A stands for amorphous, due to its disordered, non-crystalline structure. Opal A can have moderate inter- and intra-granular porosity, due to the high intraskeletal porosity in many species of diatoms and radiolarians. Opal A undergoes a standard diagenetic sequence from opal A → opal CT → microcrystalline quartz. Each of these reactions is a dissolution-reprecipitation reaction. Transformation of opal A to opal CT can result



Figures/ch1_first_fold_fig.png

FIGURE 1.6: A forced fold and shallowly emplaced sills imaged on seismic data in the Rockall basin. [Redacted]

in a porosity loss of up to 30% (Isaacs, 1981). This transition accompanies a significant increase in bulk density and p wave velocity, which leads to a high reflection coefficient and hence a relatively bright seismic reflection. The primary control on the opal A-CT transition is temperature (Kastner and Gieskes, 1983). However, other controls include pore water chemistry, grain size, pressure and clay content.

In Chapter 5, the idea of the opal A-CT boundary representing an isothermal boundary is explored by mapping the opal A to CT boundary in three dimensions and comparing it to the spatial distribution of sills underlying it, *sensu* Rateau et al. (2013). A database of opal A to CT depths is then collated from DSDP, ODP and IODP wells around the world. This database is used to parameterize the reaction kinetics to model the boundary. Modelling the boundary allows us to study whether the boundary shows evidence for fluid flow, and the relationship between the boundary and the sills underlying it.

1.2.3 Statistically testing fluid flow around sills

Rateau et al. (2013) outlined a theoretical model for how sills and igneous intrusions could focus fluid (and potentially petroliferous fluid) around a sedimentary basin. The idea hinged around sills either working as barriers or conduits for fluid flow. In the model, two end-member possibilities exist. First, sills can act as a barrier due to low intergranular porosity within the basalt and thus fluids flow preferentially around sills and are focused off sill tips. Secondly, sills have well-developed columnar jointing networks within them, and fluid may migrate through this fracture network leading to the same effect of concentrating fluid flux at the sill tip. In Chapter 6, statistical methods are used to re-examine the data originally used in the study. In the original study, maps were shown and described as showing a correlation between more shows being found nearer sill edges than away from sill edges. This description is formalized as that the number of wells with hydrocarbon shows should correlate with measured distance from sills if the model is representative of migration in the basin. This idea is tested statistically, and then Monte Carlo methods are used to simulate what should be seen if this relationship was real, and compare it with our own and published data.

1.3 Thesis outline and research questions

As so far outlined, sills can have a number of impacts on global climate and on petroleum systems. This thesis studies many of these effects and tests a number of hypotheses. In this section, the main focuses and hypotheses to test in each chapter are listed. In order, these are:

Chapter 1 (this chapter), which outlines the current state of knowledge in relation to sill occurrence, size distributions, emplacement mechanisms, climatic effects and effects on petroleum systems. This chapter then describes the various study areas used to investigate each of the following research questions.

Chapter 2 describes the technical information for each seismic survey used to investigate research questions in the following chapters.

Chapter 3 focuses on different geometrical measurements of sills such as sill diameter, sill thickness, sill transgressive height and sill emplacement depth. These measurements are used to test hypotheses relating changes in sill measurements between different sedimentary basins and different sill shapes. The chapter then tests hypotheses of how the number of sills within a geographic area (sill area-density) vary with distance from the Iceland mantle plume and with sedimentary basin water depth. At the end of the chapter a number of sill and dyke emplacement models are tested using the geometrical measurements on sills.

Chapter 4 examines causes of the “Sill thickness – forced fold amplitude discrepancy” — the observation the amplitude of a forced fold is of less than the thickness of the sill causing it. This chapter tests the hypothesis that this discrepancy may simply be due to post emplacement compaction, rather than processes happening during emplacement, such as are currently prevalent in the literature.

Chapter 5 examines an unusual seismic reflection found in the northeast Rockall Basin, and explains its morphology and characteristics as likely to be an opal A–CT transition. A new model is created for the chemical kinetics of opal A–CT transitions, with the aim of understanding the undulating nature of the boundary. Arising from this, a new hypothesis is suggested involving convection cells driven by thermal energy from underlying sills to explain the reflection geometry.

Chapter 6 tests a popular model for hydrocarbon migration around a cold, already emplaced sill. Data from the original study that proposed the model is re-examined, along with extra data from the Rockall Basin, and new statistical methods are created to test the underlying hypotheses of the sill focused fluid flow.

Chapter 7 discusses the wider implications of the work in chapters 3 — 6, and talks about links and central themes tying them together.

Chapter 8 summarises the work in previous chapters.

1.4 Study areas

The age, causes of magmatism, and the host rock sequences intruded are important background information for the studies in this thesis. This section will give a brief geological overview of each study area to give context to the following chapters. The datasets themselves will be introduced in Chapter 2.

1.4.1 Atlantic margin basins

Figures 1.7, 1.8 and 1.9 show datasets studied in the Atlantic margin basins — the Porcupine Basin, the Rockall Trough, the Hatton Basin and the Faeroe-Shetland Basin. The Atlantic margin basins formed following orogenic collapse of the Caledonian mountain belt in the Silurian–Devonian. In the Permo–Triassic the basins were a series of minor half grabens opening in response to the breakup of Pangea. Rifting occurred from the Triassic until the Cretaceous in discrete diachronous rifting episodes (Coward et al., 2003). From the Late Cretaceous or Early Paleocene onwards, all basins were thought to be undergoing post-rift thermal subsidence (Dean et al., 1999; Tate et al., 1999; Turner and Scrutton, 1993). Magmatism in the Atlantic margin basins is thought to cover a wide range of time from the Campanian (Cretaceous) to the Lutetian (Paleocene), with the main phase extending from the Danian to the Thanetian (Egbeni et al., 2014a; Magee et al., 2014a; Parnell-Turner et al., 2014), coinciding with the initial emplacement of the Iceland plume and generation of the North Atlantic Igneous Province (NAIP). Sills are mainly found within the shale-rich Cretaceous sequences in the Atlantic margin basins (Schofield et al., 2017). Cretaceous sequences are represented by the Shetland Group in the Rockall Trough and FSB, which comprise marine deep water shales with later shallow deltaic sequences which prograded into the basin (Doré and Lundin, 1996; Schofield et al., 2017). In the Porcupine basin, the Cretaceous is mainly chalks and carbonaceous sediments. A smaller proportion of sills are found in the Paleocene sequences, even extending up to the Early Eocene sequences (Magee et al., 2014a). These sequences mainly comprise deep water fine-grained sequences, with discontinuous sands. Submarine fans developed during this time, first filling fault-controlled basin floor deeps, and later covering these local depocentres and filling the basin to onlap the continental shelves, driven by uplift from the Icelandic mantle plume (White et al., 1997). Where penetrated, the texture of the igneous intrusions in the Atlantic margin basins vary with intrusion size, are generally medium to coarse grained, and have a MORB to T-MORB composition (Gibb and Kanaris-Sotiriou, 1988). Suberial, seaward dipping lavas, agglomerates, and hyaloclastites were deposited off Rockall Bank and in the North of the

Rockall Basin during this time. These sequences cause major seismic imaging problems, which make imaging intrusions challenging.

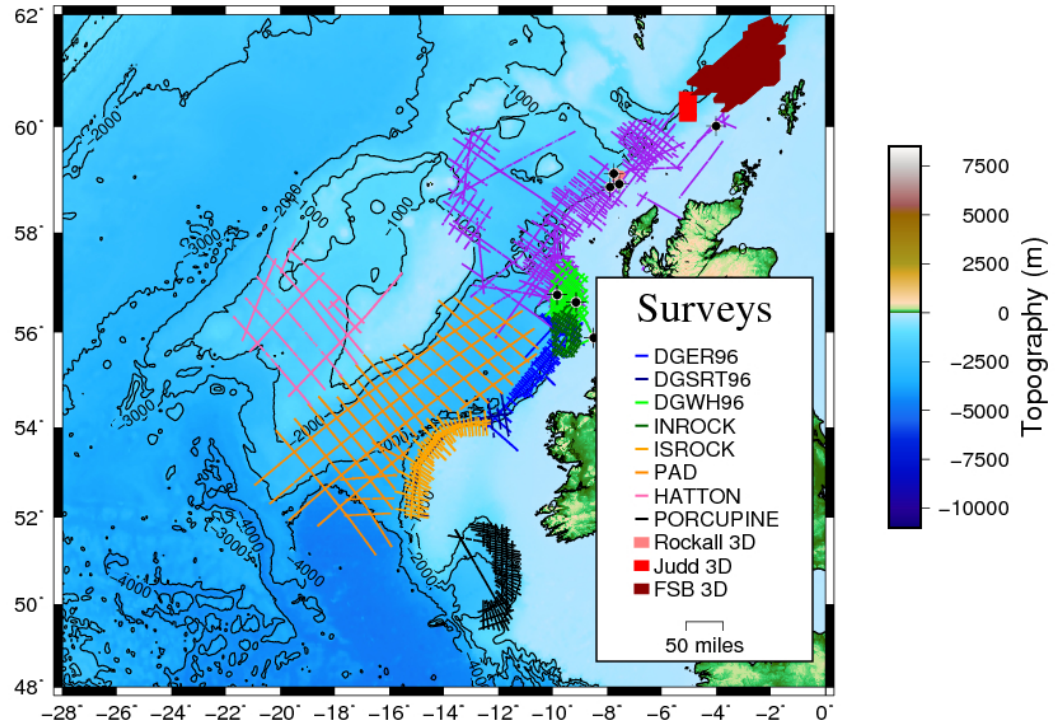


FIGURE 1.7: Datasets used in the Atlantic margin basins. Base map show shows bathymetry (data: ETOPO1 ([Amante, 2009](#))).

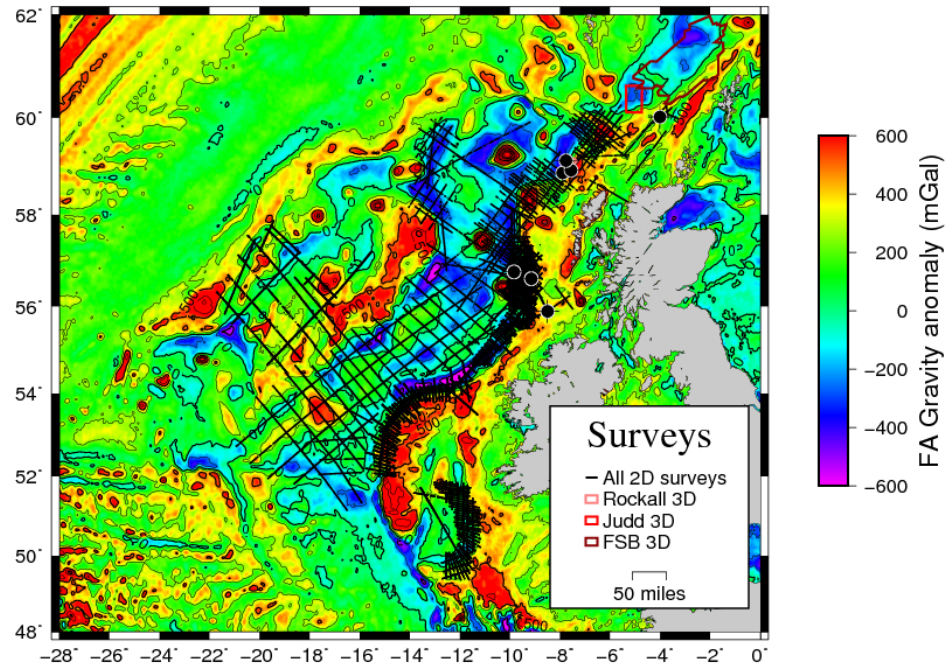


FIGURE 1.8: Datasets used in the Atlantic margin basins. Base map shows FA gravity anomaly (data: WGM2012 (Bonvalot et al., 2012)).

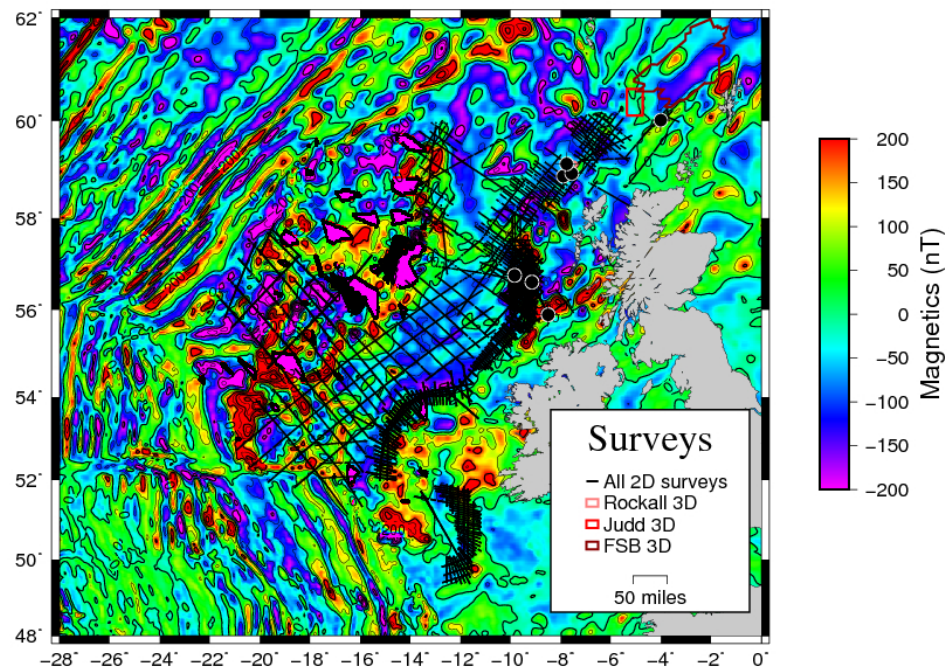


FIGURE 1.9: Datasets used in the Atlantic margin basins. Base map shows magnetic anomaly (data: GGM02 (Tapley et al., 2005)).

1.4.2 Bight Basin

The Bight Basin is located to the southwest of Australia (figure 1.10). It is an east–west trending Jurassic-Cretaceous basin, spanning water depths of 200 m to in excess of 4000 m. The basin has five main depocentres, the Bremer, Ceduna, Duntroon, Eyre and Recherche sub-basins (Norvick and Smith, 2001). Data from the Ceduna sub-basin, at the eastern end of the Bight Basin, is used in this thesis. The Bight Basin began opening in the Jurassic – Cretaceous (Norvick and Smith, 2001), which led to deposition of restricted marine and shallow marine sequences. The earliest intruded sequence within the Bight Basin study area was the Tiger Supersequence, which consists of coastal plain and shallow marine facies. Overlying the Tiger Supersequence is the Hammerhead Supersequence, which comprises thick deltaic sands and muds (Totterdell and Krassay, 2003). At the top of the Cretaceous is a major unconformity, which accompanies a phase of gravity-driven extensional faults which detach onto deeper horizons, with compressional features outboard. From the Paleocene onwards the Bight Basin was a relatively sediment-starved passive margin. This saw deposition of marine, marginal marine and deltaic sequences of the Wobbecong Supersequence (MacDonald et al., 2012; Totterdell and Krassay, 2003). Igneous activity is widespread along the southern margin of Australia, evidenced by intrusive and extrusive sequences both onshore and offshore. Melt production has been attributed to a factors such as mantle plumes, mantle shearing and small scale convection at steps in lithospheric thickness (Reynolds et al., 2017). Magmatism was mainly focused around the Mid Eocene. In the Ceduna sub-basin, intrusions are found within the Cretaceous Tiger and Hammerhead Supersequences, and the Paleocene – Eocene Wobbecong Supersequence (Jackson et al., 2013).

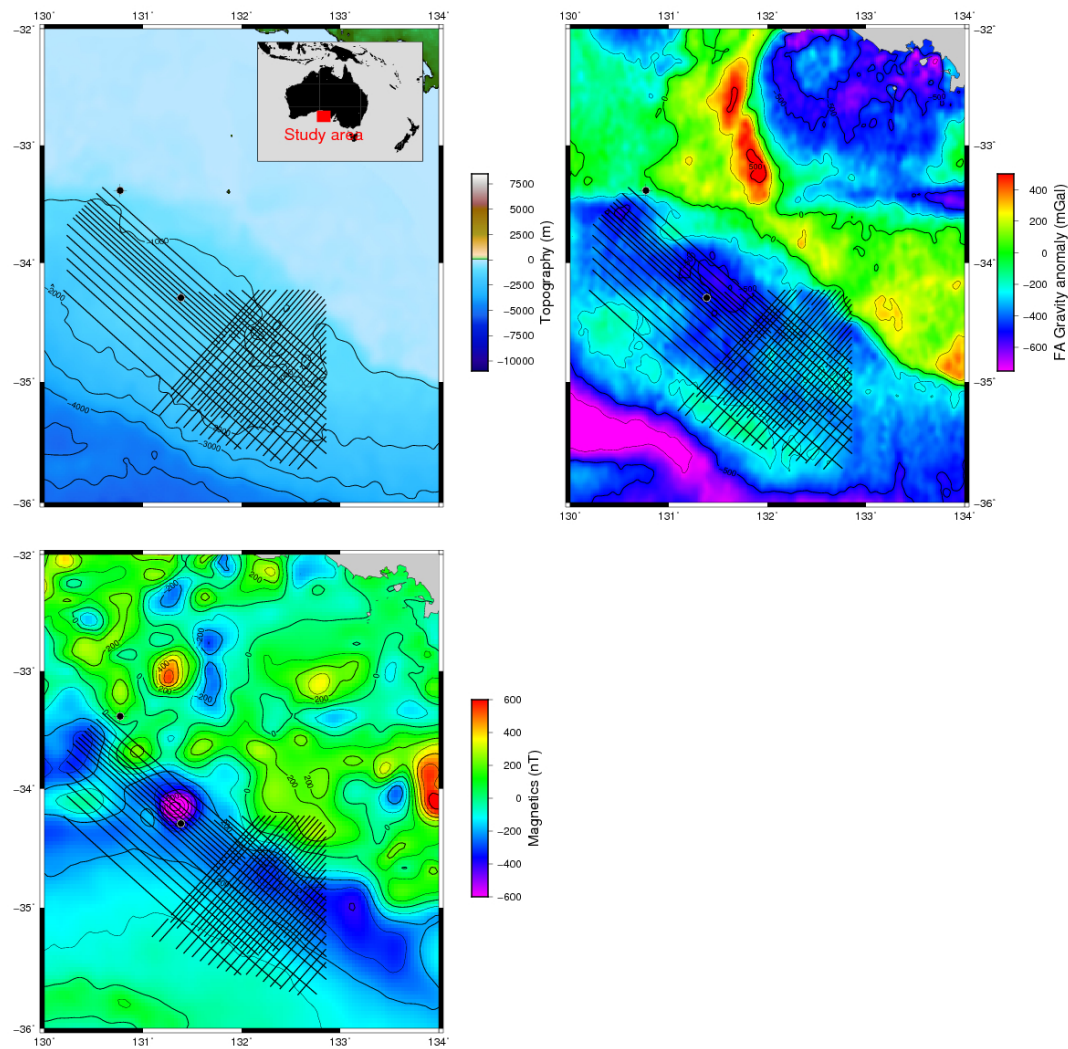


FIGURE 1.10: Datasets used in the Bight Basin. Top left shows bathymetry (data: ETOPO1 ([Amante, 2009](#))), top right panel shows FA gravity anomaly (data: WGM2012 ([Bonvalot et al., 2012](#))), and bottom left shows magnetic anomaly (data: GGM02 ([Tapley et al., 2005](#))).

1.4.3 Canterbury Basin

Figure 1.11 shows the dataset used in the Canterbury Basin, located offshore southwest New Zealand, which contains a sediment thickness of 5 km or more. Rifting started in the Early to Middle Cretaceous during the breakup of Western Gondwana, when New Zealand split from Western Antarctica, forming isolated half grabens and grabens. The oldest known sediments are the Middle Cretaceous Clipper Formation, which comprises mud-rich conglomerates, sandstones and some coals, and are restricted to the deeper grabens ([Killops et al., 1997](#)). These sequences are thought to be best candidates for mature source rocks in the basin. Rifting continued through the Late Cretaceous, and fluvial and paralic sandstones and siltstones of the Katiki Formation were deposited,

overtopping the grabens (Laird and Bradshaw, 2004; Lu et al., 2003). By the latest Cretaceous rifting had ceased and thermal subsidence took over. This accompanied widespread marine transgression and deposition of marine mudstones and shales of the Moeraki formation. Subsidence continued throughout the Paleocene, resulting in deposition of thick paralic coal measures. From the Paleocene to the Oligocene, the basin became fully open marine, which saw the Hampden formation marine shales be deposited over much of the area. The Late Oligocene onwards saw uplift of the area due to transpression along the Alpine Fault system, which increased the input of terrigenous clastic sediment to the basin, and caused a marine regression, leading to shallow marine conditions for the basin through the Late Oligocene and Miocene. This leads to the deposition of the sandstones and limestones. The Neogene sequences consist of thick prograding sediments of the Tokama and Kowai Formations (Lu et al., 2003; Reeves et al., 2017). Very little is known about the magmatism in the Canterbury Basin. Compared with the scale of magmatism in the Karro and Atlantic margin basins, the Canterbury Basin magmatism appears to be very low volume. The magmatism can be constrained to around the middle Miocene, based on onlap onto forced folds in the area (Reeves et al., 2017).

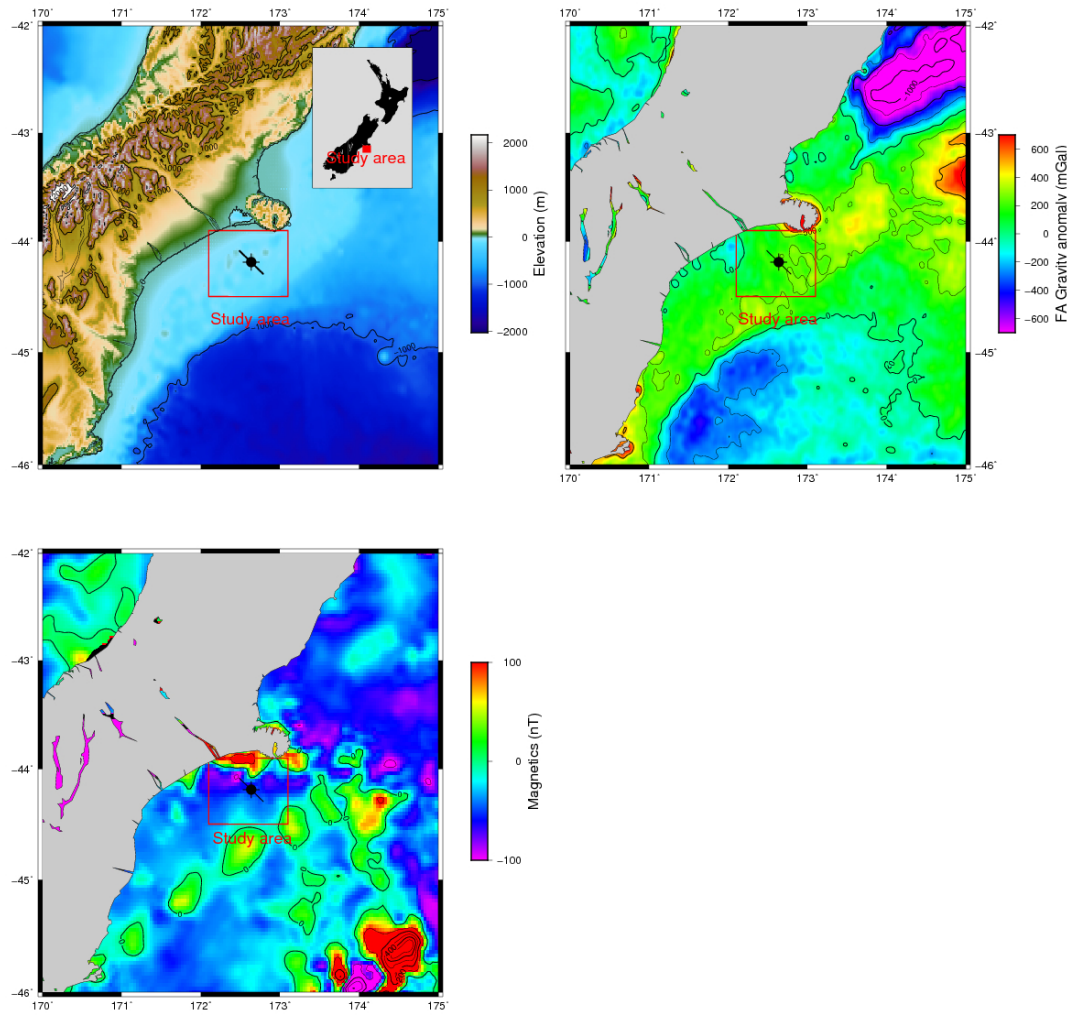


FIGURE 1.11: Datasets used in the Canterbury Basin. Top left shows bathymetry (data: ETOPO1 (Amante, 2009)), top right panel shows FA gravity anomaly (data: WGM2012 (Bonvalot et al., 2012)), and bottom left shows magnetic anomaly (data: GGM02 (Tapley et al., 2005)).

1.4.4 Carnarvon Basin

The Carnarvon Basin is a mainly Mesozoic marginal rift basin found off the Northwest shelf of Australia (figure 1.12). Basement rocks are mainly Archean and Proterozoic, with Ordovician to Carboniferous pre-rift strata deposited in a possible intracratonic basin. Rifting started around the Late Devonian, in association with the opening of Palaeo-Tethys and the breakup of Gondwana. This was associated with marine, deltaic and glacial deposits into large scale roughly N-S trending rift basins (Metcalf, 2013). Rifting continued through the Late Carboniferous to Early Permian, which saw fluvial and glacial sediments overlain by marine clastic and carbonate deposits which record a transgressive deepening sequence. The Triassic saw deposition of deep marine silts and muds. The end of the Triassic saw major rifting which formed the Ceno-Tethys

ocean. Shelfal siltstones and marls were then deposited in shallow marine conditions within large northeast trending basins. These deposits are overlain by Middle Jurassic silt and mudstones (Exon et al., 1992; McClay et al., 2013). The Early Cretaceous saw regional rifting and deposition of deltaic sediments. The Berriasian to Aptian saw regional uplift and erosion corresponding to the initial break-up of India from Australia. Igneous intrusions along the Western Australia margin are generally interpreted to be the result of transient magmatism around the Oxfordian and Valanginian associated with this breakup (McClay et al., 2013). Following this continental breakup, the area formed a passive margin which saw deposition of mainly fine grained sequences in the post rift succession.

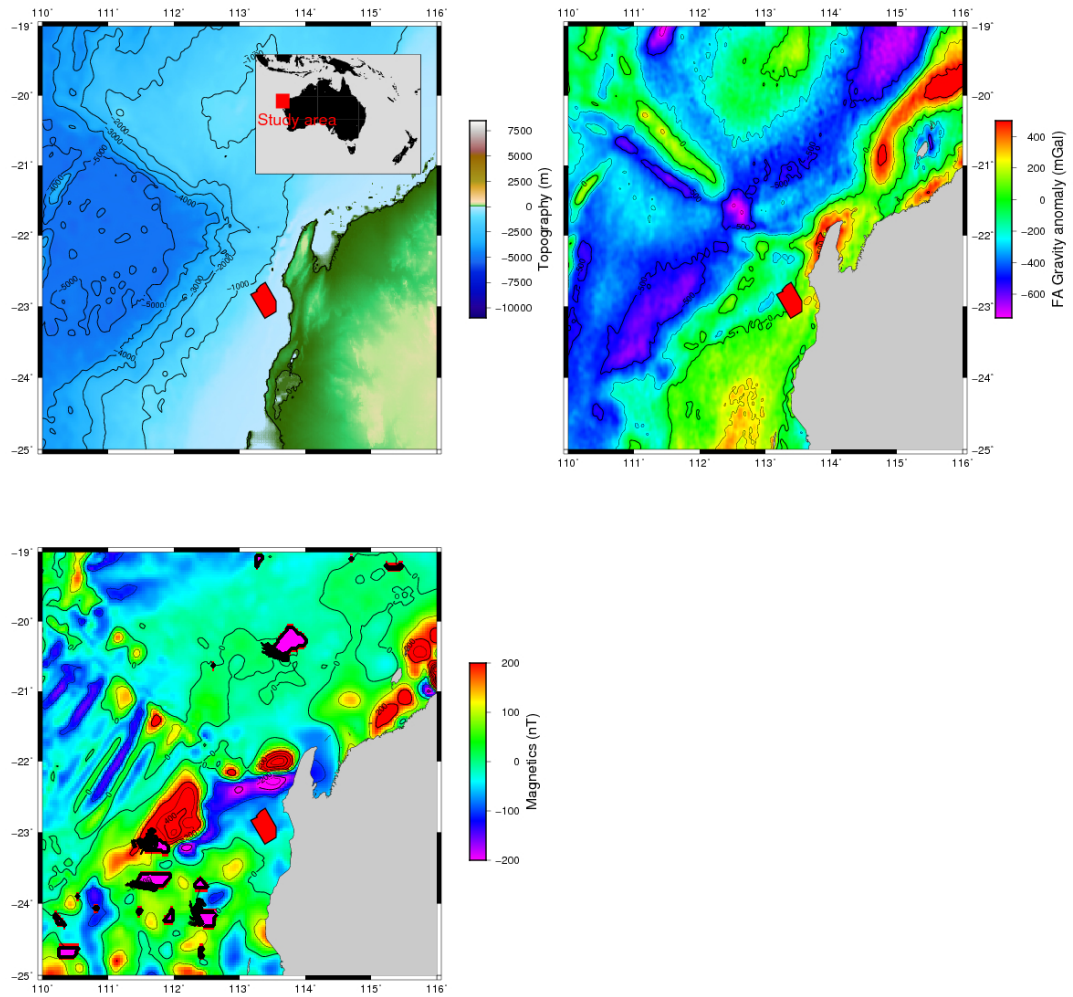


FIGURE 1.12: Datasets used in the Canarvon Basin. Top left shows bathymetry (data: ETOPO1 (Amante, 2009)), top right panel shows FA gravity anomaly (data: WGM2012 (Bonvalot et al., 2012)), and bottom left shows magnetic anomaly (data: GGM02 (Tapley et al., 2005)).

1.4.5 Karoo Basin

The Karoo Basin is a large foreland basin system which covers more than half of South Africa. It has around 6 km of sediment fill ranging from Late Carboniferous to Jurassic in age, comprising mostly marine strata, with some fluvial and aeolian sediments (Smith, 1990). Figure 1.13 shows a geological map of South Africa, with the major units and sill outcrop. Sills can be seen to intrude all major units of the Karoo Supergroup. The earliest sediments are the Dwyka Group, comprising diamictites and tillites. Overlying this is deltaic muds of the Eccca Group. This is followed by the shales and lenticular sandstones of the Beaufort group. Finally, the stratigraphically youngest intruded unit is the Stormberg Group, comprising aeolian desert sands and minor swamp like terrestrial deposits (Svensen et al., 2006). Magmatism was focused ~183 Ma (Encarnación et al., 1996; Svensen et al., 2006) during the emplacement of the Karoo / Ferrar LIP. This intrusion event saw intensive intrusion of dolerite and gabbroic sills, which locally make up > 70% of the basin volume (Du Toit, 1920), as well as eruption of extensive flood basalt lavas which make up the Lesotho highland.

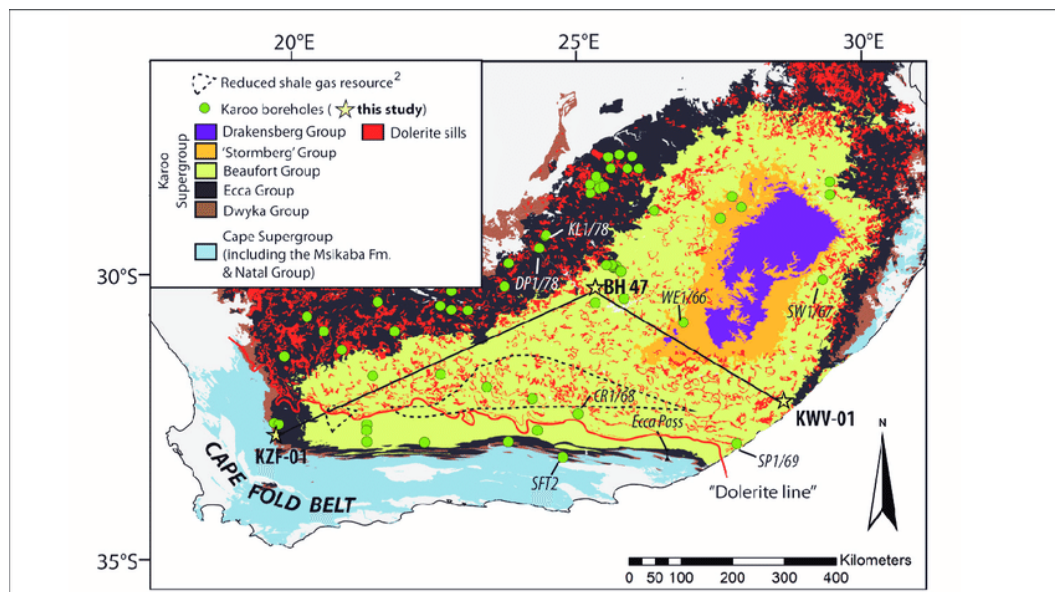


FIGURE 1.13: Geological map of the Karoo Basin and outcropping intrusions. After De Kock et al. (2017).

Chapter 2

Datasets

2.1 Introduction

Many of the conclusions in subsequent chapters which are based on statistical data rely on sample measurements being representative of the sill populations. Multiple seismic datasets were used throughout this thesis, each with different survey acquisition parameters which could lead to varying resolutions and hence potential bias to measurements. This chapter introduces each dataset, shows example images of the datasets, and lists key technical details of each survey. The section concludes with an analysis of potential bias introduced into measurements by different surveys, and concludes that variations in measurements between surveys due to differing survey resolution is insignificant compared to the length scales of igneous features being measured.

2.2 2D seismic data

2.2.1 UK Oil and Gas Authority (OGA) survey

The UK Oil and Gas Authority 2D seismic survey was released to the public as open access data in 2015. It was used in work in chapters [3](#), [4](#), [5](#) and [6](#). A map of the dataset can be found in figure [1.7](#). Key acquisition and processing details are found below.

Acquisition

- Total seismic line length: 10013 km
- Acquisition year: 2015
- Record length: 10 s
- Streamer length: 10000 m

- Group spacing 3.125 m
- Streamer: Slant, 8-35 m tow depth
- Source volume: Bolt 5085 cu inches
- Source pressure: 2000 psi
- Source depth: Delta 3 source, 9-6-9 m array
- Shot interval: 18.75 m
- Sample rate: 4 ms

Processing

- Noise attenuation and deghosting
- Radon Demultiple
- PRIMAL Demultiple
- Velocity analysis (2 km spacing)
- Prestack Time Migration
- Post migration Radon
- Residual Normal Moveout
- Poststack filtering / scaling
- Polarity: Zero phase, SEG reverse polarity, trough = increase in acoustic impedance.

Fold of coverage (often just referred to as fold) is the number of times a point in the subsurface is sampled in common mid point sorting. It is important as higher folds are more effective at averaging out background seismic noise and hence improving the signal to noise ratio. Fold can be calculated as

$$n_f = \frac{n_g \Delta g}{2 \Delta s} \quad (2.1)$$

where n_f is the fold, n_g is the number of receiver groups, Δg is the group spacing, and Δs is the shot point spacing. Equation 2.1 gives the fold in the OGA dataset as 178. Figure 2.2 shows the frequency spectrum for the OGA survey, while figure 2.1 shows an example of the seismic data itself.

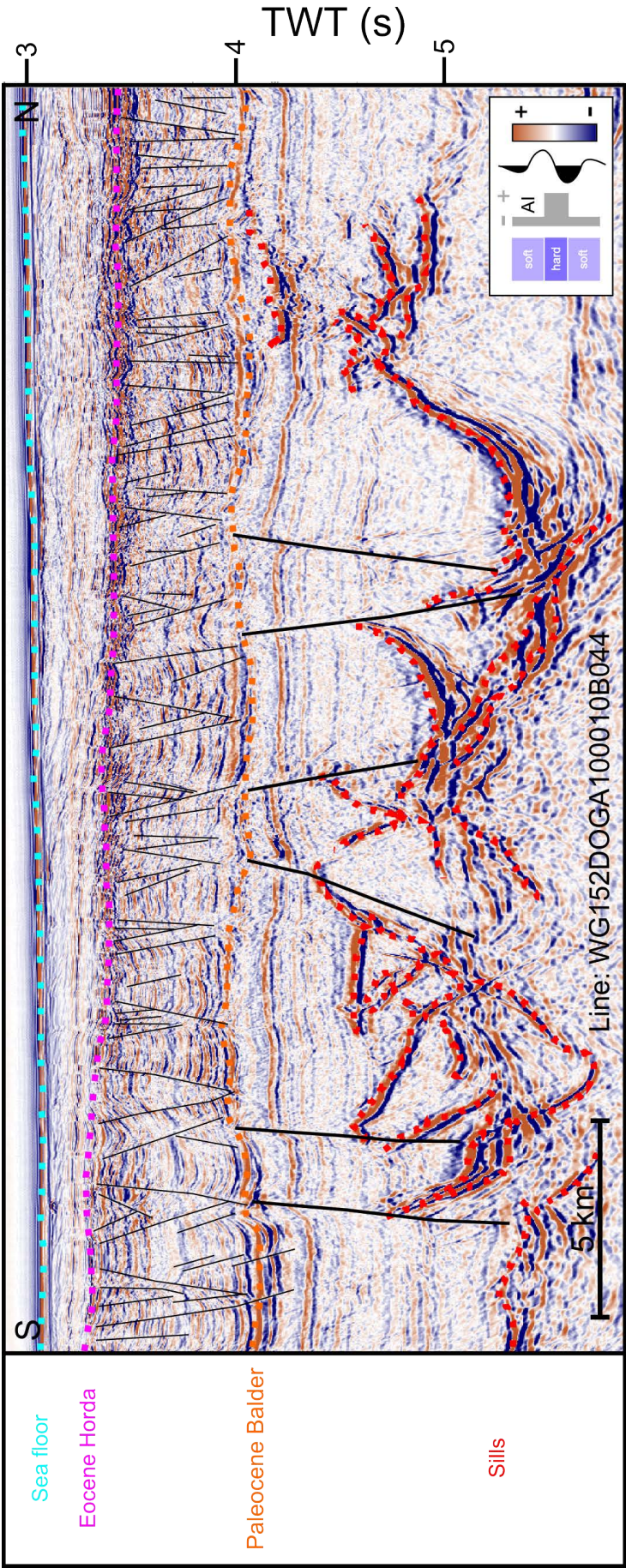


FIGURE 2.1: Example seismic line from the OGA survey, with interpretation

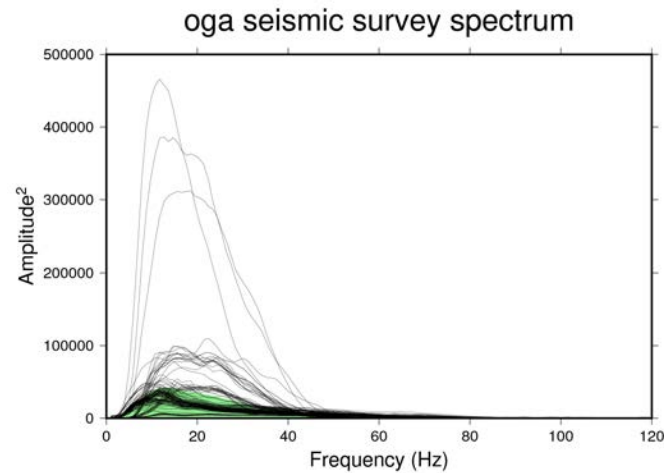


FIGURE 2.2: Power spectral density estimates for the OGA survey. Individual black lines are power spectral density estimates for individual seismic lines in the survey, while green curve is the mean of the individual lines.

2.2.2 Petroleum Affairs Division (PAD) survey

The Irish Petroleum Affairs Division 2D seismic survey was given to the University of Birmingham in 2017. It was used in work in Chapter 3. A map of the dataset can be found in figure 1.7. Key acquisition and processing details are found below.

Acquisition

- Total seismic line length: 18000 km
- Acquisition year: 2013
- Record length: 12 s
- Streamer length: 10 km
- Streamer: Straight
- Source: Single source G-gun
- Source depth: 8 m
- Shot interval: 37.5 m
- Group interval: 12.5 m
- Number of groups: 804
- Sample rate: 4 ms

Processing

- 3 Hz low cut filter
- Shot and channel edits
- Designature and zero phase conversion
- Spherical divergence correction
- Swell noise attenuation

- Despiking
- Surface Related Multiple Elimination (SRME)
- Pick preliminary velocities (2 km spacing)
- Shot domain taup deconvolution and dip mute
- Receiver domain taup deconvolution and dip mute
- 60 deg angle mute
- High resolution Radon demultiple
- Pick migration velocities (2 km spacing)
- Prestack Time Migration
- High resolution radon demultiple
- Automatic velocities pick (100 m spacing)
- Inner and outer mute
- Stack
- Polarity: zero phase, SEG reverse. Trough = increase in acoustic impedance.

Equation 2.1 gives the fold as 134. Figure 2.3 shows the frequency spectrum for the PAD survey, while figure 2.4 shows an example of the seismic data itself.

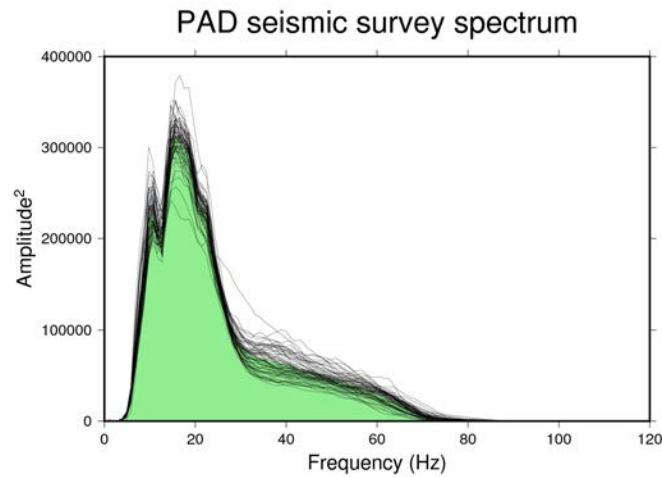


FIGURE 2.3: Power spectral density estimates for the PAD survey. Individual black lines are power spectral density estimates for individual seismic lines in the survey, while green curve is the mean of the individual lines.

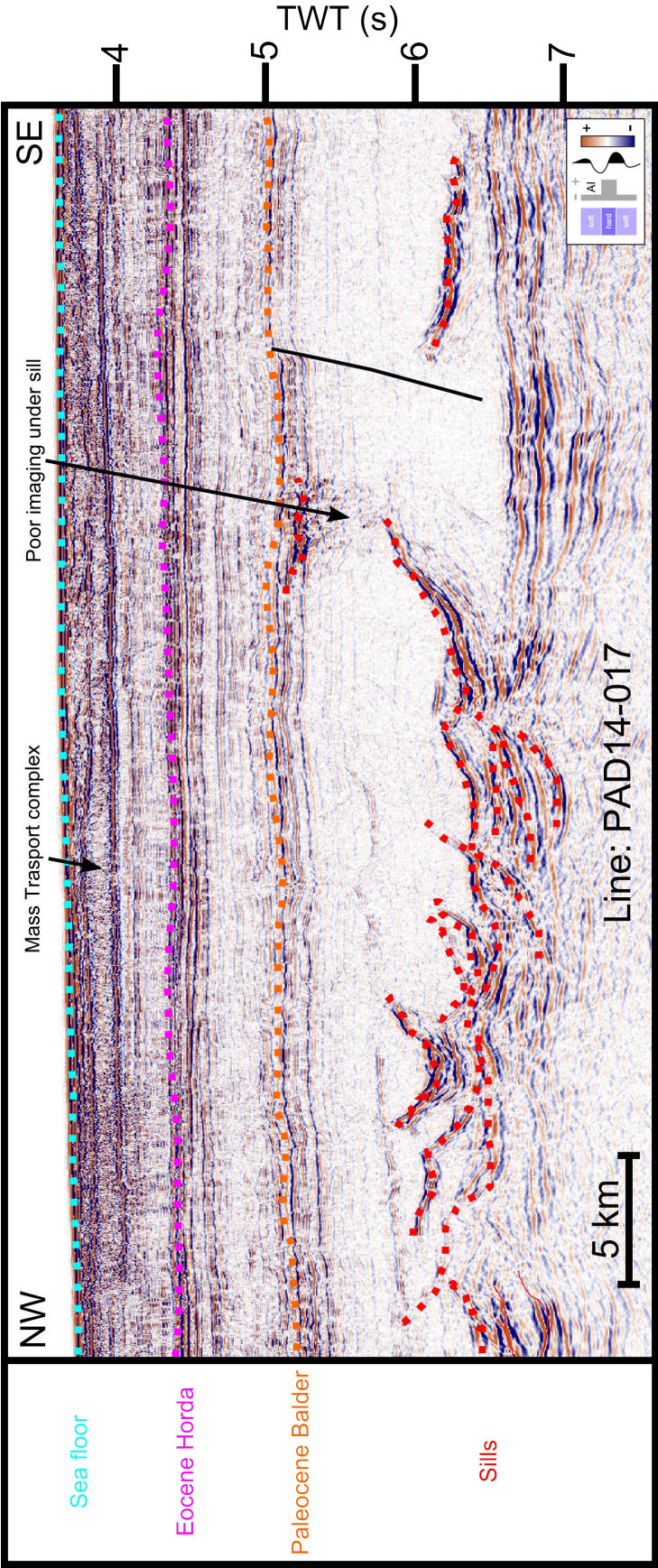


FIGURE 2.4: Example seismic line from the PAD survey, with interpretation

2.2.3 Spectrum INROCK (reprocessed) survey

The commercial INROCK 2D seismic survey was kindly given to the University of Birmingham in 2013 by Spectrum geophysics. It was used in work in chapters 3 and 4. A map of the dataset can be found in figure 1.7. Key acquisition and processing details are found below.

Acquisition

- Total seismic line length: 1531 m
- Acquisition year: 1996
- Record length: 8 s
- Streamer length: 4000 m
- Source: 3000 cu in
- Source pressure: Unknown
- Source depth: 6 m
- Shot interval: 25 m
- Group interval: 12.5 m
- Number of groups: 320
- Sample rate: 4 ms

Processing

- Zero phase designature
- Spherical divergence correction
- Low cut filter 3Hz
- Swell noise attenuation
- SRME demultiple
- Velocity analysis (2 km spacing)
- High resolution Radon demultiple
- Diffracted noise attenuation
- Kirchhoff PSTM
- Automatic 4th order velocity analysis
- Normal moveout corection
- Outer and inner trace mute
- Stack
- FK coherence enhancement
- Polarity: Zero Phase SEG Reverse - Trough=Increase in Acoustic Impedance

Equation 2.1 gives the fold as 80. Figure 2.5 shows the frequency spectrum for the INROCK survey, while figure 2.6 shows an example of the seismic data itself.

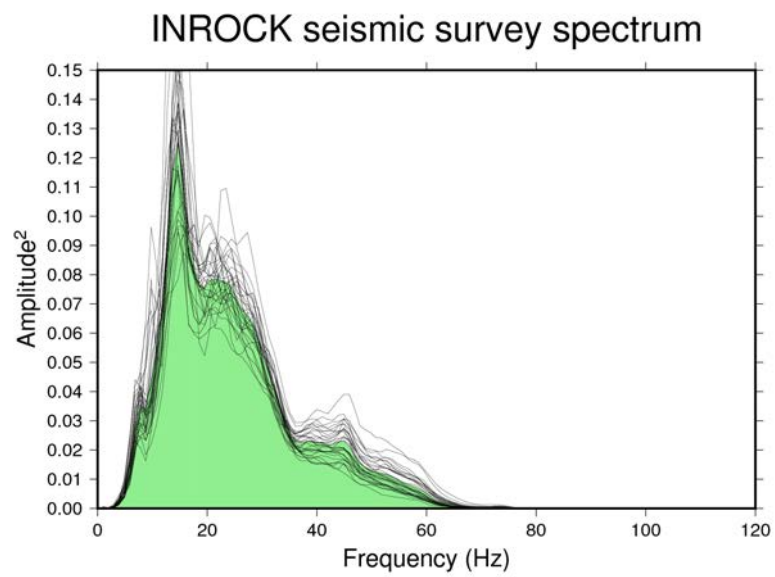


FIGURE 2.5: Power spectral density estimates for the INROCK96 survey. Individual black lines are power spectral density estimates for individual seismic lines in the survey, while green curve is the mean of the individual lines.



Figures/inrock_96-09.png

FIGURE 2.6: Example seismic line from the INROCK96 survey, with interpretation. [Redacted]

2.2.4 Spectrum ISROCK (reprocessed) survey

The commercial ISROCK 2D seismic survey was kindly given to the University of Birmingham in 2013 by Spectrum geophysics. It was used in work in chapters 3 and 4. A map of the dataset can be found in figure 1.7. Key acquisition and processing details are found below.

Acquisition

- Total seismic line length: 2930 km
- Acquisition year: 1996
- Record length: 10 s
- Streamer length: 4500 m
- Source: 3000 cu in
- Source depth: 6 m
- Shot interval: 37.5 m
- Group interval: 12.5 m
- Number of groups: 360
- Sample rate: 4 ms

Processing

- Zero phase designature
- Spherical divergence correction
- Low cut filter 3Hz
- Swell noise attenuation
- SRME demultiple
- Velocity analysis (2 km spacing)
- High resolution Radon demultiple
- Diffracted noise attenuation
- Kirchhoff prestack time migration
- Velocity analysis (1 km spacing)
- Automatic 4th order velocity analysis
- Normal move out
- Outer and inner trace mute
- Stack
- FK coherence enhancement
- Eigenvector filter
- Expanding gate Alpha Trim AGC
- Polarity: Zero Phase SEG Reverse - Trough=Increase in Acoustic Impedance

Equation 2.1 gives the fold as 60. Figure 2.7 shows the frequency spectrum for the ISROCK survey, while figure 2.8 shows an example of the seismic data itself.

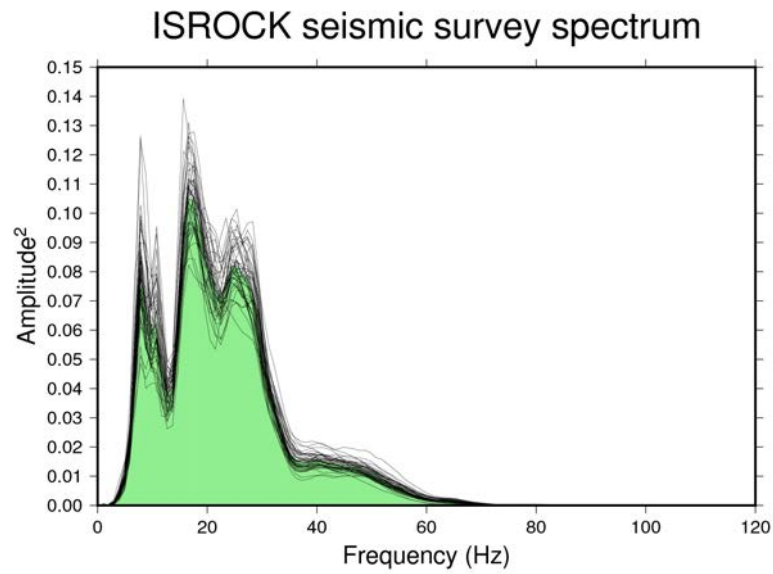
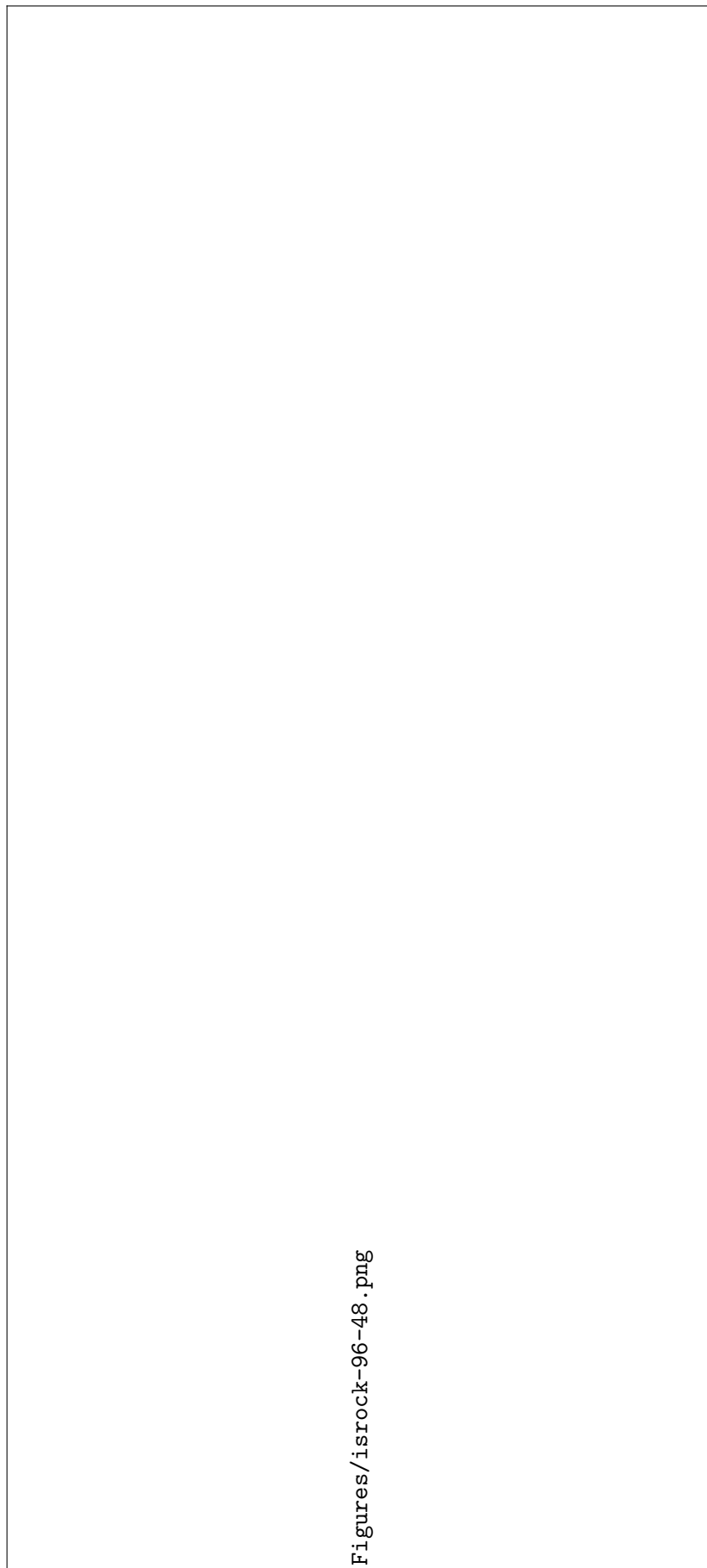


FIGURE 2.7: Power spectral density estimates for the ISROCK96 survey. Individual black lines are power spectral density estimates for individual seismic lines in the survey, while green curve is the mean of the individual lines.



Figures/isrock-96-48.png

FIGURE 2.8: Example seismic line from the ISROCK survey, with interpretation. [Redacted]

2.2.5 Spectrum DGER96 (reprocessed) survey

The commercial DGER96 2D seismic survey was kindly given to the University of Birmingham in 2013 by Spectrum geophysics. It was used in work in chapters 3 and 4. A map of the dataset can be found in figure 1.7. Key acquisition and processing details are found below.

Acquisition

- Total seismic line length: 2741 km
- Acquisition year: 1996
- Record length: 8 s
- Streamer length: 4500 m
- Source depth: 7 m
- Shot interval: 25 m
- Group interval: 12.5 m
- Number of groups: 360
- Sample rate: 4 ms

Processing

- Zero Phase Designature
- Spherical Div
- Low cut filter 3Hz
- Swell Noise Attenuation
- Surface related multiple elimination
- Velocity analysis (2 km spacing)
- High resolution radon demultiple
- Diffracted Noise Attenuation
- Velocity analysis (1 km spacing)
- Kirchhoff prestack time migration
- Automatic 4th order velocity analysis
- Normal move out
- Outer and inner trace mute
- Stack
- FK coherency enhancement
- Spatial anti-alias filter
- Eigenvector filter
- Expanding gate Alpha Trim AGC

Equation 2.1 gives the fold as 90. Figure 2.9 shows the frequency spectrum for the DGER96 survey, while figure 2.10 shows an example of the seismic data itself.

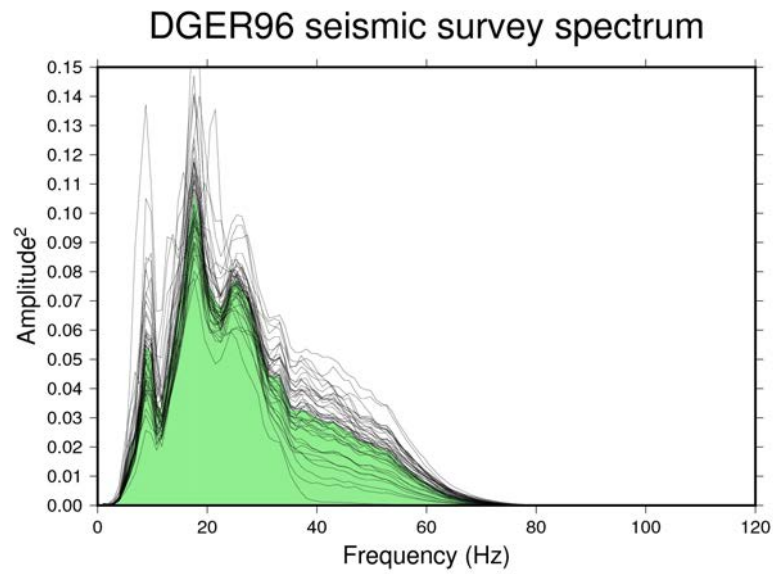


FIGURE 2.9: Power spectral density estimates for the DGER96 survey. Individual black lines are power spectral density estimates for individual seismic lines in the survey, while green curve is the mean of the individual lines.

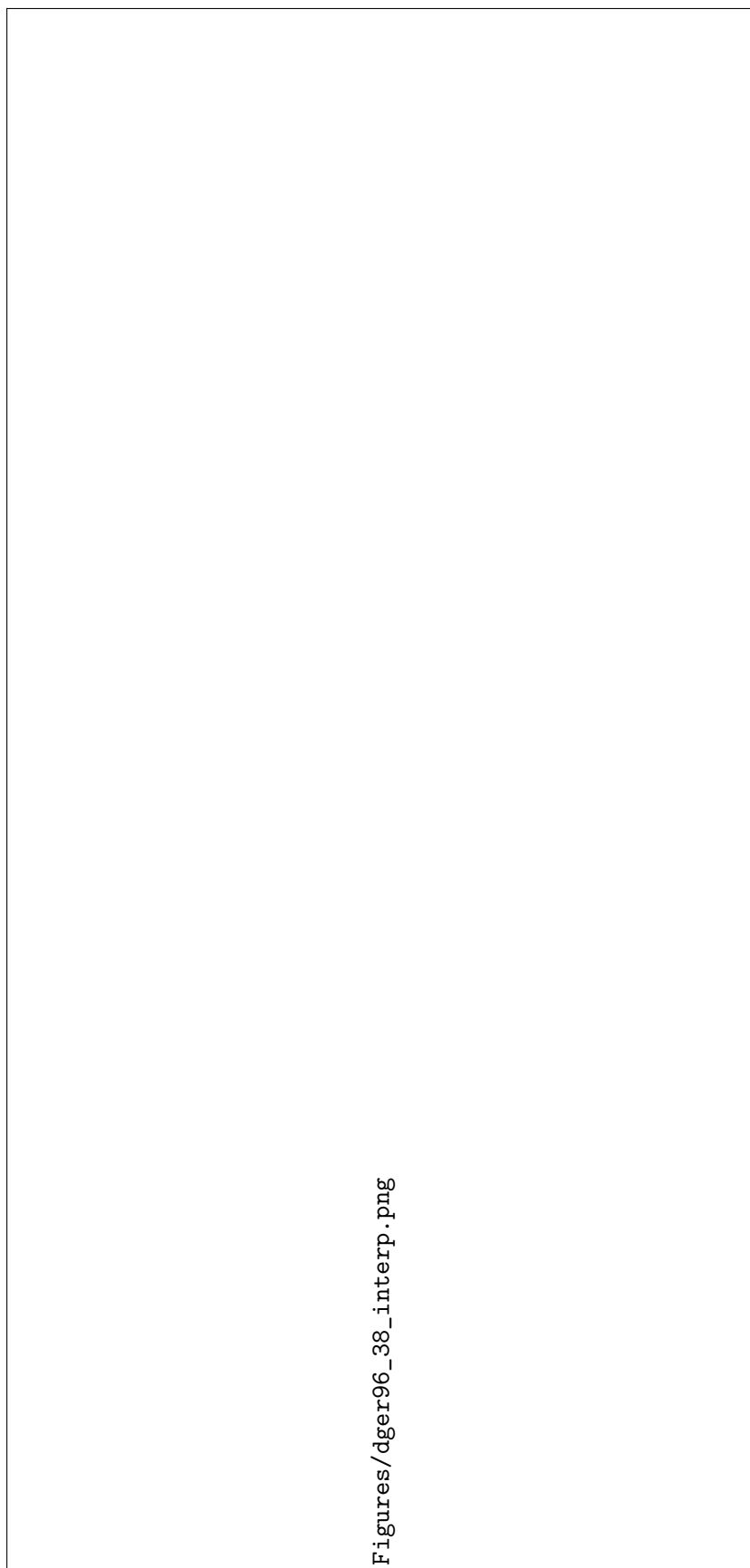


FIGURE 2.10: Example seismic line from the DGER96 survey, with interpretation. [Redacted]

2.2.6 Spectrum DGSRT96 (reprocessed) survey

The commercial DGSRT96 2D seismic survey was kindly given to the University of Birmingham in 2013 by Spectrum geophysics. It was used in work in chapters 3 and 4. A map of the dataset can be found in figure 1.7. Key acquisition and processing details are found below.

Acquisition

- Total seismic line length: 662 km
- Acquisition year: 1996
- Record length: 8s
- Streamer length: 4500 m
- Source depth: 7 m
- Shot interval: 25 m
- Group interval: 12.5 m
- Number of groups: 360
- Sample rate: 4 ms

Processing

- Zero Phase designation
- Spherical divergence correction
- Swell noise attenuation
- SRME demultiple
- Velocity analysis (2 km spacing)
- High resolution radon demultiple
- Diffracted noise attenuation
- Kirchhoff PSTM
- Velocity analysis (1 km spacing)
- Automatic 4th order velocity analysis
- Normal move out
- Outer trace and inner trace mute
- Stack
- FK coherence enhance
- Spatial anti alias filter
- Eigenvector filter
- Expanding gate alpha trim AGC
- Polarity: Zero Phase SEG Reverse - Trough=Increase in Acoustic Impedance

Equation 2.1 gives the fold as 90. Figure 2.11 shows the frequency spectrum for the DGSRT96 survey, while figure 2.12 shows an example of the seismic data itself.

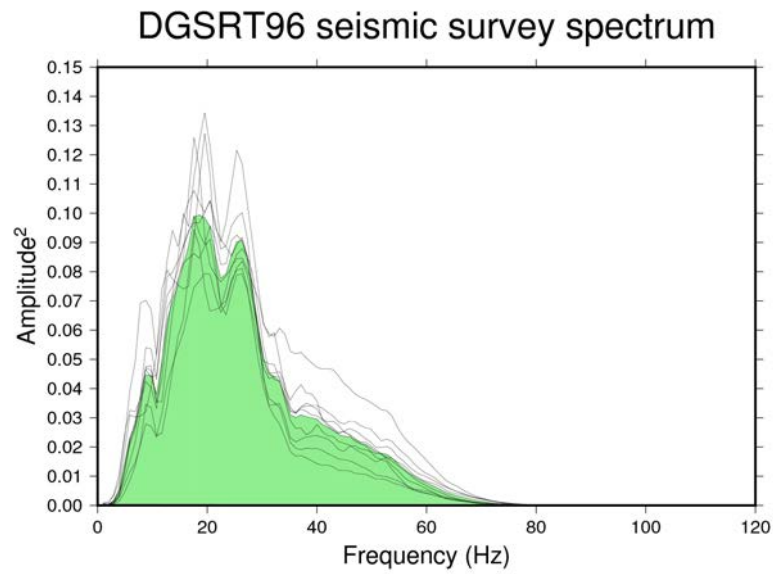
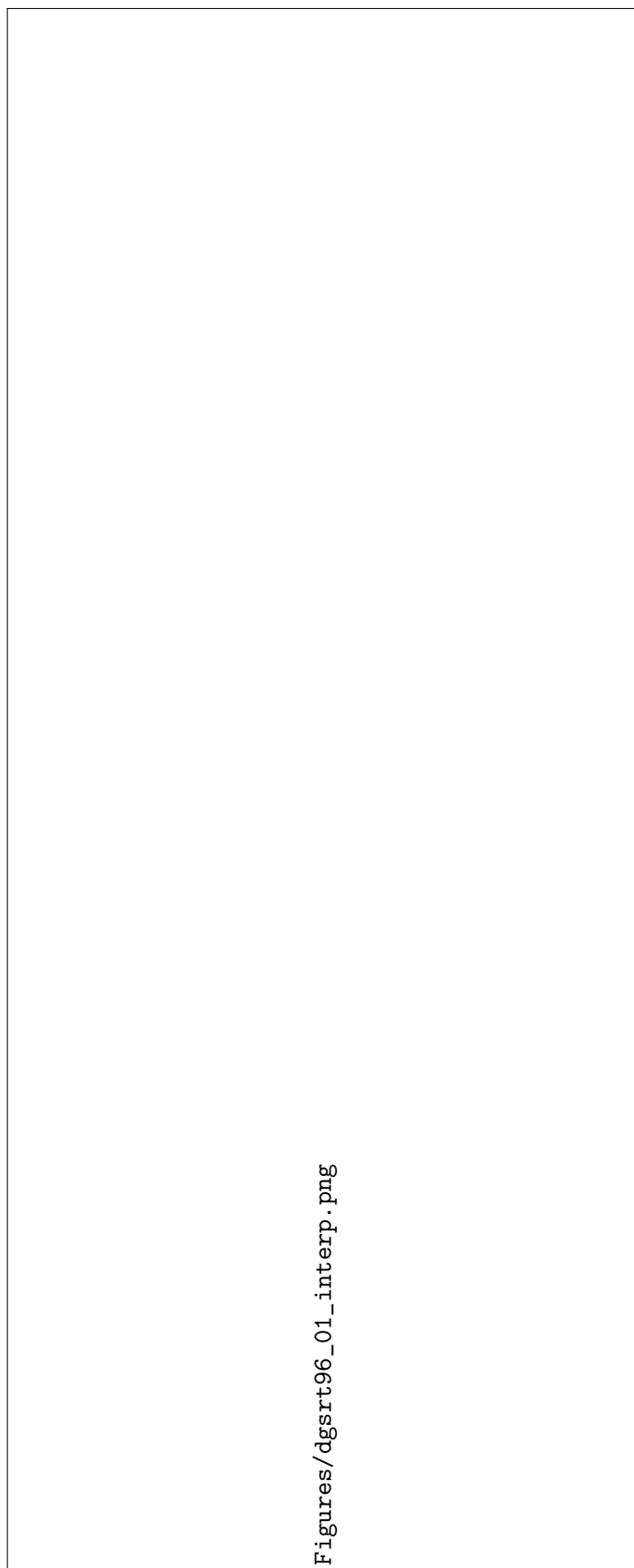


FIGURE 2.11: Power spectral density estimates for the DGSRT96 survey. Individual black lines are power spectral density estimates for individual seismic lines in the survey, while green curve is the mean of the individual lines.



Figures/dgsrt96_01_interp.png

FIGURE 2.12: Example seismic line from the DGSRT96 survey, with interpretation. [Redacted]

2.2.7 Spectrum DGWH96 (reprocessed) survey

The commercial DGWH96 2D seismic survey was kindly given to the University of Birmingham in 2013 by Spectrum geophysics. It was used in work in chapters 3 and 4. A map of the dataset can be found in figure 1.7. Key acquisition and processing details are found below.

Acquisition

- Total seismic line length: 2422 km
- Acquisition year: 1996
- Record length: 8 m
- Streamer length: 4500 m
- Source depth: 7 m
- Shot interval: 25 m
- Group interval: 12.5 m
- Number of groups: 360
- Sample rate: 4 ms

Processing

- Zero phase designature
- Spherical divergence correction
- Swell noise attenuation
- SRME Demultiple
- Velocity analysis (2 km spacing)
- High resolution radon demultiple
- Diffracted noise attenuation
- Kirchhoff PSTM
- Velocity analysis (1 km spacing)
- Kirchhoff PSTM
- Automatic 4th order velocity analysis
- NMO
- Outer and inner trace mute
- Stack
- FK coherence enhancement
- Spatial anti-alias filter
- Eigenvector filter
- Expanding gate Alpha Trim AGC
- Polarity: Zero Phase SEG Reverse - Trough=Increase in Acoustic Impedance

Equation 2.1 gives the fold as 90. Figure 2.13 shows the frequency spectrum for the DGWH96 survey, while figure 2.14 shows an example of the seismic data itself.

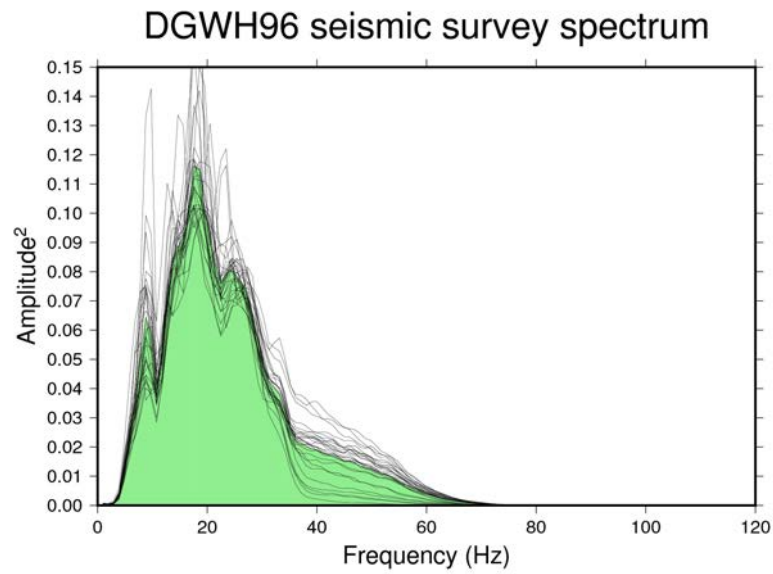


FIGURE 2.13: Power spectral density estimates for the DGWH96 survey. Individual black lines are power spectral density estimates for individual seismic lines in the survey, while green curve is the mean of the individual lines.

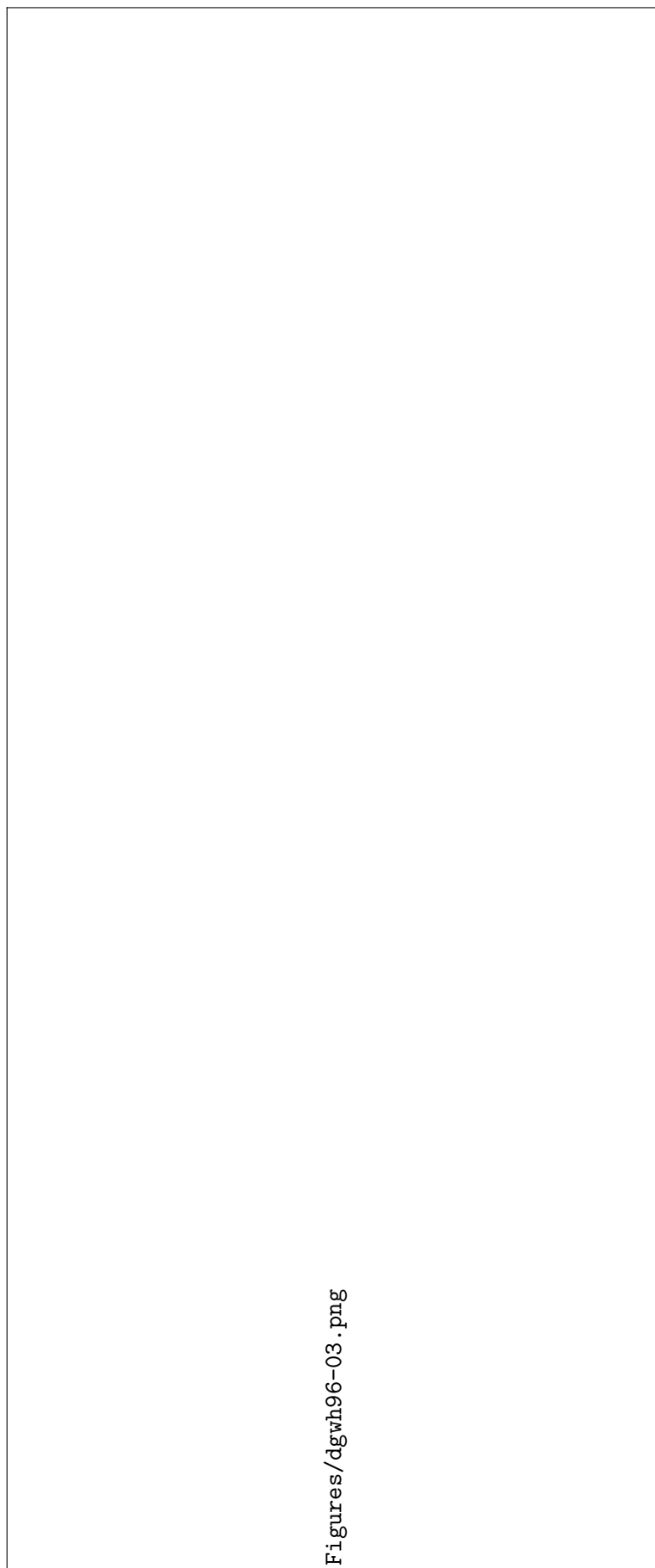


FIGURE 2.14: Example seismic line from the DGWH96 survey, with interpretation. [Redacted]

2.2.8 Spectrum PORC96 (reprocessed) survey

The commercial PORC96 2D seismic survey was kindly given to the University of Birmingham in 2013 by Spectrum geophysics. It was used in work in chapters 3 and 4. A map of the dataset can be found in figure 1.7. Key acquisition and processing details are found below.

Acquisition

- Total seismic line length: 4345 km
- Acquisition year: 1997
- Record length: 8.5 s
- Streamer length: 4800 m
- Source depth: 6 m
- Shot interval: 25 m
- Group interval: 12.5 m
- Number of groups: 384
- Sample rate: 4 ms

Processing

- Zero Phase Signature
- Spherical Divergence correction
- SRME Demultiple
- Hi-Resolution Radon demultiple
- Diffracted Multiple Attenuation
- PSTM
- Automatic 4th order velocity analysis
- Outer and inner trace mute
- Stack
- Remove T Square Gain, apply V Square T Gain
- Gun and Cable Static corrections
- Automatic Gain Control
- Polarity: Zero Phase SEG Reverse - Trough=Increase in Acoustic Impedance

Equation 2.1 gives the fold as 96. Figure 2.15 shows the frequency spectrum for the PORC97 survey, while figure 2.16 shows an example of the seismic data itself.

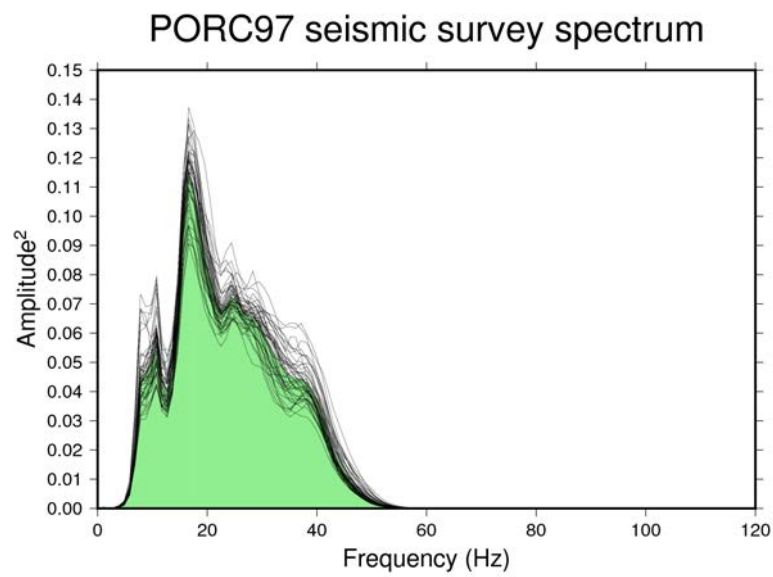


FIGURE 2.15: Power spectral density estimates for the PORC97 survey. Individual black lines are power spectral density estimates for individual seismic lines in the survey, while green curve is the mean of the individual lines.

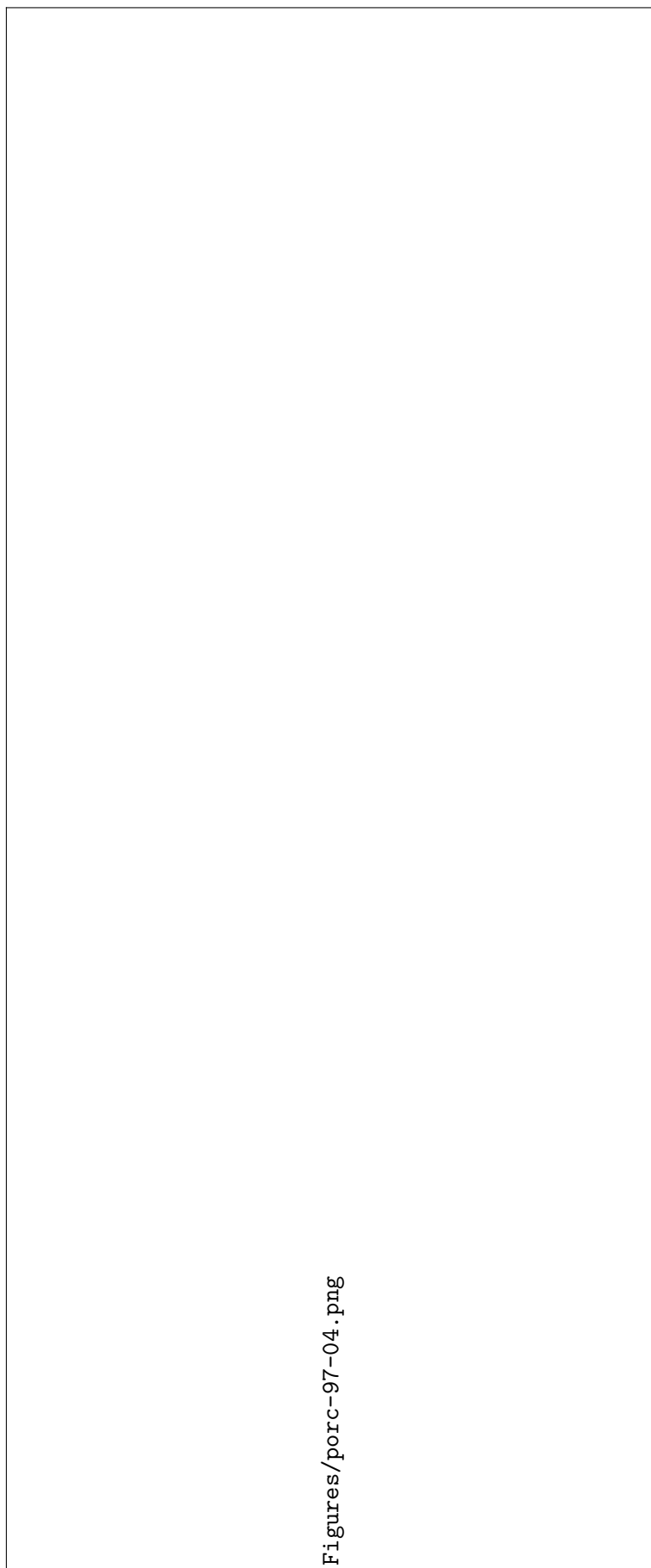


FIGURE 2.16: Example seismic line from the PORC97 survey, with interpretation. [Redacted]

2.2.9 Hatton Basin survey

The Hatton Basin 2D seismic survey was kindly given to the University of Birmingham in 2014 by Rob Hardy (<http://www.tomnta-energy.com/>). It was used in work in chapters 3 and 4. A map of the dataset can be found in figure 1.7. Key acquisition and processing details are found below.

Acquisition

- Total seismic line length: 2789 km
- Acquisition year: 2004
- Record length: 4 s
- Streamer length: 1200 m
- Source: single 2000psi sodera 210 cu in GI gun
- Source depth: 5 m
- Shot interval: 25 m
- Group interval: 12.5 m
- Number of groups: 96
- Sample rate: 1 ms

Processing

- Static shift according to observers logs for time-break static
- Gain compensation: t-squared
- Deconvolution: 12ms gap, 75ms operator single trace
- Radon demultiple
- Velocity analysis 1000m interval
- Diversity stack 64ms window length
- Deconvolution: 12ms gap, 75ms operator single trace
- Deconvolution: 18ms gap, 22ms operator single trace
- Anti-alias filter followed by resample to 2ms
- Steep dip time migration using smoothed stacking velocity field
- TVF 8,12,180,220 at 0s 8,12,90,120 at 3s
- AGC (2 second window)

Equation 2.1 gives the fold as 24. Figure 2.17 shows the frequency spectrum for the Hatton survey, while figure 2.18 shows an example of the seismic data itself.

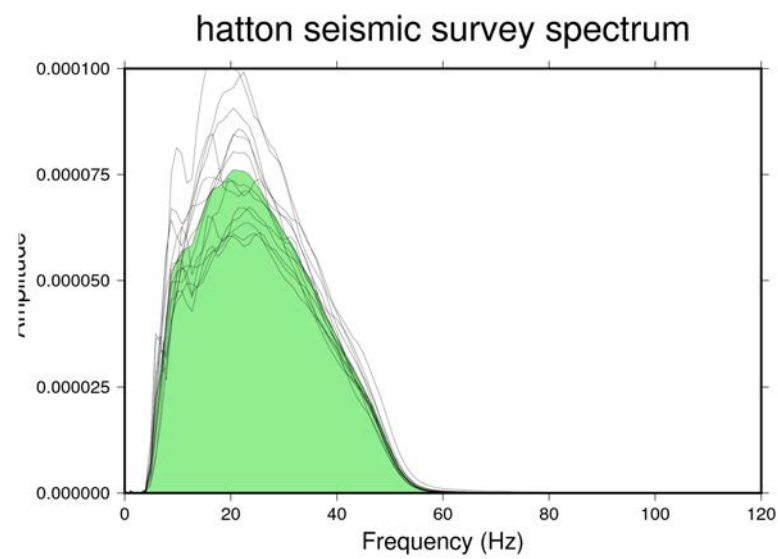


FIGURE 2.17: Power spectral density estimates for the Hatton survey. Individual black lines are power spectral density estimates for individual seismic lines in the survey, while green curve is the mean of the individual lines.

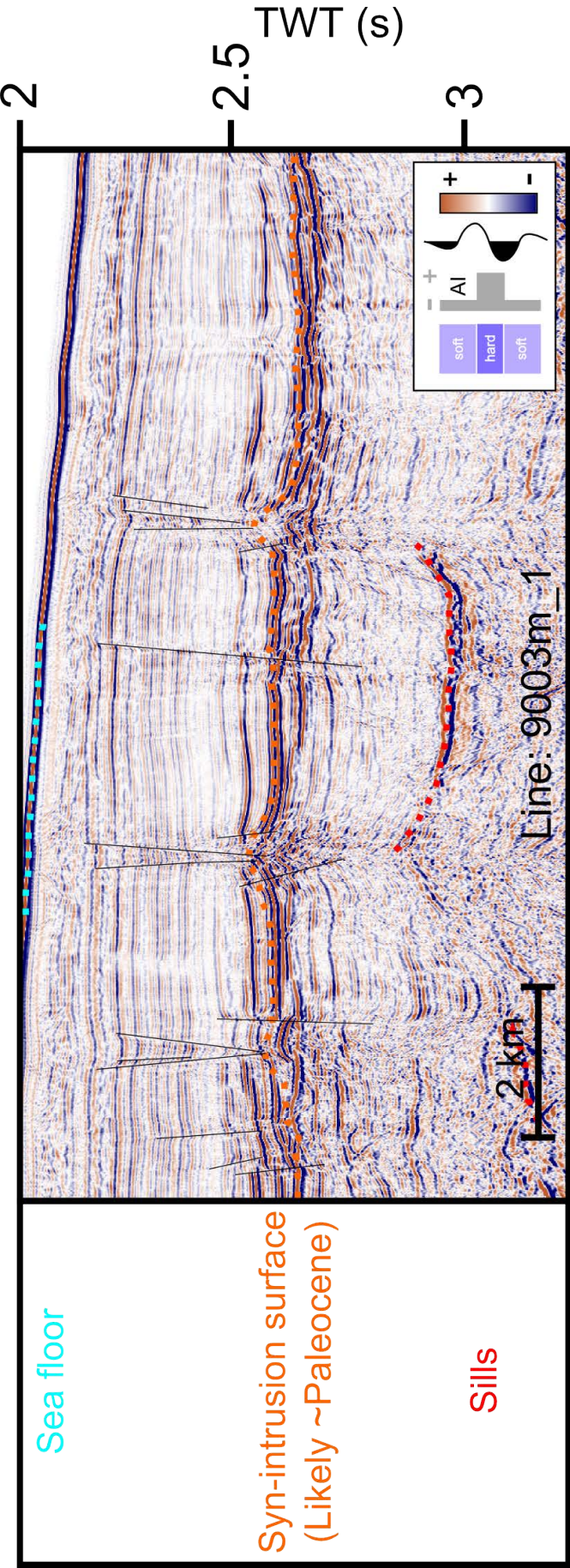


FIGURE 2.18: Example seismic line from the Hatton survey, with interpretation

2.2.10 Bight Basin

The Bight Basin 2D seismic survey is listed as released by the Australian Government, but files online were listed as missing. A copy was kindly given to the University of Birmingham in 2017 by Prof. Chris Jackson at Imperial College London. It was used in work in chapters 3 and 4. A map of the dataset can be found in figure 1.10. Key acquisition and processing details are found below.

Acquisition

- Total seismic line length: 8089 km
- Acquisition year: 2001
- Record length: 9 s
- Streamer length: 6000 m
- Source depth: 5 m
- Shot interval: 25 m
- Group interval: 12.5 m
- Number of groups: 480
- Sample rate: 4 ms

Processing

- Geometric spreading amplitude compensation
- Band-Pass filter
- Outer trace mute
- Swell noise attenuation
- Velocity analysis (1 km spacing)
- Deterministic zero phase conversion
- Radon multiple attenuation
- Phase only inverse Q filter
- Dip move out correction
- Normal move out correction
- Outer and inner trace mute
- Stack
- Poststack migration
- Amplitude gain correction

Equation 2.1 gives the fold as 120. Figure 2.19 shows the frequency spectrum for the Bight survey, while figure 2.20 shows an example of the seismic data itself.

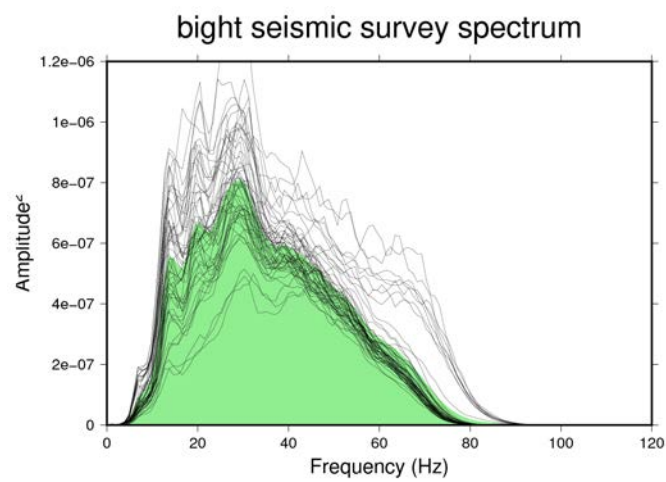


FIGURE 2.19: Power spectral density estimates for the Bight survey. Individual black lines are power spectral density estimates for individual seismic lines in the survey, while green curve is the mean of the individual lines.

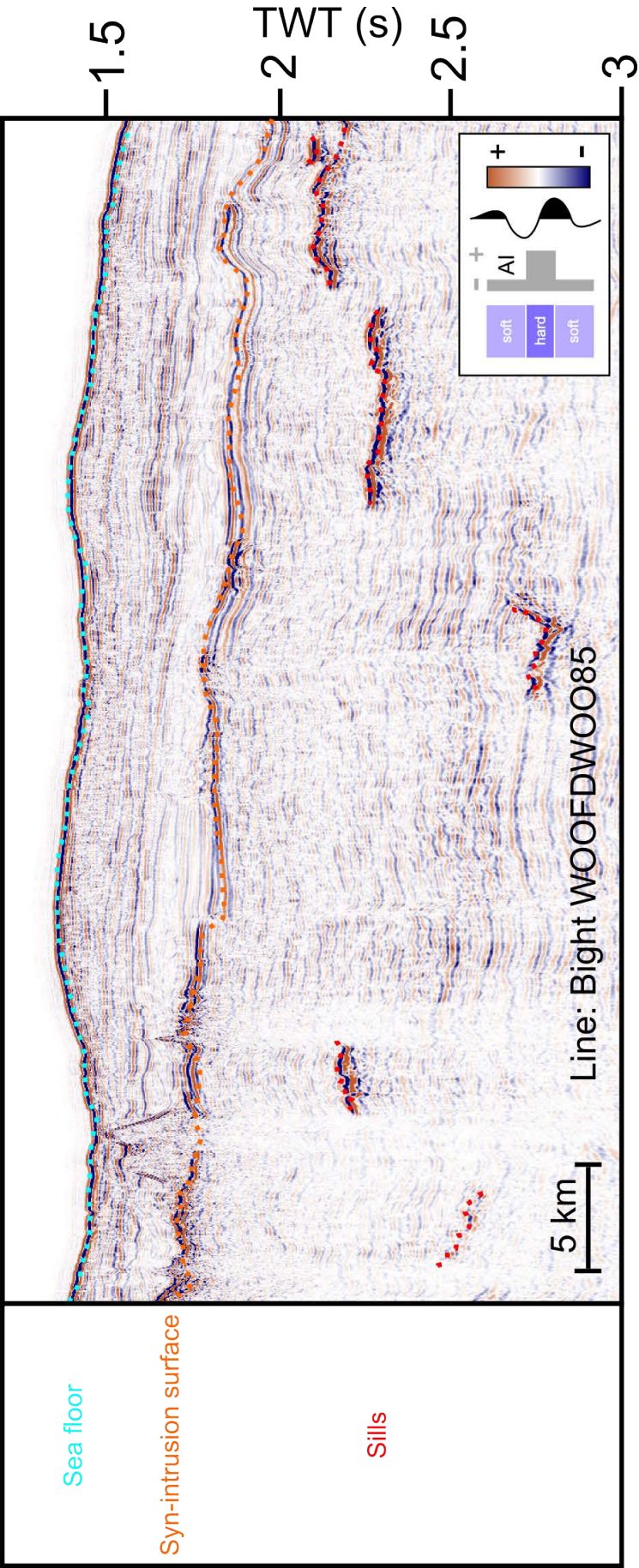


FIGURE 2.20: Example seismic line from the Bight survey, with interpretation

2.3 3D seismic data

2.3.1 NE Rockall survey

The NE Rockall survey's origin is unknown — it has been in the Earth science department at the University of Birmingham for at least 15 years. A map of the dataset can be found in figure [1.7](#).

Acquisition

- Acquisition year: 1997
- Record length: 7.5 s
- Source: 3397 cu in
- Source depth: 8 m
- Shot interval: 25 m
- Group interval: 12.5 m
- Sample rate: 4 ms
- Streamer length: Unknown

Processing

- Minimum phase conversion
- Amplitude recovery tt^2 function
- Spatial anti alias filter and trace drop
- fx sp interpolation
- Radon demultiple
- 3D dip moveout correction
- 3D pre-stack time migration
- Amplitude balance
- fx trace interpolation
- fx migration
- Gun and cable static correction

Information on the streamer length and number of groups was not available, so it was not possible to calculate the fold of coverage. Figure [2.21](#) shows the frequency spectrum for the Rockall 3D survey, while figure [2.22](#) shows an example of the seismic data itself.

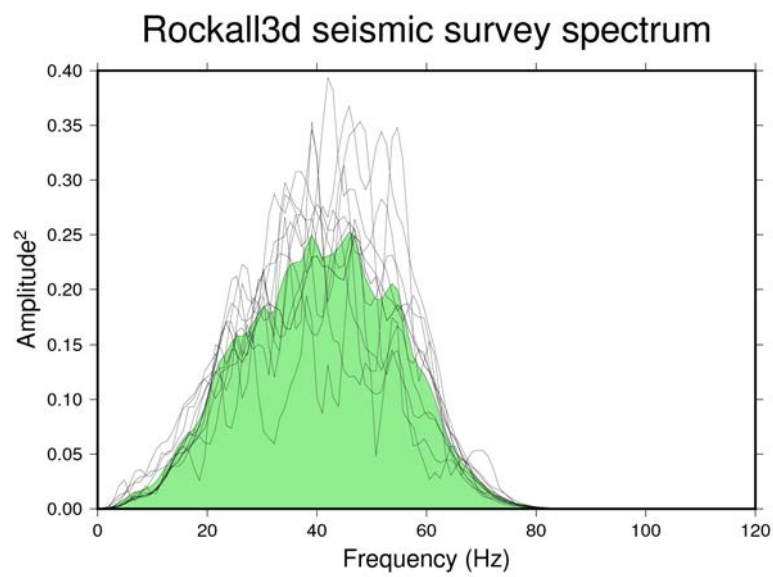


FIGURE 2.21: Power spectral density estimates for the Rockall 3D survey. Individual black lines are power spectral density estimates for individual inlines in the survey, while green curve is the mean of the individual lines.

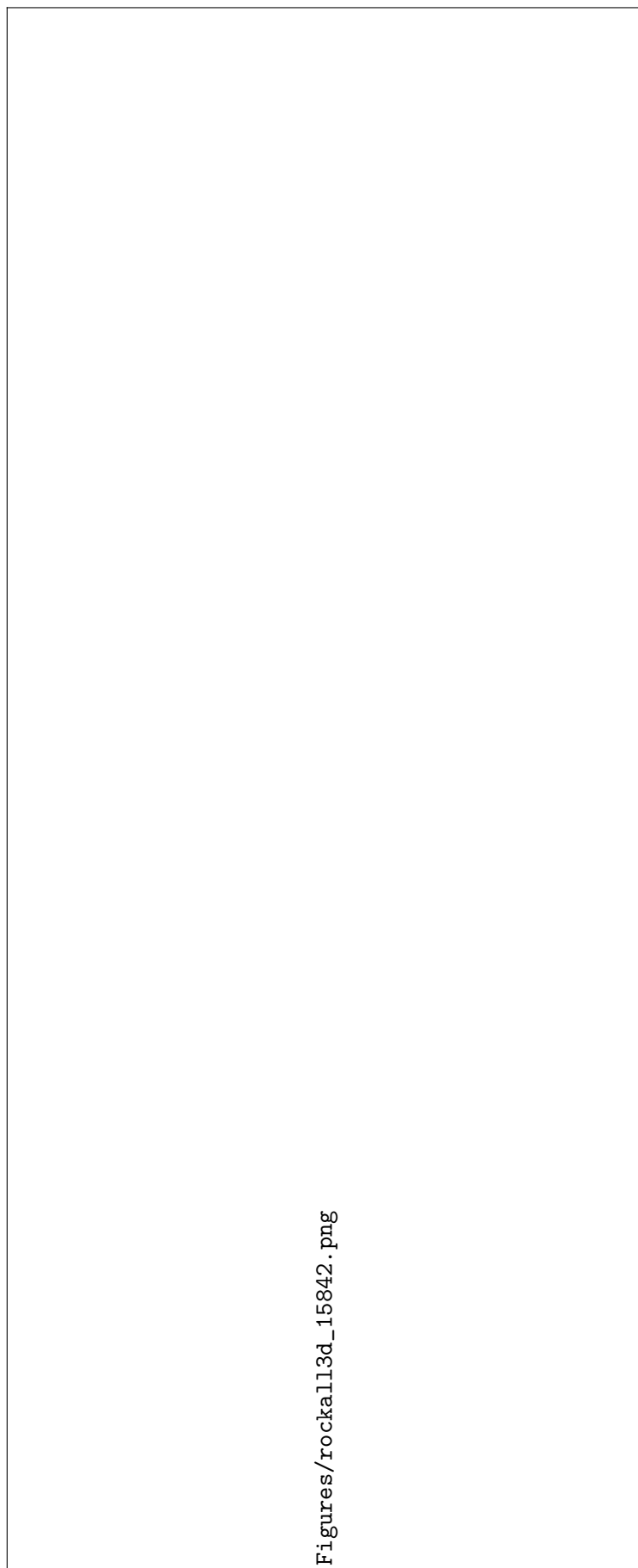


FIGURE 2.22: Example seismic line from the Rockall 3D survey, with interpretation. [Redacted]

2.3.2 Judd survey

Similar to the 3D NE Rockall survey, the Judd basin survey's origin is unknown — it has been in the Earth science department at the University of Birmingham for at least 15 years. No acquisition or processing information was available for the Judd survey, as associated files have been lost. A map of the dataset can be found in figure 1.7.

Figure 2.23 shows the frequency spectrum for the OGA survey, while figure 2.24 shows an example of the seismic data itself.

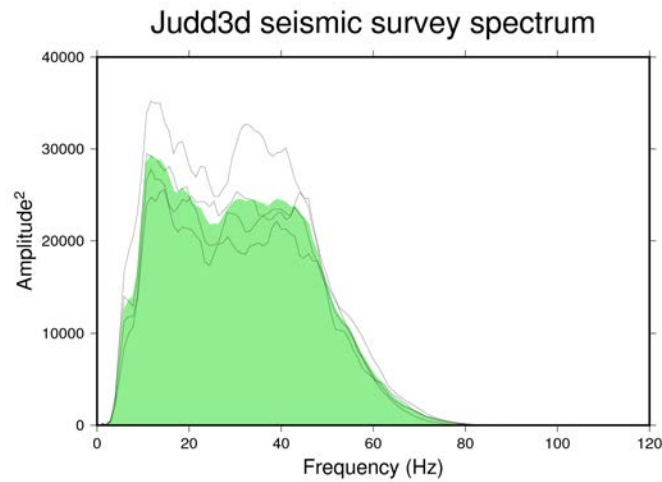


FIGURE 2.23: Power spectral density estimates for the Judd 3D survey. Individual black lines are power spectral density estimates for individual inlines in the survey, while green curve is the mean of the individual lines.

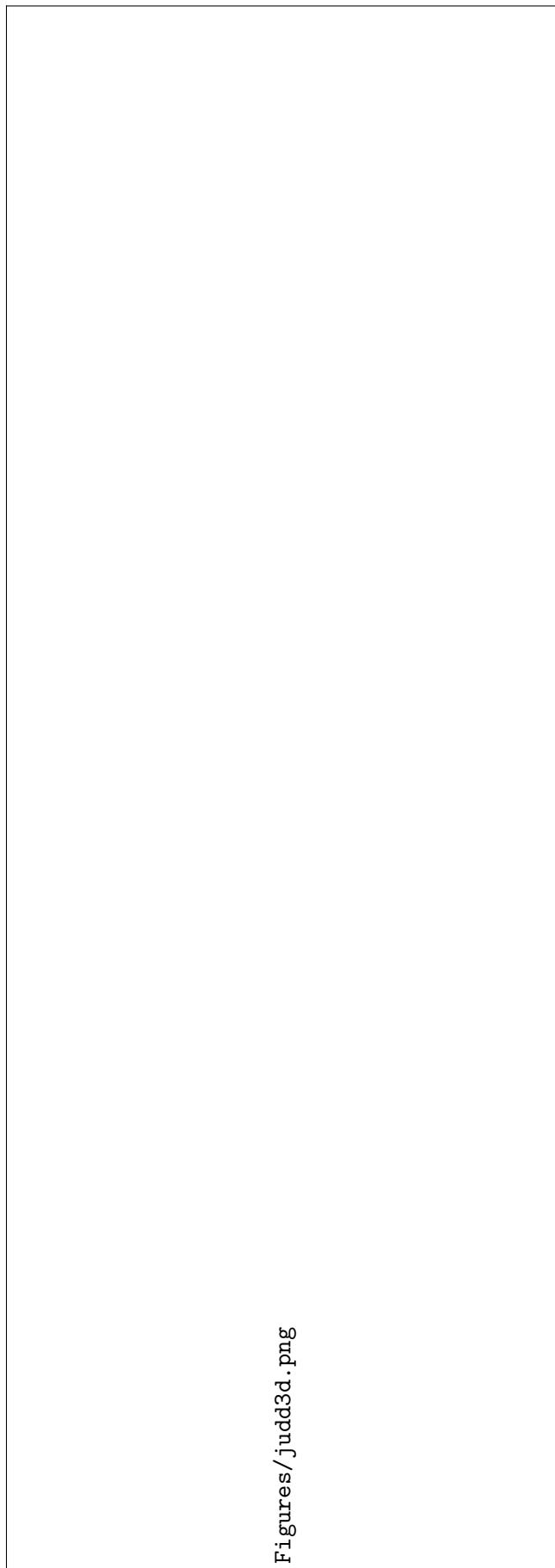


FIGURE 2.24: Example seismic line from the Judd 3D survey, with interpretation. [Redacted]

2.3.3 TGS FSB Megasurvey Plus survey

The commercial FSB Megasurvey Plus dataset was given to Joanne Murray by TGS while she was a PhD student in the Geosystems research group at the University of Birmingham. Interpretation of sills and their measurements were done by Joanne and given to the author. Details of acquisition and processing were commercially sensitive and were not available to the author. A map of the dataset can be found in figure [1.7](#).

2.3.4 Carnarvon survey

The commercial Carnarvon dataset was worked on by the author during several weeks at Imperial College London, during work with external supervisor Dr. Craig Magee. Details of acquisition and processing were commercially sensitive and were not available to the author, and the dataset was not available afterwards to make further images from. A map of the dataset can be found in figure [1.12](#).

2.4 Well data

Eighteen wells were used to tie the seismic data (i.e. to calibrate the age of different horizons). The wells are all released by the Oil and Gas Authority (OGA). A table of the names of the wells used, and the seismic lines each well intersect, is given in table [2.1](#).

TABLE 2.1: Wells used in this thesis, and seismic lines each well intersects.

Well name	Seismic line intersected	Basin
132/06-1	WG152DOGA1000043A049	Rockall
	WG152DOGA1000078A033	
	AMWG14-022	
132/15-1	DGWH96-29	Rockall
	INROCK-96-12	
	DGWH96-21	
	INROCK-96-08	
	WG152DOGA1000078A033	
	WG152DOGA1000079A045	
	WG152DOGA1000003A032	
	DGWH96-04	
	WB93-117B	
	DGWH96-28	
	DGWH96-29	
154/01-1	WG152DOGA1000032A225	Rockall
	WG152DOGA1000036A015	
154/03-1	WG152DOGA1000037A003	Rockall
164/25-1	WG152DOGA1000028A211	Rockall
	WG152DOGA1000073A249	
	WG152DOGA1000034A013	
	WG152DOGA1000037A003	
164/25-2	WG152DOGA1000029A212	Rockall
164/27-1	WG152DOGA100002A012	Rockall
	Rockall 3D	
164/28-1	WG152DOGA1000036A015	Rockall
	Rockall 3D	
202/08-1	WG152DOGA1000074A201	Judd
	WG152DOGA1000089A246	
204/30-2	WG152DOGA1000089A246	Judd
205/26-1	WB93-158	Judd
	WG152DOGA1000074A201	
204/22-2	Judd 3D	Judd
204/16-1	Judd 3D	Judd
204/26-1	Judd 3D	Judd
6004/12-1	Judd 3D	Judd
6004/16-1	Judd 3D	Judd
6005/15-1	Judd 3D	Judd
43/13-1	PORC-97-16	Porcupine
	PORC-97-60	

2.5 Remote sensing data

Sill measurements from the Karoo basin were made by Gina Wright while she was an MSci student at the University of Birmingham, before being given to the author. Google satellite imagery data was used, and was interpreted in Global Mapper software (figure 2.25). Google satellite imagery data combines Landsat data with high resolution proprietary airborne imagery. Horizontal resolution for much of the Karoo is around 2-5 meters, giving similar orders of magnitude resolution to seismic data. No thickness measurements, transgressive limb measurements, emplacement depth measurements or shape classifications were made in the Karoo data (these measurements and classifications are defined in section 3.2). No method currently exists to estimate the amount of material eroded from exposed sill tips, so no corrections were applied to any of the measurements made in the Karoo, meaning Karoo sill measurements represent a lower bound of the measurement made.

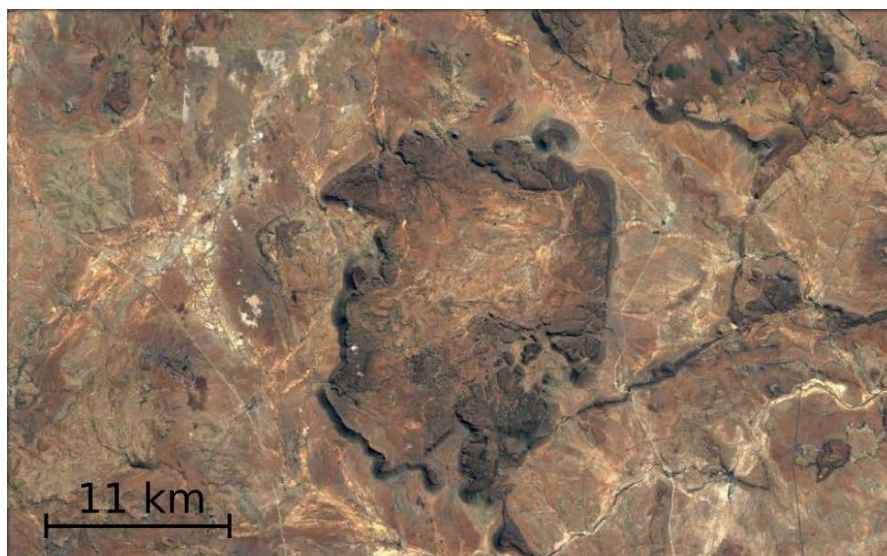


FIGURE 2.25: Example of a sill on the remotely sensed data. Data is from Google Earth, accessed October — May 2013.

2.6 Literature data

Other sill measurements were taken from the literature, or from released PhD theses. These can be found in appendix A.

2.7 Implications of different surveys on measurement resolution

Table 2.2 shows a summary of the survey parameters for each dataset. The similarity or difference between surveys is important in the following chapters due to the potential bias in measurements any difference in resolution could confer. Vertical resolution will be defined and discussed in detail in section 3.2.1, but is calculated in table 2.2 based on the survey dominant frequency (the peak frequency for each survey spectrum), and a sill velocity of 6000 m s^{-1} . Horizontal resolution on unmigrated data is equal to the fresnel zone, however this is collapsed by the migration procedure to somewhere around $\lambda/4$, where λ is the seismic wavelength. As all surveys are migrated, horizontal resolution is hence taken as $\lambda/4$.

Seismic data processing flows can have dramatic effects on data resolution. Analysis of the preceding sections on seismic data processing steps for each seismic survey shows that all surveys have undergone standard and similar processing flows. Therefore processing is not expected to bias measurements. For the streamer length, fold, vertical resolution and horizontal resolution, table 2.2 shows that most parameters are similar. The Hatton survey stands out as having relatively low values for streamer length and fold. However, the sills measured on the Hatton survey were well resolved in the shallow sections due to geological reasons (specifically, a relatively homogeneous deep water strata being intruded - see figure 2.18). Vertical resolution does vary between surveys, however this is only important for measuring sill thickness. Measuring sill thicknesses on seismic data was found to be very difficult; few sills are thicker than tuning thickness regardless of the survey the sills were measured on and hence bias in the sample was more important than between survey resolution variability, as described in section 3.3.3. Horizontal resolution also varies between surveys, from a resolution of a few meters for the satellite Karoo dataset to close to a hundred meters for the deeply emplaced Judd dataset. This undoubtedly introduces errors of similar scales into measurements. However, as section 3.2.2 outlines, the average sill diameters in different datasets varies between $\sim 3000 \text{ m}$ and $\sim 12000 \text{ m}$, hence errors in horizontal resolution are expected to be $\sim 1\%$ of the measured values. Thus, the datasets used for investigating sill populations are not expected to introduce significant errors into measurements between surveys.

TABLE 2.2: Summary of resolution parameters for datasets used in this thesis.

Dataset name	Streamer length (m)	Fold	Vertical resolution (m)	Horizontal resolution (m)
Rockall 3D	Unknown	Unknown	18 - 36	36
Judd 3D	Unknown	Unknown	46 - 92	92
Porc97	4800	96	37.5 - 75	75
ISROCK	4500	60	37.5 - 75	75
INROCK	4000	80	42 - 83	83
DGSRT	4500	90	39 - 78	78
DGWH	4500	90	37.5 - 75	75
DGER	4500	90	39 - 78	78
PAD	10 000	134	37.5 - 75	75
FSB Megasurvey Plus	Unknown	Unknown	Unknown	Unknown
Hatton	1200	34	31 - 62	62
Bight	6000	120	25 - 50	50
Carnarvon	Unknown	Unknown	Unknown	Unknown
Karoo	NA	NA	NA	2 - 5

Chapter 3

A global analysis of sill dimensions

3.1 Introduction

Chapter 1 outlined two current research targets in the area of sill research: first, the lack of quantitative parameter knowledge of sills to feed into palaeoclimate modelling, and secondly the absence of any studies testing numerical sill models against real data. This chapter will address these two issues.

When sills intrude organic rich mudrocks, thermogenic methane is produced and vented to the atmosphere. Through production of methane and venting to the atmosphere, sill intrusion has been suggested as a driver for major palaeoclimate events, such as the PETM (Svensen et al., 2004), the End Permian mass extinction (Burgess et al., 2017) and the Toarcian ocean anoxic event (Svensen et al., 2012b). For sill intrusion to be a realistic driver for palaeoclimate warming, a large enough volume of magma needs to be intruded within a short enough timescale to perturb the global climate. As yet, no geologically realistic gas emission models for a LIP exist. This is in part due to a lack of dimensional statistics for sills, which the chapter will explicitly address. Dimensional statistics are not the only information needed for a gas emission model for a LIP. The spatial location and timing of magmatic emplacement need to be known, and source rock location, thickness and richness also need to be known. These are outside the scope of this work, but will be addressed by Jones *et al.*, (in prep.).

The second goal of this chapter is testing sill emplacement models against real world datasets. A selection of sill emplacement models was presented in Chapter 1, including mathematical, analogue and conceptual models. The commonality between these

studies is that they did not have a large amount of statistical data to test their models. For example, [Johnson and Pollard \(1973\)](#) compared their numerical models against the Sawtooth Ridge and Trachyte Mesa sills in the Henry Mountains, USA. However, these intrusion are not completely exposed, where they are exposed they have been eroded, and the dataset comprised only two intrusions. These intrusions are also laccoliths, and the validity of conflating these with sills is not understood. [Goulty and Schofield \(2008\)](#) presented a variation of [Johnson and Pollard's \(1973\)](#), and did not use any real data to test their model. [Malthe-Sørenssen et al. \(2004\)](#) did not test their model against real data, although they do mention similarities in gross morphology to some sills observed in the Karoo basin. [Mathieu et al. \(2008\)](#) also did not test their analogue models against any real world data. [Goulty's \(2005\)](#) models are made with reference to the Midland Valley and Whin Sills in Scotland and Northern England, two sills with relatively poor exposure and hence low confidence of the parameters used to calibrate the model. [Kavanagh et al. \(2006\)](#) do not test their analogue models against real sills. [Galland et al. \(2009\)](#) test their analogue models against the Tulipan Sill offshore Norway and the Golden Valley Sill in the Karro, and find a poor fit to these two pieces of data. To point out this lack of testing against real sill measurements is not simply nit-picking published studies. Testing and calibrating models against real data adds value to the original studies by increasing confidence in their model predictions. On the other hand, testing against real data can highlight when a model is inappropriate because of model assumptions which may not apply in all cases. In this chapter a database of sill measurements is assembled to fill this knowledge gap, by testing theoretical sill models against sill measurements taken from seismic data.

3.2 Methods and definitions

The database introduced in this chapter comprises over 400 sills newly interpreted and measured on seismic data, and a further 600+ sills extracted from the literature and from remote sensing data. The decision to concentrate on seismic data was made because of particular interest in the 3D geometry of the sill for its aforementioned importance to palaeoclimate and sill emplacement studies. Unlike seismic or remote sensed data, field data rarely gives a clear picture of a sill's full 3D geometry as the most common site of exposure of a horizontal sill is normally a cliff section. By definition, if the sill is exposed then some sill mass must have been lost to erosion, and thus measurements of the full extent will require extrapolation. However, there is only one known technique for extrapolating missing sill volume in field studies to a sill's original dimensions (see [Richardson et al., 2015](#)). [Richardson et al.'s \(2015\)](#) method assumes a Laplacian-spline surface within sill boundaries and assumes sills extend no more than 0.5 km from their

field exposures. No evidence to support these assumptions is given in [Richardson et al. \(2015\)](#), and sill diameter data later in this chapter suggests that these assumptions may be erroneous.

Sills are generally easy to interpret on seismic data. Sills were identified based on 5 criteria: (1) high amplitude, (2) positive polarity reflection forming the top of the sill, and (3) a corresponding negative reflection forming the base of the sill. The reflection is (4) laterally discontinuous, and (5) commonly locally transgresses stratigraphy (e.g. [Smallwood and Maresh, 2002](#)). After interpretation key quantities were measured and/or derived. These quantities are defined as follows. Sill diameter is defined as the maximum measured horizontal length of a sill at its time of emplacement (fig 3.1). If basins had been inverted or deformed this would have required unfolding of strata before measurement. However, this was not necessary in any of the datasets. Note that this is the maximum horizontal dimension (labelled A in figure 3.2), not the total in-plane length (labelled B in figure 3.2). This decision was taken due to the volume of data being measured - measurement A is simpler to carry out as measurement B required the data to be depth converted to obtain the correct vertical distance before measurement, and not all data was available with velocity information (see later in this section for details on depth conversion). On 3D seismic data, diameter was taken as the maximum horizontal dimension. On 2D seismic data, diameter was taken as the chord of intersection between the 2D seismic line and the sill. The validity of this approach, which is the same approach as used by multiple other authors in the literature (e.g. [Jackson et al., 2013](#); [Magee et al., 2014a](#)), is modelled and discussed in section 3.2.2. The sill diameter results are discussed in section 3.3.2, and used to test numerical sill models in section 3.5.

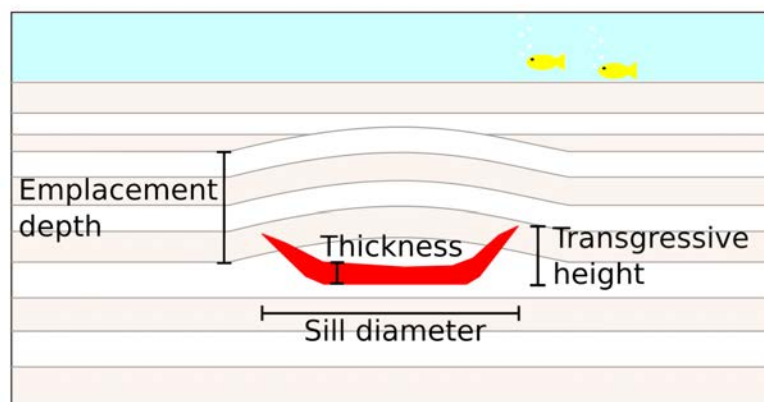


FIGURE 3.1: Definitions of measurements taken on each sill in the sills database.

Sill thickness was also measured (fig 3.1). All seismic data used in this study was interpreted in time not depth. The top and base time of each sill was recorded if the sill had a coherent top and base reflection. Only the top time was recorded if the sill was

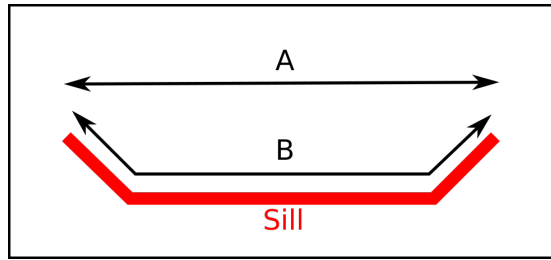


FIGURE 3.2: Definition of sill diameter, as measured for the sill database. Measurement A was made on each sill instead of measurement B. See text for discussion.

below seismic tuning thickness (Brown, 2011; Simm and Bacon, 2014). Sill thickness was then found from the relationship

$$d = \frac{TWT \cdot V_s}{2} \quad (3.1)$$

where TWT is the two way travel time, d is the vertical distance between the top and base of the sill reflections, and V_s is the average seismic velocity. Sill velocities (V_s) used to derive sill thicknesses were taken from Smallwood and Maresh (2002) in all cases, who found sill V_s to vary between 4500 ms^{-1} and 6500 ms^{-1} with a modal value of 6000 ms^{-1} . This range of sill velocities could be due to a number of factors: amount of fracturing or jointing, primary mineral content, secondary hydrothermal alteration, presence of layering, mixing or mingling of magmas, and other factors. Unfortunately, these cannot be predicted from seismic data alone, and without pre-stack seismic data (unavailable for the work in this thesis) the range of seismic velocities for any sill cannot be narrowed down. Sill thickness is discussed in section 3.3.3 and modelling results using sill thickness are discussed in section 3.5.

Sill emplacement depth was defined as the distance between syn-emplacement surface and the top of the sill at the middle of its diameter. The syn-emplacement surface is typically identified based on onlapping forced fold relationships (Hansen et al., 2004; Trude et al., 2003a) or on the surface where hydrothermal vent structures (Hansen, 2006) are found. Depth to the top of the forced folds and to the top of sills were derived from measurements of the time domain seismic data using second order polynomial regression functions fitted to borehole checkshot surveys. This approach was used in the Rockall and Bight basins, where sufficient well data was available (fig 3.3). In other basins well data was not available at the time of this study, so an average velocity of 2 km s^{-1} was used. This simple model has the major advantage of being simple to understand, and is trivial to undo by other researchers should they have access to velocity information. Emplacement depth measurements are discussed in section 3.3.5.

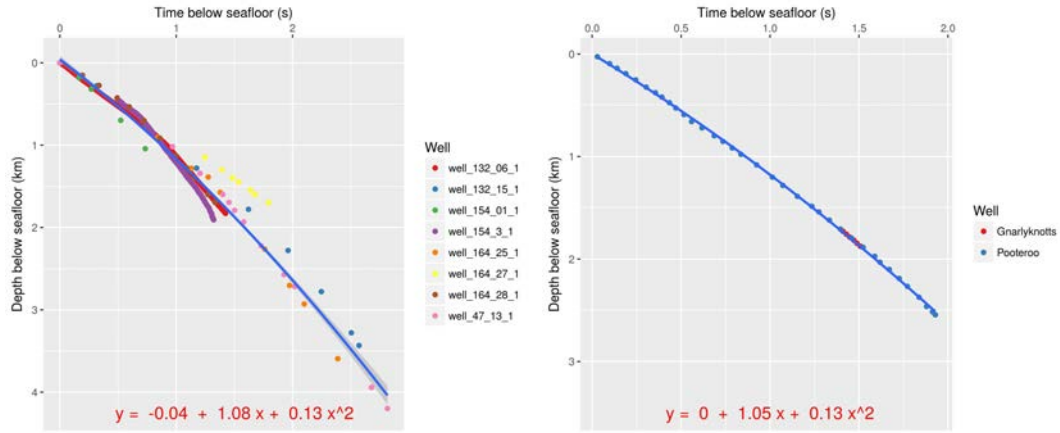


FIGURE 3.3: Checkshot surveys for the Rockall (left panel) and Bight (right panel) Basins, used for depth conversion of seismic data. Second order polynomial regression lines are in blue, with pale blue envelope representing a 95% confidence interval.

Transgressive height was measured for all sills interpreted on seismic data (figure 3.1). Transgressive height was defined as the distance from the lowest point of a sill to the highest extent a single sill limb climbed to. Transgressive height measurements are discussed in section 3.3.4.

Finally, sills were assigned to one of six gross morphologies. These six categories were saucer shaped, flat, inclined, transgressive, laccolithic or irregular. This scheme combines definitions from Planke et al. (2005), Fernandes (2011), Jackson et al. (2013) and Reynolds et al. (2017). Sill shapes are shown schematically in figure 3.4. Saucer shaped sills have either a flat base and inclined rims, or a smooth bowl shaped intrusion without an obvious flat base. Flat sills were horizontal at time of intrusion, and did not contain significant steps or transgress stratigraphy. Transgressive sills have a flat base and transgress on a single side only, while inclined sheet intrusions transgress stratigraphy without a flat base. Laccoliths have a base close to flat and a domed top. Laccoliths are almost always accompanied by deformation of the overburden to accommodate the space problem - the question of how volumetric space can be created to accommodate the additional intruded magma volume. Irregular intrusions are those intrusions that do not fit into one of the other categories. These are likely to be one of the other sill morphologies that has been poorly imaged on seismic data. Many of the examples of irregular sills in the sills database came from the literature rather than interpreted by the author. The origin of these irregular intrusions was not a central goal of the project, so these were not investigated further. A final point should be made about the exclusion of “Fault block” type sill from the scheme in figure 3.4. Fault block sills were defined by Planke et al. (2005) as those sills found layer parallel inside fault blocks and intruded the faults bounding the fault block. Many examples were found of sills intruding fault

blocks, but none were found to exploit faults and yet be bound by fault blocks as described in [Planke et al. \(2005\)](#). However, generally these sills cut stratigraphy inside the tilted fault blocks and often cut straight through faults, which make them one of the other sill types — normally the flat or transgressive morphologies. The results of this classification are discussed in section 3.3.1, and are used in subsequent sections to split sills for analysis.

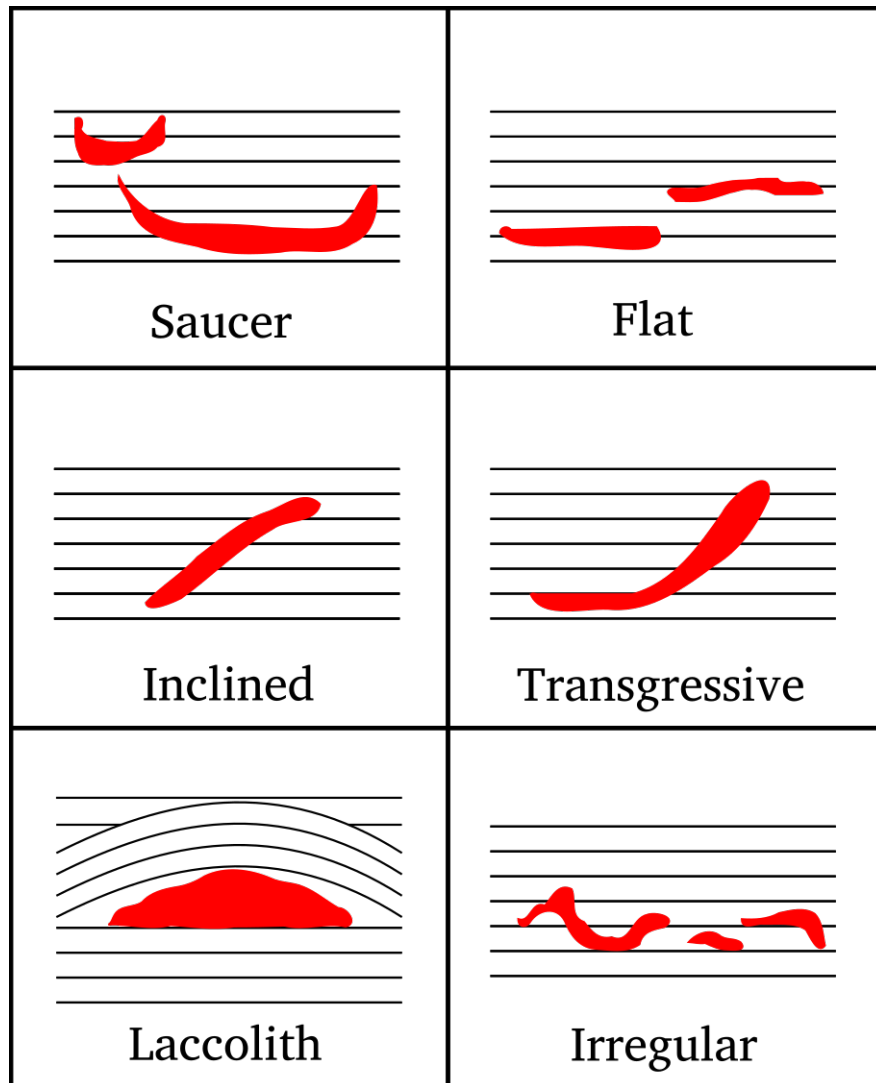


FIGURE 3.4: Definitions of sill shapes. Sill shapes are used to subset data in later analysis

3.2.1 Seismic resolution of sills

Seismic resolution is commonly considered in terms of vertical and horizontal resolution ([Brown, 2011](#); [Simm and Bacon, 2014](#); [Widess, 1973](#)). Vertical seismic resolution controls whether the top and base of a sill are imaged separately, or as a tuned reflection package. This is well understood for sills (e.g. [Eide et al., 2017a](#); [Magee et al., 2015](#); [Smallwood](#)

and Maresh, 2002; Thomson, 2005a). However, for measuring the diameters of sills, it must first be asked whether the sill as measured is a true representation of the sill's true diameter. Seismic resolution is formalised by the concepts of separability and detectability (e.g. Brown, 2011; Simm and Bacon, 2014). Seismic separability refers to the distance apart of two reflectors before their reflections begin to interfere and therefore the two reflections become one single non-separable reflection (see figure 3.5). The thickness at which this occurs is termed the tuning thickness (Widess, 1973), defined by the relation

$$\frac{\lambda}{8} \leq T_t \leq \frac{\lambda}{4} \quad (3.2)$$

where T_t is the tuning thickness, λ is the dominant wavelength of the seismic signal. λ can be found from the relation

$$\lambda = \frac{V_p}{F_d} \quad (3.3)$$

where V_p is the seismic velocity of the sill and F_d is the dominant frequency in a window around the sill. T_t controls whether a sill thickness can be measured on seismic data. Seismic detectability is defined as whether or not a reflection can be observed, and is thus controlled by the amplitude of the reflection compared to the background noise level. Given that sills are generally considered to gradually decrease to zero thickness (i.e. they have sharp tips, as opposed to having blunt tips), and that most sills are on the length scale of tens of kilometers in diameter, the limit of detectability controls the point where a sill is no longer visible when it narrows to zero thickness and therefore controls to what point sill diameter can be measured.

The question of detectability can be studied with a wedge model, set up as in figure 3.6. Taking a hypothetical sill of 10km diameter and 250m thickness, the average taper of the sill is ≈ 2.9 degrees (assuming greatest thickness in the centre of the sill). The wedge model is set up by defining four 5000×450 matrices, and within these matrices filling a wedge of rock properties such that the wedge takes up 250m on the right hand side of the matrix, and narrows smoothly to 0m on the left hand side of the matrix. The first matrix represents the compressional velocity V_p , and is filled with values of 1750, 6000, and 1750 ms^{-1} as representative theoretical velocities for an igneous intrusion sandwiched between two sedimentary rocks (See top left panel of figure 3.6). The top right hand matrix represents the rock density ρ , which are modelled as having densities of 2100, 2900, and 2100 kgm^{-3} for the upper sediment-intrusion-lower sediment stratigraphy, respectively. The acoustic impedance can then be calculated as $AI = V_p\rho$, and

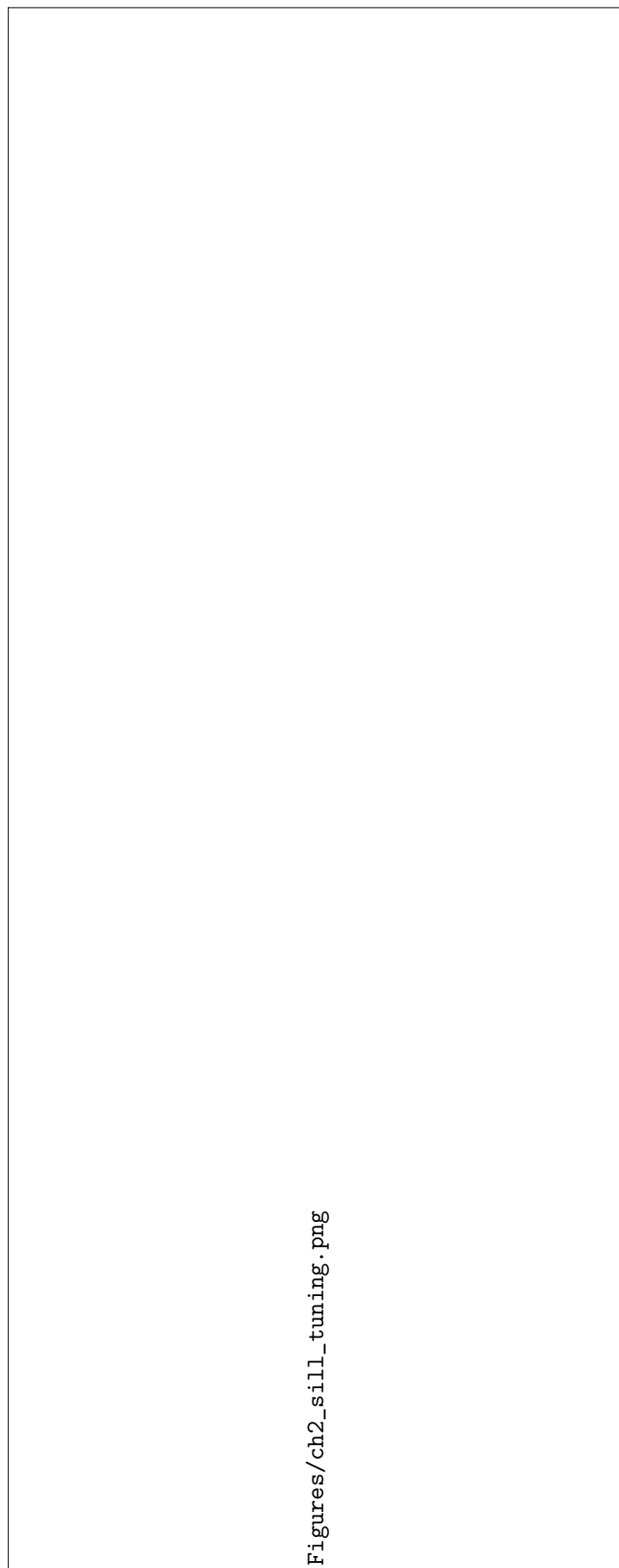


FIGURE 3.5: An example of a sill above and below tuning thickness in the Rockall basin. [Redacted]

the reflection coefficients can be calculated by slicing matrix operations, numerically approximating the vertical derivative. See figure 3.6 for the model setup.

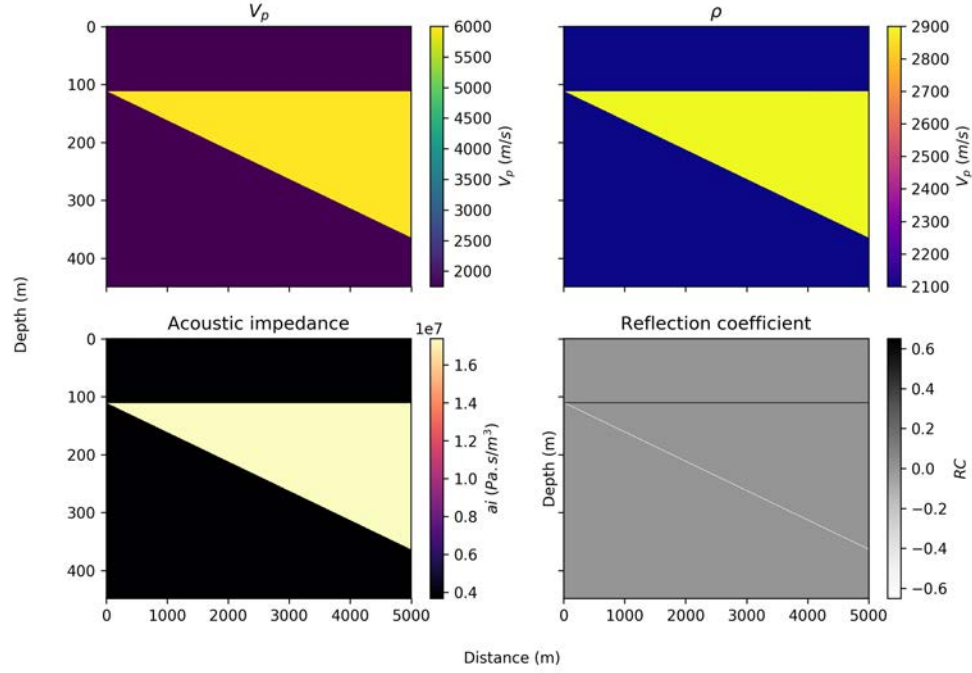


FIGURE 3.6: Setup for the synthetic wedge model without noise, used to study the importance of seismic resolution on measurements. Top left is P-wave velocity. Top right is density. Bottom left is the acoustic impedance, which is the product of P-wave velocity and density. Bottom right is the reflection coefficient, the depth derivative of the acoustic impedance.

The reflection coefficient matrix was then convolved along the vertical axis with a 0.1 s long Ricker wavelet (e.g. [Simm and Bacon, 2014](#)), defined as

$$A = (1 - 2\pi^2 f^2 t^2) e^{-\pi^2 f^2 t^2} \quad (3.4)$$

where A is the amplitude, f is the peak frequency and t is the time. In a seismic dataset, frequency varies with depth and laterally. Thus, if an individual sill was to be modelled the dominant frequency should be calculated from a window around the sill. However, the intention in this section is to look at the problem of lateral imaging of sills in a general sense. Frequency spectra for each dataset are found in Chapter 2, which show peak frequencies of all seismic surveys to be in the region of 20 Hz, which is used as the peak frequency for the generated Ricker wavelet.

The results of convolving the Ricker wavelet with the reflection coefficient matrix can be seen in figure 3.7. This shows clearly that the sill is visible well beyond onset of tuning

(which occurs at around 2500m on the x axis). Figure 3.7 also shows the amplitude curves for the top surface of the wedge, which shows similar results as in [Smallwood and Maresh \(2002\)](#) and [Thomson \(2005a\)](#). Amplitude is seen to be constant until the onset of tuning is reached at $\approx 2500\text{m}$, at which point it increases non-linearly to the point of maximum constructive interference at around $\approx 1100\text{m}$. Amplitude then decreases to zero as the zero thickness wedge is approached. The amplitude as measured in this wedge model can be defined as the actual amplitude as measured along the true location of the sediment-sill interface, or apparent amplitude as the maximum amplitude in a window of 20 milliseconds around the true location of the sediment-sill interface. Apparent amplitude is then what most interpreters will autotrack on seismic interpretation software. The results of the wedge model show that constructive interference near the edges of the sill will actually help improve resolution (as compared to actual amplitude) near sill edges and hence increase the chances of seismic interpretation of a sill being representative of sill diameter.

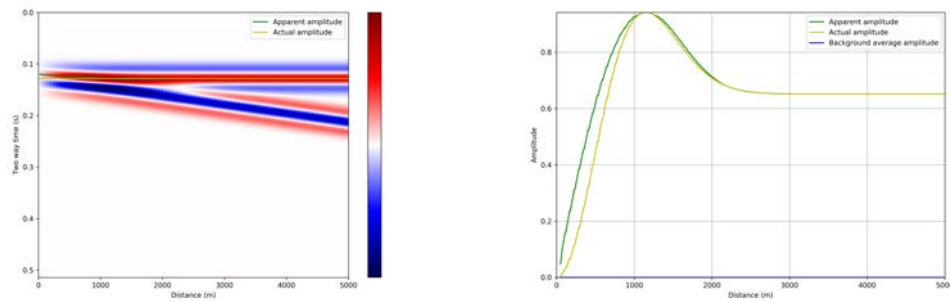


FIGURE 3.7: Results of the noise free synthetic wedge experiment. Actual amplitude is measured along the true location of the sediment-sill interface. Apparent amplitude is the maximum amplitude in a window of 20 milliseconds around the true location of the sediment-sill interface.

Figures 3.6 and 3.7 show that in the presence of no other noise, theoretically a sill will be imaged all the way to its termination. However, this is an unrepresentative case, as seismic data always contains other noise. Seismic noise is generally considered coherent (i.e. multiples, diffractions and other reverberations) or incoherent (i.e. random). Seismic processing steps are often aimed specifically at reducing or removing coherent noise. Coherent noise is not thought to be a major issue for the majority of the interpreted and measured sills in the dataset, as an experienced seismic interpreter can normally identify coherent noise. The amount of incoherent seismic noise is generally the bigger problem for whether a sill is detectable to its full extent, as it controls the background level of noise for which the sill reflection must be higher amplitude than.

Figure 3.8 shows the model results of running the same experiment but with added incoherent noise. Random Gaussian noise was generated and added to the original model

setups in 3.6. The amount of noise to add is subjective — each seismic survey is different, and the amount and content of random noise is a function of many factors including the geology and seismic acquisition system, seismic processing work flow, weather conditions during survey acquisition and many other factors. To keep the model simple, the amplitude of the random Gaussian noise was added until the seismic section looked similar to that observed during interpretation of sills on real seismic data. In this case this involved addition of noise with a mean of 0 and a standard deviation of 0.1 added to the reflection coefficient matrix before convolution.

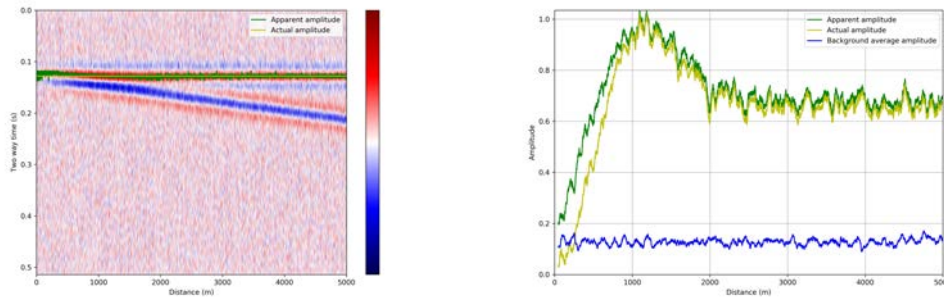


FIGURE 3.8: Results of the synthetic wedge experiment with added Gaussian noise, simulating the random component of seismic noise.

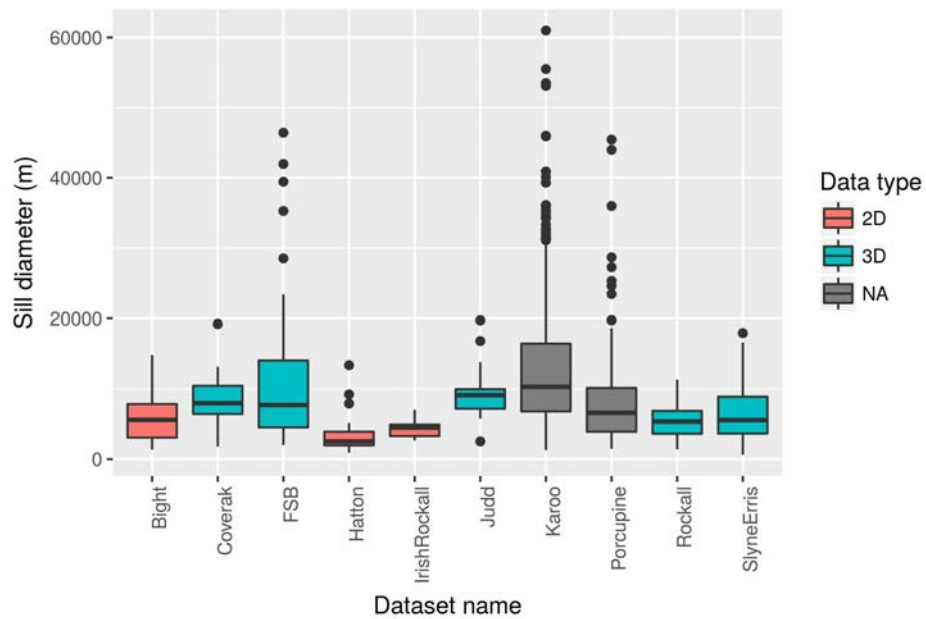
Figure 3.8 shows that the amplitude curve is much less smooth, as variations in the reflection coefficient due to the random noise make noticeable changes in the final amplitude. The key result involves the blue curve of average background noise, which was computed as the average of 10 samples in a window of the background not containing reflectivity from the sill wedge. As the background noise content is increased the blue curve rises higher on the graph. When the blue curve is equal to or higher than the yellow and green curves, the sill will no longer be interpretable.

From running this model with different noise parameters, it can be seen that the noise content has to be very large before the sill reflection disappears. This approach shows that should a sill be imaged, the reflection terminations will truly be very close to the terminations of the actual sill. This should therefore give confidence that the sills interpreted on real seismic do represent very close to the true sill diameters, and not an arbitrary lower fraction of the sill diameter as would be the case should the sill only be detectable to a certain critical thickness.

3.2.2 The difference in statistics between 2D and 3D seismic data

The data in the sills database is from both 2D and 3D seismic data sets. If it is assumed that sills are roughly circular in map view, and we also assume whoever is planning the

seismic surveys does not know the location of the sills, intuitively it may be expected that any single seismic line will almost never cut through the centre of a sill. Therefore, the measured diameter on a 2D seismic line is highly unlikely to be fully representative of the sill's diameter. The variation of sill diameters with sills shapes and basins will be studied in detail later in this work. However, the data studied in later sections can be used to ascertain whether a difference between 2D seismic vs. 3D seismic is apparent, by colouring data sets by type (figure 3.9). Immediately apparent from figure 3.9 is that the 3D seismic datasets have yielded predominantly higher medians and interquartile ranges than the majority of the 2D datasets. This clearly represents a systematic bias.



[h]

FIGURE 3.9: Box and whisker plot of sill diameter data, coloured by whether the seismic data measurements were collected from 2D or 3D data. Points represent outliers, defined as less than the lower quartile (LQ) plus 1.5 times the interquartile range (IQR) or the upper quartile (UQ) plus 1.5 times the IQR. The box extents represents the upper and lower quartiles, hence the IQR is the UQ - the LQ. The horizontal line through the box is the median. The upper and lower whiskers represent the LQ plus 1.5 times the IQR, and the UQ plus 1.5 times the IQR, respectively. Karoo Basin data is marked NA due to it being measured from satellite data. Porcupine Basin data is marked NA as it has close to equal proportions of 2D and 3D data, however the 2D and 3D data in Porcupine is from different spatial regions within the basin and so is not fair to split and directly compare.

With such bias in mind, it would be useful to be able to correct 2D population measurements to yield a better estimate of the true diameter. Correction of this bias has not yet been published on, so a method of correcting for this is suggested as follows. Where and how a 2D seismic line intersects a sill is an inherently stochastic process, given the random distribution of sills relative to a seismic line. Thus, it can be posed as a Monte Carlo problem. Figure 3.10 shows the setup of the Monte Carlo model. An array of hypothetical sills with diameters ranging from 100 m to 100,000 m is

created in steps of 100. Sills are assumed to be circular in planform. This simplification is made for computation purposes mainly. In the author's experience most sills are mildly elliptical, however, a significant proportion of sills are close to circular. If the semi-major axis of an ellipse is the same size as the diameter of a circular sill, the effect of the sill measurements be greater than for simply a circular sill, due to the random orientation of the ellipse further decreasing the chance of the seismic line intersecting the semi-major direction. The random intersection of a seismic line is modelled as choosing a random number from a uniform distribution between zero and the sill diameter, which corresponds to point ω . κ is then defined as the length of the chord which corresponds to the measured diameter for a 2D seismic line intersecting a sill at point ω , which can be found from rearrangement of the pythagorean theorem, such that

$$\kappa = 2\sqrt{\gamma^2 - \beta^2} \quad (3.5)$$

where γ is the sill radius, and β is $\gamma - \omega$. This is done one thousand times for each sill, and the maximum, minimum, mean and standard deviations are found for the intersected chords representing the measured diameters on a 2D seismic line. Figure 3.11 shows the results of this modelling. This modelling confirms that a diameter measured on 2D seismic can be anywhere between zero as a lower bound, and the true diameter as the upper bound. The median measured sill diameter can be seen to be a little over 3/4 of the true diameter. The envelope defined by the interquartile range shows that for any true diameter, the likely measured diameters form a bounded distribution with a strong left skew, meaning the measured diameter is likely close to the true value, but is almost certainly not representative of the true value.

This has important implications for studying sill size distributions across different basins where different seismic data types dominate. Firstly, true size distribution cannot be measured from 2D seismic data alone. The histogram in figure 3.12 shows that the distribution is exponential in shape, and thus correcting to the mean or median will result in very much unsatisfactory results as the gross distribution shape will not change.

The simulations thus far have shown that individual sill diameter measurements made on 2D seismic data cannot be satisfactorily corrected to their true lengths. However, instead of looking at individual lengths, it may be more sensible to test whether samples statistics (e.g. sample mean sill diameter) can be corrected to closer to the true mean sill diameter. This can be studied by using nested Monte Carlo simulations to repeat the previously described Monte Carlo simulations, for random samples of sills with increasing mean diameters taken from a specified distribution. It would be expected that sample means would be less than the actual means, however we are interested in the shape of

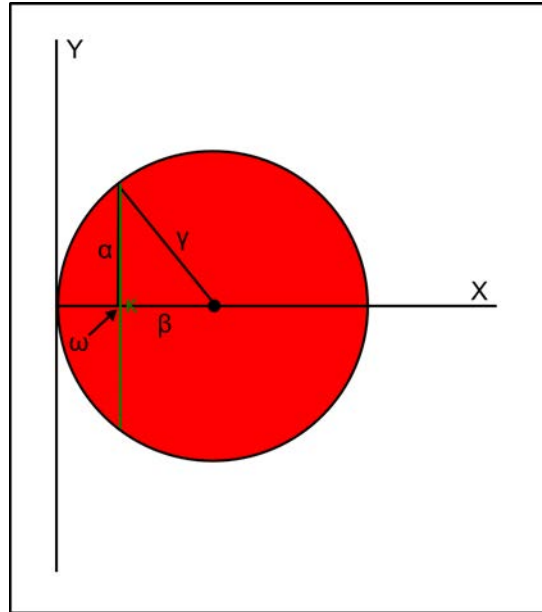


FIGURE 3.10: Setup for the Monte Carlo model investigating random intersection of a 2D seismic line with a sill.

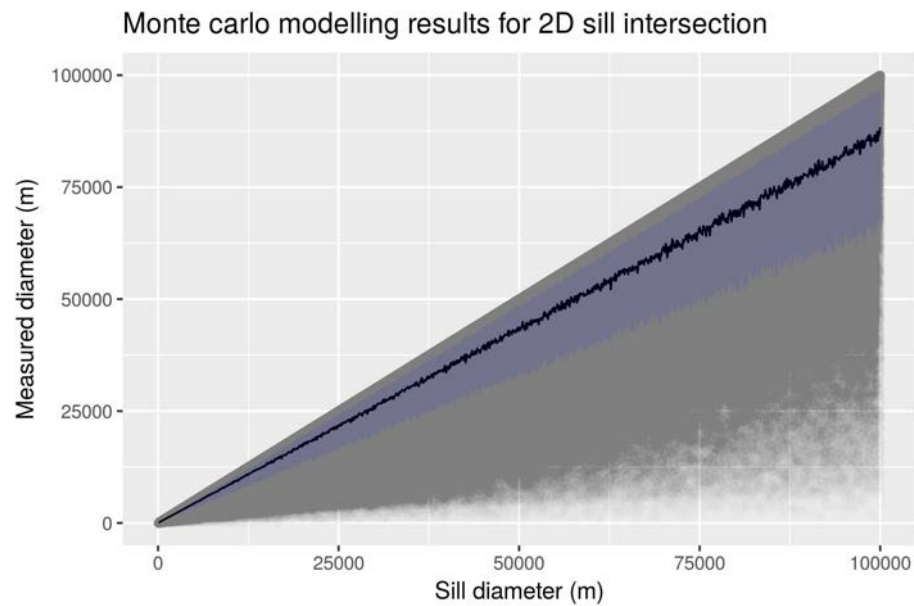


FIGURE 3.11: Monte Carlo modelling of random intersections of a seismic line with a sill. Black line is the median value. Purple envelope represents the interquartile range.

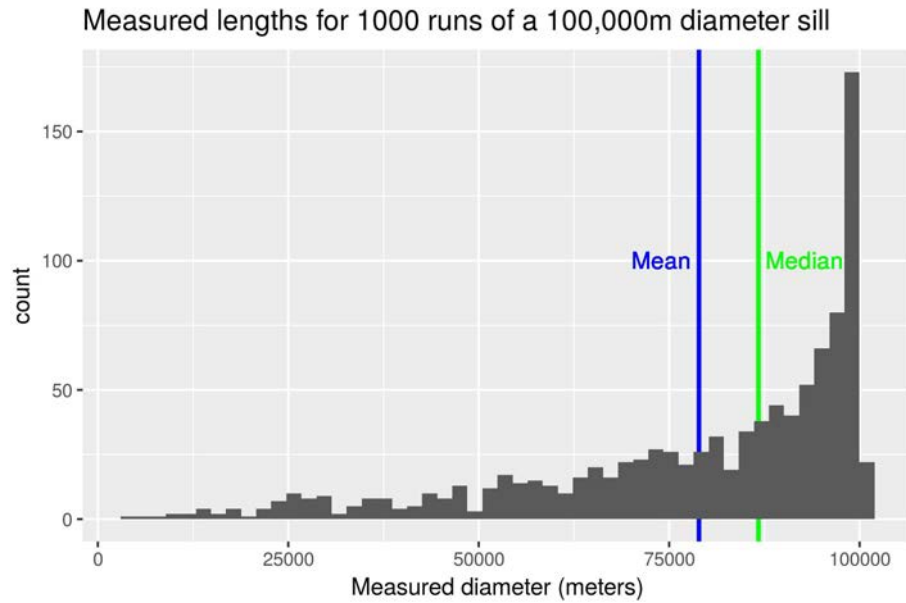


FIGURE 3.12: Histogram of the Monte Carlo run results for a 100000 m diameter sill

such a relationship. If the relationship is a smooth function, corrections can be found for 2D seismic data to correct sample means to be closer to the true population means. Figure 3.13 shows the results of this, for samples from a normal distribution.

Figure 3.13 shows that population means can be corrected satisfactorily, if the underlying distribution is close to normal, by multiplying by factors of 1.15 to 1.3. This relies on many assumptions: sills being circular, the underlying distribution being close to normal and sills being randomly sampled within a basin. It is difficult to expand further on how appropriate this correction is without applying it to further seismic data where both 2D and 3D seismic exist in the same area. This will make a good target for future research.

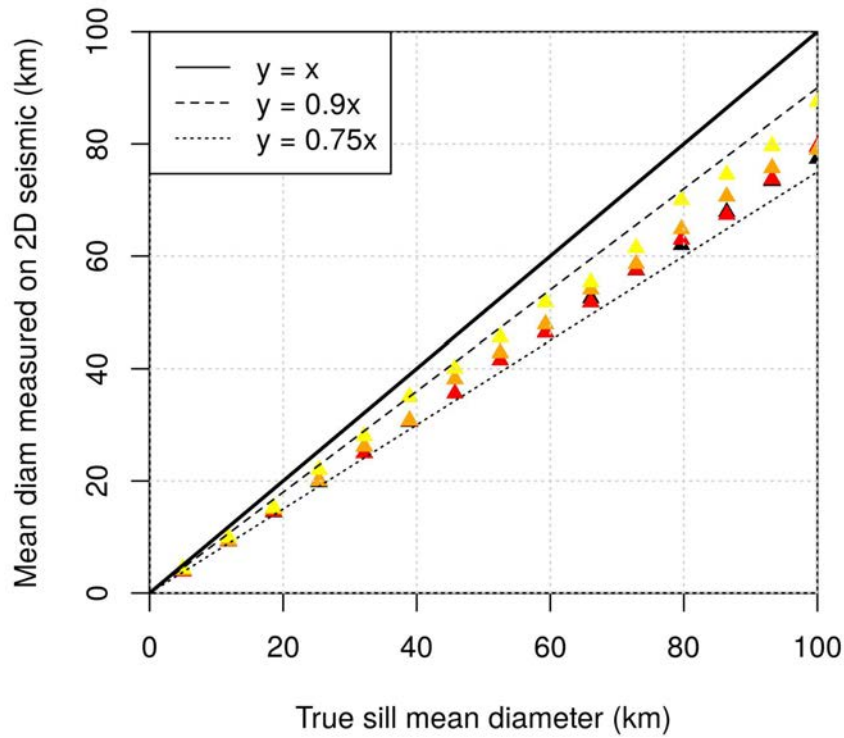


FIGURE 3.13: Monte Carlo modelling results for simulated random samples of circular sills of increasing mean diameter taken from a normal distribution.

3.3 Sill statistics

3.3.1 Sill shape

Gross sill morphology and shape may be important for understanding thermal effects on host sediments, but has not been studied in great detail by other authors. Sill shape is associated with sill volume, and therefore on conductive heating and thermal maturation of surrounding sediments. Sill shape may also be a factor in seal breach, because flat sills are significantly less likely to pierce a top seal compared to an inclined, transgressive or saucer shaped sill (e.g. [Cartwright et al., 2007](#)). Different shaped sills may also be more or less important for hydrocarbon migration - if sills do control hydrocarbon migration it is easy to see how differently orientated sheet intrusions could funnel fluids in different directions (e.g. [Rateau et al., 2013](#)).

Figure 3.14 shows the proportions of sill shapes within the basins studied. Saucer shaped sills are the most common across most data sets, although the Bight basin is dominated by flat sills, and Carnarvon is dominated by transgressive sills. The Karoo Basin is

known to contain huge numbers of saucer shaped sills; however, the Karoo dataset did not have records of sill shape ascribed to it. Carnarvon sills were intruded into fault blocks and may have been intruded syn-rift, which may explain the high proportion of transgressive sills. The observed difference in sill shape proportions may be due to the different mechanical properties of the host sediments (e.g. lithology and porosity) and stress states in the basins, leading to different sill types being formed. It may be suspected that this is the dominant factor controlling sill shapes rather than magma type, pressure or injection rate, as multiple basins in the NAIP clearly have different proportions of sill shapes, despite presumably having similar magma compositions and injection rates.

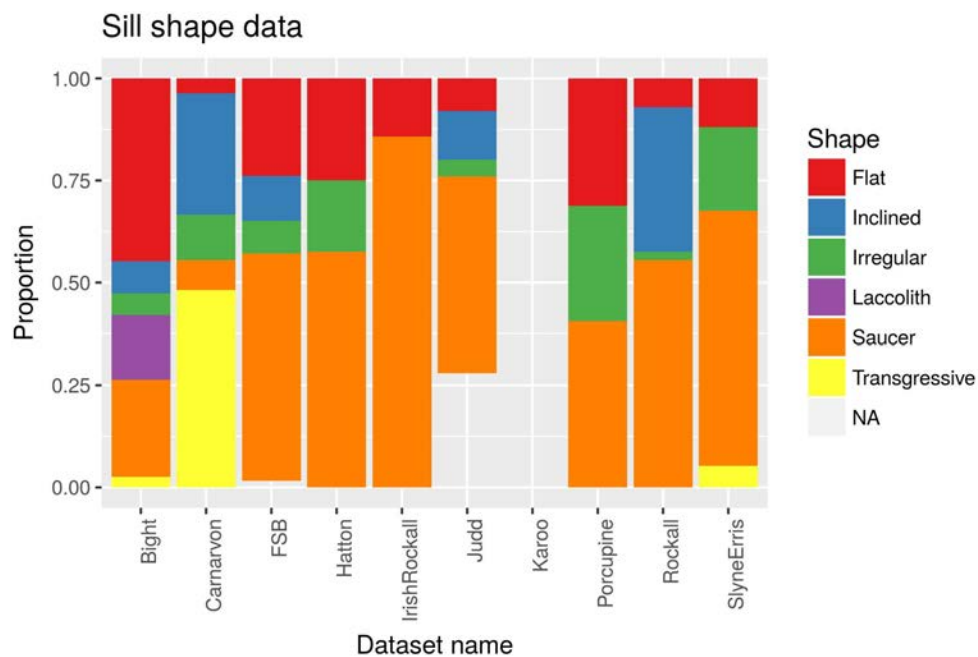


FIGURE 3.14: Stacked bar graph of proportions of sill shapes inside the study basins

Published datasets to compare this data to is sparse. [Jackson et al. \(2013\)](#) and [Reynolds et al. \(2017\)](#) both use the same seismic data from the Bight basin used in this thesis (i.e. the Bight Basin dataset described in chapter 2), and find the same essentially the same proportions of sill shapes. Similarly, data from [Fernandes \(2011\)](#) is used directly in the sills database (as described in 2, also see appendix A). [Planke et al. \(2005\)](#) studied the Vøring and Møre basins and found the majority of the sills they studied were equivalent to the saucer shaped and flat classification in this study, and thus this fits well with the majority of the basins studied, with the possible exception of Coverack. As mentioned earlier, Coverack was potentially intruded synrift or soon after rifting ceased ([McClay et al., 2013](#)), which would therefore likely have a very different stress state and could possibly lead to faults being intruded more easily, leading to more transgressive sills (*sensu lato* [Magee et al., 2013b, 2014b](#)). This is in contrast with the rest of the basins

in the NAIP. Magmatism in the NAIP was temporally coincident with rifting west of the Hatton bank, but was post-rifting for the sedimentary basins studied here (i.e. the FSB, Hatton basin, Rockall basin, Judd basin, Slyne-Erris basin and Porcupine basin).

3.3.2 Sill diameter

To study sill diameter trends, sills were first subset by basin (figure 3.15). Mean sill diameters range from 3175 m at the lowest basin mean (Hatton Basin) to 12,373 m for the greatest basin mean (Karoo Basin), representing 4 times as great a value. Similarly, the greatest and smallest median values are found to belong to the Karoo and Hatton basins, with values of 10,300 m and 2,515 m respectively.

Some basins appear to show a distribution close to normal (Bight, Coverack, Irish-Rockall, Judd, New Zealand, Rockall, Slyne-Erris). Other basins show a right-skewed distribution (Faeroe-Shetland, Karoo, Porcupine). Minimum values are not sensible to discuss here — as demonstrated in section 3.2.2 — because 2D seismic can intersect the edge of a sill and give anomalously small values. The question of the minimum sizes of a sill is still an interesting question that should be studied in the future, as the minimum size sills and minimum thickness sills may say interesting things about the minimum size batches of magma which can transgress the crust. Interquartile ranges vary widely between basins, from 1,629 m as the lowest IQR for the Irish Rockall basin, to 9,650 m for the highest IQR for the Karoo basin. Finally, the maximum values measured for any basin was in the Karoo at 61,000 m, while the minimum was in the Irish-Rockall basin at 7,034 m.

Figure 3.16 shows sill diameters split by sill shape (for definitions of sill shapes, see figure 3.4). It can be seen that sill diameters appear to be much more evenly spread between different sill shapes than they are for different basins. Maximum sill sizes range from 5,289 m for laccoliths to 46,427 m for saucer shaped sills, respectively. Median values range from 3,236 m at the lowest for laccoliths to 6,710 m at the greatest for transgressive sills. The majority of the interquartile ranges are very close together and generally overlap ranges. The greatest interquartile range is 5,917 m for transressive sills, and the least is 3294 m for laccoliths. However, note that this is not a fair comparison, as laccoliths have the smallest number of observations in them. Minimum values range from 631 m for saucer shaped sills to 1,775 m for transgressive sills.

From this basic statistical analysis, a natural follow-on question is whether these differing observations represent fundamentally different observations? Or whether these observations might be from the same population, but the variation in summary statistics is just due to random sampling? To put these questions another way, are the sills

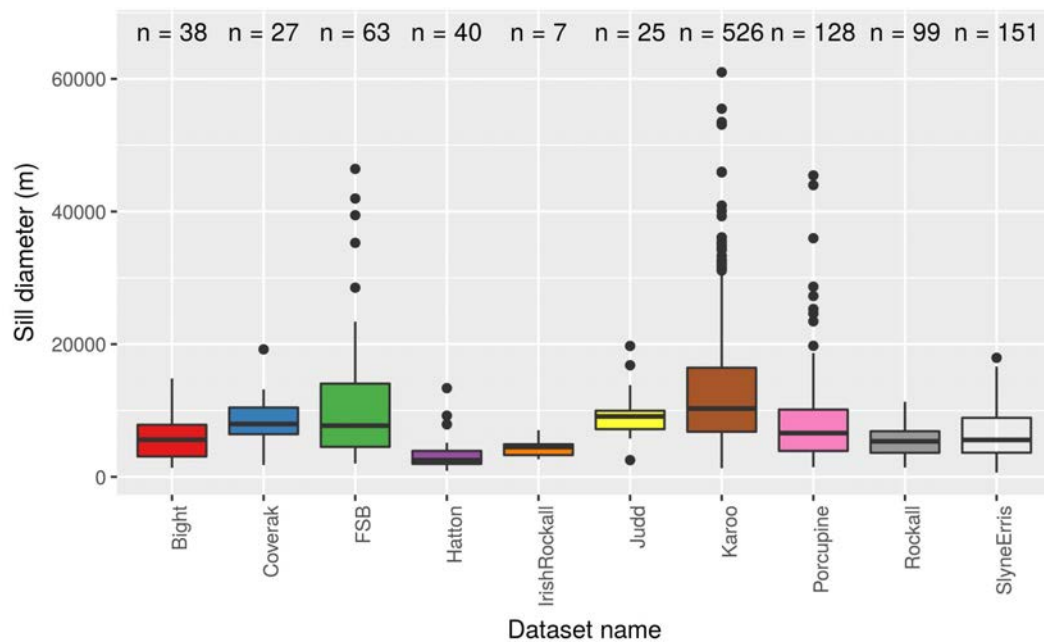


FIGURE 3.15: Sill diameter data, split by basin. For how to read box and whisker plots, see figure 3.9 caption.

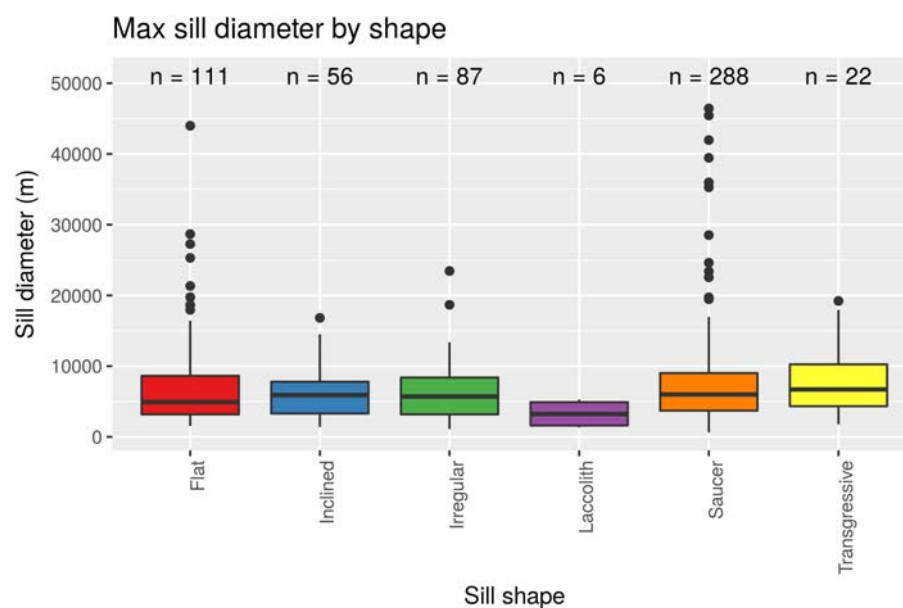


FIGURE 3.16: Sill diameter data, split by sill shape. For how to read box and whisker plots, see figure 3.9 caption.

in the Karoo basin truly bigger on average than those in the Faeroe-Shetland basin, or is the difference just due to the sampling methodology? If they are truly different, this has interesting implications for scaling up observations in one basin to province scale, such as was done in [Svensen et al. \(2004\)](#) for the North Atlantic Igneous Province. This type of question is the realm of inferential statistics. Much of inferential statistics was developed for medical statistics. To illustrate a hypothetical medical situation, imagine

two patient groups with diabetes. The first group is the control group and are given a placebo. The second group are given a new medicine. At the end of the trial, a very small increase in health is observed in the treatment group. What is the probability that this increase in health is due to the experimental medicine, rather than other factors (e.g. someone in the group giving up smoking, or another person in the group changing diet)? This is where inferential statistics are used to give a concrete answer to whether the observation is likely real, or just a sampling effect. Such inferential techniques can be used to help ascertain if the observed differences in sill diameters are likely real, or due to natural random variability.

Because there are multiple independent groups (in our case, multiple sedimentary basins) an analysis of variance (ANOVA) test is appropriate. The results of the ANOVA test give information on whether any of the measurements (i.e. sill diameters) in the groups (i.e. sedimentary basins) are different, but the ANOVA cannot give further information on *which* groups are different (for example, ANOVA might indicate that some groups are different from the others, but it cannot specify whether it is the Rockall vs. FSB data that are significantly different, or Rockall vs. Porcupine, etc.). Some of the data, as noted earlier, have a right skew and this invalidates the assumption of normality of ANOVA. The data were therefore log transformed, which then satisfied the test assumptions. ANOVA results indicate that some groups are highly likely to be different than others. However, to understand specifically *which* groups are different, a post-hoc ANOVA test was required. The Tukey Honestly Significant Difference test (TukeyHSD) was used, which gives information on which of the groups are different in a statistically significant sense, while controlling error propagation over the multiple comparisons. Figure 3.17 shows the results of performing the TukeyHSD test. The most interesting result to come out of this analysis is that Rockall and Porcupine, Rockall and Judd, Hatton and Faeroe-Shetland, Rockall and Faeroe-Shetland, and Slyne-Erris and Faeroe-Shetland basins are all statistically significantly different in terms of their sill diameter populations. This has important implications for up-scaling of seismic measurements and estimates for one basin to the province scale, such as done by [Svensen et al. \(2004\)](#) and [Reynolds et al. \(2017\)](#). The variation and spread of the data also highlights the need for separate studies and parameterization on a per-basin basis should this data be needed for modelling in, for example, Monte Carlo simulations to estimate the number of sills in a basin.

Recently, [Passarelli et al. \(2014\)](#) suggested that intrusions may be self similar (i.e. fractal [Turcotte, 1991](#)) in some dimensions. This idea can be tested by plotting the length against the number of samples greater than that length. If the resulting plot has a clear linear relationship over part of the range it is ascribed a fractal, or power law, relationship. This can also be done with maximum likelihood estimation, but using a graph can give a more visual picture of the data. There is no requirement in assigning a

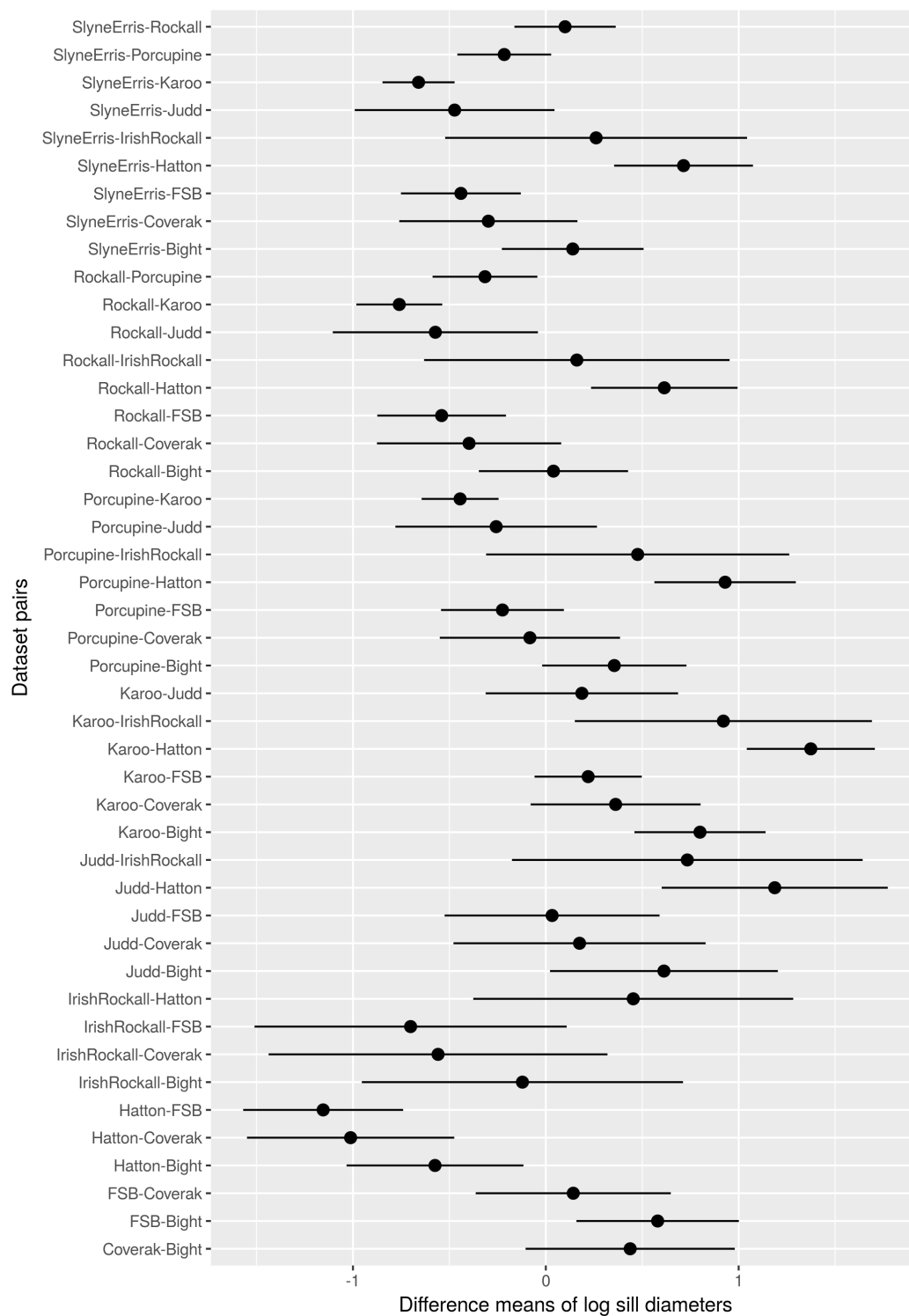


FIGURE 3.17: Results of the Tukey HSD multiple comparisons test. This shows the differences in means of the log of sill diameter between different pairs of datasets. For each pair of datasets compared, an estimate of the difference between the means of the populations is shown as a point, with error bars showing the 95% confidence intervals for these estimates. If the error bars overlap 0, then there is evidence that there could be no difference between means of the datasets, and hence there is no statistical evidence that the means of the log sill diameters from those datasets are different.

power law relationship for the data to be linear over its entire range. It is assumed that, at the extremes of the data, deviations from a linear trend correspond to difficulties detecting smaller intrusions, and similarly at the upper end that there are so few huge intrusions that they will not be sampled properly either, causing a deviation from a linear trend. There is an extensive literature on this subject in the earthquake magnitude literature (e.g. [Pickering et al., 1995](#), and references therein). Figure 3.18 shows the results of plotting the data in this way. No clear evidence is seen for a linear relationship at any point along the graph, which therefore does not support this idea. Analysis of which distribution do fit the data better is given in section 3.4.

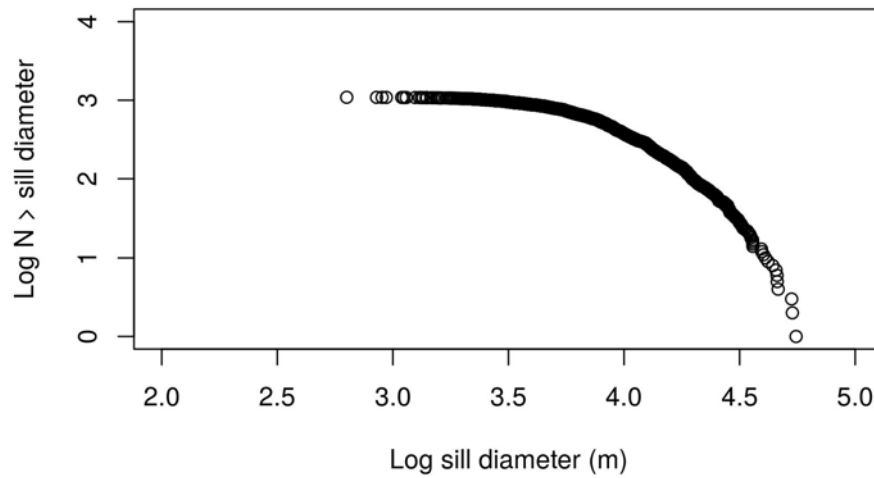


FIGURE 3.18: Fractal plot for sill diameter data. A linear section on the data would imply a fractal relationship. The data appears to curve smoothly, arguing against a fractal relationship.

3.3.3 Sill thickness

For studying sill thicknesses with statistical methods, seismic data is often not appropriate. This is because seismic data only images sills which are thick enough to have individual reflections of the top and base of the sill without causing seismic tuning effects (e.g. [Smallwood and Maresh, 2002](#); [Thomson, 2005b](#)). This means that any measurements taken from seismic data are strongly biased against thin sills. Therefore, sill thicknesses were measured in borehole and well data, as well as extracted from published studies. Well data is not without problems however: wells might be expected to be planned to not intersect thick sills due to potential drilling hazards (e.g. low rate of penetration, or loss of circulation through columnar joint networks) and therefore will

not be representative of thicker sills. However, it can be considered a sensible random sample of sill thicknesses for thin and medium thickness sills.

Data for studying sill thicknesses was first extracted from seismic data where top and base of the sill could be imaged. This only constituted 44 intrusions, mostly found in the Bight and Irish-Rockall basins. Depth conversion was done based on values in [Smallwood and Maresh \(2002\)](#) (see section 3.2). Figure 3.19 shows the sill thickness data. As can be seen, data follow a slightly right skewed distribution. Mean values for the minimum depth converted estimates are 179.5 m, and 291.7 m for the maximum. The smallest sill thicknesses are 47.4 m and 77.0 m, respectively. Maximum sill thicknesses range from 500.0m to 812.5 m. This emphasises the errors that choice of depth conversion velocity and introduce into analysis for sill thickness measured from seismic.

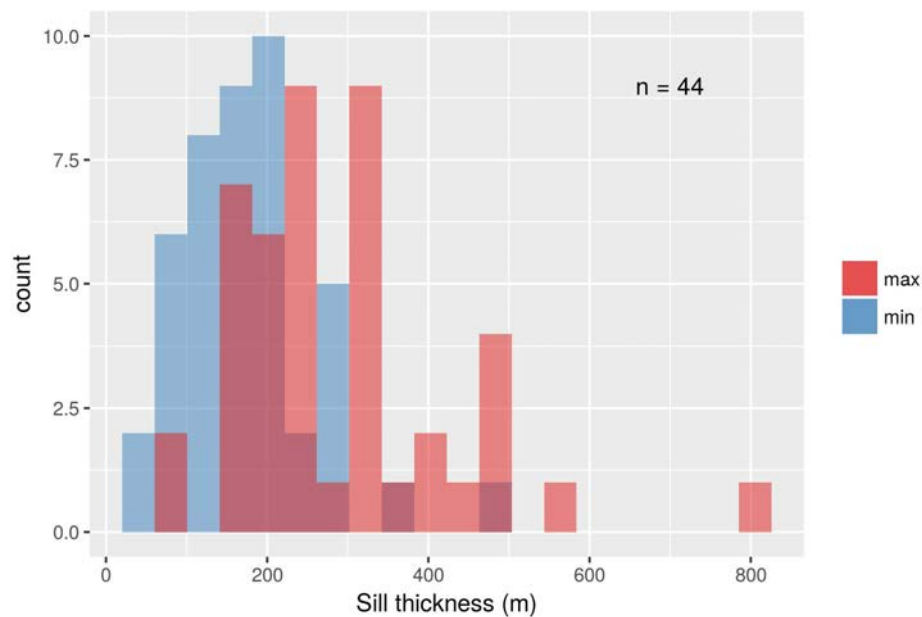


FIGURE 3.19: Histogram of sill thickness measured from seismic data, depth converted with values of 4500 m s^{-1} (min) and 6000 m s^{-1} (max) (after [Smallwood and Maresh, 2002](#)).

Following this, a larger volume of sill thickness data was extracted from field and well data from the literature (see appendix B for sources). Figure 3.20 shows the distributions of all the sill thickness data. The mean sill thickness is 19.25 m, median is 10 m, and the interquartile range is 15 m. The distribution has a skewness of 2.43 and kurtosis of 9.08. Skewness is 0 for a symmetrical distribution, and this therefore indicates a strong right skew to the distribution. Kurtosis measures the heaviness of the tails of the distribution, where a kurtosis of 3 indicates a standard normal distribution, and the value of 9.08 therefore shows the distribution to have a very heavy tail.

The measurements can be split by basin, but only for the largest datasets. Therefore, data from the Buchan Rift, Karoo Basin, Raton Basin, Greenland margin, Voring Basin,

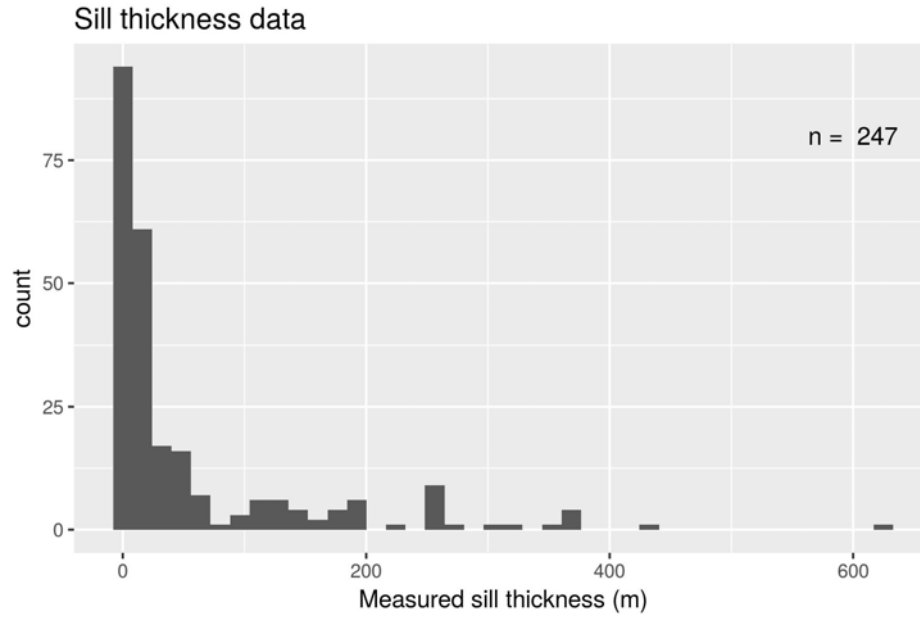


FIGURE 3.20: Histogram of sill thicknesses from well and field data

Ferrar province, Colorado Basin, Gunnedah Basin, Cape Verde Rise, Paran Basin, Rundle Basin, Eastern Atlantic margin, Jiyang Basin and Newfoundland margin are not plotted here, due to each only containing a few observations. The data remaining is from the Faeroe-Shetland Basin (FSB), Midland Valley and Rockall basin (Figure 3.21). All three of the Rockall Basin, FSB and Midland Valley have similar distributions and summary statistics. ANOVA tests on the three datasets shown in figure 3.21 returns a p-value of 0.549, which is well above the standard statistical cutoff of 0.05 (which represents a 95% confidence level). This indicates there is no evidence that the sill thicknesses in these three datasets are significantly different.

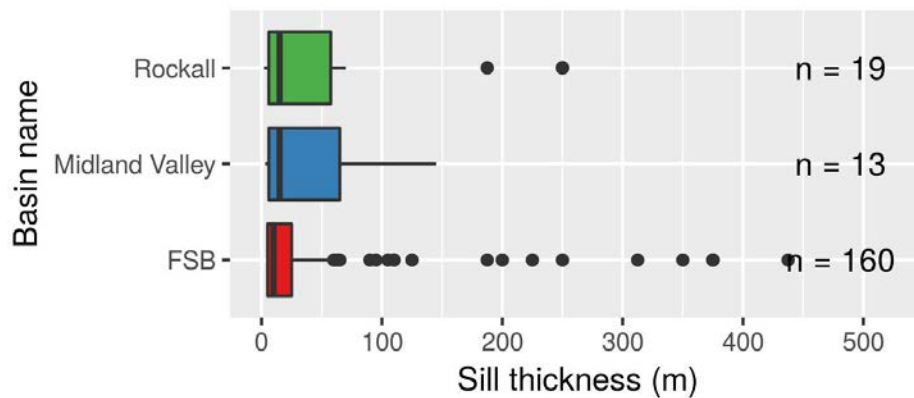


FIGURE 3.21: Box and whisker plot of sill thicknesses split by basin, for basins with more than 10 datapoints. For how to read box and whisker plots, see figure 3.9 caption.

As sill thickness is so difficult to measure on seismic data, a useful relationship would be to predict sill thickness (which is normally below vertical seismic resolution) from sill

length, which can be reliably measured on seismic (see section 3.2.1). Figure 3.22 shows the results of this. The left panel of figure 3.22 shows a linear regression to predict sill thickness from sill diameter. The R^2 value is around 0.31, meaning that around 30% of the variability of the data is explained by the model. Bearing in mind how easy it is to measure the diameter of a sill, this is a powerful model for its simplicity. Also note, while this coefficient of determination may seem to be low, the model still has value as long as it is used with an understanding of the variability in the data. The right hand panel of figure 3.22 shows the same data, but with the regression line forced through the origin. This results in a slightly worse fitting model to the data. However, it may be more robust in its geological interpretation — a sill with no length will naturally have no width, so forcing through the origin makes sense. This will likely make it generalise to smaller sills better. Conversely, many sills grow from dykes — which do have a finite thickness — and thus it could be argued forcing the regression model through the origin is not necessary. This set of relationships may also only be applicable to mafic sills, which make up the vast majority of this dataset. It is likely that different length – thickness relationships exist for felsic and ultramafic sills, however little data exists to test such relationships.

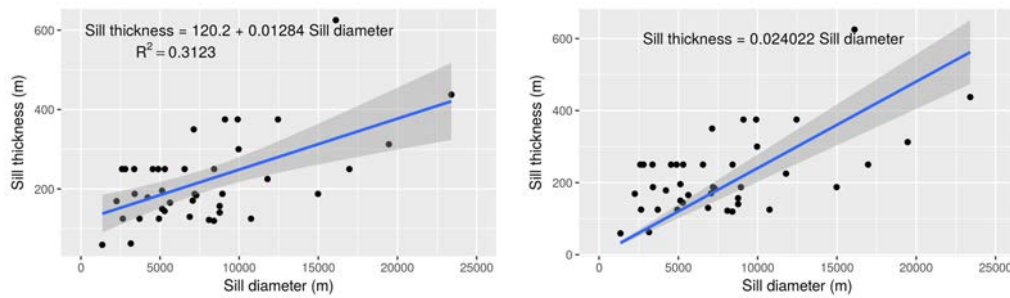


FIGURE 3.22: Left: Sill diameter vs sill thickness scatter plot and regression line. Right: Sill diameter vs sill thickness scatter plot, with regression line forced through the origin. Note no R^2 value for the right hand panel, as the intercept is used in the equation for calculating R^2 , so comparison of R^2 values is not valid.

As with section 3.3.2, it is also worth investigating whether sill thicknesses appear to be power law / fractal, to test the relationships shown by Krumbholz et al. (2014) and Passarelli et al. (2014). Figure 3.23 shows the results of this. Similar to section 3.3.2, there is no evidence of a fractal relationship, with the graph having no clear linear relationship at any point.

The relationships found in figure 3.22 can be used to model the thickness of all the sills where diameter information is known, to find an estimate of sill volume; although it is noted that there is additional scatter in the data in figure 3.22 which the model does not take account of. Figure 3.24 shows the results of this. Again, no clear evidence of a power law relationship is seen in the plot. This is directly at odds with Passarelli et al.

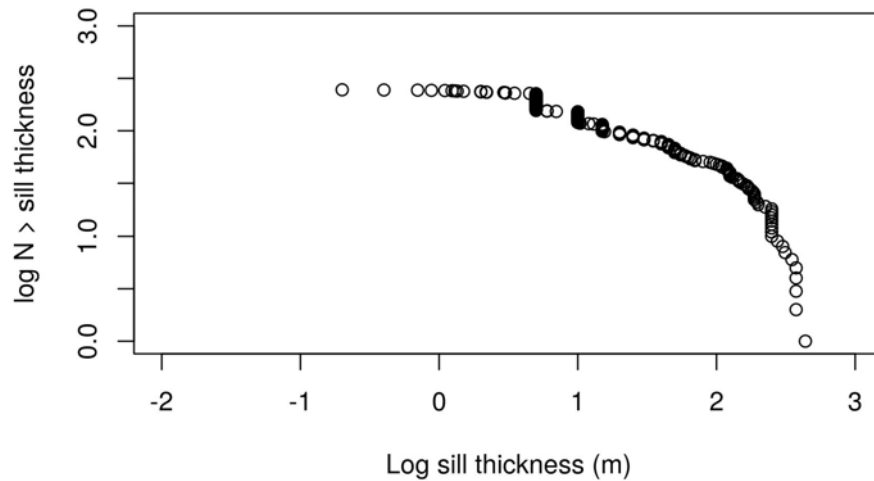


FIGURE 3.23: Fractal plot for sill thickness. A linear section on the data would imply a fractal relationship. The data appears to curve smoothly, arguing against a fractal relationship.

(2014), who find such a relationship in dykes. However, their datasets are small (34 observations, versus the 247 in this study) which should make the results presented here more reliable. However, errors in volume estimate for both the methods used in this study and the geodetic inversion schemes used in the publications cited by [Passarelli et al. \(2014\)](#) are difficult to estimate without further work. Quantification of the errors in volume estimation for this study and for the studies in [Passarelli et al. \(2014\)](#) would be worthy of future investigation to shed light on whether intrusions volumes truly display power law behaviour or not. Finally, it is noted that [Passarelli et al. \(2014\)](#) considers dykes rather than sills; many intrusion models consider sill intrusion mechanisms to be essentially the same as dykes (e.g. [Lister, 1990](#); [Lister and Kerr, 1991](#)) and if this is true the lack of evidence for fractal behaviour is very interesting. The other possible conclusion is that this shows evidence for sills intruding via different mechanisms when compared to dykes. This will be explored further throughout this chapter.

3.3.4 Sill transgressive height

Transgressive height is defined as the distance from the lowest point of the top surface of a sill to the highest point of the top surface of a sill. To calculate transgressive height seismic data must be depth converted, as all seismic data were delivered in time (see section 3.2 for depth conversion method). Figure 3.25 shows the transgressive height data, split by basin. As can be seen, the data IQRs range widely, with minimums found

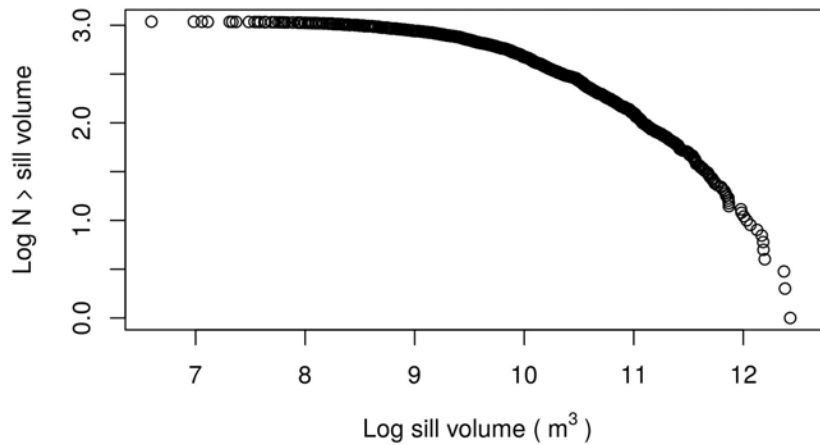


FIGURE 3.24: Fractal plot for sill volume. A linear section on the data would imply a fractal relationship. The data appears to curve smoothly, arguing against a fractal relationship.

in the Bight and Irish-Rockall datasets, and the maximum found in the Norway dataset. The Norway dataset — which was taken from the literature (from [Hansen \(2004\)](#) and [Polteau et al. \(2008\)](#)) — shows significantly greater values in general. This possibly indicates a very different basin or magmatic intrusion event, a different interpretation of the shape definitions, or errors in depth conversion in the original studies or this study. Datasets in this study used all available well data resulting in three different depth conversion functions. Despite the different methods, measured transgressive height ranges in this study are similar between the three different depth conversion methodologies, suggesting it is the methods of [Polteau et al. \(2008\)](#) and [Hansen \(2004\)](#) that are causing the discrepancy.

The minimum transgressive height recorded in most basins was zero. However, zeros were not always recorded in the literature, making comparison between minimum transgressive height data presented here and published studies difficult. Mean values range from 100 m (Porcupine) to 990 m (Norway). Median values range from 150 m (Irish Rockall) to 981 m (Norway). One way to interpret transgressive height in a physical context is the excess magma pressure after magma has started propagation in a direction other than vertical (assuming a dyke feeder). In this case, the transgressive height records the overpressure between the propagating dyke and the feeder magma chamber before pressure is balanced. Thus, the range of transgressive heights records the range of overpressures within which dykes change into sills.

Figure 3.26 shows the sill transgressive height data, split by sill shape. The IQR of

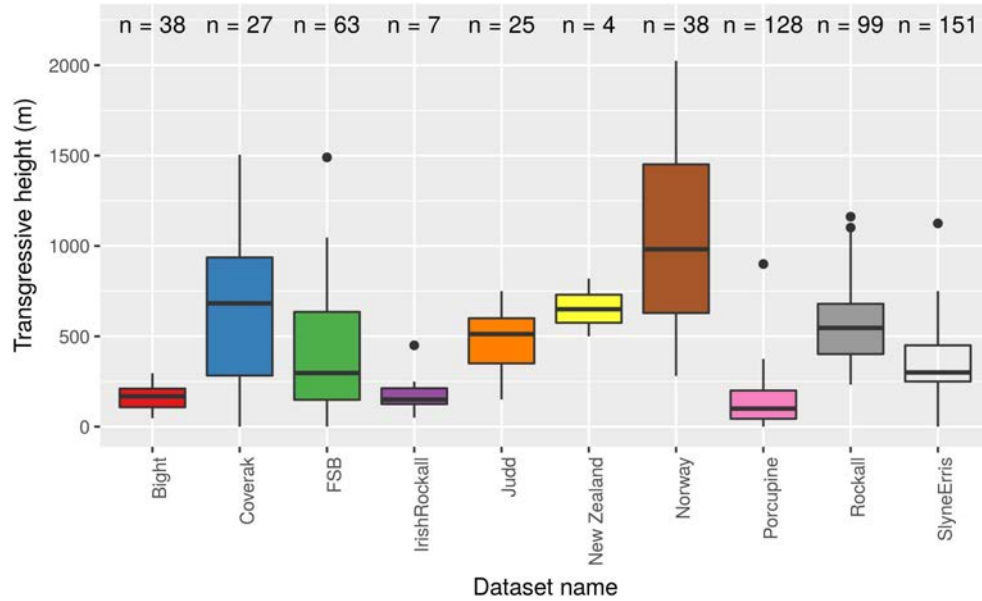


FIGURE 3.25: Box and whisker plot of transgressive height measurements, split by basin. For how to read box and whisker plots, see figure 3.9 caption.

inclined, transgressive and saucer shaped sills can be seen to convincingly overlap, while irregular overlaps strongly with saucer shaped sills. Flat sills occupy lower values in general. Flat sills have the lowest median value of 97 m, while inclined and trasgressive sills have similar medians at 487 m and 553 m, respectively. Flat sills have the lowest maximum transgressive height at 297 m, while the greatest trasgressive height was for a trasgressive sill at 1505 m. In general, the trasgressive height data split by shape show what would be expected. Flat sills show little to no transgressive height (the transgressive height shown in the data for flat sills is expected as few sills are expected to have a zero degree dip, and hence the boundary between a flat and an inclined sills will be open to interpretation). The greatest trasgressive heights are observed for inclined, trasgressive or saucer shaped sills. Irregular sills occupy a middle ground between flat sills and transgressive/inclined/saucer shaped sills. This is expected, and likely reflects that some irregular sills are mis-classified due to the intersection of 2D lines through the edge of sills.

3.3.5 Sill emplacement depth

Emplacement depth is the depth below the contemporaneous seafloor that a sill was emplaced. Sill emplacement depth is interesting to study because the average depth of emplacement of sills and variance around the average may hold information about the magma overpressure (Pollard, 1973; Smallwood and Maresh, 2002) or about the preferred

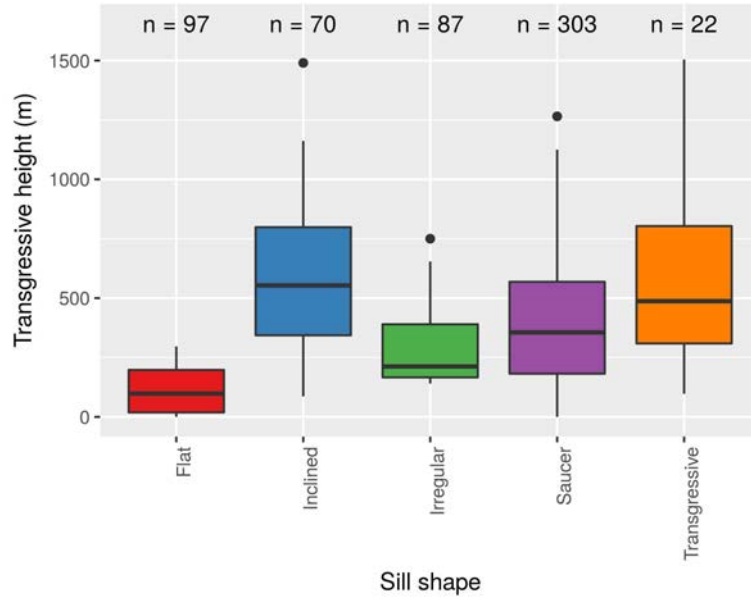


FIGURE 3.26: Box and whisker plot of transgressive height, split by sill shape. For how to read box and whisker plots, see figure 3.9 caption.

lithologies sills intrude (Schofield et al., 2012). If the dominant control on sill emplacement is the host rock lithology, then emplacement depth will allow us to estimate the porosity at time of intrusion, which is implied to be the dominant control in some models (e.g. Schofield et al., 2010). In addition to information about the magmatic plumbing system that sill emplacement depth likely holds, emplacement depth has implications for petroleum source rock maturation. Sills can play a major part in the maturation of source rock sequences. Source rocks are not deposited evenly or randomly with depth; they are deposited in specific beds at specific depths. Comparison between source rock depth histograms and sill emplacement depths therefore can indicate whether sills may have matured organic rich rocks or not. Calculations of maturation due to sills needs to be done with emplacement depth rather than present day depth, as for maturation calculations the background temperature of the hostrock needs to be taken into account, which will be different today due to continued basinal subsidence. Knowing emplacement depth can also be important for other investigations, such as for parameters for modelling sills during intrusion, e.g. the overburden thickness from Johnson and Pollard (1973), or for investigating the true geometry of sills using backstripping (e.g. Smallwood, 2009).

To find emplacement depth, two steps are required: depth conversion and decompaction. Depth conversion is handled by the simple method of using an average velocity and assuming a straight seismic ray path. Neither of these assumptions are accurate; however, given that no velocity data is available for a number of basins, this method is preferred for it's ease of understanding. See section 3.2 for details on depth conversion.

Following depth conversion, sediments are decompacted from the palaeoseafloor to the top of the sill. After burial, sediments lose volume by destruction of porosity due to the increasing weight of the overburden during burial. This is described by [Sclater and Christie \(1980\)](#) and [Allen and Allen \(2013\)](#), and applied to sills by [Smallwood \(2009\)](#). In brief, the exponential porosity-depth trend is commonly expressed as

$$\phi = \phi_0 e^{\frac{-z}{\lambda}} \quad (3.6)$$

where ϕ is the porosity, ϕ_0 is the initial porosity, z is the depth, and λ is the compaction length scale (typically around 2 km, e.g. [Sclater and Christie, 1980](#)). If the proportion of the rock matrix m is written as the complement of porosity, then:

$$m = 1 - \phi \quad (3.7)$$

Finally, in the absence of erosion conservation of mass throughout the compaction process can be assumed, such that

$$\int_{z_1}^{z_2} m \, dz = \int_{z_3}^{z_4} m \, dz \quad (3.8)$$

where z_1 is the present day top sill depth, z_2 is the present day palaeoseafloor depth, z_3 is the original depth of emplacement of the sill, and z_4 is the original palaeoseafloor depth (set to 0). Substitution of equations 3.6 and 3.7 into 3.8 and integration gives

$$z_1 - z_2 = (z_3 - z_4) + \frac{\phi_0}{\lambda} (e^{\frac{z_4}{\lambda}} - e^{\frac{z_3}{\lambda}} + e^{\frac{z_1}{\lambda}} - e^{\frac{z_2}{\lambda}}) \quad (3.9)$$

λ is assumed to be 1.96 (corresponding to shale) after [Sclater and Christie \(1980\)](#), based on the observation of most NAIP sills intruding Cretaceous sections, dominated by shale. Figure 3.27 shows the results of this, for emplacement depths both with and without the decompaction procedure applied, while table 3.1 shows the differences in summary statistics. The entire distribution is moved to the right by decompaction. Mean and median values for both are around 0.9 km to 1.2 km, while the maximum intruded depth goes from close to 3.5 km to close to 4 km.

Once emplacement depth has been calculated, it can be used to investigate models involving sill venting. For example, the emplacement depth disputes [Jamtveit et al.'s \(2004\)](#) model to explain occurrences of hydrothermal vents with depth in basins. [Jamtveit et al. \(2004\)](#) state that at depths deeper than 1.1 km venting is not expected, as the

TABLE 3.1: Differences in sample statistics when using decompaction routines on sill emplacement depth data. Measurements are in km.

	Min	LQ	Median	Mean	UQ	Max
Compacted	0.0047	0.4423	0.9000	0.9491	1.3000	3.3000
Decompacted	0.0329	0.6194	1.2200	1.2790	1.7210	3.9230

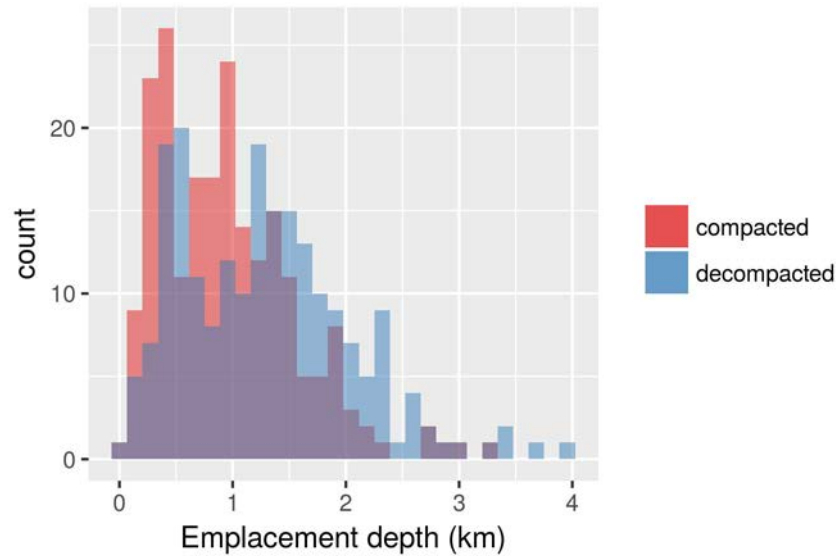


FIGURE 3.27: Semi transparent histograms showing the comparison between data presented here before and after decompaction for sills in the sills database. Note purple corresponds to overlapping semitransparent red and blue bars.

lithostatic pressure exceeds the critical pressure. 85 sills with overlying vents were found in the datasets studied in this thesis. Data were collected on these hydrothermal vents. Figure 3.28 shows data for sill emplacement depth where a hydrothermal vent was associated with it as red bars, against the model of [Jamtveit et al. \(2004\)](#). The data clearly dispute the model, with occurrences of sills with vents well below 1.1 km palaeo-emplacement depth. Alternatively, this discrepancy between model and data possibly reflects that fluids are not steam but rather supercritical pore fluids, which may necessitate a different model. Whichever the case, this data does not support the model of [Jamtveit et al. \(2004\)](#).

3.3.6 Implications of sill statistics

3.3.6.1 Sill shape

The discovery in this chapter that the variation of sill shapes is not constant between different basins indicates that there may be a basinal control. Candidate mechanisms for such a mechanism could be differing magma pressures, host rock mechanical behaviours

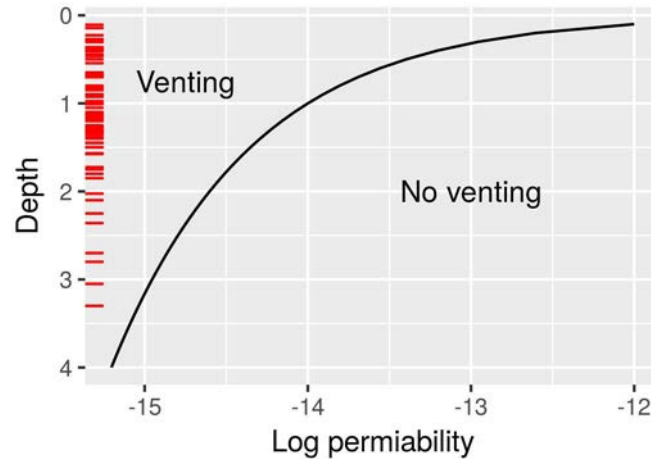


FIGURE 3.28: Model of [Jamtveit et al. \(2004\)](#) for hydrothermal venting associated with sill intrusions. Red bars on the depth axes represent the intrusion depth of a sill where an associated hydrothermal vent has been interpreted on seismic.

and ambient pressures. Other authors have noticed similar patterns, albeit with less sill shape data than presented here. [Svensen et al. \(2006\)](#) claims there is evidence that more deeply emplaced sills in the Karoo Basin are larger and flatter, which would indicate a mechanical or pressure control on the sill shape. This was not investigated in this thesis, but could be investigated by binning sill shape statistical data into backstripped emplacement depths and looking for trends. Variation in sill shapes may be important to study in the future due to the effectiveness of different sheet geometries to transport magma through the crust. Different patterns of ground deformation are also caused by different intrusion geometries (e.g. [Kavanagh et al., 2015, 2017, 2018](#))

3.3.6.2 Sill diameters implications

First, summary statistics for each measurement were examined, and split either by basin or by sill shape (section 3.3). All basins have different proportions of sill shapes - i.e. each basin was found to be unique. Sills in different basins were found to have technically different diameter sills. This implies the basin is a fundamental differentiator on sill dimensions and this, by extension, implies factors such as magma supply rate and mechanical parameters are the important controlling factors for sill emplacement and the final dimensions of the sill. This has not been reported in the literature before. How similar or different sill populations are across basins and regions is an open research question. Furthermore, as well as sill populations being different in different basins, the work in this thesis shows that sill populations are different even between basins experiencing the same large scale magmatic event; the emplacement of the proto-Iceland plume. This helps to remove the magma type and generation rate as factors controlling

sills shapes, as they are likely to be either the same or similar across the province. This leaves lithology and stress states within basins as the most likely controlling factors for sill shapes, possibly in addition to a component of randomness.

3.3.6.3 Transgressive height implications

Transgressive height showed strong overlap in ranges for most sill shapes. Predictably, the inclined and transgressive shaped sills transgressed the greatest amount of stratigraphy. Within the datasets, the Carnarvon Basin stood out as an outlier. The Carnarvon Basin is the only basin thought to have synrift intrusions and has the second greatest observed transgression heights of any basin. It also had the greatest proportion of fault usage of any basin studied (figure 3.29), suggesting that if faults are active and in a favourable orientation to the regional stress field to slip (e.g. Zoback, 2010), and in a favourable intersection direction (e.g. Magee et al., 2013b), that they may be easier to intrude. This has implications for magma transport in regions such as the east African rift, where both active extension and magma generation are occurring. An interesting study was done by Cartwright and Hansen (2006), who showed magma transport through the crust for over 12 km, and one sill of which transgressed ~ 6 km of strata alone. The greatest vertical distance transgressed by a single sill in this study was around 2 km, possibly indicating that we may have interpreted multiple sills where other authors have interpreted one. Alternatively, this may be the result of the amount of 2D seismic data analysed in this study not showing the full extents of some of the larger sills. Finally, it could simply be that the Vøring basin studied by Cartwright and Hansen (2006) has a very different population of sills in it than those studied in this thesis, with much larger transgressive height sills being present. This is entirely possible, and is in line with other findings of this study showing basins to each be unique in terms of the sills they contain. This could be a valid target for future research; how magma moves from deep within the crust to shallow levels is still largely unknown, and finding places to push the limits of imaging of the deeper parts of the shallow magma plumbing system could shed light on processes so far unobserved.

3.3.6.4 Sill thickness implications

Section 3.3.3 discussed how sill thickness is difficult to study using seismic data, due to vertical seismic resolution issues. A separate database was made by supplementing sill thickness measurements on seismic data with measurements from well data and published studies. What can be inferred from this combined seismic and well measurement dataset should be treated with care. Petroleum exploration wells are normally targeted

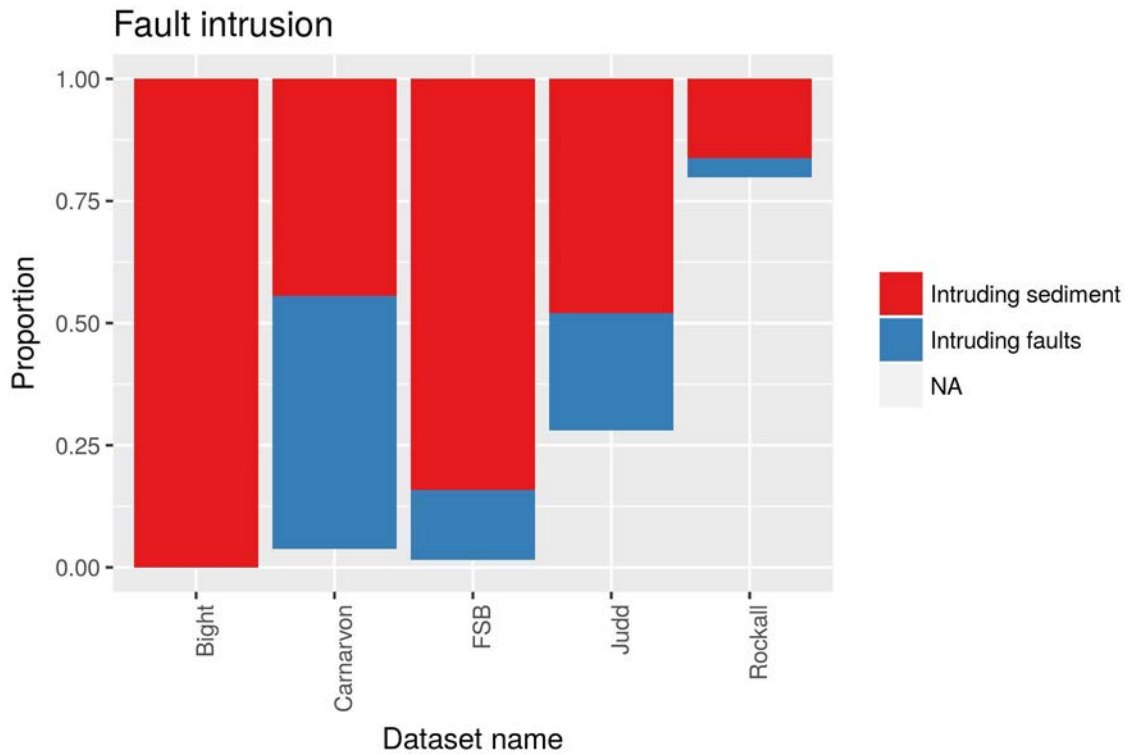


FIGURE 3.29: Stacked proportional bar graph for sills intruding faults versus sills intruding sediments, in a selection of basins. The highest proportion of fault intrusion is in the Coverack dataset, which images sills likely to have been intruded synrift.

specifically where there are fewer and thinner sills. On the other hand, seismic data preferentially images the thickest sills. Therefore neither of these two datasets are random; they are each biased. These datasets therefore cannot be used with standard inferential statistical methodologies. However, this dataset is the largest in the literature, and is likely the best that can be collected without access to significant further amounts of commercial data (which would still be biased in the same ways as the sample analysed in this thesis, but). The dataset studied in this thesis indicates that, while sill thicknesses in different basins do vary, they do not vary by much. Thickness ranges also overlap considerably. The data indicate very few thick sills (> 250 m) exist in any basin. Anecdotally, fieldwork from the Isle of Skye in Scotland indicates that there are few sills thinner than around a metre. This observation may fit with the physics of such systems (e.g. [Lister, 1990](#); [Lister and Kerr, 1991](#)). Magma is a viscous fluid and therefore does not flow easily into narrow cracks; work must be done to overcome viscous forces ([Lister, 1990](#)). The narrower the crack, the greater the force needed to drive magma into it (see section 3.5, and especially equation 3.12). However, if the force is greater, more energy is available to widen the intrusion. Hence the observation of few very thin sills (or indeed sills only being thin at their tips) makes sense considering magma as a viscous fluid. Equally, once a crack is longer than a few meters, the energy to propagate the crack is very low, hence the crack is more likely to increase its length without increasing its

width significantly (Zoback, 2010). This explains the overlap observed in sill thicknesses in different basins, and also the lack of many very thick sills.

Additionally, there is no clear evidence of a fractal or power law relationship in the sill thickness data, which is very important for future studies on sill intrusion and parameterization of magma intruding the shallow crust. This is at odds with Passarelli et al. (2014), who found scaling relationships in the volume of dykes in Ethiopia and Iceland. However, their sample size was extremely small (< 20) while ours is significantly larger (1150 observations for sill diameters, 44 seismic observations for sill thickness, 247 well bore observations for sill widths).

3.3.6.5 Sill emplacement depth implications

Sill emplacement depth is important both at the basin and global scale. At the basin scale, sill emplacement depth controls the sill's proximity to petroleum system components such as reservoirs and source rocks. The depth below the palaeoseafloor also controls the expression of any forced fold formed by sill intrusion, although different basins have different strengths of host rocks, and therefore the function defining forced fold behaviour will be different across different basins. At the global scale, if sills mature enough greenhouse gas to be vented to the atmosphere then they can cause global climate change (Svensen et al., 2004). Sill emplacement depth is a measure of the depth range sills are intruded into, and if this coincides with the depth range of organic rich source rocks, then greenhouse gas can be produced.

3.4 The missing sills test

A common problem with studying basins containing igneous intrusions is that they are often “frontier” basins - i.e. basins without good seismic data coverage. This often means the basin is covered with limited 2D seismic data, rather than 3D seismic data with superior spatial resolution. The lack of spatial resolution between 2D seismic lines is a particular problem for mapping the number of sills in a basin. Understanding the number of sills, spatial extent of sills, and volume of magmatic products in a basin can have a number of benefits. First, when intruding sedimentary sequences, sills bake host rocks and cause thermal metamorphism. This can cause thermal maturation of organic rich sequences, which may lead to maturation of hydrocarbons (e.g. Aarnes et al., 2010; Raymond and Murchison, 1991; Svensen et al., 2004). It is therefore important to know how many sills are present in a basin for regional maturation modelling. Secondly, sills and other igneous intrusions may affect the flow of groundwater and hydrocarbons in

the subsurface, hence knowing where high densities of intrusions are shows where such fluid flow systems may behave differently to normal. Sills can also form forced folds, which are potential hydrocarbon traps (Hansen and Cartwright, 2006a). Thus maps of sill extent feed into play fairway mapping for trap distribution and migration pathways. Aside from such industrial applications, understanding the number of sills in a basin has received very little mention in the literature to date, and thus how the number of sills in a basin vary with potential magma generation mechanisms is unknown. Thirdly, as explained in Chapter 1 and in the introduction to this chapter, a number of global mass extinctions have been linked to thermogenic methane generation around sills, and estimation of gas generation volumes and budgets is highly dependent on the number of sills in a basin, as well as their shapes and volumes. This section introduces the concept of a “missing sills test”. The missing sills test is applied to 2D datasets to understand how magmatism varies in different basins within a large igneous province.

Fernandes (2011) was the first to use a Monte Carlo approach to estimate the number of sills unobserved within the footprint of a 2D seismic grid. Fernandes (2011) found that the number of sills observed corresponded to around 100 times less than number in the basin. Generalisation of this to other data sets requires further work, however. In this study, a number of improvements are made on the original work of Fernandes (2011). First, clearly the number of sills intersected verses the number of sills in the area studied will depend on the seismic line density and layout, thus every survey should be modelled separately. Secondly, sills were generated within a rectangular geographic area in the work of Fernandes (2011), but this is unlikely to answer the sort of questions that would be asked in industry or in palaeoclimate studies, which is more likely to be how many sills are present *within the survey area*. For this reason the Monte Carlo model was implemented to only generate sills within 20 km of at least one seismic line, effectively forming a polygon around the survey, and also not generating sills within any large gaps inside the 2D seismic survey (such as found in the OGA seismic survey). Lastly, Fernandes (2011) generated randomly distributed sills with diameters taken from a uniform distribution. Such a distribution was not observed in measurements of sills in this study. Instead, sill statistics are used to parameterize the best theoretical distribution from which to draw random sill diameters. The methodology for doing this is outlined below.

3.4.1 Parameterizing the missing sills test

There are a large number of theoretical probability distributions. A probability distribution (PD) is a mathematical function which describes the probability of a certain

outcome from an experiment. The aim of the missing sills test is to model sill diameters, so a continuous PD is used. There are at least seventy continuous PDs, so methods have been used to ascertain the most appropriate PD for a given data set. One method involves plotting the square of the skewness of the sample against the kurtosis of the sample, giving a Cullen and Frey graph (Cullen et al., 1999), which compares samples to distributions in the kurtosis — skewness² space. This serves as a good estimator for which PD may be a good representative of the sample. Figure 3.30 shows a Cullen and Frey graph for the sills measured on 3D surveys in the Rockall Trough. Bootstrapping (repeated sampling from the sample with replacement) is carried out to give an estimate of the sampling distributions — skewness and kurtosis can have quite wide sampling distributions, especially for small samples. In figure 3.30, the yellow bootstrapping estimates form an envelope around the actual estimate (the blue point). The yellow area can be thought of as akin to a confidence interval for the square of skewness and kurtosis of the population. From Figure 3.30, Rockall’s sill diameters are likely well represented by either a uniform, normal, beta, gamma or lognormal PD. Beta distributions are only defined between 0 and 1 and thus data needs transformation. This causes extra complication, so Beta distributions will not be used. At low values of skewness gamma and lognormal distributions are essentially equal, so the lognormal distribution alone will be tested here for brevity. Therefore, the PDs remaining to be tested are the uniform, normal and lognormal distributions.

The three PDs are fitted to the sill diameter data by maximum likelihood estimation to find the PD parameters to make the PD fit the sample data as well as possible. Figure 3.31 shows the results of the best fitting distributions for normal, uniform and lognormal distributions. From the top left panel of histograms and theoretical density curves, the uniform model is clearly a poor fit to the data. The lognormal distribution appears to be the best fit, fitting the slight right skew of the data better than the normal distribution. The top left figure shows cumulative distribution functions for the theoretical curves and the data. Both the normal and lognormal distribution seem to fit the data well, with the normal distribution fitting the centre of the data best. The bottom left plot is a quantile-quantile plot, which plots actual against expected quantiles. The QQ plot shows that the normal distribution fits the data poorly at low values, while the lognormal distribution fits poorly at higher values. Note that specifically for application to the missing sills test, good fit at low diameter values is more important than high values, as larger sills have a higher chance of being intersected by a seismic line and are thus more likely to be counted in the test. Hence, there is less benefit to having a small increase in accuracy of fit for larger values than there is for smaller values. The uniform distribution is clearly not an accurate representation of the sample. Finally the bottom left plot shows a probability plot, where the empirical cumulative distribution function

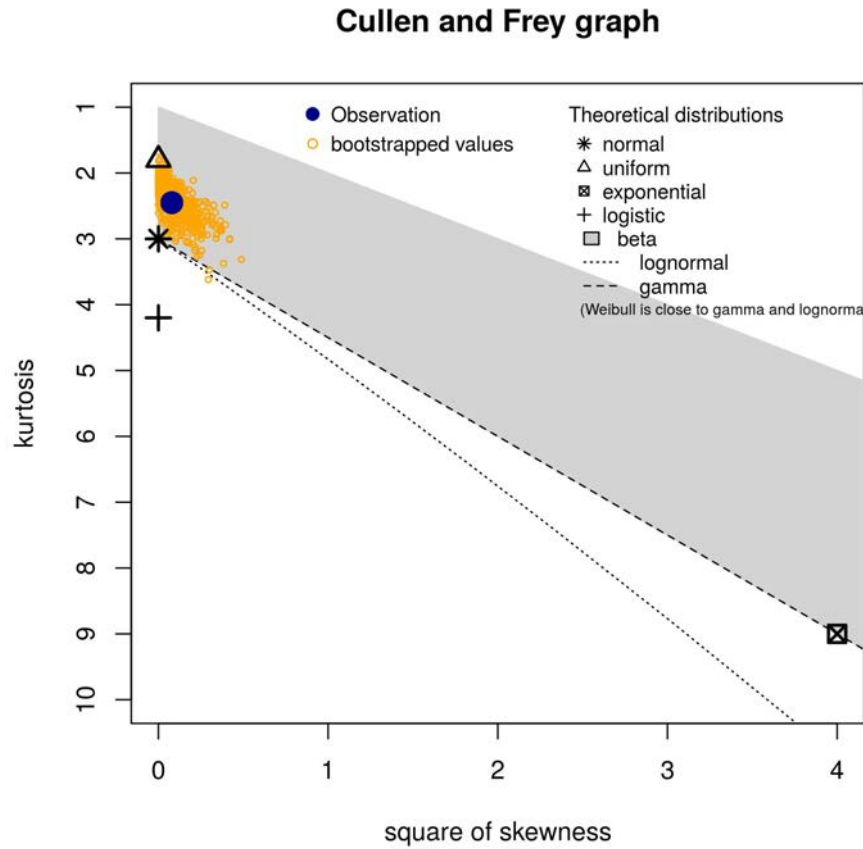


FIGURE 3.30: Cullen and Frey plot, showing the theoretical probability distributions that can be used to model sill lengths. Blue point shows the square of skewness and kurtosis for the sill diameter sample being investigated. Yellow points show bootstrapped samples, indicating a confidence region for the blue point.

is plotted against the theoretical cumulative distribution function. The probability plot shows the normal and lognormal distributions to be close to equal in the context of representing the sample.

3.4.2 North Atlantic Igneous Province results

From the results of these four plots, the most appropriate distribution to model the sill diameters in the NE Rockall 3D dataset appears to be the lognormal distribution. A Monte Carlo simulation was then set up, generating sill diameters with a random diameter drawn from a lognormal distribution, and longitude and latitude drawn from a uniform distribution. As [Fernandes \(2011\)](#) discussed, sill distribution in some basins appears to be clustered rather than uniformly random; an observation mirrored by [Schofield et al. \(2017\)](#), who found the greatest density of sills in association with the Flett and Corona ridges in the FSB. The effect of this on the missing sills test is a worthy

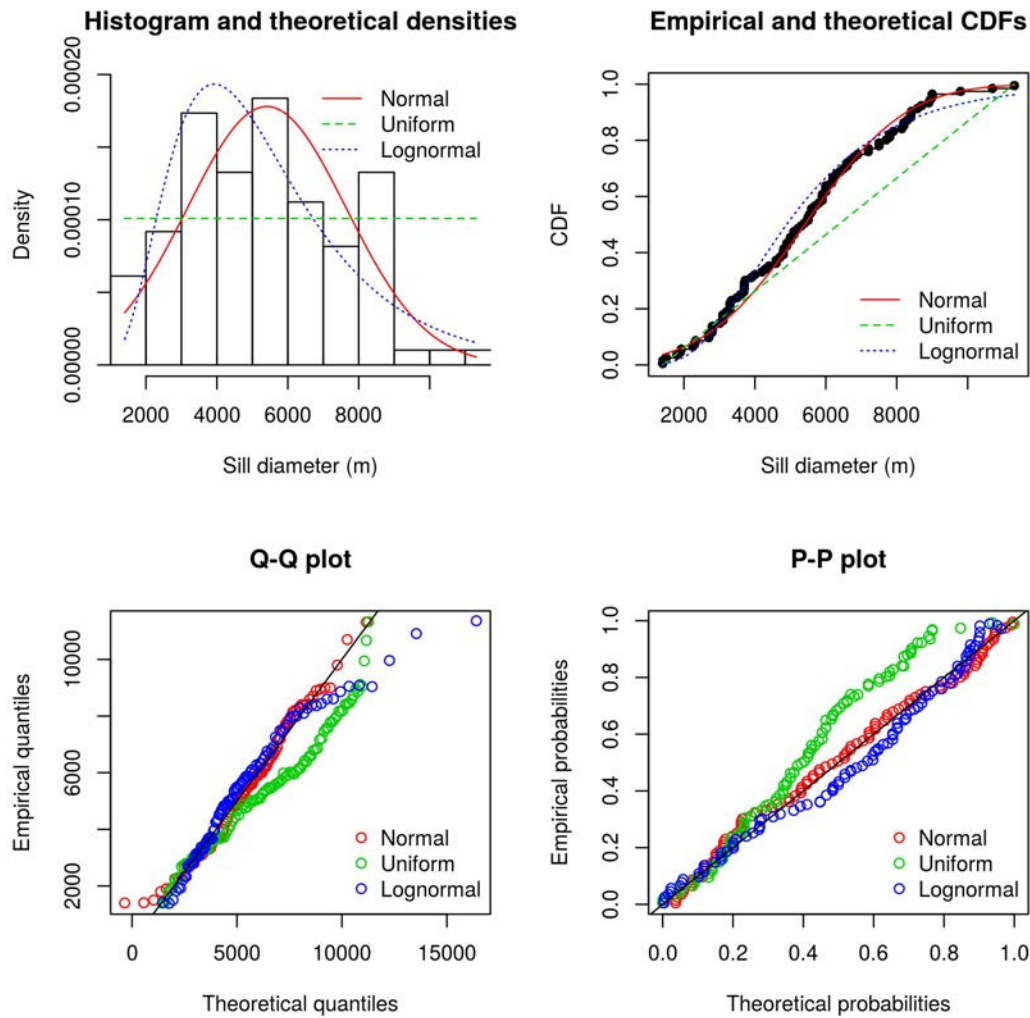


FIGURE 3.31: Results of fitting uniform, normal and lognormal distributions to the Rockall sill diameter samples.

target for future research; however, it adds an additional layer of modelling complexity and will not be modelled here. Ideally, if the seismic survey plan has roughly equally spaced lines then the effect of sill clustering should be minimal, while if the seismic survey footprint has areas with less coverage and a sill cluster fell in a gap or directly over a seismic line the missing sills test would under or overestimate the number of sills in the survey area, respectively. This would have the effect of widening the error bars for the estimate of the number of sills, but should not change the estimate itself significantly. After a sill is randomly generated, the distance of the sill is then checked to be less than 20 km away from the nearest seismic line. The 20 km distance was chosen to be greater than the average seismic line spacing, allowing sills to be generated in between seismic lines. This allows avoidance of the problem in [Fernandes \(2011\)](#), where sills were generated within a rectangular geographic area, which is only sensible if the seismic survey is also rectangular in plan view. Computationally, measuring each point

to the nearest line is inefficient — a ray tracing based point in polygon algorithm is significantly faster — however, a point in polygon methodology causes problems if holes are present in the middle of surveys, such as for the case of the OGA Rockall survey (see section 2.2.1, and figure 3.32). The missing sills test is sped up as much as possible by using the Douglas-Pecker algorithm to down sample the seismic survey lines to reduce computation steps. Figure 3.32 shows an example of a single run for this for the OGA Rockall survey, with 100 sills generated.

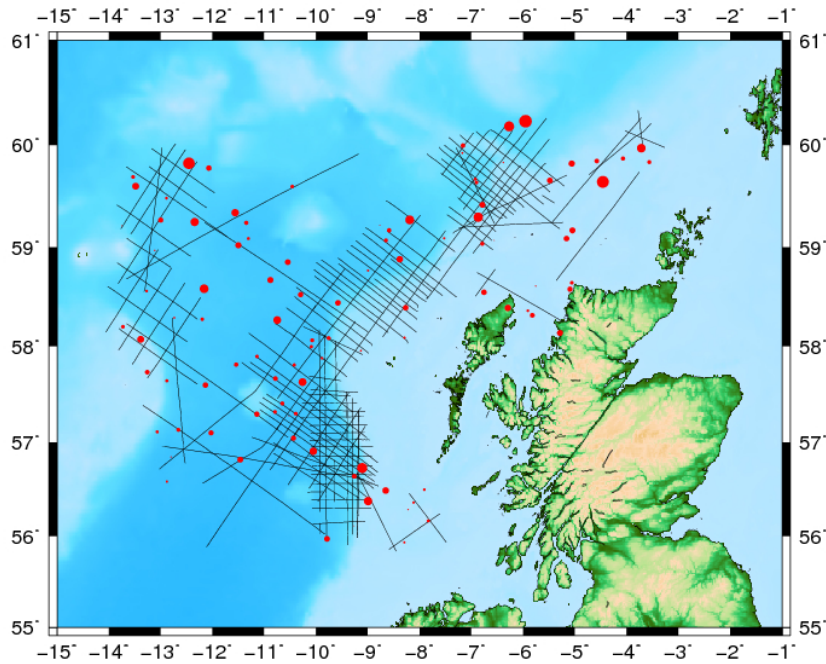


FIGURE 3.32: One run (out of 1200) of the Monte Carlo missing sills test

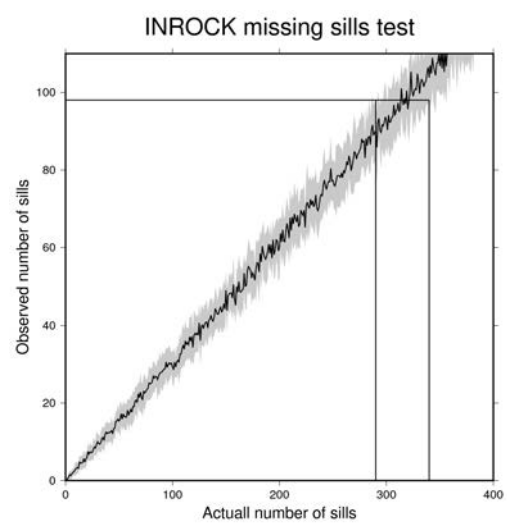
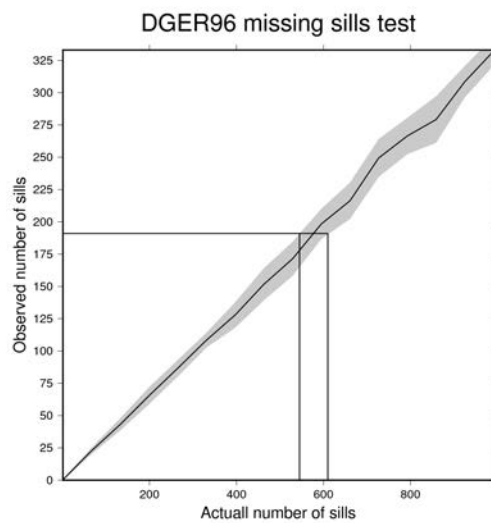
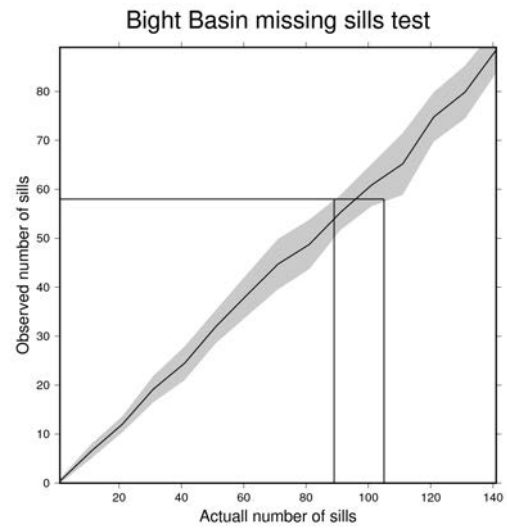
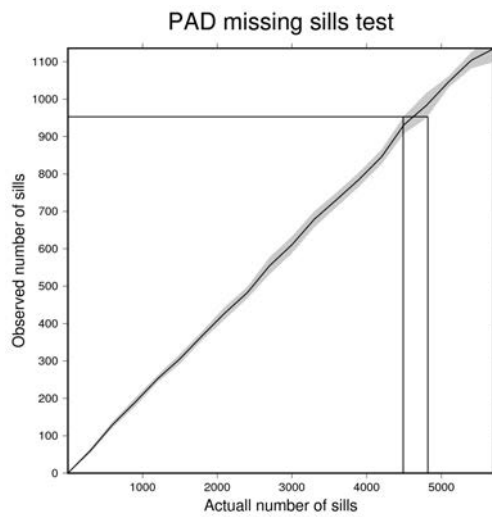
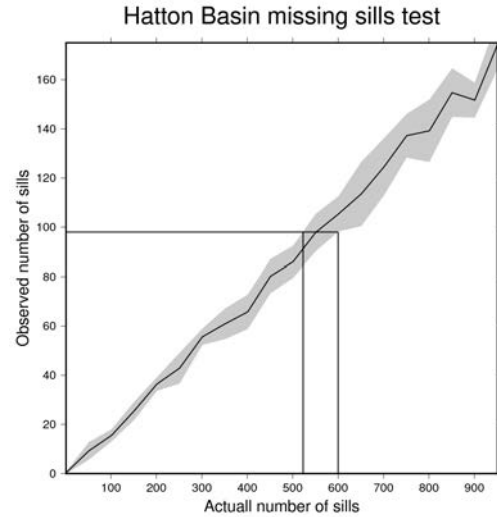
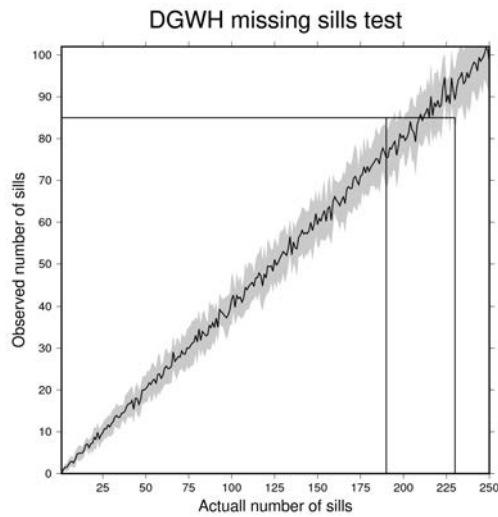
The missing sills test was then applied to each 2D seismic dataset to estimate the true number of sills within the seismic survey footprint. Figure 3.33 shows the results of this, while table 3.2 summarises the results. In figure 3.33, the observed number of sills and the upper and lower estimated bounds have been marked. As should be expected, the seismic surveys with the largest footprints (the OGA and PAD surveys, in the UK and Irish sectors of Rockall) correspond to the greatest number of observed sills. As would be expected, the surveys with the widest line spacing (Hatton and PAD) correspond to both the greatest increase, corresponding to between 4 and 6 times the number of sills observed on the seismic surveys, and also the widest error bars on those values. The seismic surveys with the tighter line spacings (e.g. Bight, DGWH96) correspond to the smallest corrections of only 1 to 3 times the number of observed sills. This is summarised more clearly in figure 3.34, which shows an overlay of all of the models. The slope of the lines correspond to the correction from observed sills to actual sills - the shallower the

TABLE 3.2: Results of the missing sills test for 2D seismic surveys.

Survey Name	No. sills observed	Minimum estimate	Maximum estimate
OGA	671	2050	2180
DGWH96	85	190	230
ISROCK	46	108	139
INROCK	98	290	340
Hatton	98	523	600
PAD	953	4490	4820
DGER96	191	545	610
PORC96	23	46	58
Bight	58	89	105

slope the greater the correction. The Hatton and PAD surveys stand out as the greatest corrections, corresponding to the greatest seismic line spacing.

Having confidence bounds for the maximum and minimum expected number of sills in a basin allows us to investigate relationships which have not yet been studied in the literature. One relationship that may exist is a correlation between the sills area-density — the number of sills per square km (sills km⁻²) — and the great circle distance from the palaeo-plume head location. Another relationship that may exist is a relationship between the sill area-density and the crustal thickness. However, crustal thickness requires very deep imaging with seismic reflection data, or good coverage of seismic refraction data, neither of which are available in the study areas. There normally exists a correlation between water depth and crustal thickness (e.g. [Allen and Allen, 2013](#); [McKenzie, 1981](#); [Tate et al., 1993](#)) and so instead the relationship between sill area-density and water depth will be investigated. In both these cases what we are really interested in, and what any correlation is likely to show, is a relationship between the amount of magma generated and distance to the palaeo-plume head or the crustal thickness. However, the problems of seismically imaging through extrusive basalt ([Maresh et al., 2006](#); [Shaw et al., 2008](#)) and under sills ([Eide et al., 2017b](#); [Fernandes, 2011](#)) makes estimating the amount of magma difficult, thus the sill area-density is a simpler measurement that would be expected to be related to the amount of generated magma. The number of sills within the survey footprint — found with the missing sills test — was then divided by the survey footprint area to give the sill area-density (sills per unit area). This was estimated as the convex hull around the end points of the seismic survey, thus representing an upper bound to the survey area. The distance between the palaeo-plume head and a seismic survey was found by measuring the great circle distance between the average of the x and y coordinates of the seismic surveys. The greatest uncertainty in the distance between the mid point of a seismic survey and the centre of a palaeo-plume head is the location of the palaeo-plume head, which is model dependent. We use the



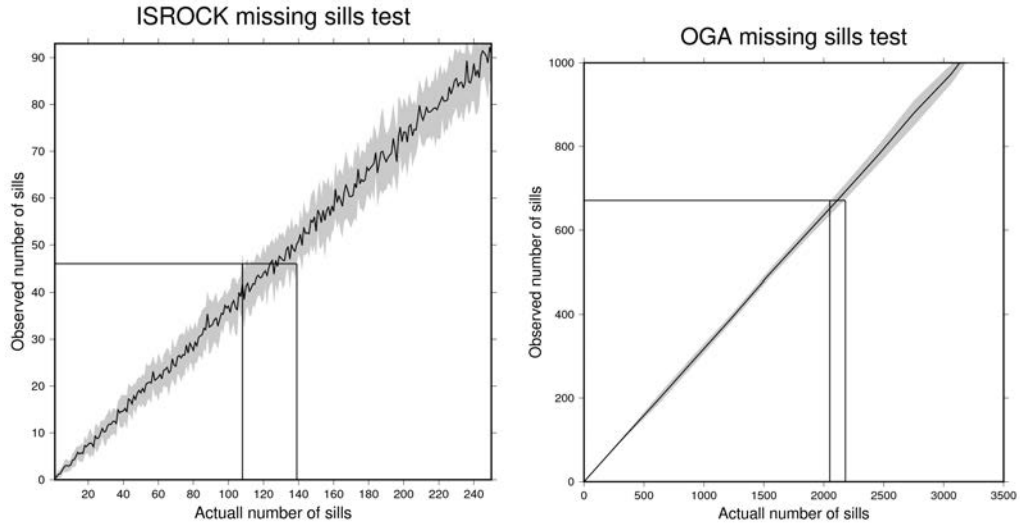


FIGURE 3.33: Results of applying the missing sills test to different 2D seismic surveys. The number of sills observed, and the corresponding minimum and maximum bounds for the number of sills predicted is shown for each survey.

palaeo-plume head locations of [Nisbet et al. \(2009\)](#) and [White and Mckenzie \(1989\)](#) as upper and lower bounds for an estimate of palaeo-plume head. The great circle distance is then found with the Haversine formula. Figure 3.35 shows the great circle distances between the survey midpoints and the centre of the palaeo-plume heads. Figure 3.36 shows the results of plotting the sill area-density estimates against the distance from the survey mid point to the palaeo-plume head centre. A negative correlation can be seen. This makes sense intuitively, as we may expect more magma generation closer to the palaeo-plume head; however, this is the first time it has been quantitatively shown with sill data. The correlation may be stronger than this, as the point representing the OGA data should be significantly higher — there are parts in the OGA survey where there are so many sills that individual sills cannot be interpreted, and in the Northwest of the survey thick extrusive basalt lava precludes imaging of sills underneath. Both of these factors will increase the sill area density in the OGA survey.

The average water depth in a survey was found by sampling the ETOPO1 global bathymetry grid ([Amante, 2009](#)) at all seismic shotpoints, and finding the average and standard deviation of the sampled bathymetric points. Figure 3.37 shows histograms of the sampled bathymetry for each seismic survey, while figure 3.38 shows the results of plotting mean bathymetry against sill area-density. A weak negative correlation can be seen, albeit much noisier than seen in figure 3.36.

Multiple linear regression was performed to relate the average distance from the palaeo-plume head and the mean bathymetry to the sill area-density. The results of this are shown in table 3.3. The first interesting observation is the multiple R^2 . These can be

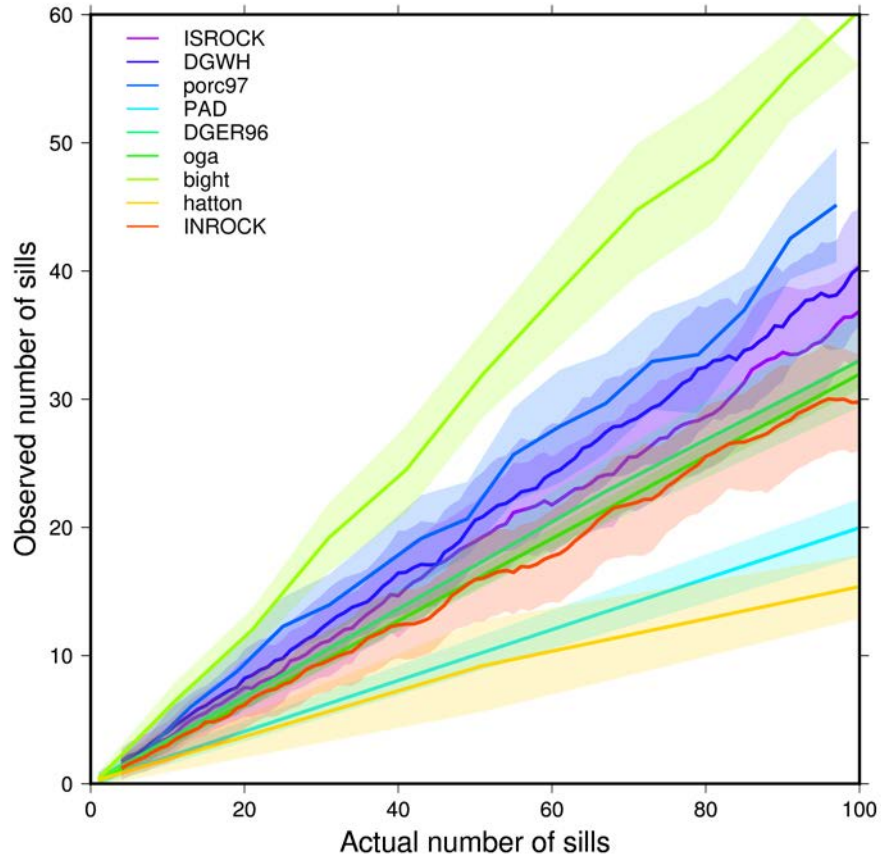


FIGURE 3.34: Curves of observed sills against actual sills within seismic survey footprint, from the missing sills test. Envelopes are two standard deviations wide.

interpreted as the proportion of the data that can be explained by the regression model, in this case around 85%. This tells us that the relationship is a moderately strong linear relationship, although clearly with some scatter as figures 3.36 3.38 indicate. The standard error of the intercept is large and it has a corresponding large p-value, while the bathymetry and plume distance coefficients have small standard errors and statistically significant p-values. This indicates that while the slope of the regression line is well defined, it can be moved vertically within quite a large confidence interval without affecting the accuracy of the model much. This is an indicator of the scatter of the points, and shows they do not lie perfectly on a plane in three dimensional space. The coefficients for both the distance from the palaeo-plume centre and the bathymetry are negative as would be expected - showing that sill area density is highest in deep water (corresponding to thin crust) and nearest the plume centre. This makes sense physically, as this is the region most likely to be associated with high magma production.

Figure 3.36 indicates that the trend of the regression line might not be linear, but may be better fit by a polynomial. The multiple linear regression analysis was rerun with polynomial terms, such that the starting model was of the form

Distances from seismic surveys to plume centres

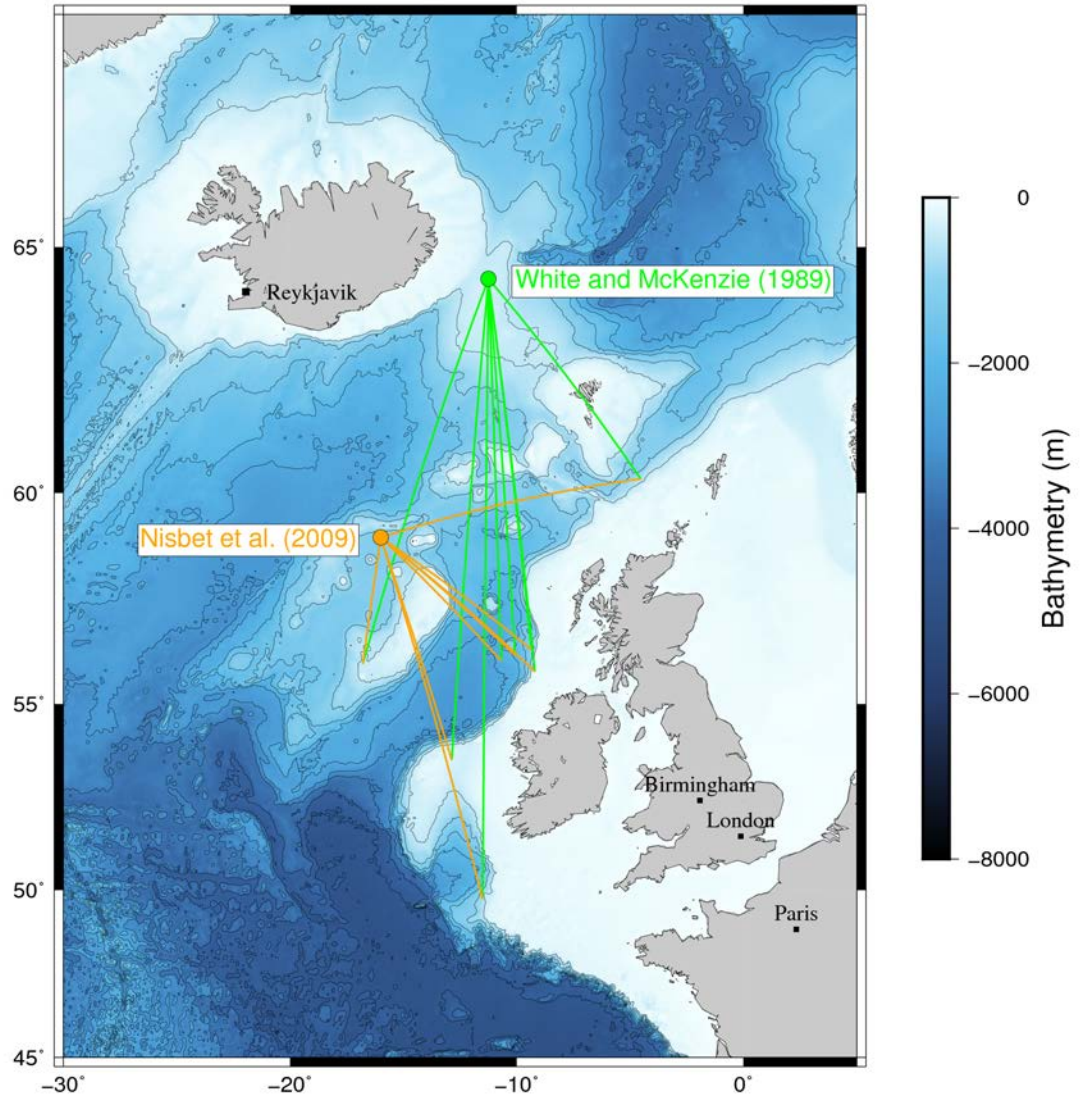


FIGURE 3.35: Great circle distances from palaeo-plume centres of White and McKenzie (1989) and Nisbet et al. (2009) to mid points of 2D seismic surveys. Bathymetry data from ETOPO1 (Amante, 2009).

$$SAD = a_1*B + a_2*B^2 + a_3*PD + a_4*PD^2 + a_5*B*PD + a_6*B^2*PD + a_7*B*PD^2 + a_8*B^2*PD^2$$

where SAD is sill area density, B is bathymetry, PD is plume distance and a_x is the coefficients for the x th term in the model. After making the initial linear regression model, terms were removed sequentially starting with the term with the largest p-value and recalculating the model. This was continued until all terms were found to be significant. The results of this analysis can be seen in table 3.3. This process results in a

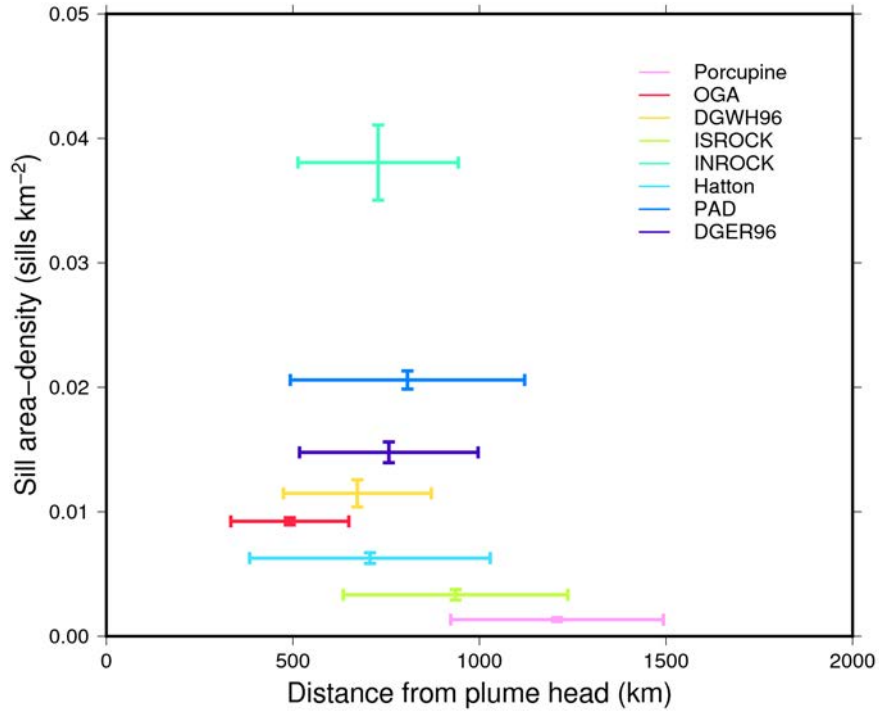


FIGURE 3.36: Scatter graph of distance of the mid point of each survey from the centre of the palaeo-plume head models of [White and Mckenzie \(1989\)](#) and [Nisbet et al. \(2009\)](#), against sill area-density.

significantly better regression model, explaining around 94% of the variance of the data with the model. The standard error on the intercept term has shrunk by a large amount and is now statistically significant. Plume distance² is found to be a more important term than plume distance. This might be related to the geometric spreading of the plume head, although with so few data points to fit this model to interpretation of the model should be done cautiously. The coefficient of the bathymetry term has reversed sign in this new model. This is interpreted to be due to the interplay of other terms in the model, and likely serves as a reminder to not over-interpret linear regression model coefficients rather than to have any physical meaning.

To summarise the results of the linear regression and polynomial linear regression analysis, the analysis indicates there is a strong correlation between bathymetry, distance from the palaeo-plume centre, and sill area density. The distance from the palaeo-plume centre appears to be a polynomial of degree 2, which might be related to the shape of the spreading head of the plume, however this should be interpreted with caution. Adding more terms to the model results in a better model fit, but more difficulty in interpreting the model in terms of the underlying physics of the magmatic system.

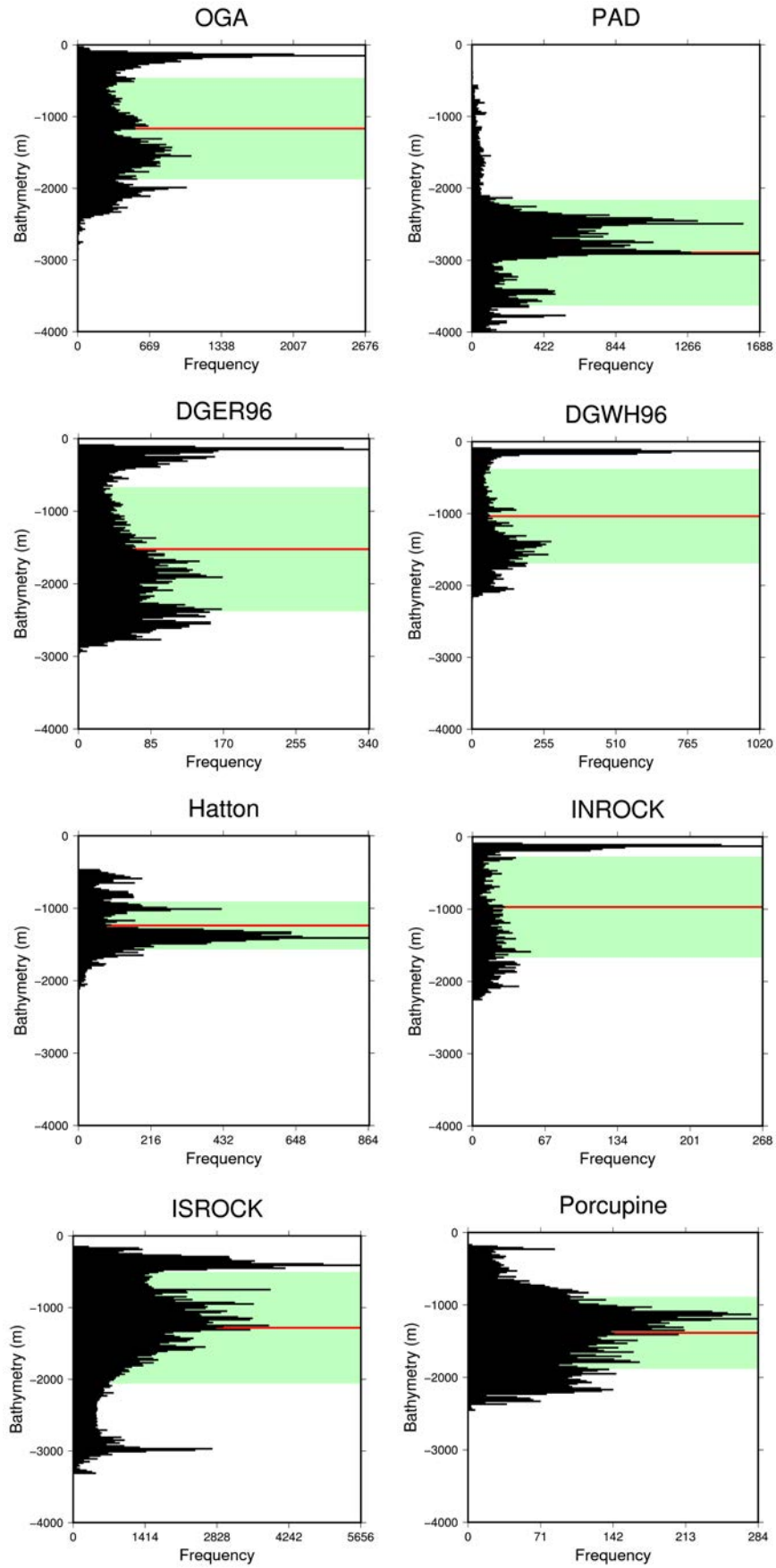


FIGURE 3.37: Histograms of bathymetry extracted from each survey. Red line is mean, while green envelope is two standard deviations.

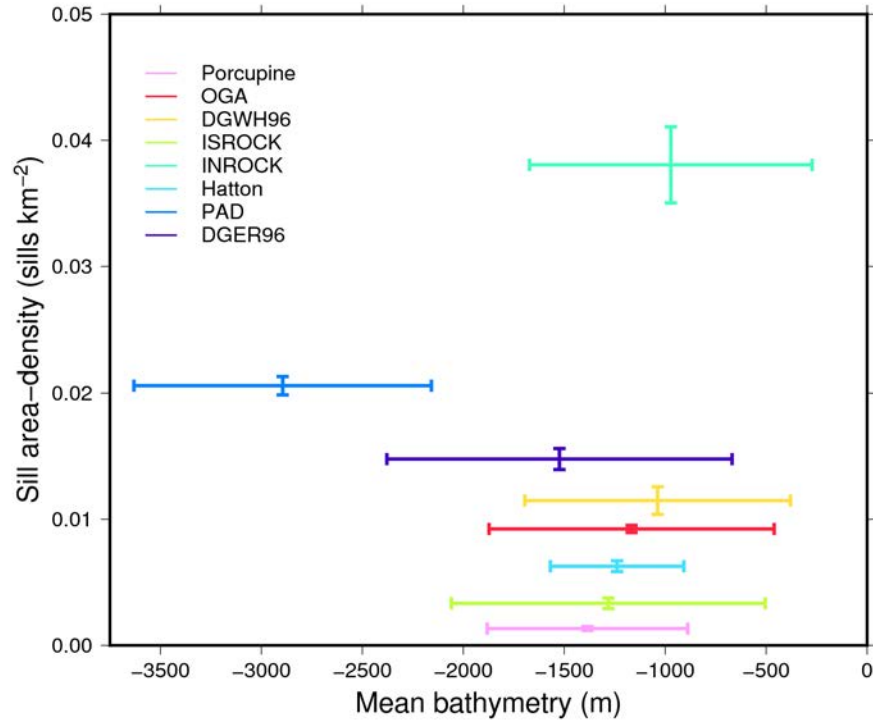


FIGURE 3.38: Scatter graph of sill area density against mean survey bathymetry, extracted from ETOPO1 ([Amante, 2009](#)).

	Value	Standard Error	t value	$Pr(> t)$
Intercept	2.501e-2	0.5727949	1.335	0.23928
Bathymetry coefficient	-2.908e-6	0.0002179	-4.294	0.00776
Plume distance coefficient	-2.036e-5	0.0005540	-2.851	0.03577
Multiple R^2	0.8499			
Adjusted R^2	0.7899			

TABLE 3.3: Multiple linear regression model coefficients to predict sill area density from distance to the palaeo-plume centre and the water depth (a proxy for crustal thickness).

	Value	Standard Error	t value	$Pr(> t)$
Intercept	5.267e+00	1.761e+00	2.992	0.0403
Plume distance ²	-4.613e-06	1.292e-06	-3.570	0.0234
Bathymetry	3.175e-03	1.373e-03	2.313	0.0818
(Plume dist * bathy) ²	2.160e-12	7.169e-13	3.014	0.0394
Multiple R^2	0.9479			
Adjusted R^2	0.9089			

TABLE 3.4: Polynomial multiple linear regression model coefficients to predict sill area density from distance to the palaeo-plume centre and the water depth (a proxy for crustal thickness).

3.5 Using the sill database to test emplacement models

There are a number of different emplacement models for igneous intrusions. Many early models envisaged igneous intrusions as a fluid filled crack in an isotropic elastic medium. Later models incorporated increasingly complex host rock properties, such as defects (Magee et al., 2013b; Pollard, 1973), mechanical contrasts (Gudmundsson and Lotveit, 2014) and poroelastic / plastic behaviour (Scheibert et al., 2017; Schofield et al., 2012; Spacapan et al., 2017) into models. To date almost none of these models have been tested against an independent dataset, and that is the focus of this section. First in this section the order of magnitude estimates of Lister (1990) and Lister and Kerr (1991) will be used to introduce the main force balances that control the geometries of igneous intrusions, and the datasets introduced in the preceding parts of this chapter will be used to test these order of magnitude estimates. The order of magnitude estimates are found to be a poor fit to the sills data. Following this, the fundamental Linear Elastic Fracture Mechanics (LEFM) model for a fluid filled crack (e.g. Rubin, 1995) is tested against the sills data. This is also found to be a poor fit to the data, and it is hypothesised that the poor fit is due to the sill observations in this study being relatively shallowly emplaced, meaning the isotropic host rock assumption is violated. Finally the overlying elastic plate model of Johnson and Pollard (1973) is tested against the sills data, and this is found to be a significantly better fit to the sill data.

3.5.1 Intrusion modelling context

Before discussing modelling parameters and results, there is value in discussing key components of the different sill intrusion models in the context of what can be observed on seismic data versus in field data. As described in Chapter 1, sill emplacement models can be split into three main categories: LEFM based models, fluidization models and viscous indenter models. Each of these models comes with different implications for

structures and effects on host rock around intrusions that may be used as diagnostic for which model is more appropriate for that formation and intrusion of that sill:

- For LEFM based models, field observations that would support the model would include the lack of evidence for a fluidized carapace around the majority of the sill, and a lack of compressional and/or ductile deformation both around the sill and specifically around the sill tip. The sill tip is expected to taper to a sharp point. Seismic evidence in support of LEFM based sill models may include intrusions with gradual changes in sill thickness (in contrast to fluidization and viscous indenter based models, which could have more variable thicknesses), maximum sill diameter and maximum sill thickness measurements as predicted by LEFM models, and sill thickness profiles in accordance with the dimensionless versions of the LEFM models ([Johnson and Pollard, 1973](#); [Pollard, 1973](#)).
- For fluidization based models, field observations in support of the model may include the observation of a fluidized carapace around the sill. This zone may be expected to be particularly well developed near any sill steps or changes in sill dip (i.e. the base of transgressive sill limbs). Sill tips are expected to be blunt ended or ragged ([Schofield et al., 2012](#); [Thomson and Schofield, 2008](#)). The seismic evidence for fluidized models may include lateral changes in sill thickness ([Schofield et al., 2012](#)). These are no current mathematical models relating geometry of sills to the fluidized mechanism of emplacement, so such models are difficult to test quantitatively.
- For viscous indenter models, field evidence in support of the model could include compressional structures around the sill, and particularly concentrated around the sill tip. This is because the host rock is modeled as behaving as either an elasto-viscous material or as a viscous fluid which deforms or fails due to the work done by the intruding magma. Blunt ended sill tips are also likely, while sharp sill tips are unlikely ([Schmiedel et al., 2017](#)). Seismic evidence for the viscous indenter model might include a sill which does not taper as much as for the LEFM models, and evidence for blunt sill tips.

It is important to note that if a sill was exposed in the field from tip to tip that this could be used to derive the same numerical parameters as for seismic, and thus would be equally used to test the sill models. However, it is very uncommon to find such well exposed sills in the field. This is a major advantage of seismic data over field data for testing large scale sill emplacement models.

An important caveat to all of the models examined is that they grew in a single intrusion episode, not as the result of multiple magma pulses. It is difficult to predict the geometries of intrusions formed from multiple episodes of magma injection as this has received

little study in the literature. However, there would likely be seismic observations which would indicate that the intrusion may have grown from multiple pulses, allowing it to be excluded from the analysis. First, the later magma batches would need to have been fed through the same dyke as the initial magma batch that formed the sill, otherwise additional reflections from inclined magma sheets acting as feeders may be observed. Second, the new magma must be emplaced above, below or through the original sill without transgressing away from the original sill until past the original sill's tips, as otherwise a thickness step change would be observed on seismic data. These two factors not being identified on the measured sills allow some confidence that the measurements obtained are from single intrusion event sills and thus are fit for testing intrusion models. However, there is a small chance that a sill may be formed from multiple pulses and it having no obvious seismic expression, and this remains as an uncertainty in the following data – model comparison.

3.5.2 Intrusion modelling parameters

Certain material properties and parameters need to be known so an intrusive sill can be modelled. While the length of the intrusion is known to a high degree of precision from measuring it on seismic data, the magma pressure, Poisson's ratio and shear modulus are unknown for all data sets. For subsequent modelling, we use the following wide parameter ranges in table 3.5. The parameter ranges are purposefully wide here, as the goal in the following modelling sections is to fully constrain the expected ranges of predicted sill measurements, rather than to try to predict an exact value for a sill measurements and add a confidence estimates to it.

TABLE 3.5: Parameters used in LEFM models

	Symbol	Minimum	Maximum
Pressure difference	ΔP	$2 \times 10^6 \text{Pa}$	$40 \times 10^6 \text{Pa}$
Poisson's ratio	ν	0.05	0.5
Shear Modulus	μ	$5 \times 10^9 \text{Pa}$	$35 \times 10^9 \text{Pa}$

The minimum and maximum values for magma pressure are from [Kusumoto et al. \(2013\)](#) and [Hautmann et al. \(2009\)](#), minimum and maximum values for Poisson's ratio are from [Gerçek \(2007\)](#) and minimum and maximum values for shear modulus are from [Baechle et al. \(2005\)](#). Depth conversion of sills was done using velocities from 4000ms^{-1} to 6500ms^{-1} , from [Smallwood and Maresh \(2002\)](#). The ranges of these parameters and deliberately the widest that could be found in the literature. This is because a range of sills are being modelled, normally in an uncertain lithology, and at varying emplacement

depths. The wide parameter ranges are thus an attempt to quantify the uncertainty in subsequent modelling.

3.5.3 Order of magnitude intrusion estimates

Lister (1990) and Lister and Kerr (1991) provided a now much cited analysis of pressure scales inside a propagating magma filled crack. This analysis has been used by a number of authors to provide context for studies of both dykes and sills (e.g. Kavanagh et al., 2006; Menand, 2008). Here Lister's (1990) analysis is used to introduce the forces and pressures experienced by an intruding magma body, and the various force balances are applied to measured sills from shallow sedimentary basins introduced earlier in this chapter. The following models are often applied to dykes and less commonly to sills; however, note that the models actually specify only a crack in a host solid and the the orientation of the crack is specified in the model, therefore testing them for sill emplacement is appropriate.

Lister (1990) and Lister and Kerr (1991) imagine an infinite elastic solid, with a fluid filled crack embedded in it. Four pressure scales uniquely define the regime of crack propagation within the solid, and define the shape and sizes of the crack, and how the crack propagates through the host solid. Each pressure scale is derived by balancing forces. These pressure scales are: (1) the pressure required to open the crack against the host rock material's elastic forces:

$$\Delta P_e \sim \frac{mw}{l} \quad (3.10)$$

where m is defined as $m = G/(1 - \nu)$, G is the shear modulus and ν is Poisson's ratio, w is the width of the crack and l is the length of the crack. (2) The buoyant hydrostatic pressure, derived from the density difference between the magma and the host rock:

$$\Delta P_h \sim g\delta\rho h \quad (3.11)$$

where g is the acceleration due to gravity, $\delta\rho$ is the density difference between the host rock and the magma, and h is the vertical distance to the bottom of the feeder region (if connected). (3) The restive viscous forces arising from flow in the crack:

$$\Delta P_v \sim \frac{\mu ul}{w^2} \quad (3.12)$$

where μ is the fluid viscosity and u is the velocity scale; and (4) pressure required to extend the crack:

$$\Delta P_c \sim \frac{K}{l^{\frac{1}{2}}} \quad (3.13)$$

where K is the critical stress intensity factor. The balances between these pressures control how the crack propagates, and crucially, its final length and width. [Lister \(1990\)](#) describes a thought model of crack propagation in the situation where $\Delta P_h = 0$, i.e. that hydrostatic pressure is negligible. This may be applicable to sill emplacement, as this would describe the emplacement of a sill not in direct connection with its feeder reservoir. Dykes are thought to close behind themselves (e.g. [Lister, 1990](#); [Spence and Turcotte, 1985](#), etc.) and thus a sill might not be expected to be in contact with its original source region. [Lister \(1990\)](#) is principally concerned with magma intruding continental or oceanic basement rocks. Magma intruding sedimentary rocks involves dense basaltic magma intruding much less dense, potentially unconsolidated, sedimentary rock. This may imply that ΔP_h must be high, otherwise the magma column would lack pressure support to overshoot the level of neutral buoyancy (where $\rho_{magma} = \rho_{sediment}$). [Lister's \(1990\)](#) approximations are given in terms of l (length) and V (volume). Here they are rearranged to find w , using the following 2 dimensional relationship:

$$V = lw \quad (3.14)$$

Taking $\Delta P_h = 0$, two possibilities exist; either $\Delta P_e \approx \Delta P_c$ or $\Delta P_e \approx \Delta P_v$. For the case where $\Delta P_e \approx \Delta P_c$, combining equations [3.10](#), [3.13](#) and [3.14](#) it can be seen that:

$$w = \frac{Kl^{\frac{1}{2}}}{m} \quad (3.15)$$

Figure [3.39](#) shows the result of plotting sills measured on seismic against the theoretical predictions, for the range of parameter values in table [3.5](#). The thick black line at the bottom of the plot is four models using equation [3.15](#) for different parameter values. As can be seen, equation [3.15](#) underestimates the thickness of the sills by several orders of magnitude, despite using wide parameter ranges. This indicates that either the balance between ΔP_e and ΔP_c is not the control on final size of these sills, or that the assumptions of the model do not hold true for these sills. Note that the majority of these observations are from 2D not 3D seismic, which means there is a possibility that the seismic line cuts a sill lobe or an irregular part of the sill. This cannot be ruled out, but is at least unlikely; these measurements are all thick enough to have a top and base reflection, and

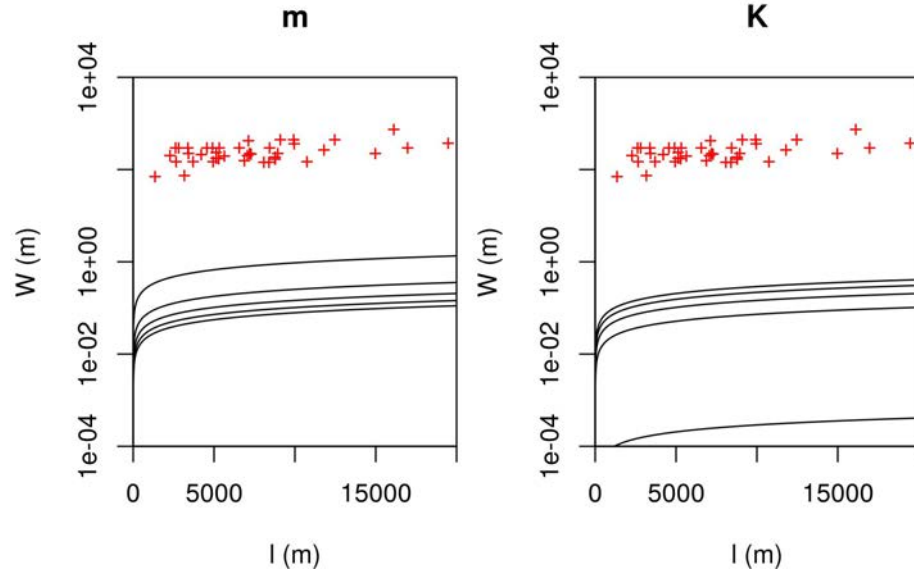


FIGURE 3.39: Measured sill data (crosses) against theoretical predictions using equation 3.15

lobes and irregular parts of sills are normally found at the sill edges, hence are very unlikely to have a top and base reflection.

This ideal model can be compared with other hypothetical end members, where $\Delta P_e \approx \Delta P_v$ (i.e. where the controlling factor is the balance between the pressure to extend the crack versus the pressure to overcome viscous forces in the crack). Combining equations 3.10, 3.12, 3.14 and 3.16 gives equation 3.17:

$$u \sim \frac{l}{t} \quad (3.16)$$

$$w = \frac{\sqrt[3]{\mu l}}{\sqrt[3]{mt}} \quad (3.17)$$

Figure 3.40 shows the result of plotting the same sills as in figure 3.39. The four models representing equation 3.17 are found at the bottom of the graph. Once again, the models are clearly not a good fit for the data, seriously underestimating the sill thickness. This contradicts the findings of Lister (1990), who finds that the viscous forces should explain the intrusion length and width, for his studied case of more deeply emplaced dykes.

The differences in predictions between the predictions of equation 3.15 and 3.17 is clearest when looking at the predictions side by side. Figure 3.41 shows the result of this comparison, clearly demonstrating that even at the maximum predicted values, sills of only a few meters thick are predicted. As Lister (1990) notes, equation 3.17 does predict

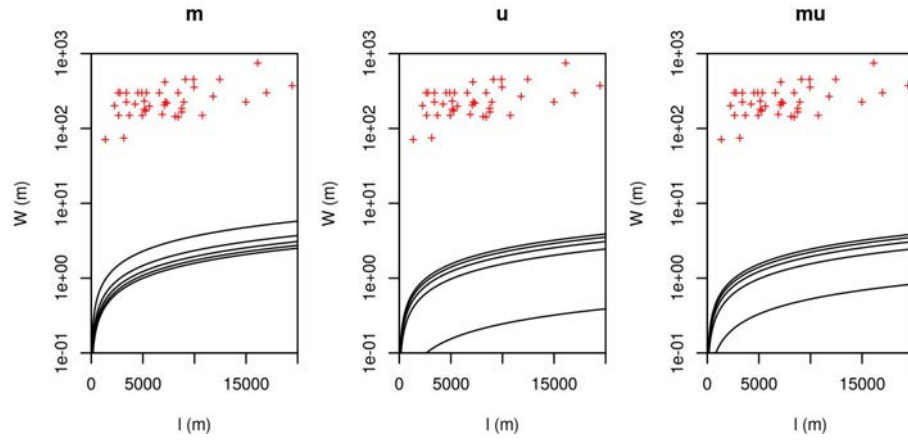


FIGURE 3.40: Measured sill data (crosses) against theoretical predictions using equation 3.17

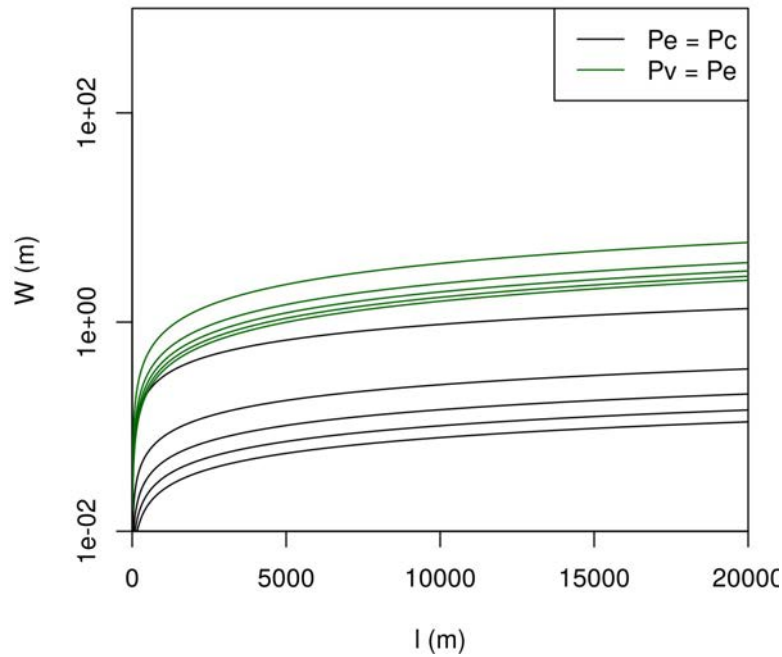


FIGURE 3.41: Comparison between equation 3.15 and 3.17

thicker intrusion than equation 3.15 and, as Lister (1990) mentions, thicknesses derived from equation 3.15 are inconsistent with magma transport over large distances in the crust due to the intrusion losing heat and freezing.

Lister (1990) continues his analysis to explain how viscous pressures will dominate crack extension pressures for the general case in the following inequality:

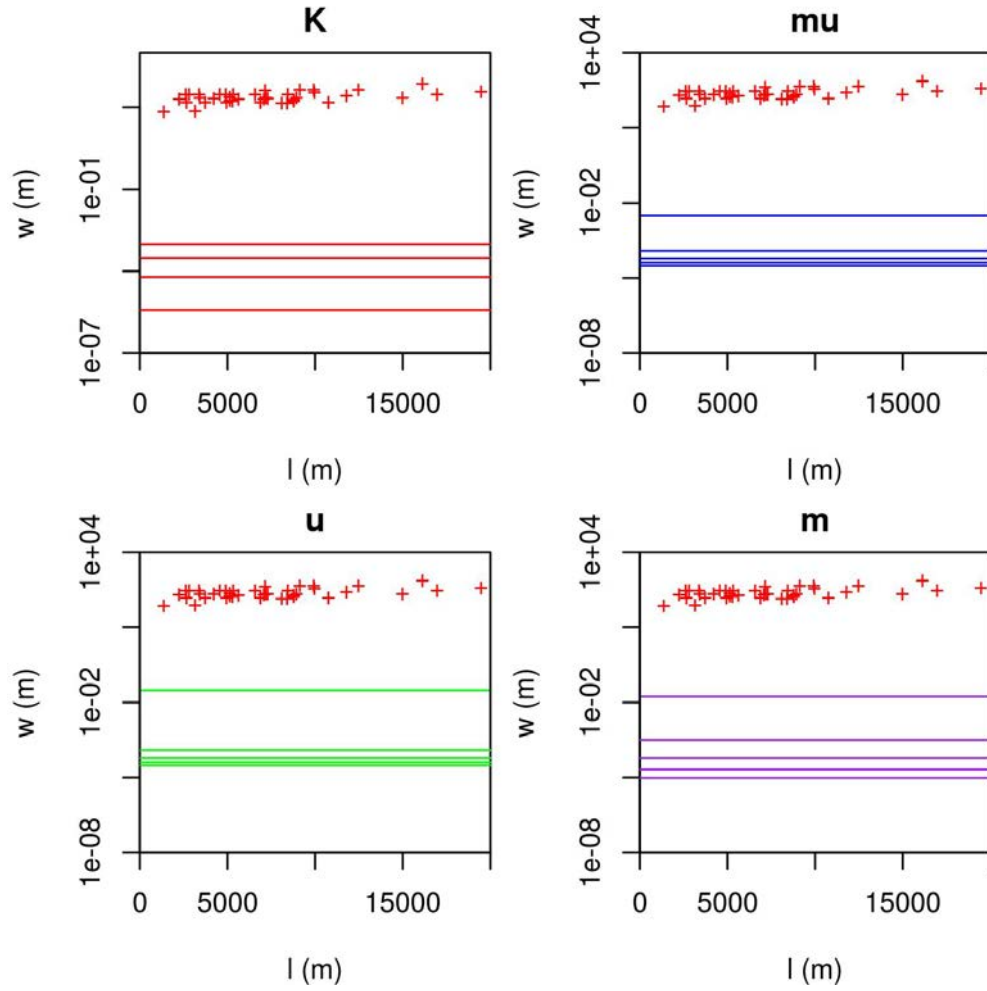


FIGURE 3.42: Comparison of real data (crosses) with inequality 3.19

$$\frac{V}{tl^n} \gg \frac{K^4}{\mu m^3} \quad (3.18)$$

which, for the 2 dimensional case, can be combined with 3.14 and rearranged to:

$$w \gg \frac{tK^4}{l\mu m^3} \quad (3.19)$$

Figure 3.42 shows that the data are in good agreement with equation 3.19, being consistently greater than the lines representing the right hand side of the inequality. This result supports Lister's (1990) prediction that viscous forces are dominant. However, the disagreement between predictions shown in figure 3.40 suggests that the sills measured do not exactly conform to Lister's (1990) models.

Lister (1990) then goes on to describe how the case of a stationary crack can be considered, which would mean $\Delta P_v = 0$. This gives rise to:

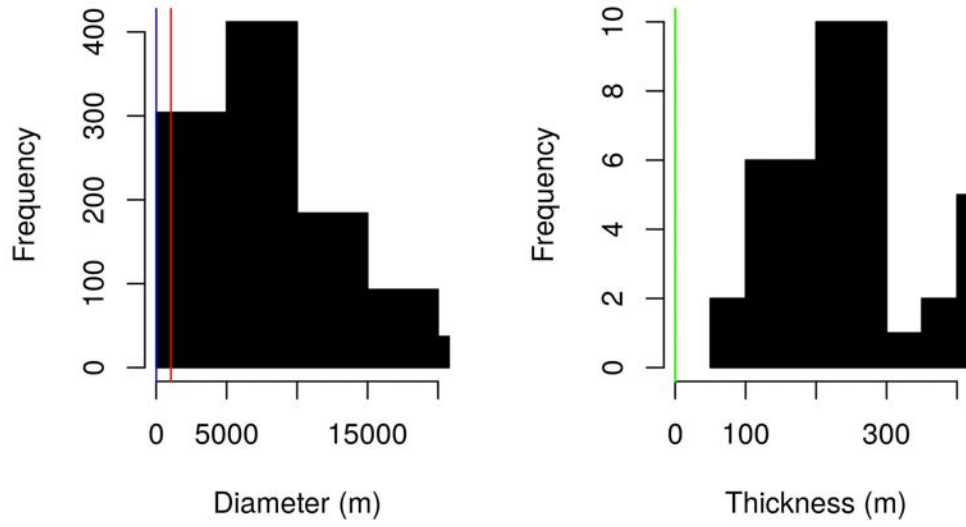


FIGURE 3.43: Histograms of sill lengths and thicknesses. Coloured lines represent the predicted maximum lengths and widths for different parameter combinations from equations 3.20 and 3.21

$$h \sim \left(\frac{K}{g\delta\rho} \right)^{\frac{2}{3}} \quad (3.20)$$

$$w \sim \left(\frac{K^4}{g\delta\rho m^3} \right)^{\frac{1}{3}} \quad (3.21)$$

These relationships form the bounds in figure 3.43. It can be seen that a small number of cases of sill measurements do match the maximum length predicted by equation 3.20 (figure 3.43, left hand panel); however, the vast majority of cases of sills measurements are significantly greater than the maximum predicted length. For sill widths (figure 3.43, right hand panel), no observed sill comes close to the maximum values predicted by 3.20. This analysis thus agrees with Lister (1990) in that the predicted values of length and width of the crack do not seem appropriate, and hence equations 3.20 and 3.21 do not seem to be a sensible models for sills as observed.

If the main force balance is elastic and hydrostatic, then setting equation 3.10 equal to equation 3.11, gives

$$\frac{h^2}{w} \sim \frac{m}{g\delta\rho} \quad (3.22)$$

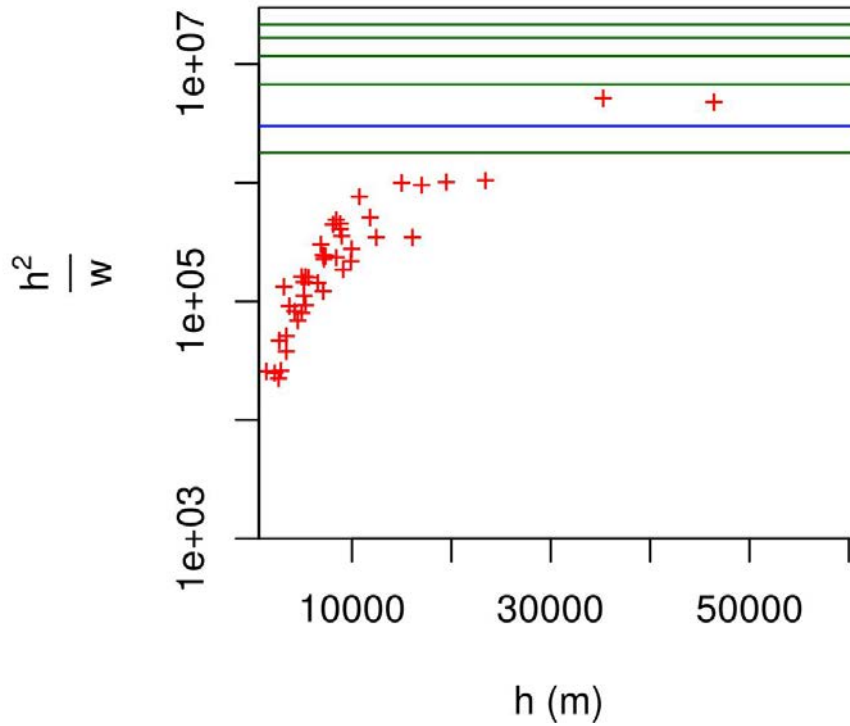


FIGURE 3.44: Measured sills (red crosses) plotted against the right hand side of equation 3.22 (green lines). The blue line shows the parameter values of Lister (1990)

This leads to the graphs in figure 3.44. Lister (1990) states that

“If $\frac{h^2}{w}$ is much less than $[\frac{m}{g\Delta\rho}]$ then we may neglect ΔP_h and the propagation of the crack is given by [equation 3.17]”

The situation shown by the sill data is found in figure 3.44. Figure 3.44 shows that for almost all cases $\frac{m}{g\Delta\rho}$ (green lines) $\gg \frac{h^2}{w}$ (red crosses). This means that ΔP_h cannot be neglected, the opposite of the findings of Lister (1990). This finding is consistent with the fundamental observation that some sort of pressure support must be present to lift the more dense magma into the less dense sediments prior to emplacement.

Figure 3.45 shows the results of rearranging equations 3.15 and 3.17 to find the optimum parameters required to fit the data. These optimum ranges can then be compared with sensible ranges of these parameters in sedimentary basins, as found in table 3.5. In figure 3.45, each black line represents one measured sill, and the parameters required to fit equations 3.15 and 3.17 to measured sills. The parameters needed to force equations 3.15 and 3.17 to fit the data points are clearly not in sensible ranges, shown by the overlap in the green and blue regions. In fact, the parameter ranges are several orders

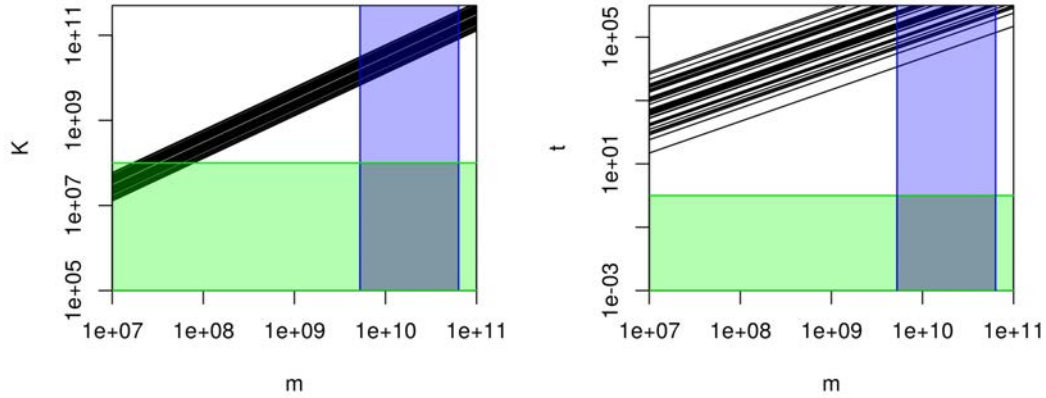


FIGURE 3.45: Left: Parameter fitting for equation 3.15. Right: Parameter fitting for equation 3.17. For both equations blue regions show the bounds of parameters in sedimentary basins for the parameter on the horizontal axis, while green regions show the bounds for parameters on the vertical axis. Where the two regions cross shows the parameters space in sedimentary basins. Both plots show modelled values fall outside of the normal parameter space for sedimentary basins, by several orders of magnitude.

of magnitude outside of the expected ranges, indicating equations 3.15 and 3.17 do not model the data well.

The main reason for the poor fit between [Lister's \(1990\)](#) models and data measured in this work may be inadvertent selective sampling of the sills measured. Seismic data suffers loss of vertical resolution with depth, due to the effect of removal of high frequency signal by the earth filter. This means that the sills that can be imaged as having a top and base — and therefore the sills which have been used in this analysis — are biased towards the shallowest and thickest sills. The shallower sills are more likely to be able to deform the overlying host rock, strongly invalidating the assumption of an infinite homogeneous elastic solid host rock. Another possibility is that the sample has underestimated the sill diameter due to the majority of the data being from 2D seismic. Given the difficulty in finding sills with a clear top and base, and the difficulty of getting hold of industry seismic data in general, excluding 2D data would result in a very low sample size to test models against. As discussed in section 3.2.2, correcting for the problem of 2D seismic line intersection with a sill is challenging. However, doubling or even tripling the diameter of sills used in this analysis does not help bring the sills within the predicted ranges from [Lister's \(1990\)](#) work. Note that the measured aspect ratios for sills in this study agree with those in [Jackson et al. \(2013\)](#) and [Pollard \(1973\)](#), as well as agreeing with aspect ratios that can be derived from information in [Hansen and Cartwright \(2006a\)](#), [Magee et al. \(2013a\)](#) and [Schmiedel et al. \(2017\)](#). This also indicates that the measurements of sills used in this study, while slightly skewed by the

aforementioned factors, are within the right order of magnitude, while [Lister's \(1990\)](#) models are not.

3.5.4 2D Linear Elastic Fracture Mechanics (LEFM) model

Following the order of magnitude estimates of [Lister \(1990\)](#), the Linear Elastic Fracture Mechanics (LEFM) intrusion models were tested. In the paradigm of LEFM, brittle fracture is idealised by the growth of cracks in an infinite isotropic elastic solid. The propagation and growth of cracks, can be solved analytically under these assumptions. In the depths of a sedimentary basin, ambient stresses are never tensile ([Zoback, 2010](#)), and therefore sill or dyke propagation always requires that the magma pressure be higher than the least principal stress by some critical value representing the fracture toughness of the material. This also implies that intrusions will always open perpendicular to the least principal stress, meaning sills would always represent a reverse faulting stress regime ([Zoback, 2010](#)). This requirement poses an immediate problem because all the sills in this study, except the Karoo Basin, occur in extensional sedimentary basins.

[Rubin \(1995\)](#) and [Gonnermann and Taisne \(2015\)](#) review magma transport in dykes and show the general equation for thickness of a two dimensional dyke in an elastic isotropic medium. The equation relating fracture width to length is:

$$b(z) = \frac{(1 - \nu)\Delta P}{\mu} \sqrt{a^2 - z^2} \quad |z| < a \quad (3.23)$$

Where b is the half width of the crack, z is the vertical coordinate, ν is Poisson's ratio, ΔP is the difference in pressure between the magma pressure in the dyke and the least principal stress, μ is the shear modulus and a is half the crack length. This model will be applied to sills by considering b to be half the sill thickness, a to be the maximum radius of the sill and z to be the horizontal coordinate.

Using the sills database to test this model is challenging, as there are a limited number of cases where both the length and width of a sill can be measured. Here two methods are used to investigate the model. First, 3D seismic observations where both sill diameter and sills thickness are imaged are compared with the predicted maximum thicknesses from the above model. Secondly the analysis is repeated for all observations from 3D and 2D seismic, irrespective of distance from sill tip.

Figure 3.46 shows the results of modelling the maximum sill thickness of measured intrusions from 3D seismic with equation 3.23. In all but a few cases, the models underestimate the sill thickness considerably, even with the wide parameter ranges used in modelling from table 3.5.

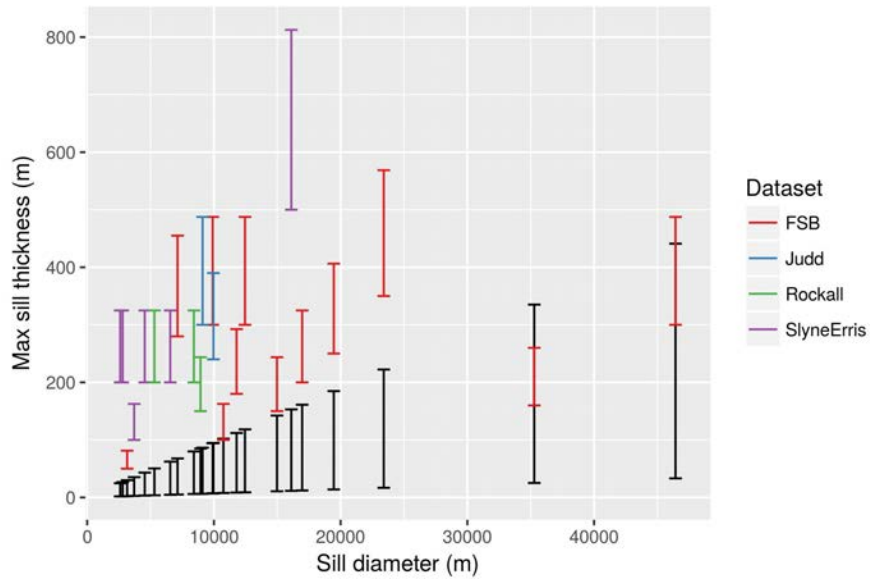


FIGURE 3.46: Results of modelling equation 3.23 using 3D seismic data, and parameters from table 3.5. Black bars are modelled values, while coloured bars are measured data points from the Faeroe-Shetland Basin (FSB), Judd Basin, Rockall Basin and Slyne-Erris Basins. Error bars on measured data points show variation due to depth conversion velocities. Depth conversion uses values in Smallwood and Maresh (2002).

The same modelling approach can be done using data from 2D seismic surveys as well. This would be expected to perform more poorly due to the increased uncertainty of where in the sill the 2D seismic line is intersecting, but this is offset by the extra information on model validity. The results of this is shown in figure 3.47.

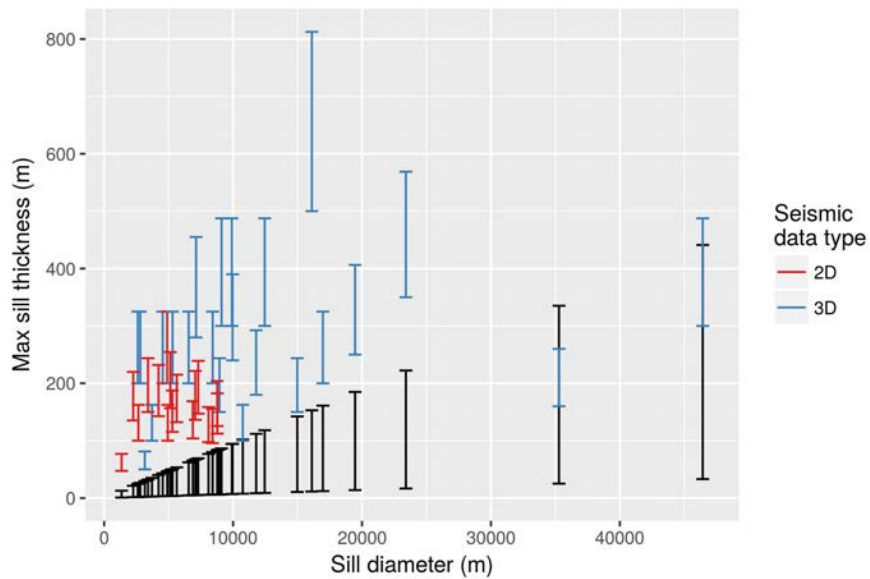


FIGURE 3.47: Modelling as in figure 3.46, but using both 2D and 3D seismic observations. Colours represent whether data is from a 3D seismic survey (blue) or 2D seismic survey (red).

From figures 3.46 and 3.47 it is apparent that the LEFM model is a poor fit to data for almost all data points, consistently underestimating the thickness of the measured intrusions. A likely explanation for this poor model — data fit is that the model assumes an infinite isotropic elastic host rock, and hence has no terms accounting for the depth to the free surface or non-elastic host rock behaviour. This may be appropriate for modelling sills deep within sedimentary basins. However, the sills measured on seismic data are naturally biased to the shallowest depths as the shallowest sills are the most clearly imaged on seismic data, hence it is possible that the data used to test the model violates too many of the model assumptions. Furthermore, as is often observed for shallow sills (Hansen and Cartwright, 2006a; Magee et al., 2014a) some sills in this dataset have forced folds above them, which is obviously a form of deformation at the free surface. The lack of a corresponding forced fold below these sills shows that the crack must be asymmetric, which also demonstrates non-isotropic host behaviour.

3.5.5 Elastic plate flexure models

The previous sections showed that models for a generic fluid filled crack in an infinite elastic solid give a poor fit to the dataset in this study. In this section a second type of model is investigated, which models accommodation of the fluid filled crack by way of flexure of an elastic plate overlying the sill.

3.5.5.1 Modelling sill profiles

Fitting an elastic plate flexure model to data requires more information than testing of the preceding models, as the emplacement depth and therefore the maximum possible thickness of the overlying elastic plate needs to be known. Therefore sill from the Rockall and Bight basins are used exclusively in this section, as good control was available to allow accurate depth conversion (section 3.2). The drawback of this dataset is that seventeen observations are from 2D seismic, while only two observations are from 3D seismic. The dataset may therefore cut a sill lobe rather than the main body of a sill, and thus give a seismic image which is not representative of the sill. Modelling in section 3.2.2 indicates that $\approx 75\%$ of the time the seismic line intersection should be fairly representative of the sill, however, a small number of measurements in the dataset may have been skewed by this effect.

The first model tested was that of Goulty and Schofield (2008). This model applies “simple flexure theory” to modelling sills and an overlying elastic plate to the roof of a sill complex. The equation the authors use is first found in Pollard (1973). The equation describing the shape of the sill is

$$w(r) = \frac{\Delta P}{64D}(R^2 - r^2)^2 \quad r \leq R \quad (3.24)$$

Where w is the width (thickness) of the sill, ΔP is the excess magma pressure, D is the flexural rigidity, R is the half length of the sill, and r is the distance from the mid point of the sill. The flexural rigidity D , is

$$D = \frac{Eh^3}{12(1 - \nu^2)} \quad (3.25)$$

Where E is the youngs modulus, ν is the poissons ratio, and h is the thickness of the overburden. Maximum sill thickness occurs at the centre, where $r = 0$, and $w_{max} = \frac{\Delta P}{64D}R^4$.

Figure 3.48 shows the results of comparing maximum measured sill thicknesses. This can be seen to be a good model in terms of the vast majority of measured sill thickness values falling within the range of modelled values. However, note that the y axis is a log scale, thus the large range of parameter values represents a considerable range in thickness estimates. Analysis of equations 3.24 and 3.25 show that h , the emplacement depth is a highly significant term, being raised to the third power. However, it is also one of the most easily measured terms on seismic data, which is a benefit of the model in this context. The main drawback in the use of this model is clearly the lack of knowledge of elastic parameters at depth and magma pressures — a feature likely to be common in many basins which require study of the intrusions they host.

To extend this analysis whole sill profiles can be modelled rather than just maximum thicknesses, and these models compared with measured sill profiles. To do this, horizons were interpreted on seismic data for the seafloor and the contemporaneous seafloor (interpreted as described in section 3.2). Data was extracted from each horizon by matching traces in the separate horizons, to end with datasets of seafloor time, forced fold time, top sill time and base sill time quadruplets. These measurements were then depth converted using the relationships in figure 3.3 to find the depth of emplacement below the contemporaneous seafloor. Decompaction was not carried out on this thickness of overburden above the sill. It is unknown how much of the overburden should behave flexurally verses plastically (unlithified sediments at the seafloor would not be expected to behave elastically) and hence this was seen as a source of confusion and further error, while adding it into the modelling would add little of importance versus the parameter uncertainties. h is therefore an upper bound on the thickness of the overburden that behaves elastically.

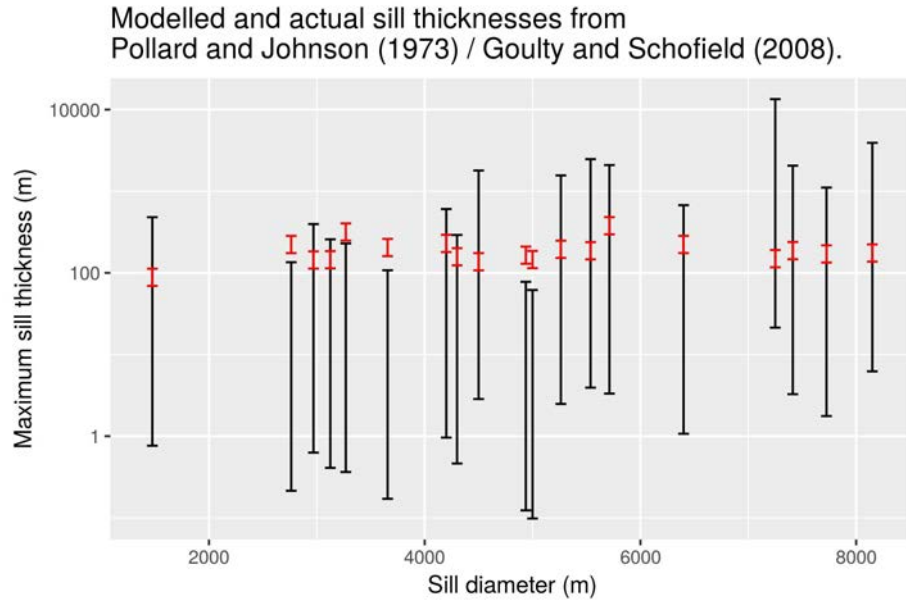


FIGURE 3.48: Model estimates versus seismic measurements for the maximum thickness of sills using the [Johnson and Pollard \(1973\)](#)’s model. Measurements are in red, with error bars reflecting uncertainty in sill V_p . Black bars are modelled values using parameters in table 3.5 and the emplacement depth and sill length measured from each sill to predict the maximum sill thickness.

Figures 3.49 and 3.50 show the results of comparing measured and modelled sill profiles, using equation 3.24. As can be seen, all modelled trends show similar overall trends to the measured profiles. A number of interesting observations can be made with regards to specific sills. In the Rockall Basin sills (Figure 3.49), sills b and g in figure 3.49 show evidence of being blunt ended sills in that they terminate abruptly and show deviation from the expected trends shown by the modelling towards their sill tips. Sill e shows a predicted thickness increase due to overburden which does correlate with an increase in thickness observed. This is a particularly interesting result, and suggests overburden thickness being a strong control on sill thickness in this case. Most profile models are a good fit for the data, with the exceptions of sills a and h, which are significantly thicker than predicted. These are two intrusions which would probably be called laccoliths rather than sills, and thus are possibly not sensible to model with equation 3.24. Other sill trends are more easily examined on dimensionless profiles, which will be covered next.

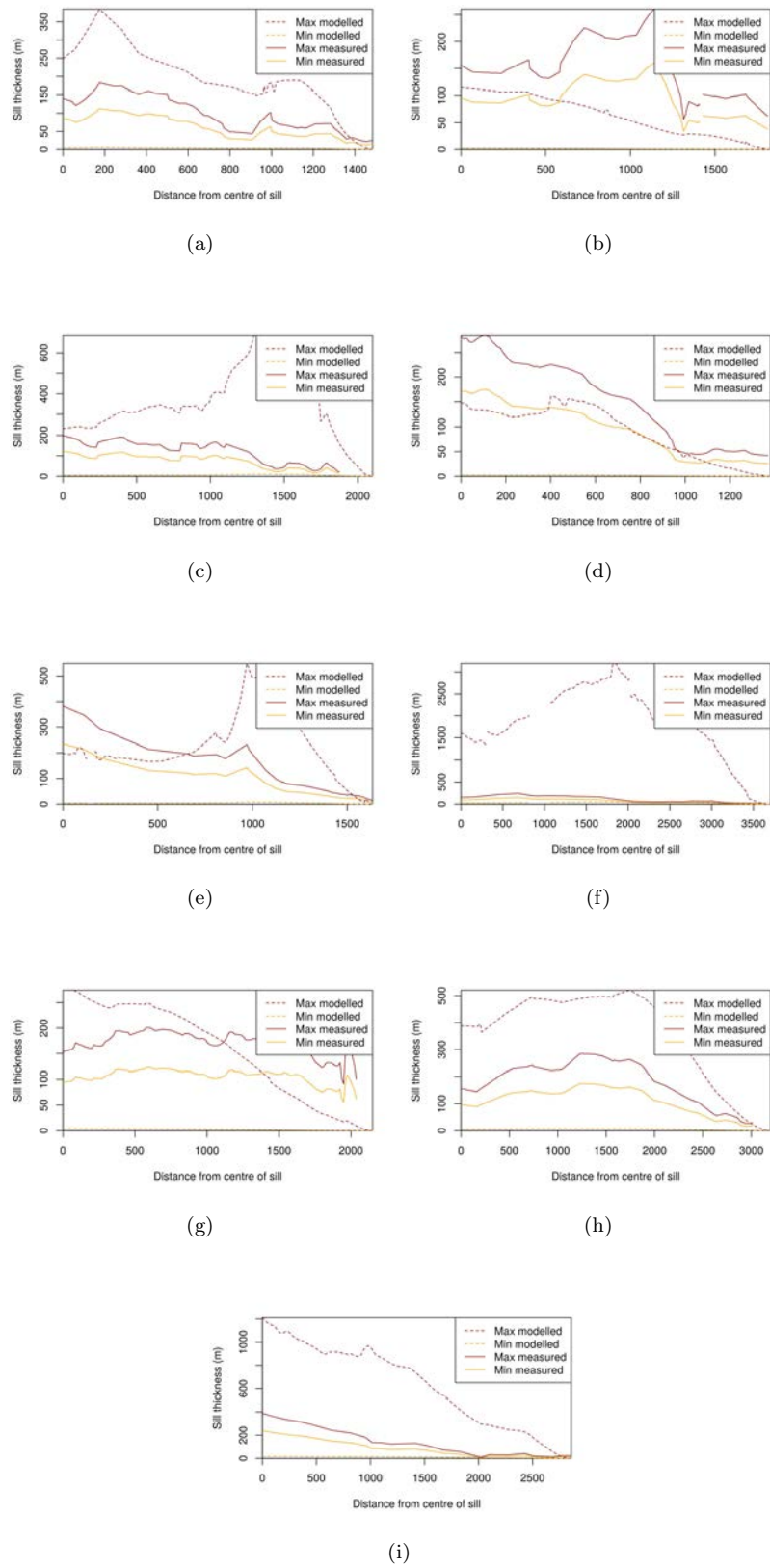


FIGURE 3.49: [Johnson and Pollard \(1973\)](#) model applied to sill profiles, using parameter ranges from table 3.5, for Rockall Trough data.

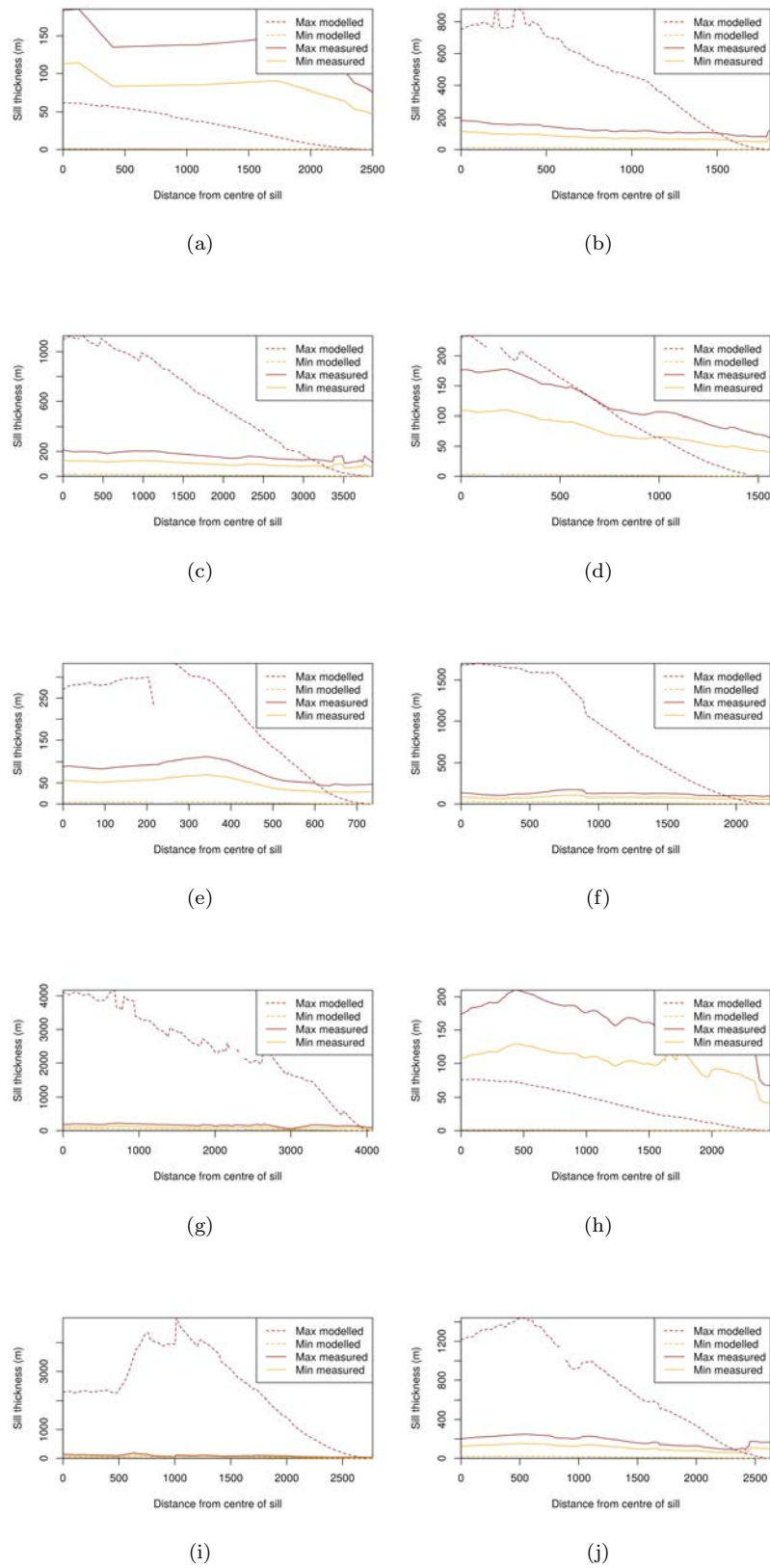


FIGURE 3.50: [Johnson and Pollard \(1973\)](#) model applied to sill profiles, using parameter ranges from table 3.5, for Bight Basin data.

3.5.5.2 Dimensionless sill profiles

Dimensionless sill profiles are profiles where the sill dimensions have been normalized to between zero and one, thus allowing profiles and shapes of the sills to be compared like for like. For the measured sill horizons, this is done by dividing by the maximum measured thickness to non-dimensionalize in the vertical direction, and by dividing by the sill diameter to non-dimensionalize in the horizontal dimension. The non-dimensionalized sill profiles can then be compared against dimensionless forms of the mathematical models. Dimensionless forms of the mathematical models are a more fundamental form of the governing equations, and terms need to be added to the governing equations to introduce dimensions.

The non-dimensionalized measured sills were compared with dimensionless forms of the [Johnson and Pollard \(1973\)](#), [Huppert \(1982\)](#), [Nye \(1952\)](#) and [Spence and Turcotte \(1985\)](#) models. Equation 3.26 shows the dimensionless version of the [Johnson and Pollard \(1973\)](#) model, which was introduced in section 3.5.5.1

$$y = (1 - x^2)^2 \quad (3.26)$$

where y is the thickness scaled by the maximum thickness and x is the distance from the middle of the sill scaled by the maximum radius, where zero is the middle of the sill and one is at the sill tip. Sill data was also compared with the [Huppert \(1982\)](#) model. The Huppert model describes the spreading of a viscous blob due to gravity, and was initially developed to model lava domes. The [Huppert \(1982\)](#) model forms an interesting case to model, as the previous section implied a strong control of overburden thickness, and the [Huppert \(1982\)](#) model can be used to simulate the end member of essentially no overburden thickness. Equation 3.27 shows the dimensionless version of the [Huppert \(1982\)](#) model

$$y = (1 - x^2)^{\frac{1}{3}} \quad (3.27)$$

The [Nye \(1952\)](#) model was developed to model valley glaciers as a form of plastic deformation under the force of gravity. Equation 3.28 shows the dimensionless version of the [Nye \(1952\)](#) model

$$y = \sqrt{1 - x} \quad (3.28)$$

Each of these dimensionless models are clearly similar, but different in the assumptions of the models. [Johnson and Pollard’s \(1973\)](#) model explicitly assumes LEFM and hence the magma sheet propagates through cracking the host rock. The models of [Huppert \(1982\)](#) and [Nye \(1952\)](#) imagine a blob of viscous fluid spreading under gravity. These models were designed to model gravity currents and glaciers respectively, but were applied to pancake-like magmatic domes on venus by [Mckenzie et al. \(1992\)](#). [Mckenzie et al. \(1992\)](#) found a good fit of the [Huppert \(1982\)](#) model to domes, and hence it is possible this model will be appropriate for some of the shallower sills.

Figure 3.51 shows the results of plotting the sills (coloured lines) against the first three models (Equations 3.26, 3.27 and 3.28). Note seismic images of these selected sills are found in chapter 4. The sills appear to fit the [Pollard \(1973\)](#) model best, looking to have similar profiles to the ideal profile. Two sills clearly stand out as having dissimilar profiles though. The brown profile of line WOOFDWO060 shows a sill which appears to have an especially blunt termination and little decrease in thickness as it approaches the edge of the sill, seeming to fit the Huppert model best. In the region around 0.2 to 0.4 units from the center of the sill, almost half of the sills seem to fit better with the viscous blob models of [Huppert \(1982\)](#) and [Nye \(1952\)](#). However, note that this result could simply be due to the small differences in models at the point. Possibly more important is the behaviour towards the end of the sill. Nearer the end of the sill, the profiles seemingly fit the [Johnson and Pollard \(1973\)](#) model best. There is undoubtedly scatter in this sill profile data. This scatter may arise from the 2D nature of much of this seismic data, which increases the chance that the observed sill could be the seismic line cutting a lobe or an irregular part of the sill. There is no way of knowing if this is the cause of the scatter without further seismic data. This explanation would fit with some of the more irregular and lobate morphologies found by [Hansen and Cartwright \(2006b\)](#) and [Thomson \(2004\)](#), and may explain some of the deviation from the ideal profiles. This a topical result in the field of sill emplacement — recently some authors have been advocating a “viscous indenter” mechanism (e.g. [Scheibert et al., 2017](#); [Spacapan et al., 2017](#)). The results here would argue against most sills on this plot having a blunt ended termination and rather fit with a tapered profile as expected for a fluid filled crack, thus arguing against the recent work of [Scheibert et al. \(2017\)](#) and [Spacapan et al. \(2017\)](#).

The same approach can be used to examine the model of [Spence and Turcotte \(1985\)](#). [Spence and Turcotte’s \(1985\)](#) model was developed to also solve the problem of magma flow within the crack as well as the fracture problem, and to relate this to rates of magma injection and sizes of end member magma filled cracks, and as such is related to [Johnson and Pollard’s \(1973\)](#) and [Lister’s \(1990\)](#) models. This model also assumes a 2D crack in a uniform elastic solid. Equation 3.29 shows [Spence and Turcotte’s \(1985\)](#) dimensionless model relating H (sill thickness) to l (distance from the sill centre):

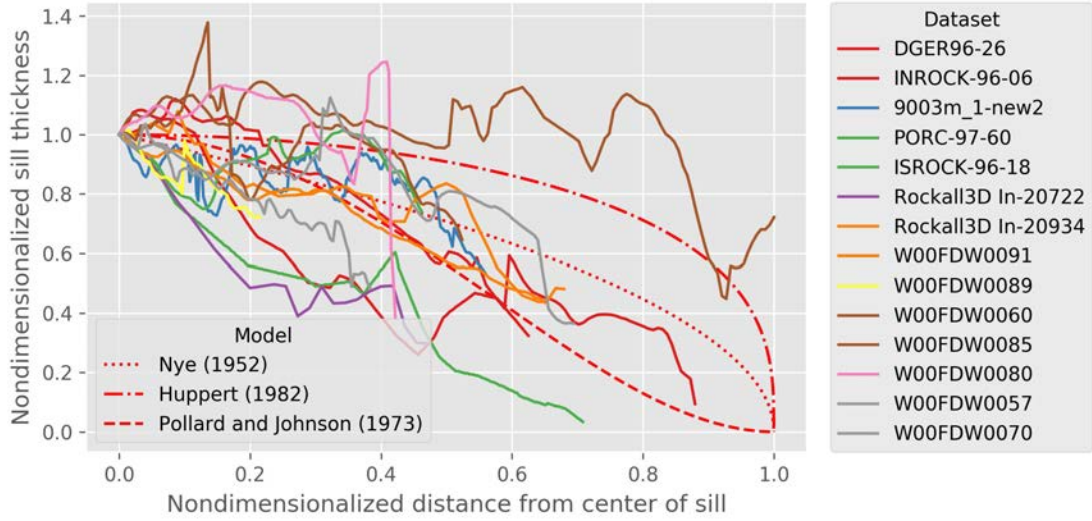


FIGURE 3.51: Non-dimensionalized measured sill profiles, plotted against equation 3.26 (the dimensionless form of the Johnson and Pollard (1973) model).

$$H(l) = A_0(1 - l^2)^{(1/2)} + \frac{Bl^2}{4} \ln \frac{1 - (1 - l^2)^{(1/2)}}{1 + (1 - l^2)^{(1/2)}} \quad (3.29)$$

Where H is the dimensionless sill thickness, l is dimensionless distance between the sill centre and the sill edge, and A_0 and B are dimensionless variables related by y (figure 3.52)

$$y = \left(\frac{4}{3\pi} \right)^{(1/4)} \frac{6A_0^3 - 1}{(1 + 12A_0^3)^{(3/4)}} \quad (3.30)$$

$$B = \frac{6A_0}{1 + 12A_0^3} \quad (3.31)$$

Equation 3.30 is difficult to express in terms of y , so a binary search algorithm was used to find values of A_0 for a specified y . B can then be found from equation 3.31

Figure 3.53 shows the correspondence between the model and the measured profiles for a variety of different y values. At values of y close to 0, the model is very similar to the Johnson and Pollard (1973) model. At higher values of y the modelled sill profiles become more blunt ended. As can be seen, the extra models for values of y larger than 0, fit the data increasingly poorly. However, at values of y around 0.25 to 0.5 the sills profiles sill have much overlap with the model. This could be scatter in the data, or this could be showing an influence of viscosity on the emplacing sills. Again, the results here would argue against most of these sills having a blunt ended termination and rather fit

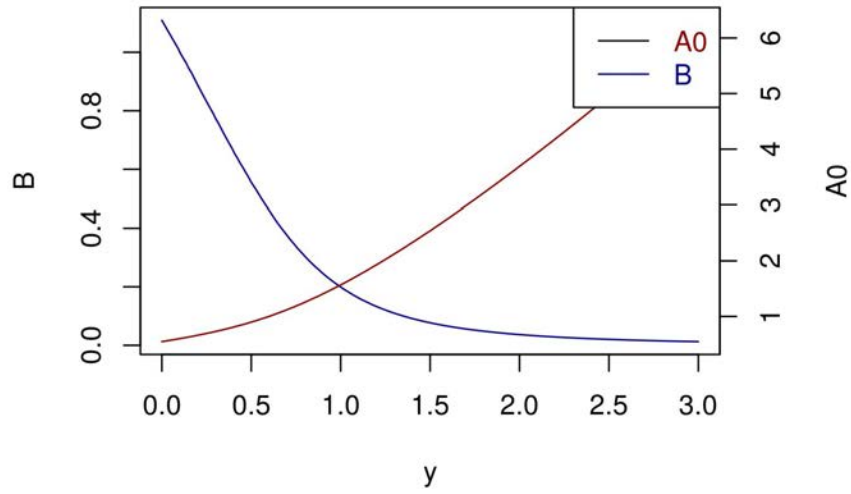


FIGURE 3.52: Relationship between A_0 , B and y , see equations 3.30 and 3.31

with a tapered profile as expected for a fluid filled crack, arguing against the recent work of Scheibert et al. (2017) and Spacapan et al. (2017).

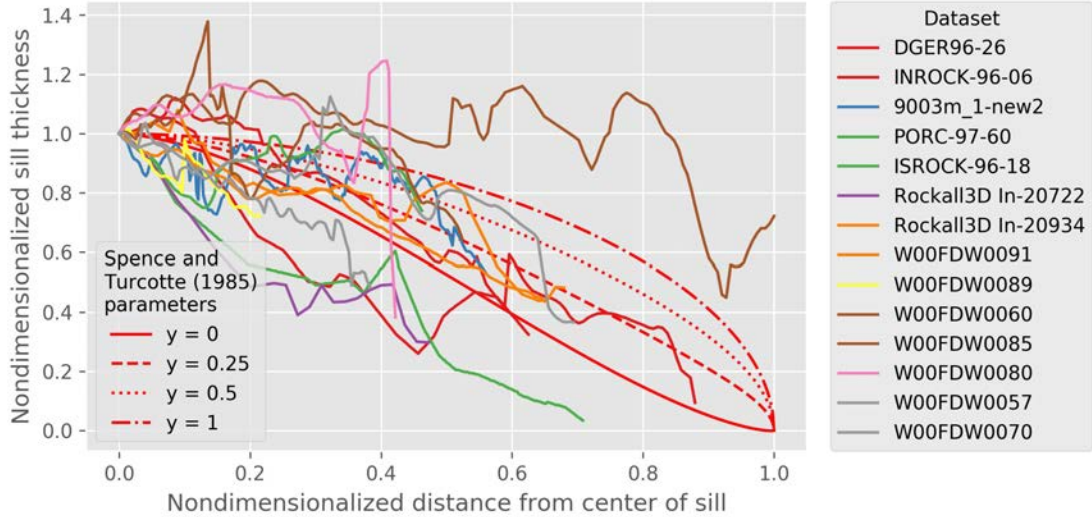


FIGURE 3.53: The dimensionless model of Spence and Turcotte (1985), plotted against non-dimensionalized sill profiles

3.6 Summary

This chapter started with a discussion of sill shape definitions used throughout the section and of the key measurements that would be explored in this chapter. The effect

of horizontal and vertical resolution on sill measurements was then outlined and modeled, and uncertainties were found to be $<1\%$ for horizontal resolution and variable for vertical resolution. The effect on sill measurements of 2D versus 3D seismic data was modelled, coming to the conclusion that a sample average sill measurement on 2D seismic data would, on average, represent 0.75 – 0.9 of the true measurement. Sill shapes were then studied in the different study areas, and were found to vary widely between basins. Sill diameters were measured, and found to have significant variation between basins. Variation was not found to be significant in most cases between sill shapes. There was no evidence of the sill diameter data being power law or fractal. Sill thickness data is very difficult to obtain, due to different sampling biases in the different data types used in this study. Furthermore, only a relatively small amount of sill thickness data was available due to seismic resolution problems. Despite this, comparison between three basins was attempted, and no statistically significant differences between the thickness samples was observed. In the cases where observations were available for both sill diameter and for sill thickness, regression analysis was performed, yielding models allowing prediction of sill thickness from diameter observations. Similar to sill diameter, there was no evidence of power law behaviour in the sill thickness data. Sill transgressive height measurements were then analysed. Sill transgressive height is found to vary widely between basins. Sill emplacement depth is also found to vary widely between basins, however, it is noted that with increasing depth seismic imaging worsens, and underneath sills seismic imaging is severely degraded. This may lead to apparent effects in sill emplacement depth that are not real; this cannot be answered with this dataset and is thus left as a question for future research. This missing sills test is then introduced to allow estimation of the true number of sills within the bounds of a 2D seismic survey. Relationships are found between distance from the centre of the Iceland mantle plume head, the average water depth within the area of the seismic survey, and the sill area-density. This is suggested to be due to melt generation — the Iceland mantle plume represents a hot spot with increased melt generation, and deep water is a proxy for thinned continental crust which should allow decompression melting should hot mantle decompress as it rises into the thin spot. Sill intrusion models are then tested using the database of sill measurements examined throughout the chapter. First, the order of magnitude estimates of [Lister \(1990\)](#) and [Lister and Kerr \(1991\)](#) are tested, and are found to be a poor fit to the data, consistently estimating sills that are too thin. This is suggested to be due to the sills measured in this chapter being predominantly shallowly emplaced and thus the key assumptions of [Lister's \(1990\)](#) model — that the host rock behaves purely elastically and isotropically — is violated due to effects at the free surface. Following this, the classic LEFM model (e.g. [Rubin, 1995](#)) is tested, and is also found to be a poor fit to the data. The model of [Johnson and Pollard \(1973\)](#) is next tested, which is different to the preceding models as it incorporates an overlying elastic plate and hence while the

host rock still behaves elastically, it is no longer assumed to be isotropic. The [Johnson and Pollard \(1973\)](#) model is found to be a significantly better fit to the data. Note that all the modelling and discussion on this has focussed around large scale geometries and not around local plastic effects, for example in the tip zone or magma fingers ([Johnson and Pollard, 1973](#); [Pollard, 1973](#); [Pollard et al., 1975](#); [Schofield et al., 2010](#)). This is a deliberate omission as the plastic tip zone processes are likely operating at the centimetre to metre scale at the tip of the intrusion, which is below seismic tuning thickness and therefore the dataset is not fit for purpose for analysis of tip zone processes.

Chapter 4

Forced folds and the amplitude / thickness discrepancy

4.1 Introduction

Forced folds are structures which form above sills during sill emplacement (Figure 4.1). Early work by [Hansen and Cartwright \(2006a\)](#) pointed out that the amplitude of a forced fold should be equal to the thickness of its underlying sill if no other processes are at work. Subsequent work observed that forced fold amplitudes are often demonstrably less than the thickness of the underlying sill (e.g. [Jackson et al., 2013](#); [Magee et al., 2013a](#)). In this chapter this discrepancy is investigated using high quality 2D and 3D seismic data, and is termed the “forced fold amplitude / thickness discrepancy”.

Both lateral propagation and vertical inflation of a sill occur during sill emplacement, to accommodate the magma volume being forced into the crust (e.g. [Thomson, 2007](#)). To accommodate the inflating sill, space must be created. Space for this expanding magma volume could occur by three mechanisms: displacement upward or downward of the surrounding host rock; elastic or plastic deformation of the host rock; or assimilation / stoping / melting of the host rock. Evidence from seismic data points to the majority of accommodation in the shallow sedimentary section being by host rock deformation ([Eide et al., 2017b](#); [Hansen and Cartwright, 2006a](#); [Wilson et al., 2016b](#)). At some depth, sills are no longer emplaced via deformation of the overburden and other processes must become dominant. This can be observed on seismic data from examples of thick sills deep in sedimentary basins without a clear forced fold signature above them. However, the transition in behaviour from deformation at the free surface to other mechanisms is not the focus of this chapter. In this chapter we focus on shallow intrusions which

display a forced fold, and specifically on examples where the forced fold’s amplitude does not appear to match the thickness of its underlying sill.

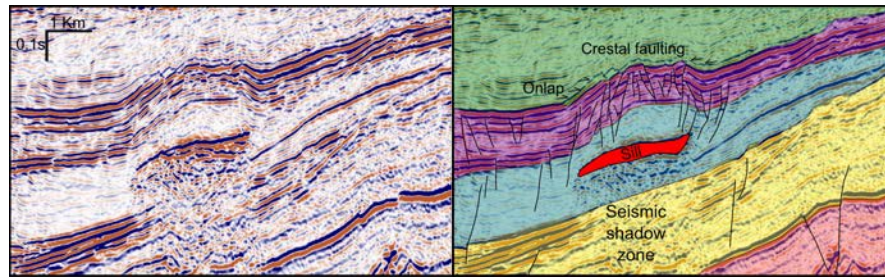


FIGURE 4.1: An example of a sill and it’s overlying forced fold from the DGSRT96 survey

Forced folds are of interest to the scientific community for three main reasons. First, they could represent a petroleum trap, commonly forming four way dip closed structures (e.g. [Hansen and Cartwright, 2006a](#)). If multiple sills are emplaced close to the seafloor, the folds can interfere to form larger composite forced folds ([Magee et al., 2014a](#)). Additionally, if several forced folds are close together spatially, depressions at the seafloor in between several forced folds can form accommodation space for density current sedimentation such as turbidites (such as in the Faeroe-Shetland Basin, *sensu lato* [Egbeni et al., 2014a](#); [Smallwood and Maresh, 2002](#)). Secondly, forced folds can be used to generate data on the thickness of underlying sills when those sills are below seismic resolution ([Hansen and Cartwright, 2006a](#)). This is important as sill thickness is required to model a sill’s effect on thermal maturation of intruded source rock sequences (e.g [Fjeldskaar et al., 2008](#)), on thermal aureole size and effect on reservoir sequences ([Aarnes et al., 2010](#); [Annen, 2011](#); [Raymond and Murchison, 1991](#)), on permeability and its importance for fluid migration ([Rateau et al., 2013](#)) and for palaeoclimate modelling ([Aarnes et al., 2010](#); [Svensen et al., 2004](#)). Thirdly, sills represent ground deformation in response to movement of magma in the shallow subsurface, which commonly precedes volcanic eruptions (e.g. [Sigmundsson et al., 2010](#)) and thus understanding such behaviour will likely be important in the future for inversion of ground deformation for hazard forecasting ([Magee et al., 2013a](#)).

As forced folds are formed by hydraulic lifting of the overburden by the sill ([Gilbert, 1877](#)), it should be expected that the amplitude of the fold would equal the thickness of the sill if no other processes were at work. [Hansen and Cartwright \(2006a\)](#) analysed profiles across sills and forced folds, and were the first to highlight a disparity between the thickness of some sills and the amplitude of their forced folds. They attributed this disparity to anomalous cementation, interference of the folds from other nearby folds, seismic imaging problems or erosion from fold crests. At odds with this, they also claimed a strong 1:1 relationship existed between fold amplitude and sill thickness, despite their

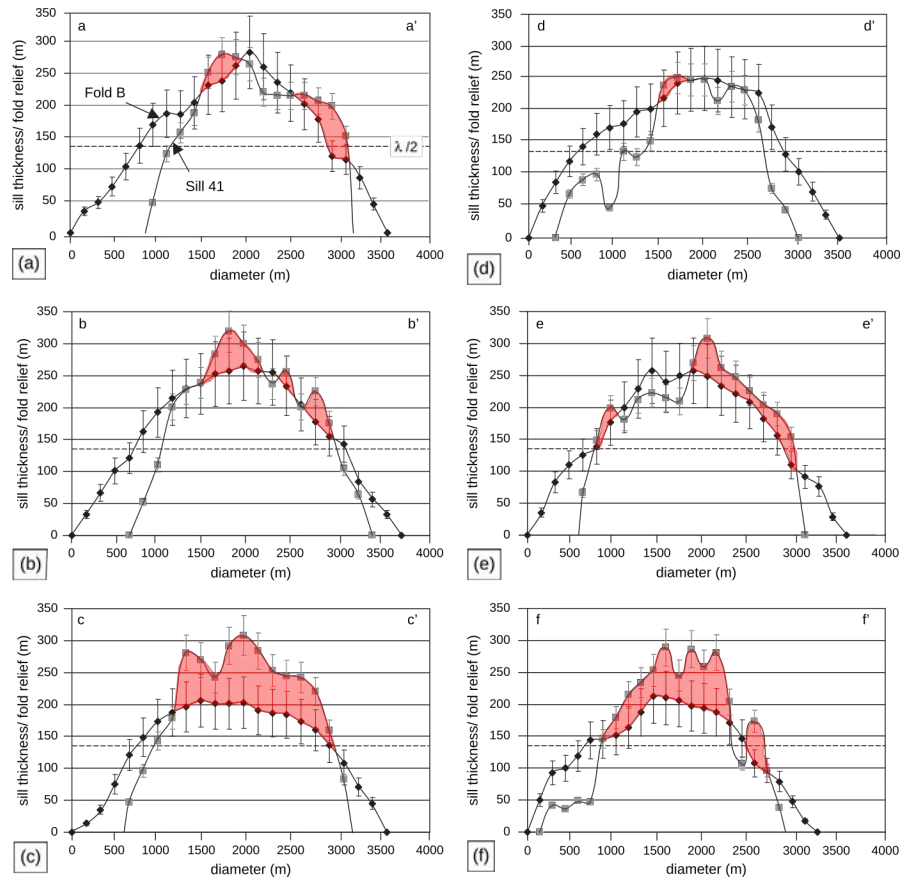


FIGURE 4.2: Reproduction of Hansen’s (2006) figure 5, with regions where there is a discrepancy between the forced fold and the sill thickness highlighted in red. Modified after Hansen and Cartwright (2006a).

own figures arguing against such a relationship. Indeed re-analysis of the data used in Hansen and Cartwright (2006a) shows that the locations where the authors find a 1:1 relationship between sill thickness and fold amplitude (i.e. Hansen and Cartwright, 2006a, figure 5a and b) are not necessarily representative of the whole structure: 1:1 relationship is found in some places but is not found everywhere. In the middle of the structure the discrepancy is most clear (i.e. Hansen and Cartwright, 2006a, figure 5e and f) (figure 4.2). Other studies which have focused on sills and forced folds have also found a clear discrepancy between the amplitude of the forced folds and the thickness of the sill forming it (figure 4.3). Magee et al. (2013a) found a 42% discrepancy, and attributed the discrepancy to complex sill-host rock interactions and plastic deformation of the host rock. Similarly, Jackson et al. (2013) found a range of discrepancies up to 80%.

To investigate the forced fold amplitude / thickness discrepancy, fourteen exceptionally well imaged intrusions and their overlying forced folds were analysed. Crucially, these sills are examples where both the top and base of the sill are imaged. Backstripping techniques are used to correct for burial and compaction of the sediments comprising

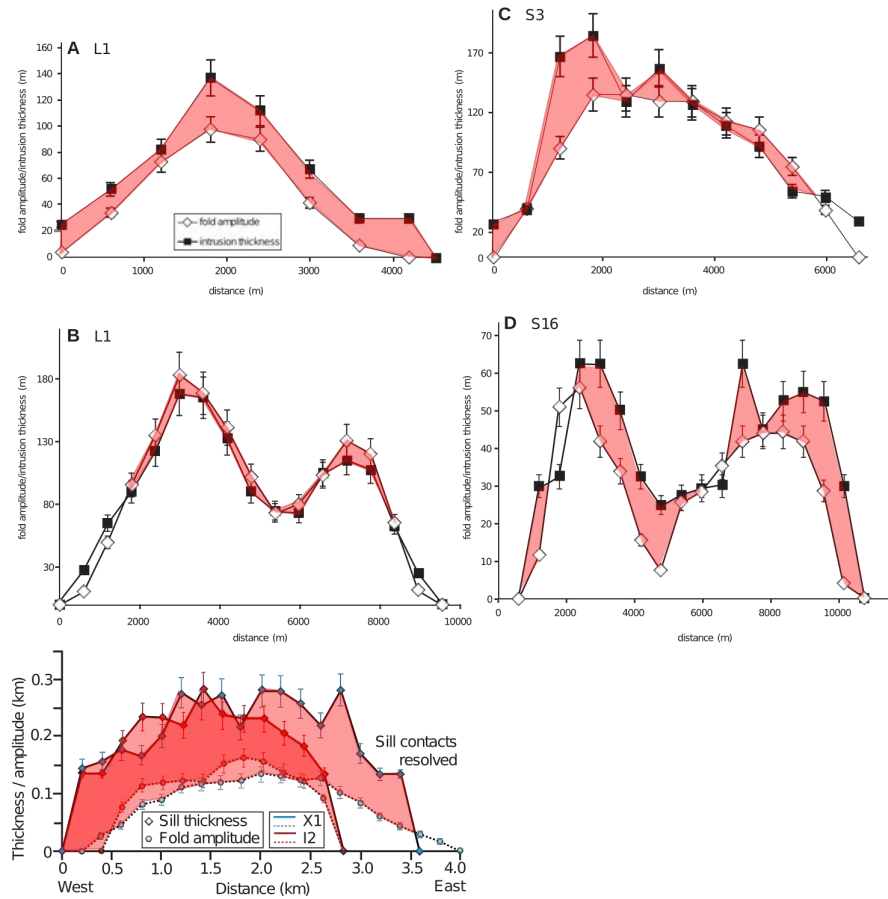


FIGURE 4.3: Reproduction of [Jackson et al.'s \(2013\)](#) figure 7 (upper four panels) and [Magee et al.'s \(2013a\)](#) figure 3 (bottom panel), with regions where there is a discrepancy between the forced fold and the sill thickness highlighted in red. Modified after [Jackson et al. \(2013\)](#) and [Magee et al. \(2013a\)](#).

the fold. A range of compaction parameters are modelled to quantify sensitivity to the backstripping parameters. This analysis finds that the majority of the discrepancy between thickness of sills and amplitude of the forced fold is due to differential compaction between the igneous sill and the sedimentary forced fold after emplacement. This means that other mechanisms are not necessary for volume loss by more exotic mechanisms (i.e. fluid expulsion, anomalous cementation, inaccurate depth conversion, or unobserved erosion/mass wasting ([Hansen and Cartwright, 2006a](#))) to account for the first order fold amplitude, thus having important implications for hydrocarbon exploration in such structures, and for models of ground deformation in present day volcanic provinces.

4.2 The amplitude/thickness discrepancy in the Rockall and Bight Basins

4.2.1 Data and methods

To study the forced fold amplitude/sill thickness discrepancy, three different seismic data sets are used: the Rockall 3D survey from the Northeast Rockall Trough (e.g. [Hansen and Cartwright, 2006a](#); [Thomson, 2004](#)), the 2D DGSRT96 survey from the north of the Irish sector of the Rockall Trough (kindly provided by Spectrum Geophysical), and the Bight Basin dataset (see Chapter 2 for descriptions of datasets). Sills were identified based on the criteria in section 3.2. Forced folds were identified based on being directly above a sill, displaying stratigraphic onlap onto the flanks of the structure, and having no other obvious causes for the folding.

Once sill and forced fold pairs were identified the seafloor, forced fold, and top and base horizons of the sill were interpreted on seismic data, and exported as text files for analysis. The exported seismic horizons were then processed to extract four different measurements taken at each seismic shotpoint (Figure 4.4). The four measurements taken at each horizontal position are: A, the two way travel time (TWT) from the sea surface to the top of the fold; B, the TWT from the sea surface to the horizontal baseline defined above; C, the TWT from the sea surface to the top of the sill and D, the TWT from the sea surface to the base of the sill. These measurements can be used directly to investigate the kinematics of forced fold formation in flat lying strata, but would need further correction if strata was dipping. The sill and forced fold pairs analysed in this study were all found in flat lying or gently dipping strata ($<5^\circ$), so no further corrections were made.

Measurements A to D were then depth converted. Good velocity control was available for the seismic surveys, and depth conversion was done using the methods in section 3.2. Seismic velocities of 4500 ms^{-1} to 6500 ms^{-1} were used to depth convert the sills, after [Smallwood and Maresh \(2002\)](#). Following depth conversion, fold amplitudes (measurement B minus A) were backstripped to find the original thickness before burial and compaction ([Sclater and Christie, 1980](#); [Smallwood, 2009](#)). The decompaction procedure is standard; a detailed description of the decompaction process can be found in section 3.3.5. In the decompaction calculation, the intrusive sill is considered to be incompressible and to not compact. Intrusive basalts typically have very low porosity of 0 - 5% ([Hyndman, 1979](#)), which will result in either no compaction, or a very low rate of compaction, thus the assumption of basalt being incompressible is justified. Estimates of initial porosity and compaction coefficient were not available, and so a range of values

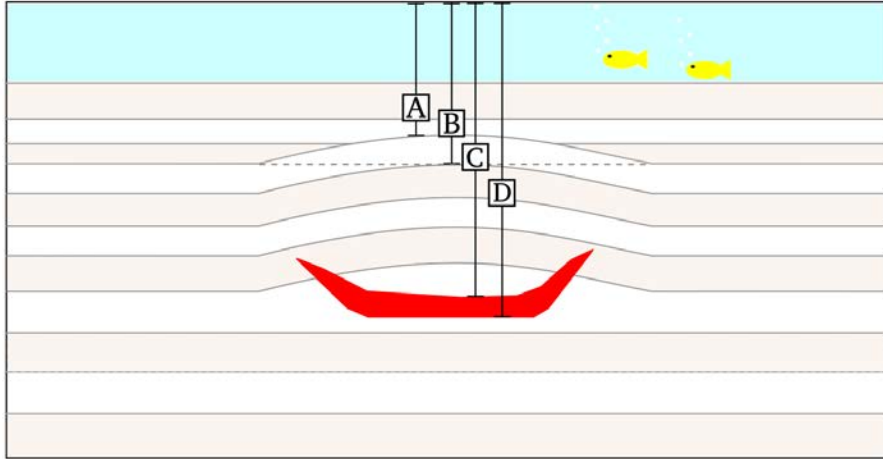
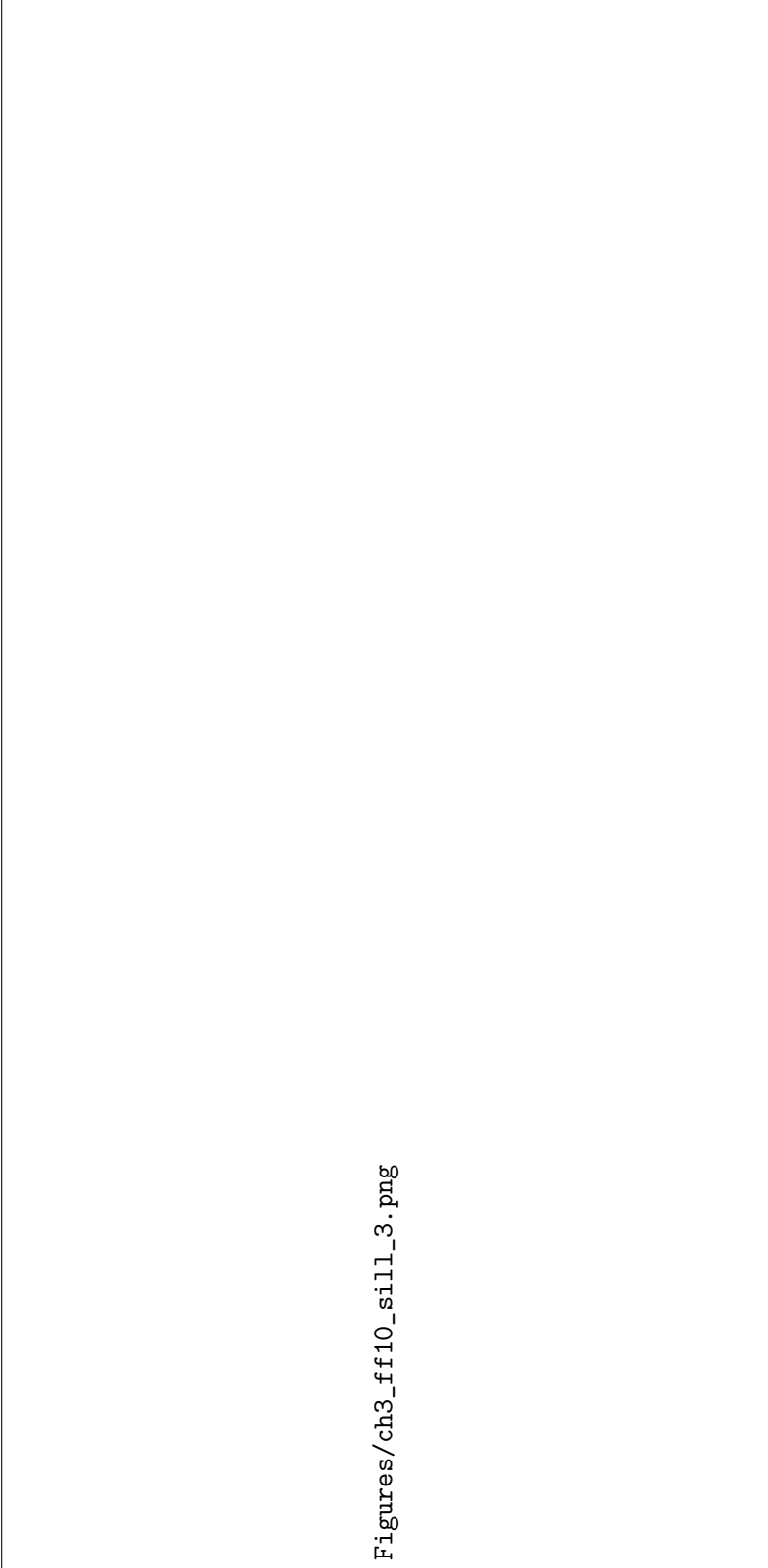


FIGURE 4.4: Schematic cartoon of measurements taken on sills and forced folds. Note arrows are offset for visual clarity, but in reality all measurements are taken at the same horizontal position, such that the shafts of the arrows would overlap.

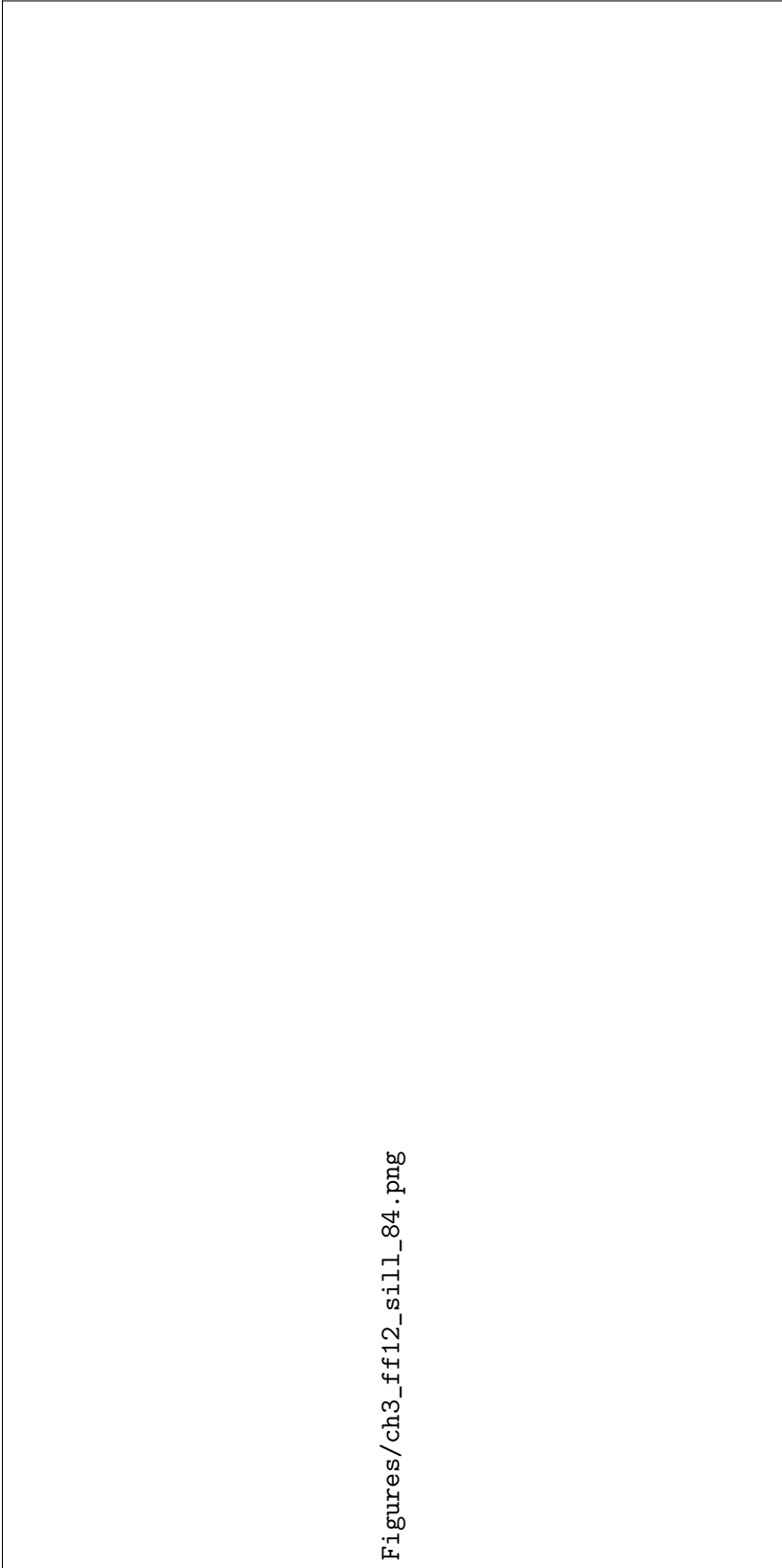
was similarly modelled, after [Sclater and Christie \(1980\)](#). Porosity ϕ was modelled to range from 0.3 to 0.56, and compaction length scale λ from 2.56 to 3.7. Lastly the folds were detrended. This was required as some of the folds were emplaced on a gently dipping regional palaeoseafloor, so this extra dip must be removed by fitting and subtracting a linear baseline to represent the deviation of the fold from the background trend.

Figures 4.5 to 4.18 show the vertical seismic profiles used for subsequent calculations. Sills were interpreted based on the criteria in section 3.2; namely a (1) high amplitude, (2) positive polarity reflection forming the top of the sill, and (3) a corresponding negative reflection forming the base of the sill. The reflection is (4) laterally discontinuous, and (5) commonly locally transgresses stratigraphy (e.g. [Smallwood and Maresh, 2002](#)).



Figures/ch3_ff10_sill_3.png

FIGURE 4.5: Seismic line DGER96-26, used in forced fold amplitude / sill thickness modelling. Yellow is top forced fold. Red is top sill. Orange is base sill. Sill is identified by (1) high amplitude, (2) positive polarity reflection forming the top of the sill, and (3) a corresponding negative reflection forming the base of the sill. The reflection is (4) laterally discontinuous, and (5) locally transgresses stratigraphy, especially to the left of the figure. The base reflection is difficult to follow, but is observed as the negative reflection with a different dip to the surrounding stratigraphy. [Redacted]



Figures/ch3_ff12_sill_84.png

FIGURE 4.6: Seismic line INROCK-96-06, used in forced fold amplitude / sill thickness modelling. Yellow is top forced fold. Red is top sill. Orange is base sill. Sill is identified by (1) high amplitude, (2) positive polarity reflection forming the top of the sill, and (3) a corresponding negative reflection forming the base of the sill. The reflection is (4) laterally discontinuous, and (5) locally transgresses stratigraphy. The base reflection is easy to observe as the only high amplitude negative polarity reflection under the sill. Lower frequency "ringing" reverberations are seen for up to three seismic loops under the sill, corresponding to inter-bed multiples generated within the sill. [Redacted]

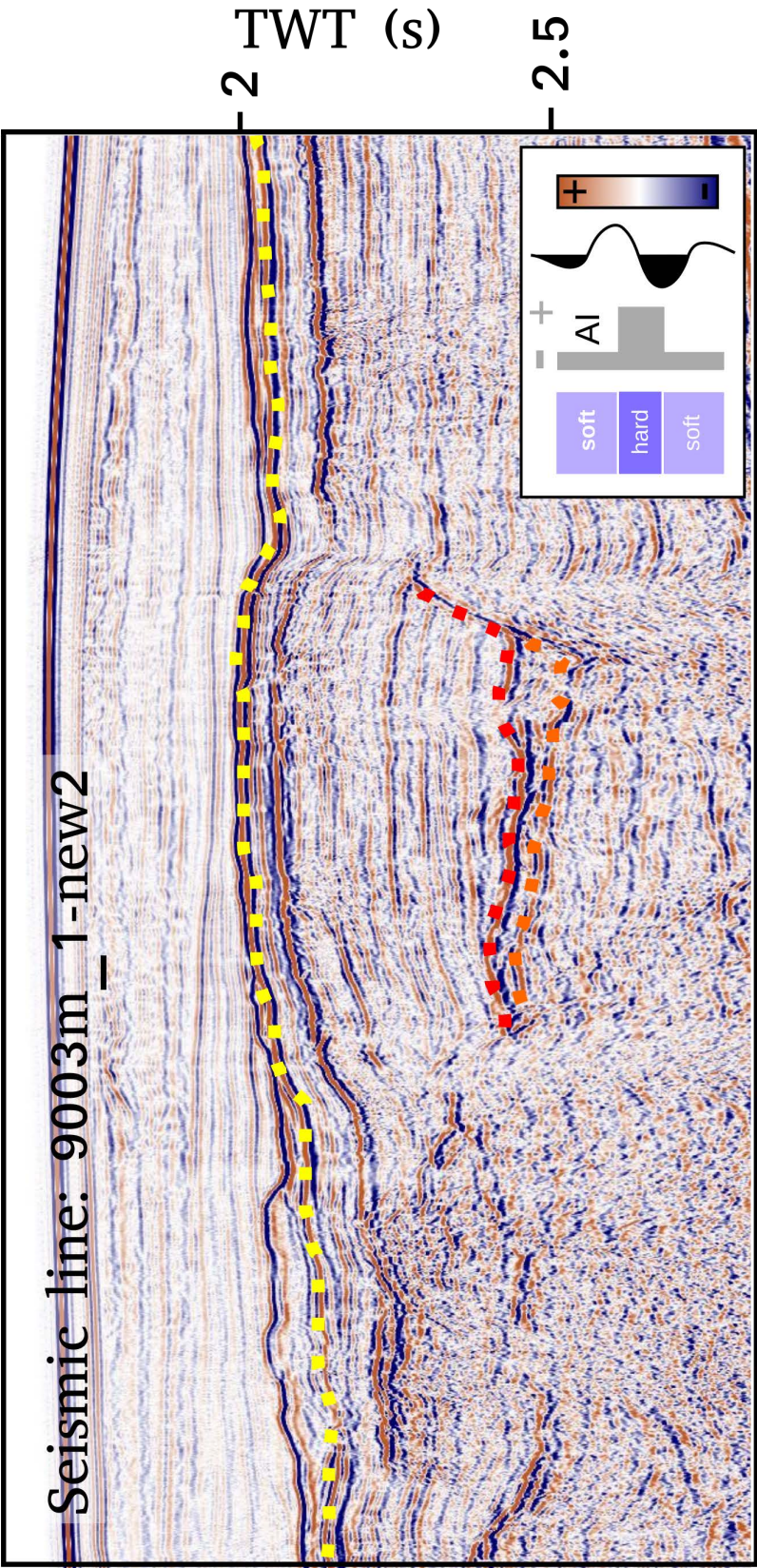
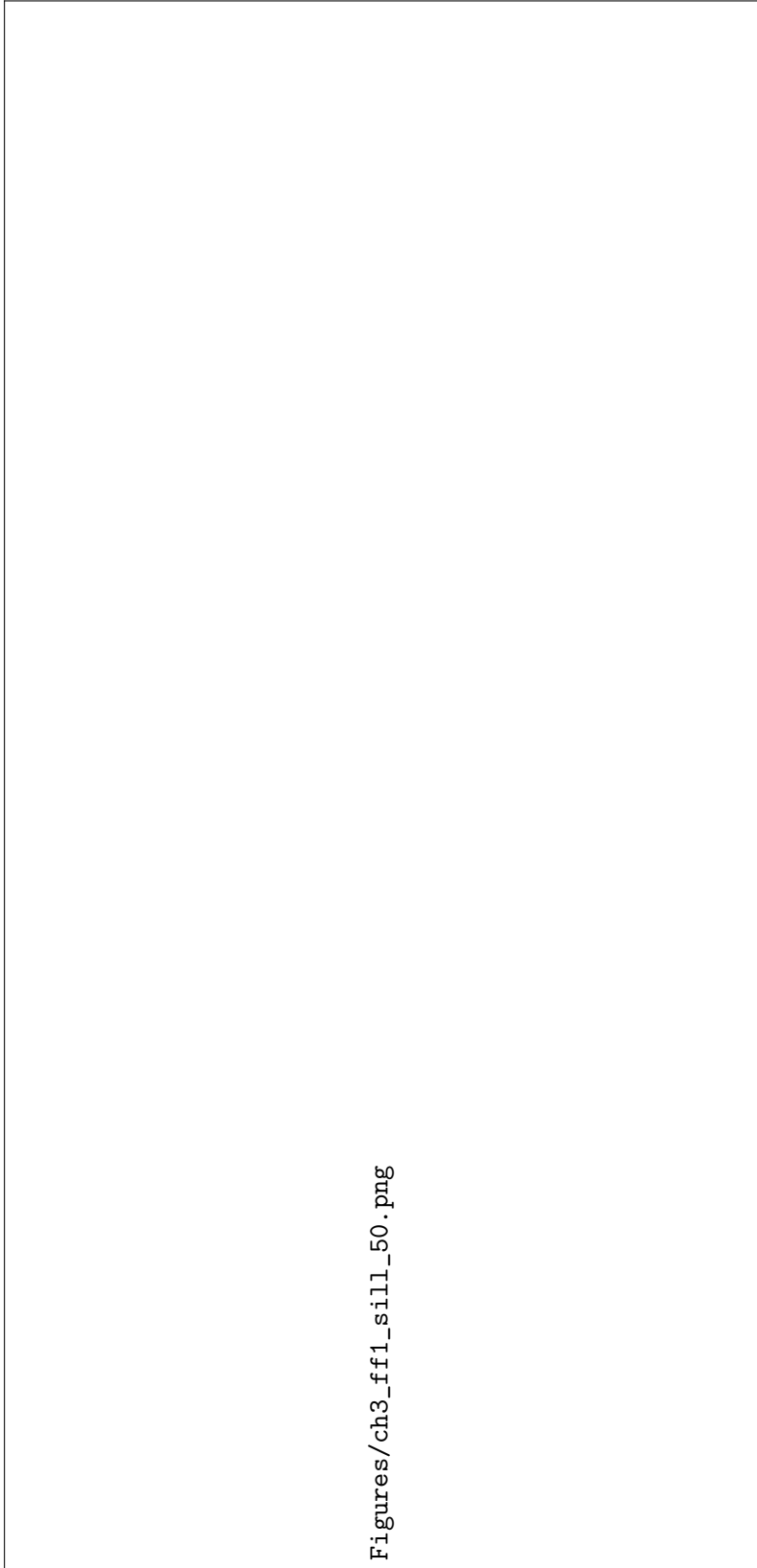
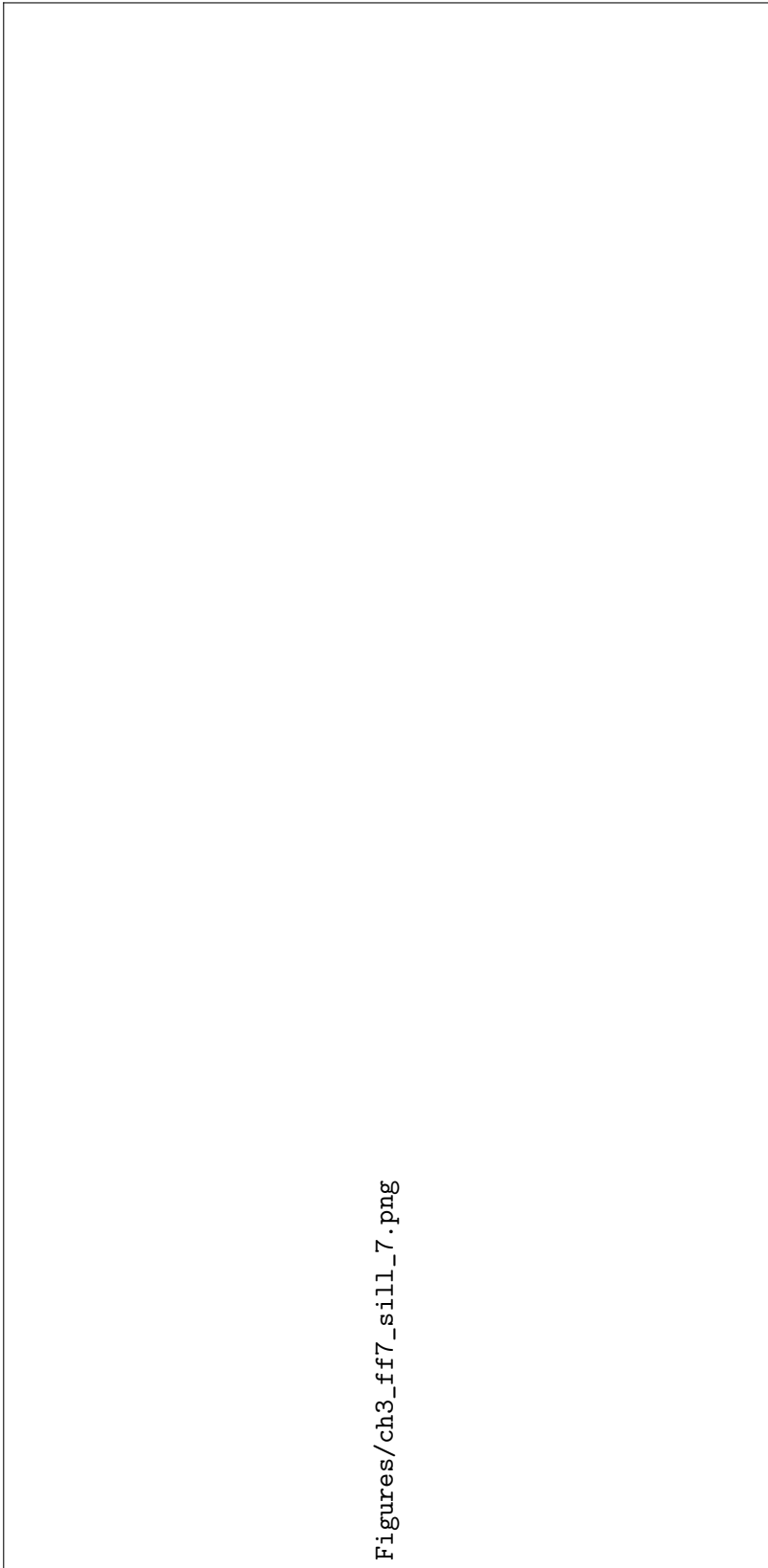


FIGURE 4.7: Seismic line 9003m_1-new2, used in forced fold amplitude / sill thickness modelling. Yellow is top forced fold. Red is top sill. Orange is base sill. Sill is identified by (1) high amplitude, (2) positive polarity reflection forming the top of the sill, and (3) a corresponding negative reflection forming the base of the sill. The reflection is (4) laterally discontinuous, and (5) locally transgresses stratigraphy. The base reflection is easy to follow, as the only continuous negative polarity reflection with a different dip to the surrounding stratigraphy. Seismic "ringing" is also observed under the sill, but is of lower amplitude and frequency making it easy to distinguish from the base reflection.



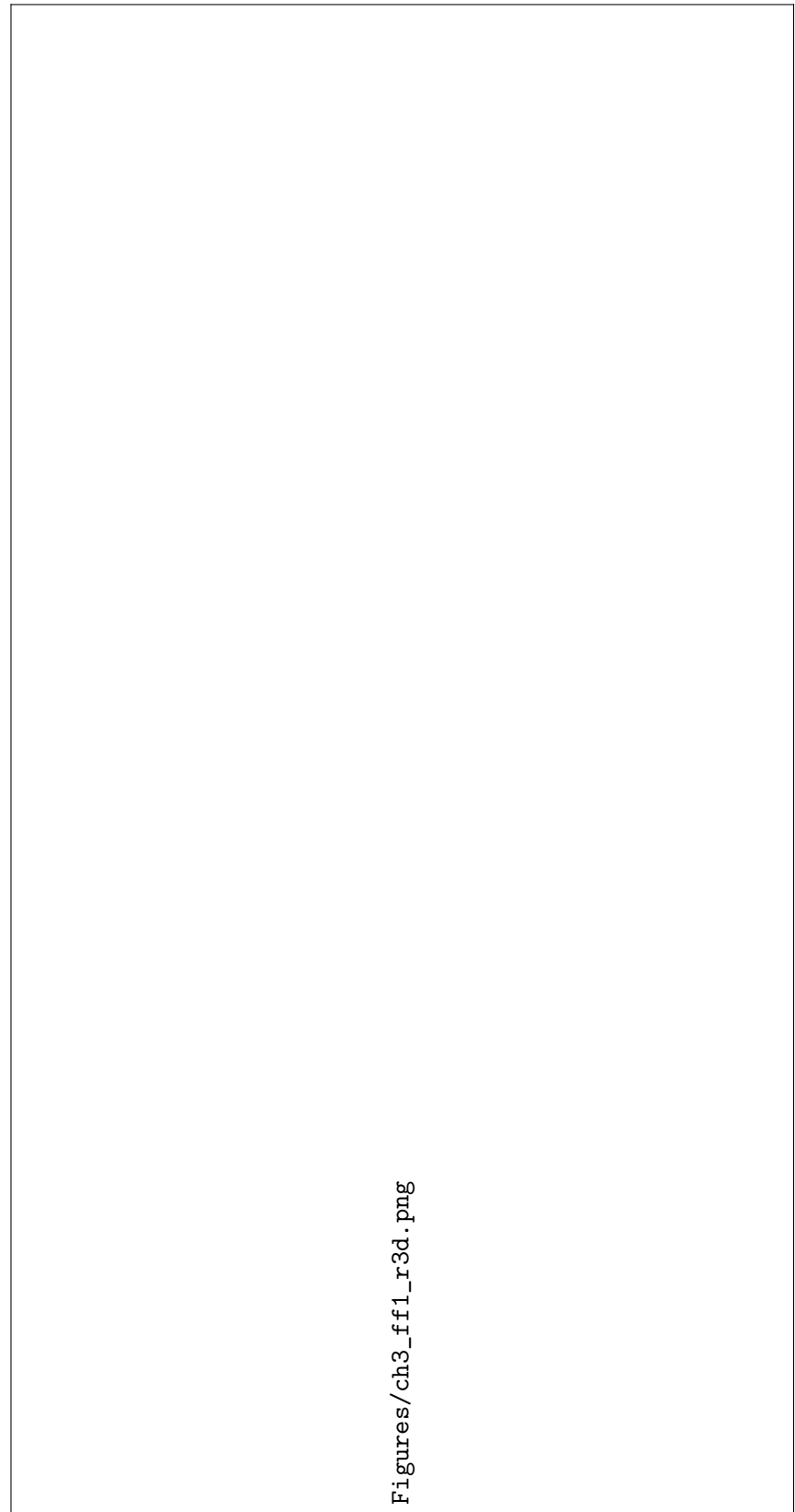
Figures/ch3_ff1_sill_50.png

FIGURE 4.8: Seismic line PORC-97-06, used in forced fold amplitude / sill thickness modelling. Yellow is top forced fold. Red is top sill. Orange is base sill. Sill is identified by (1) high amplitude, (2) positive polarity reflection forming the top of the sill, and (3) a corresponding negative reflection forming the base of the sill. The reflection is (4) laterally discontinuous, and (5) locally transgresses stratigraphy. The base reflection is easy to follow due to its differing dip to the surrounding stratigraphy, especially on the right hand side of the image. Seismic "ringing" is also observed under the sill, but is of lower amplitude and frequency making it easy to distinguish from the base reflection. [Redacted]



Figures/ch3_ff7_sill_7.png

FIGURE 4.9: Seismic line ISROCK-96-18, used in forced fold amplitude / sill thickness modelling. Yellow is top forced fold. Orange is base sill. Sill is identified by (1) high amplitude, (2) positive polarity reflection forming the top of the sill, and (3) a corresponding negative reflection forming the base of the sill. The reflection is (4) laterally discontinuous, and (5) locally transgresses stratigraphy. The base reflection is easy to follow on the left hand side, as the only continuous negative polarity reflection with a different dip to the surrounding stratigraphy. In the middle and on the right hand side the reflection becomes difficult to follow as it goes below tuning thickness, introducing uncertainty to the measurement. Seismic "ringing" is also observed under the sill, but is of lower amplitude and frequency making it easy to distinguish from the base reflection. [Redacted]



Figures/ch3_ff1_r3d.png

FIGURE 4.10: Seismic inline 20722 from the Rockall 3D survey, used in forced fold amplitude / sill thickness modelling. Yellow is top forced fold. Red is top sill. Orange is base sill. Sill is identified by (1) high amplitude, (2) positive polarity reflection forming the top of the sill, and (3) a corresponding negative reflection forming the base of the sill. The reflection is (4) laterally discontinuous, and (5) locally transgresses stratigraphy. The base reflection is easy to follow, as the only continuous negative polarity reflection with a different dip to the surrounding stratigraphy. Seismic "ringing" is also observed under the sill, but is of significantly lower amplitude and frequency making it easy to distinguish from the base reflection.

[Redacted]

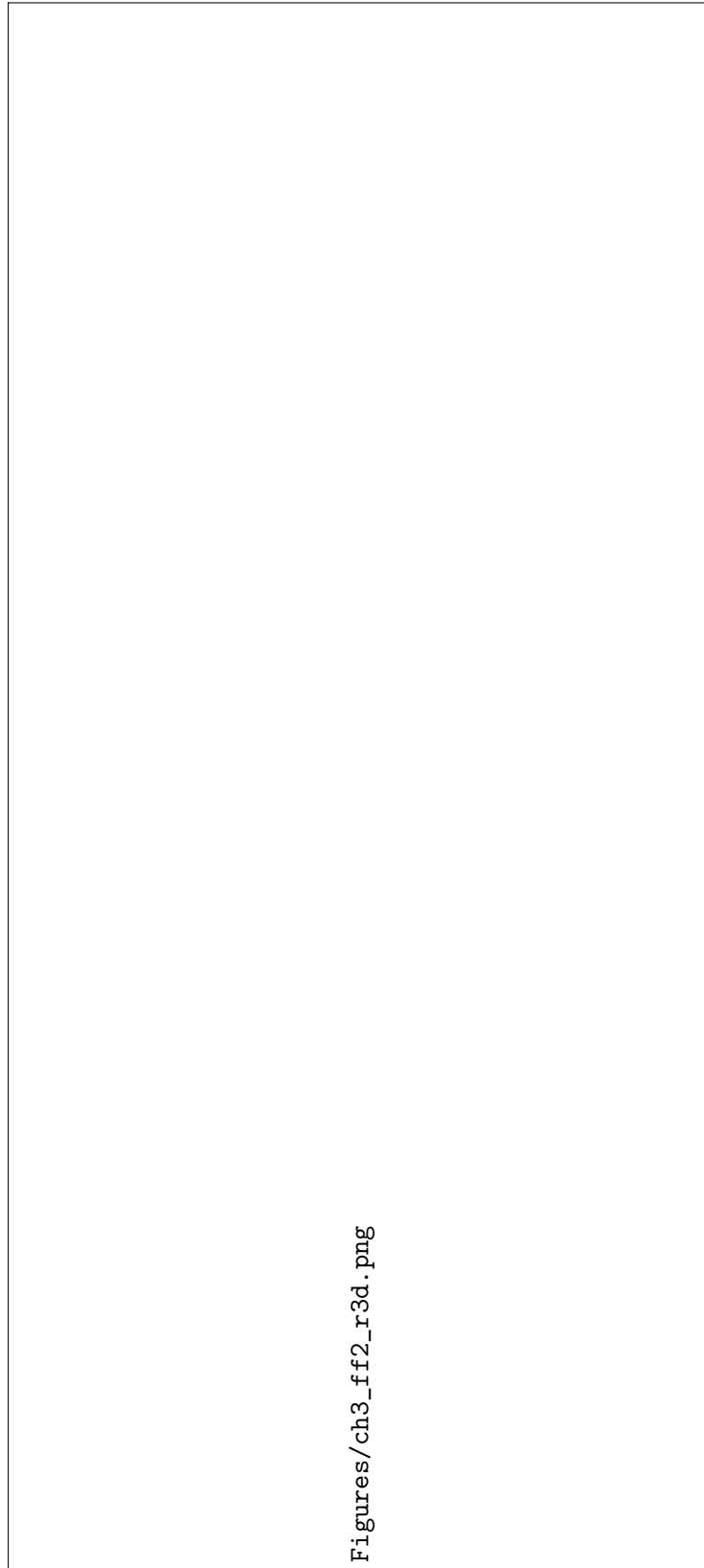


FIGURE 4.11: Seismic inline 20934 from the Rockall 3D survey, used in forced fold amplitude / sill thickness modelling. Yellow is top forced fold. Red is top sill. Orange is base sill. Sill is identified by (1) high amplitude, (2) positive polarity reflection forming the top of the sill, and (3) a corresponding negative reflection forming the base of the sill. The reflection is (4) laterally discontinuous, and (5) locally transgresses stratigraphy. The base reflection is easy to follow, as the only continuous negative polarity reflection with a different dip to the surrounding stratigraphy, especially on the left hand side of the figure. [Redacted]

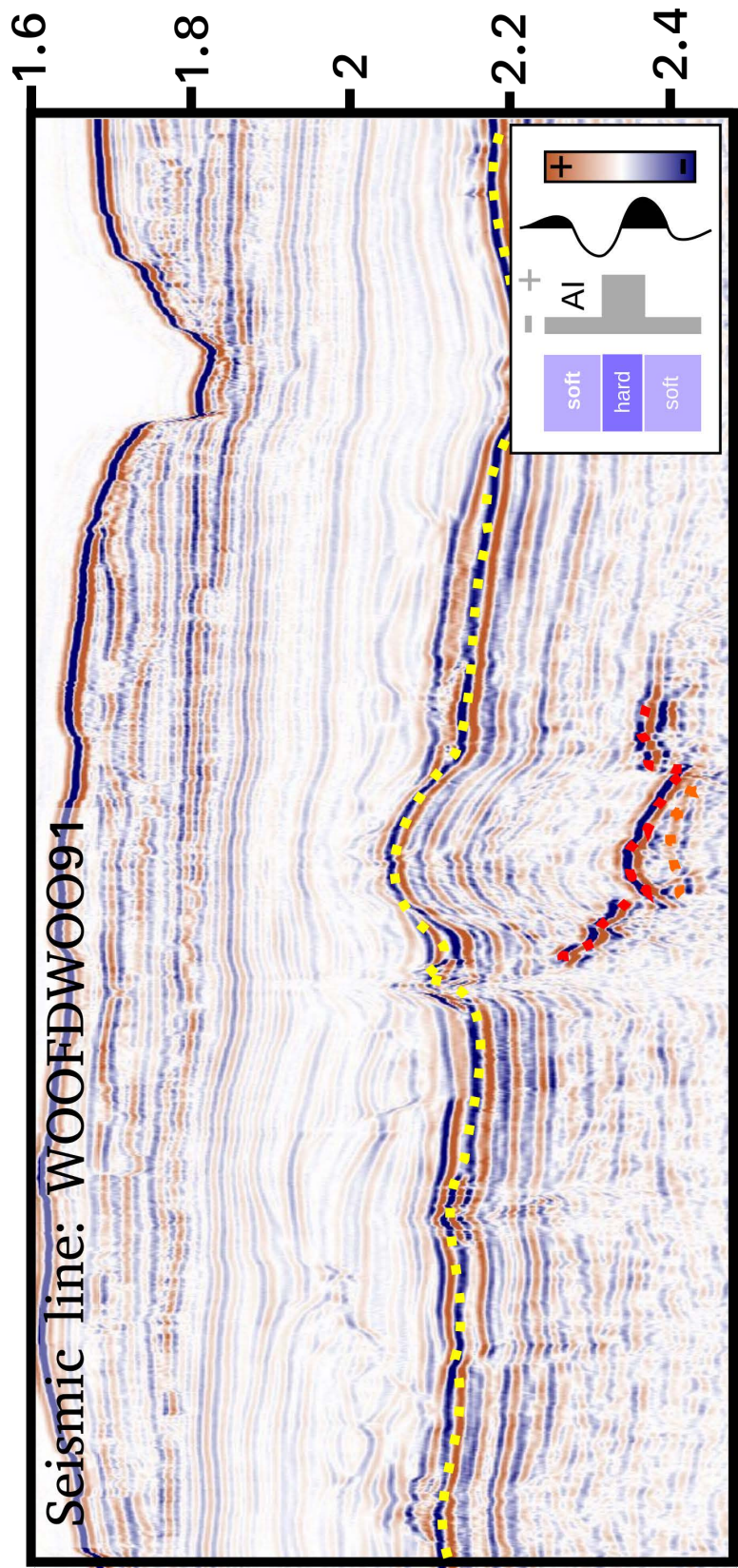


FIGURE 4.12: Seismic line WOOFDW0091, used in forced fold amplitude / sill thickness modelling. Yellow is top forced fold. Red is top sill. Orange is base sill. Sill is identified by (1) high amplitude, (2) positive polarity reflection forming the top of the sill, and (3) a corresponding negative reflection forming the base of the sill. The reflection is (4) laterally discontinuous, and (5) locally transgresses stratigraphy.

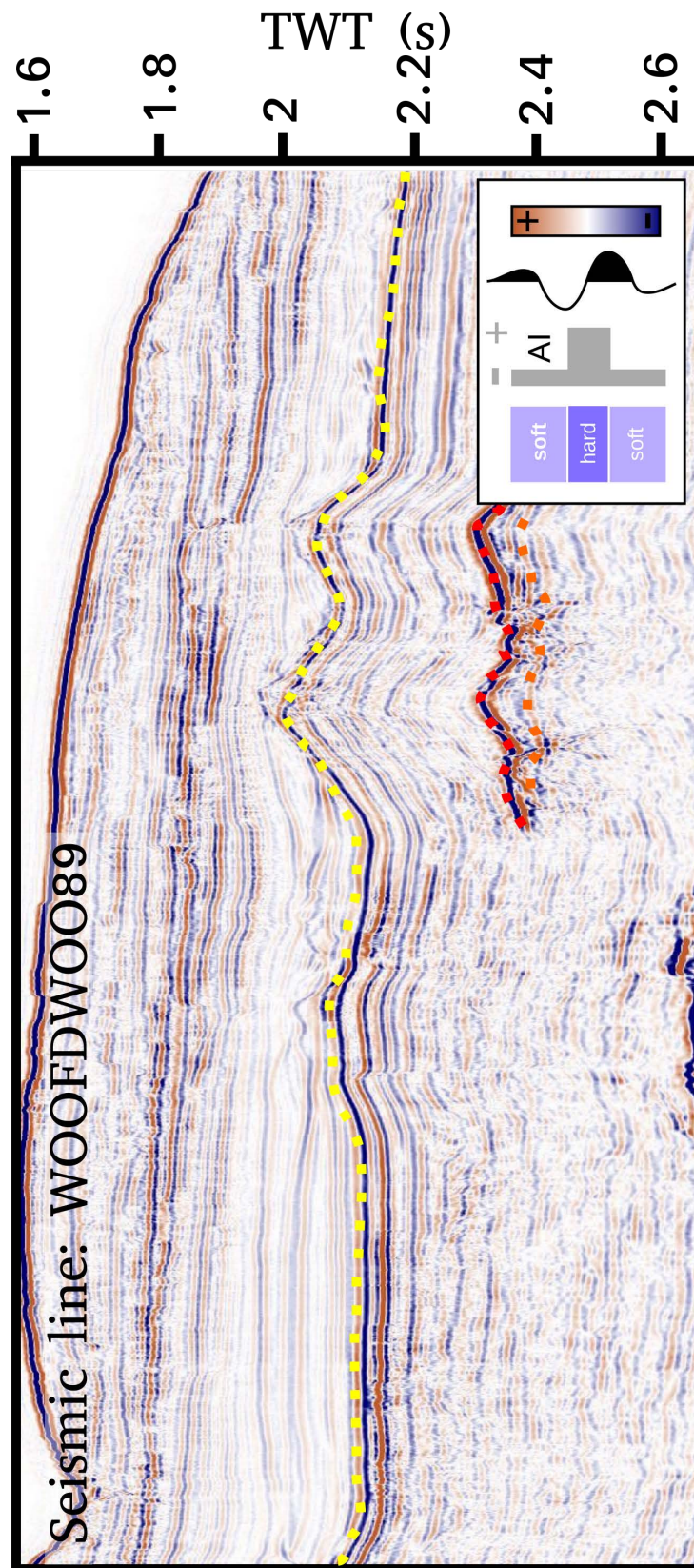


FIGURE 4.13: Seismic line WOOFDW0089, used in forced fold modelling. Yellow is top forced fold. Red is top sill. Orange is base sill. Sill is identified by (1) high amplitude, (2) positive polarity reflection forming the top of the sill, and (3) a corresponding negative reflection forming the base of the sill. The reflection is (4) laterally discontinuous, and (5) locally transgresses stratigraphy. The base reflection is easy to follow in the centre as the only continuous negative polarity reflection with a different dip to the surrounding stratigraphy. It becomes difficult on the limbs of the sill as it approaches tuning thickness, introducing some uncertainty to the interpretation.

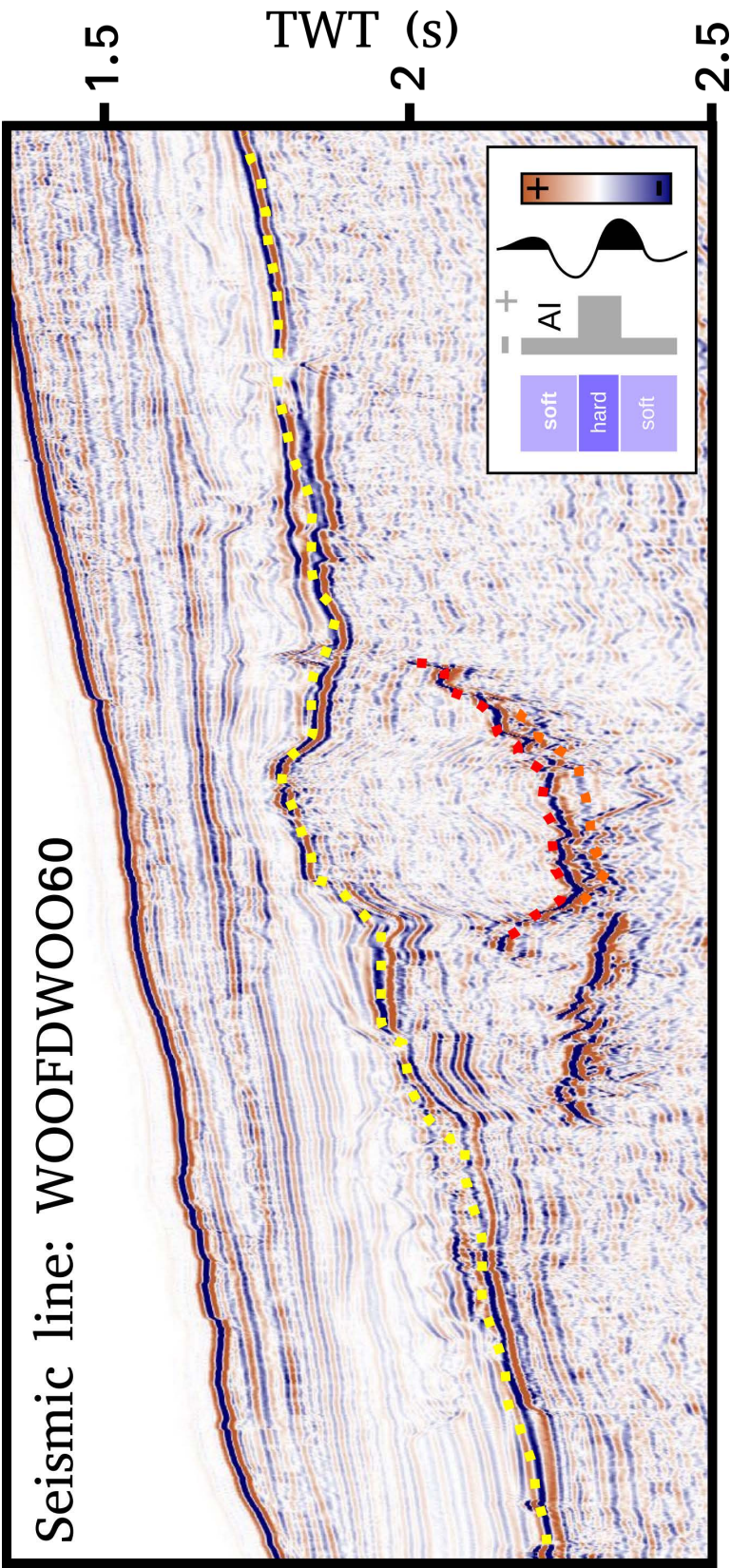


FIGURE 4.14: Seismic line WOOFDWOO60, used in forced fold amplitude / sill thickness modelling. Yellow is top forced fold. Red is top sill. Orange is base sill. Sill is identified by (1) high amplitude, (2) positive polarity reflection forming the top of the sill, and (3) a corresponding negative reflection forming the base of the sill. The reflection is (4) laterally discontinuous, and (5) locally transgresses stratigraphy. The base reflection is easy to follow, as the only continuous negative polarity reflection with a different dip to the surrounding stratigraphy.

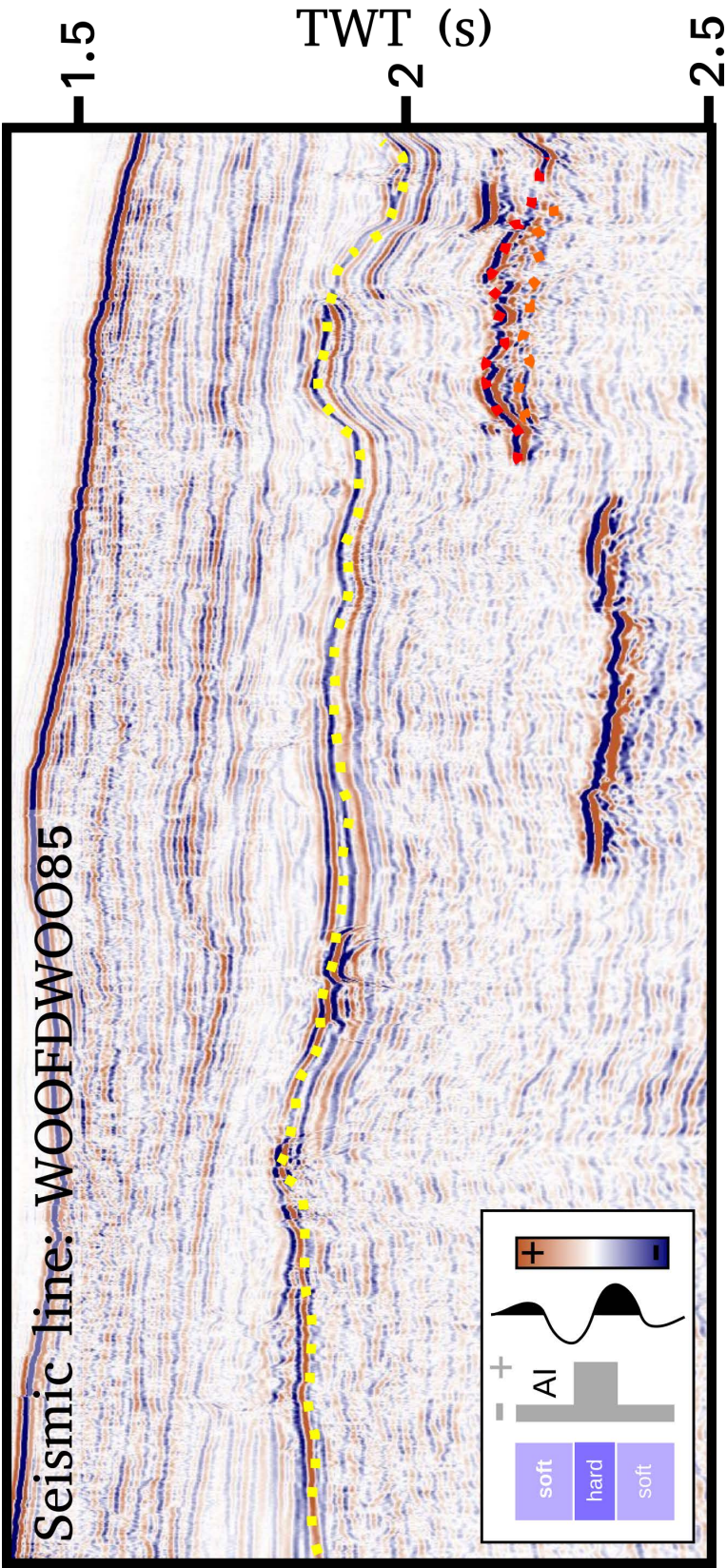


FIGURE 4.15: Seismic line WOOFDW0085, used in forced fold amplitude / sill thickness modelling. Yellow is top forced fold. Red is top sill. Orange is base sill. Sill is identified by (1) high amplitude, (2) positive polarity reflection forming the top of the sill, and (3) a corresponding negative reflection forming the base of the sill. The reflection is (4) laterally discontinuous, and (5) locally transgresses stratigraphy. The base reflection is easy to follow, as the only continuous negative polarity reflection with a different dip to the surrounding stratigraphy.

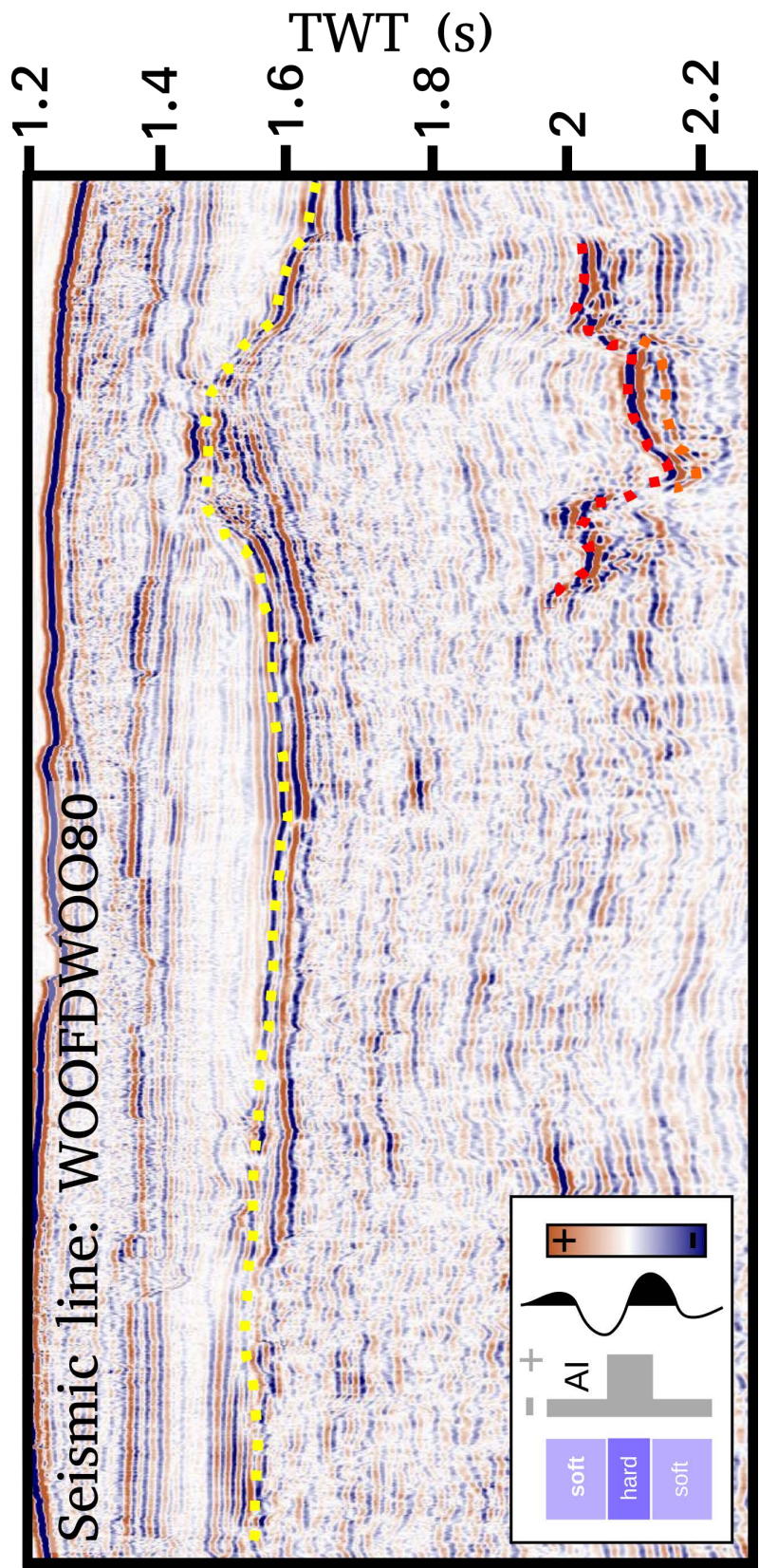


FIGURE 4.16: Seismic line WOOFDW0080, used in forced fold amplitude / sill thickness modelling. Yellow is top forced fold. Red is top sill. Orange is base sill. Sill is identified by (1) high amplitude, (2) positive polarity reflection forming the top of the sill, and (3) a corresponding negative reflection forming the base of the sill. The reflection is (4) laterally discontinuous, and (5) locally transgresses stratigraphy. The base reflection is easy to follow, as the only continuous negative polarity reflection with a different dip to the surrounding stratigraphy.

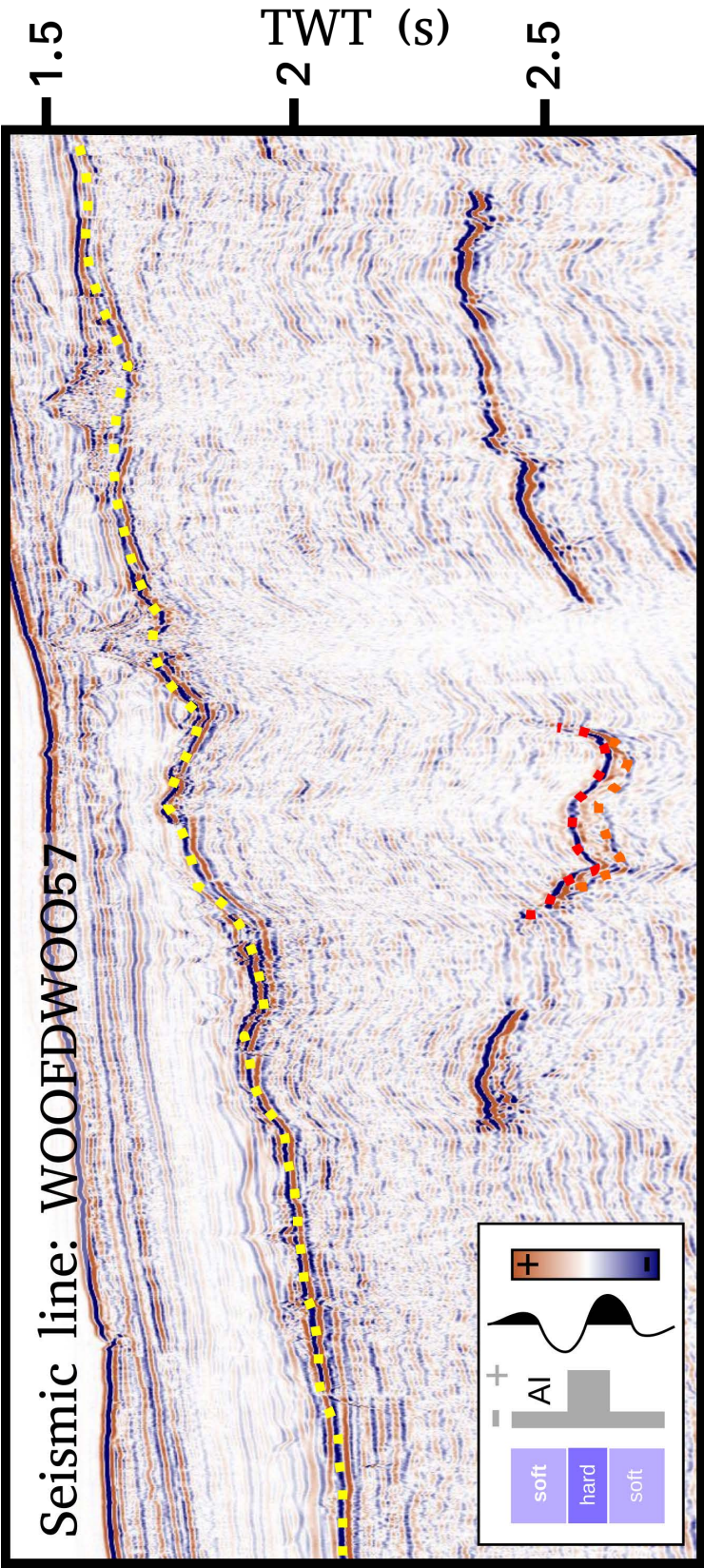


FIGURE 4.17: Seismic line WOOFDWO057, used in forced fold amplitude / sill thickness modelling. Yellow is top forced fold. Red is top sill. Orange is base sill. Sill is identified by (1) high amplitude, (2) positive polarity reflection forming the top of the sill, and (3) a corresponding negative reflection forming the base of the sill. The reflection is (4) laterally discontinuous, and (5) locally transgresses stratigraphy. The base reflection is easy to follow, as the only continuous negative polarity reflection with a different dip to the surrounding stratigraphy.

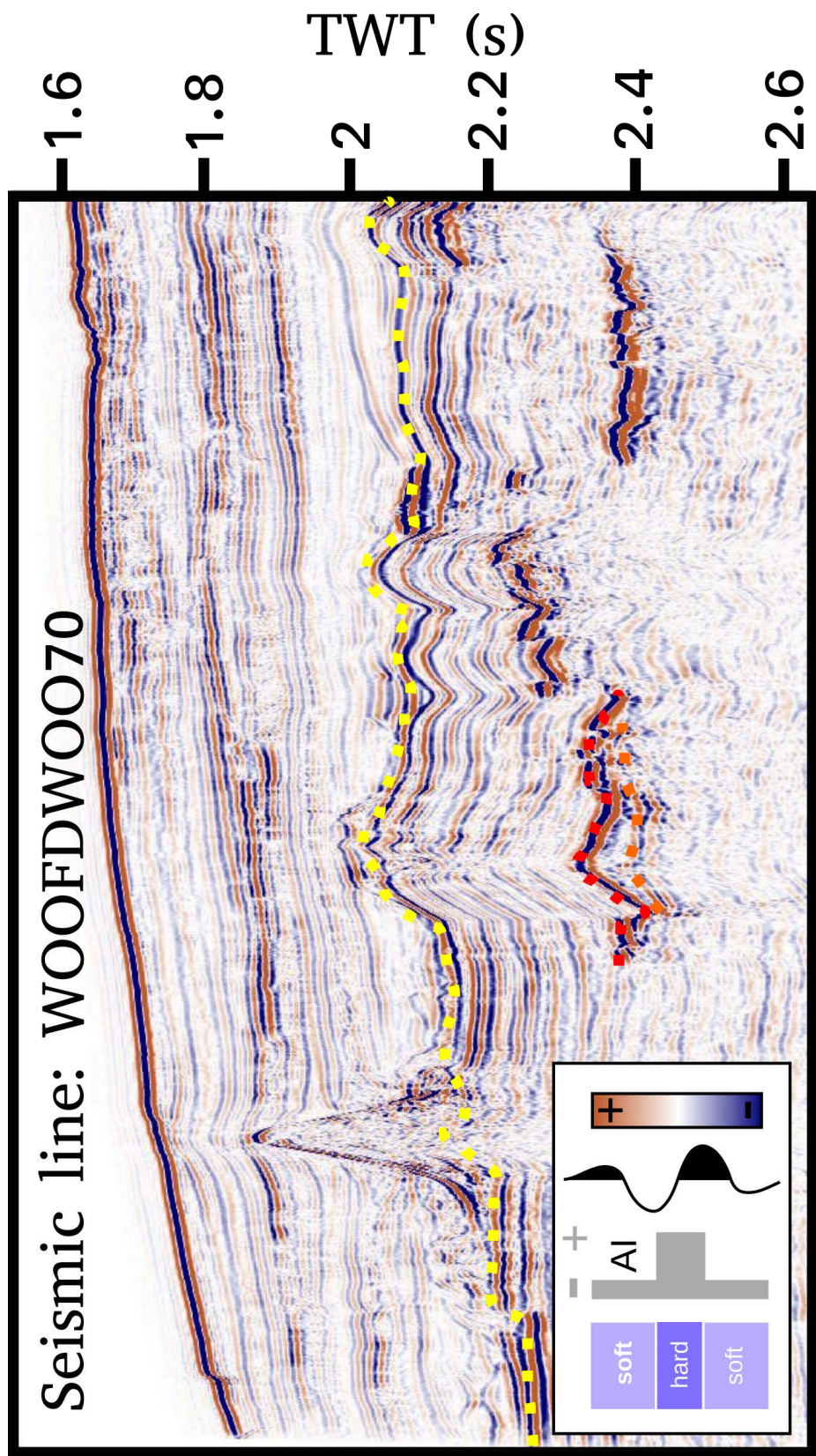


FIGURE 4.18: Seismic line WOOFDWO070, used in forced fold amplitude / sill thickness modelling. Yellow is top forced fold. Red is top sill. Orange is base sill. Sill is identified by (1) high amplitude, (2) positive polarity reflection forming the top of the sill, and (3) a corresponding negative reflection forming the base of the sill. The reflection is (4) laterally discontinuous, and (5) locally transgresses stratigraphy. The base reflection is easy to follow, as the only continuous negative polarity reflection with a different dip to the surrounding stratigraphy.

4.2.2 Results

Figures 4.19 and 4.20 show the horizons before decompaction, while figures 4.21 and 4.22 show the results of decompacting the fourteen sill / fold pairs used in this study. In these plots the pale green envelopes show the range of forced fold amplitudes from forward modelling using the range of parameters described above. The solid blue line shows the forced fold without decompaction. In most cases the sill amplitude / thickness discrepancy can be seen, i.e. the blue curve can be seen to be lower amplitude than the sill thickness, for example figure 4.19b, c, d, e, f, g and h, and figure 4.20a, c and f. Figures 4.19a and 4.20d show the uncommon case where the amplitude of the fold appears to fit well with the thickness of the sill without a backstripping correction. Similarly, sills 4.20b and half of e show uncommon examples of folds being slightly higher amplitude than their underlying sills. These two forced folds happen to have undergone amongst the shallowest burial of any of the folds, but are regardless anomalous. The thickness of the sill can be seen to correlate very well with the green envelope in most cases. Even in cases such as figure 4.19a where the sill and forced fold ranges overlap already, decompaction moves the ranges to overlap more, indicating the compaction process is significant for the measured geometry of these folds. Figures 4.19b, d, g and h show especially good examples of the data being corrected to show overlap in the ranges. Figures 4.19c, e and f and 4.20a, c and f show significant improvements in the amount of overlap between the forced fold and sill thickness ranges, even though the results are not perfect.

The findings in this section show that the majority of the forced fold amplitude/thickness discrepancy can be explained by compaction of the fold occurring after sill emplacement. This means that there is no requirement for complex models involving abnormal diagenetic alteration, unseen erosion and flank collapse, or masking by interference of folds from other sills (Hansen and Cartwright, 2006a), complex host rock interaction (Magee et al., 2013a), or fluidization and ductile flow of host sediments (Jackson et al., 2013) to explain the forced fold thickness discrepancy. The forced fold as measured today is the product of the geologically instantaneous emplacement processes, and subsequent slow modification of the fold by compaction as the basin subsides. Sill compaction is insignificant, and it is the subsequent difference in compaction between the fold and the sill which leads to the observed amplitude discrepancy. Ductile host rock deformation is known to occur at small scale (e.g. Schofield et al., 2012) figure 9., note differences in sill thickness not accommodated by deformation of overlying beds at small scale. Such small scale deformation may well be responsible for the detail of some of the shape of the folds, or indeed for interesting thickness variations shown by some sills. Differential compaction underneath the sill (due to the sill being more dense than the sediment)

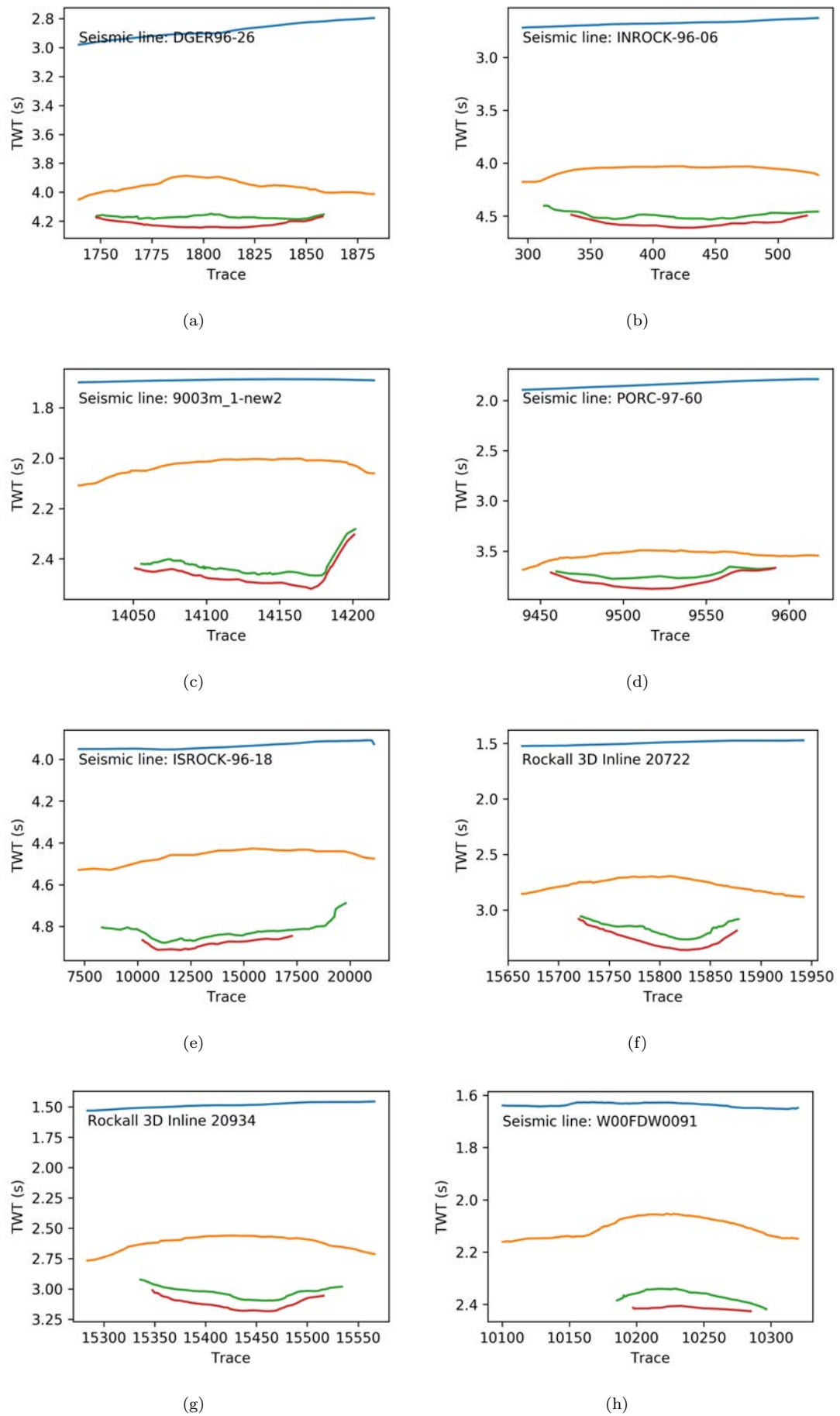


FIGURE 4.19: The first eight forced folds extracted horizons from seismic interpretations, used in the backstripping modelling. Blue is seafloor, orange is top forced fold, green is top sill, and red is base sill.

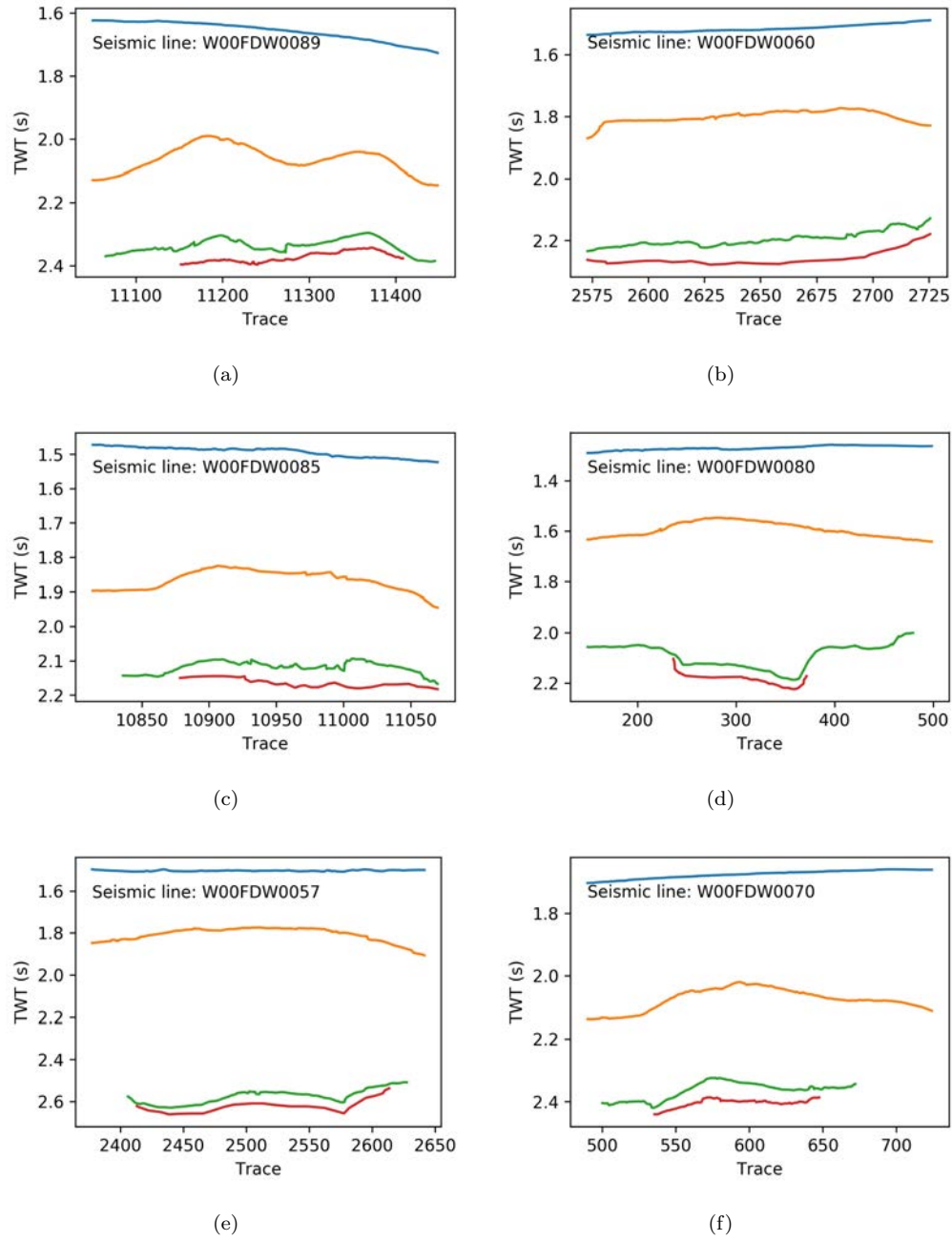


FIGURE 4.20: The final six forced folds extracted horizons from seismic interpretations, used in the backstripping modelling. Blue is seafloor, orange is top forced fold, green is top sill, and red is base sill.

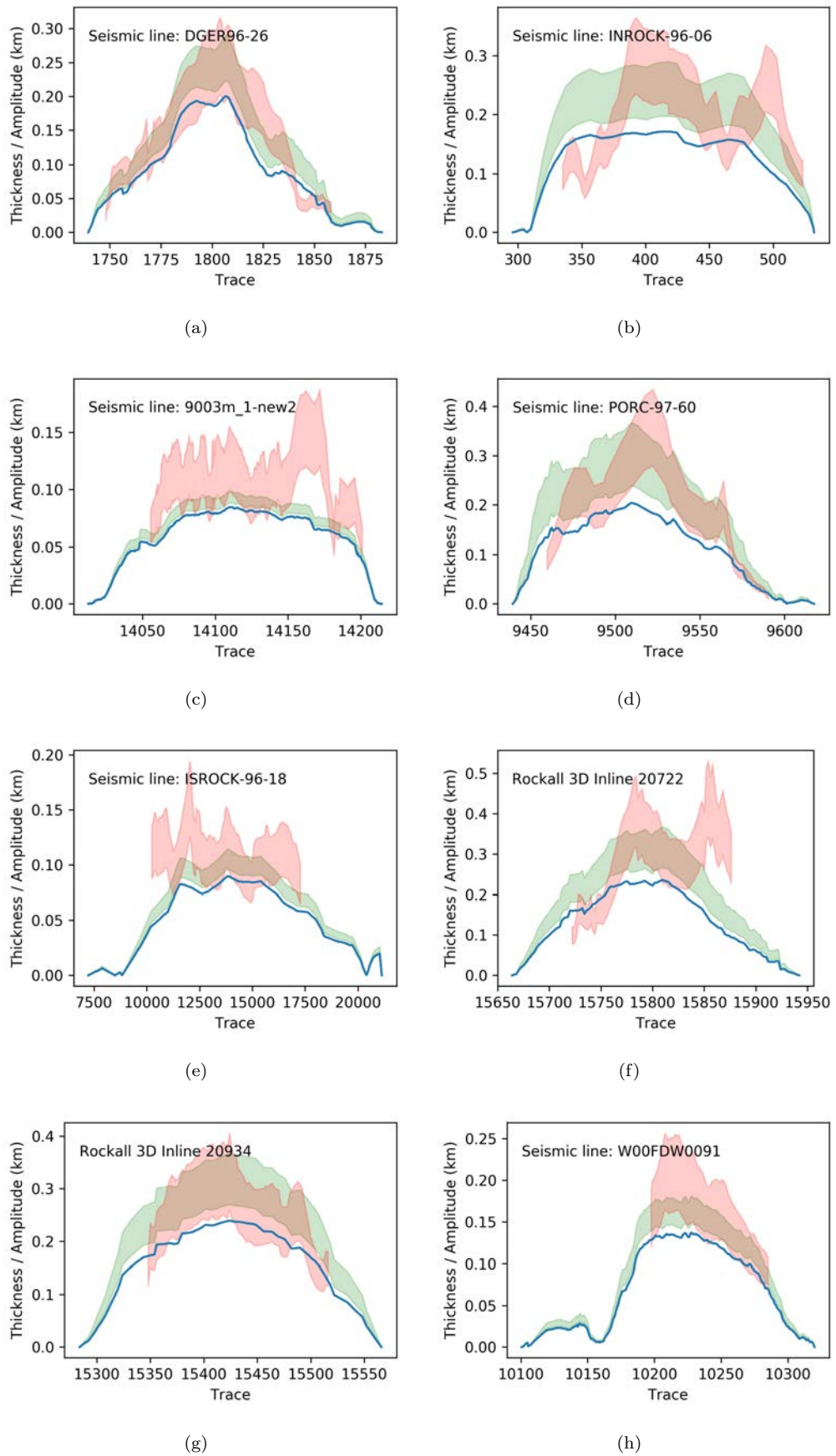


FIGURE 4.21: First eight examples of backstripping modelling. Sill thickness (red envelope) against a range of modelled original fold amplitudes. The green shaded area is the envelope of values covered by different backstripping parameters for the forced fold amplitude.

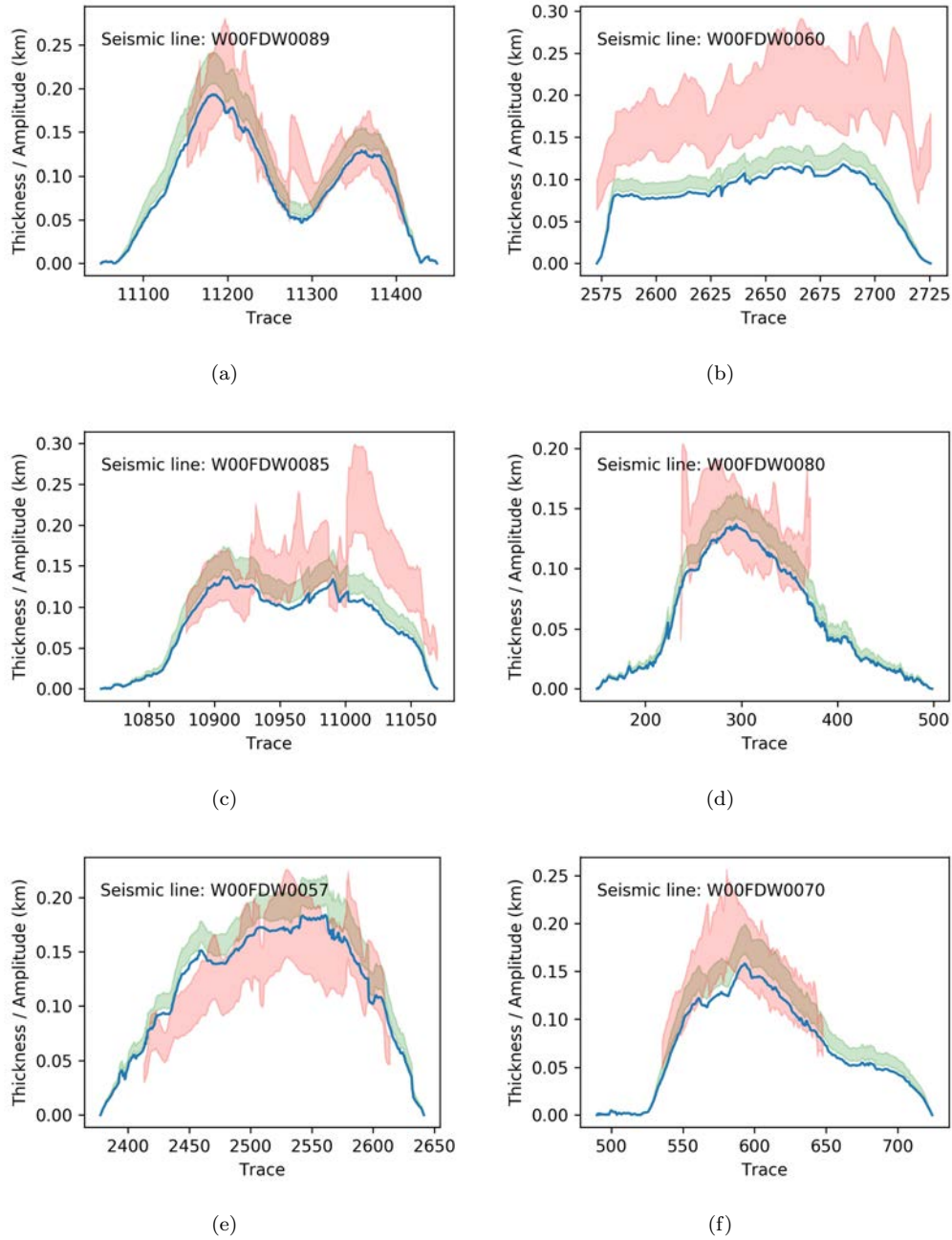


FIGURE 4.22: The final six examples of backstripping modelling. Sill thickness (red envelope) against a range of modelled original fold amplitudes. The green shaded area is the envelope of values covered by different backstripping parameters for the forced fold amplitude.

should be negligible, as this extra weight should represent a weight difference of less than 1% of the sediment column (e.g. a 200 m thick sill with a density of 2800 kg m^{-3} in a 3 km sediment column with a density of 2500 kg m^{-3} would represent a $\sim 0.7\%$ difference). Some volume loss from the host rock is clearly possible within the thermal aureole, as evidenced by the generation of hydrocarbons in organic rich shales. However, quantifying this volume loss has received little study in the literature, so exists as an uncertainty within the analysis. Similar values exist considering any extra sediment accumulating around the forced fold rather than on top of it. The results of this section also agree with results from section 3.5.5. The forced folds shown in this chapter have a wavelength very similar to the extent of the underlying sill. This implies that the host rock has little flexural strength. This matches the implications of the Johnson and Pollard (1973) model, with parameters implying low flexural strength, giving the best fit to the studied sills in chapter 3.

4.3 Case study: the Resolution-1 Amplitude/thickness discrepancy

Having developed the methodology to analyse the sill-forced fold pairs using backstripping, this methodology is now applied to the only sill-forced fold pair known of to have been intersected by a borehole or well. This allows the use of well data to test depth conversion and decompaction parameter ranges, and further validate section 4.2.2's conclusions.

The sill-forced fold pair intersected by the well is found on the Resolution-1 2D seismic survey, which is located in the Canterbury basin, situated to the East of New Zealand's South island (figure 4.23). The basin contains a thin sedimentary veneer, overlying crystalline basement. The sedimentary sequences encountered are mainly of Cretaceous and younger strata, although basement is thought to consist of some Jurassic prerift strata (see section 1.4.3). Interpreting and plotting the sill versus the amplitude of the forced fold shows the same discrepancy as reported earlier in this chapter. In this case, the Resolution-1 forced fold has an amplitude of around 100m, while the sill thickness is around 170m at its maximum thickness.

4.3.1 Data and methods

Figure 4.24 shows the Resolution-1 seismic data and interpretation, while figure 4.25 shows the wireline log data for the Resolution-1 well. As figure 4.25 shows, values in

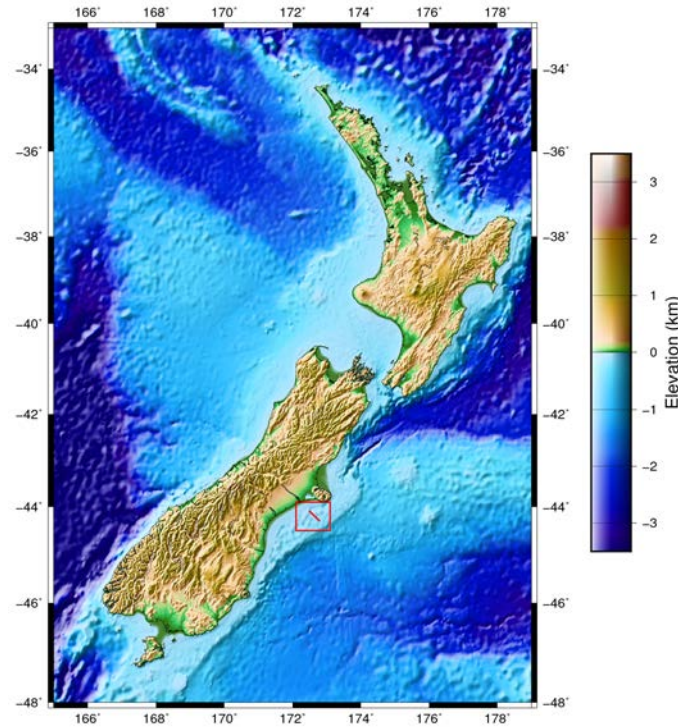


FIGURE 4.23: New Zealand, with Resolution-1 well and seismic line shown. DEM data is from ETOPO1 ([Amante, 2009](#)).

water column and the shallowest sediments were not recorded. For subsequent calculations, missing values were filled in the following way: from 0 to 64 m sonic velocities of 1500 m s^{-1} were used, and in the shallowest section velocities of 1800 m s^{-1} were used. Other log tracks were not used in this analysis.

Depth conversion is commonly one of the most uncertain steps in interpretation of seismic data in frontier areas. The case of the Resolution-1 seismic line and well represents a rare occasion where depth conversion was as confident as could be, as the well penetrated both the crest of the fold and the sill underlying it. Depth conversion of the seismic was therefore achieved by deriving average interval velocities for layers and depth converting the seismic section using this. However before this can be done, the well data must be tied to the seismic. The normal procedure for displaying a well against a seismic survey uses a time-depth curve, often derived from a checkshot survey, to convert the well into equivalent time position. Resolution-1 has extremely sparse time-depth information, so a time depth curve was derived from sonic data. First the sonic log was filtered using a median filter with a window of 5 samples, to remove spikes due to sample skipping. Following this, a time depth curve was derived as the cumulative integration of the sonic log, to give the time-depth relationship shown in figure 4.26.

Seismic data, well data, and calculated log data were loaded into IHS Kingdom software. Well tie was achieved using time-depth relationships from figure 4.3.1, and checked

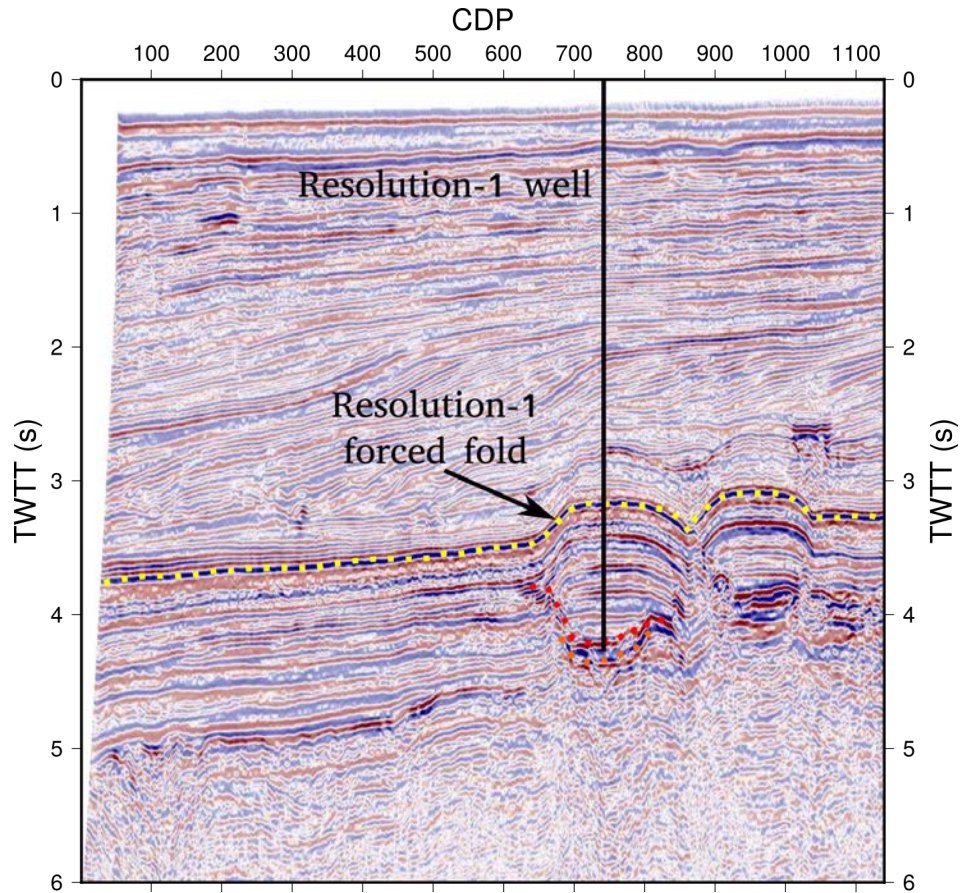


FIGURE 4.24: Seismic data crossing the Resolution-1 well and forced fold. Yellow horizon is slightly below the top of the forced fold (chosen as the top of the forced fold shows slight erosion on a crossing line), red is the top sill reflection and orange is the base sill reflection.

against formation top data. Figure 4.24 shows the interpreted seismic section for the Resolution-1 survey. Seismic sections are SEG reverse polarity, with a red peak indicating an increase in acoustic impedance. Figure 4.24 shows are two sills intruded into the sedimentary section, both showing forced folds above them. All formation tops in well data were interpreted across the seismic line, and were exported as ASCII data files for further analysis.

The same methodology as in section 4.2.1 is used to test whether the amplitude of the fold is similar to the thickness of the sill. The aim is to take advantage of the Resolution-1 well data to help constrain parameters in the analysis. This would be most effectively done by deriving a porosity curve from the well data, and using it to decompact and backstrip the fold. However only legacy sonic logs are available to derive porosity from, there were no density or neutron porosity logs acquired at the time the well was drilled. The normal method of deriving porosity from a sonic log is to use the Wyllie time-average method (Rider, 1986)

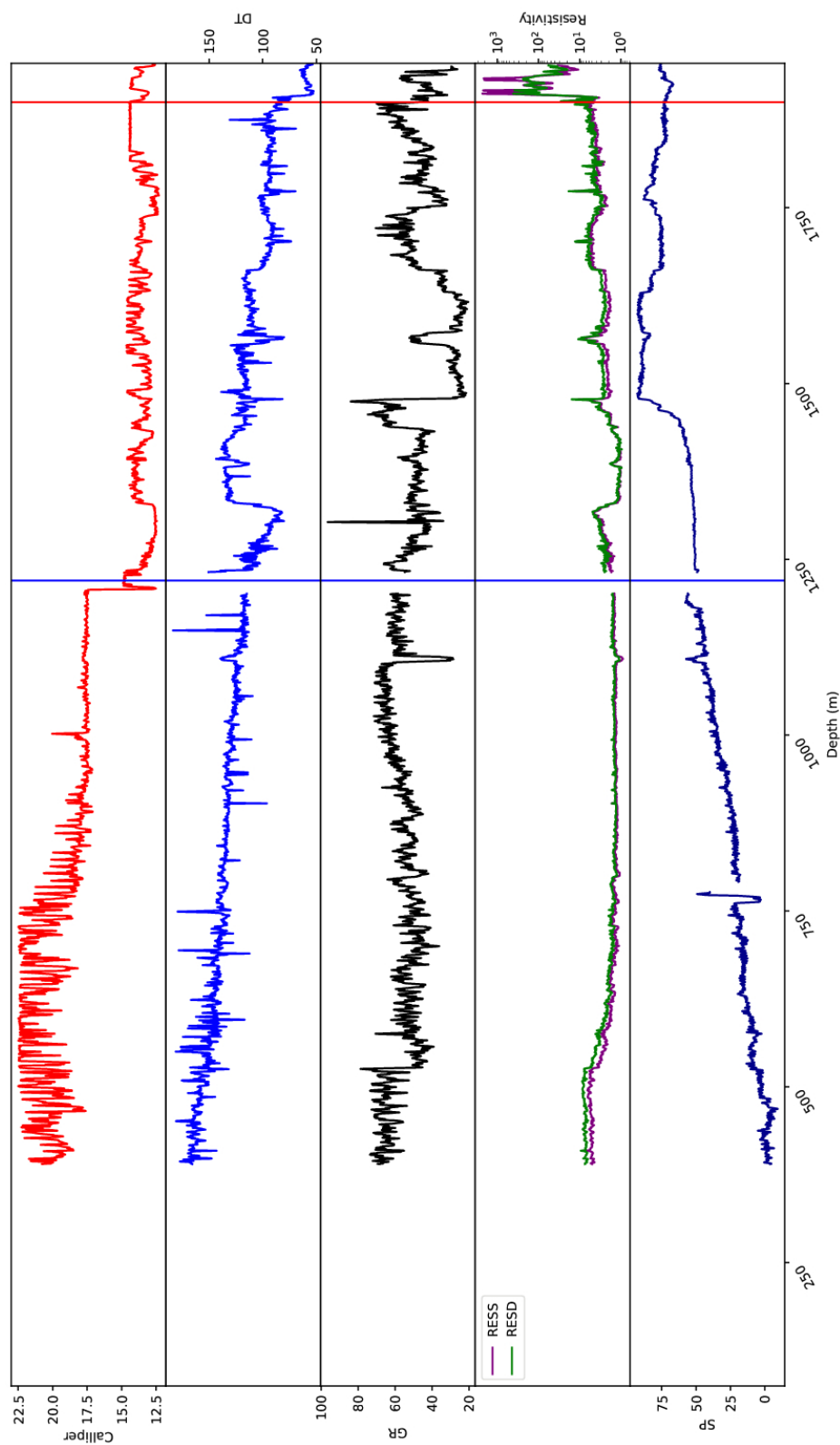


FIGURE 4.25: Wireline log data for Resolution-1 wells. Tracks are Caliper log, Sonic log (DT, $\mu\text{s ft}^{-1}$), Gamma log (API), Deep and Shallow resistivity (RESD and RESS, Ωm) and Spontaneous potential log (SP, mV). Blue vertical line denotes the top of the forced fold, while red vertical line denotes the top of the sill.

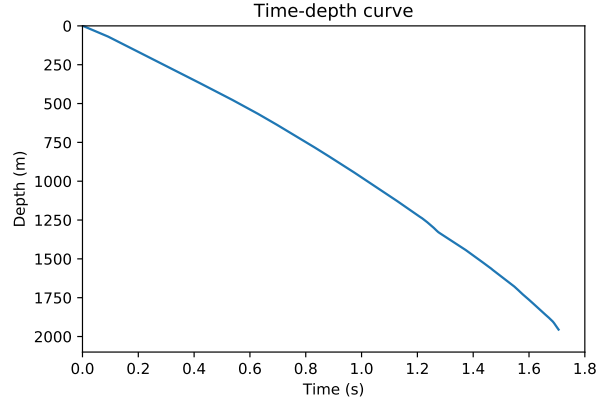


FIGURE 4.26: Time depth curve for Resolution-1, from the cumulative integration of the sonic log. This function was used to depth convert the Resolution-1 seismic data.

$$\phi = \left(\frac{\Delta t_{log} - \Delta t_{matrix}}{\Delta t_{fluid} - \Delta t_{matrix}} \right) \quad (4.1)$$

Where ϕ is porosity, Δt_{log} is the logged formation slowness, Δt_{matrix} is the matrix slowness, Δt_{fluid} is the pore fluid slowness. However the forced fold exists in a shallow sedimentary section, and the Wyllie time-average method is known to give unrealistic values near the seafloor. A correction can be derived to apply to the Wyllie time-average method by comparing it to the (more reliable) density log (Rider, 1986)

$$\phi = \left(\frac{\Delta t_{log} - \Delta t_{matrix}}{\Delta t_{fluid} - \Delta t_{matrix}} \right) \frac{1}{C_p} \quad \text{where } C_p = \frac{\Delta t_{shale} C}{100} \quad (4.2)$$

Where ϕ is porosity, Δt_{log} is the logged formation slowness, Δt_{matrix} is the matrix slowness, Δt_{fluid} is the pore fluid slowness, Δt_{shale} is the shale velocity (found from comparison with a density log) and C is a constant, normally around 1.0. However density logs were unavailable, and the nearest other offshore wells are 60km away, in a different sub basin. The last standard method to estimate porosity is the Raymer-Hunt-Gardner empirical relationship (Rider, 1986)

$$\phi = \frac{5}{8} x \left(\frac{\Delta t_{log} - \Delta t_{matrix}}{\Delta t_{log}} \right) \quad (4.3)$$

however this is highly affected by the matrix slowness chosen, for which there is no estimate, and which varies widely (Carmichael, 1982).

Due to these uncertainties in ϕ estimation, the Resolution-1 data set is instead posed as a set of forward and inverse problems. The forward problem can be tested by modelling the range of expected fold thicknesses based on different decompaction parameters (depth

conversion is not modelled and is taken as reliable, as the well penetrates the fold, so error in depth conversion should be extremely low). Similarly, the range of sill thicknesses is modelled based on the range of sill velocities from the literature (section 4.3.2.1). In this sense the forward problem is the same as in section 4.2.1

The inverse problem is to start with a best estimate of sill thickness, and use optimization techniques to find the best decompaction parameters to minimize the different between the fold amplitude and sill thickness. These estimates are then checked against sensible ranges of decompaction parameters. This has the advantage of showing the relative importance of different parameters, and how they can co-vary (section 4.3.2.2).

4.3.2 Results

4.3.2.1 Forward problem

The forward problem involves modelling all outcomes and examining the ranges they cover. The range of sill velocities in (Smallwood and Maresch, 2002) (from 4500 to 6500 m s^{-1}) is used to model sill thicknesses. Decompaction parameter ranges were 1.4 to 3.7 for λ , and 0.25 to 0.7 for ϕ (after Sclater and Christie, 1980). Figure 4.27 shows the results of this.

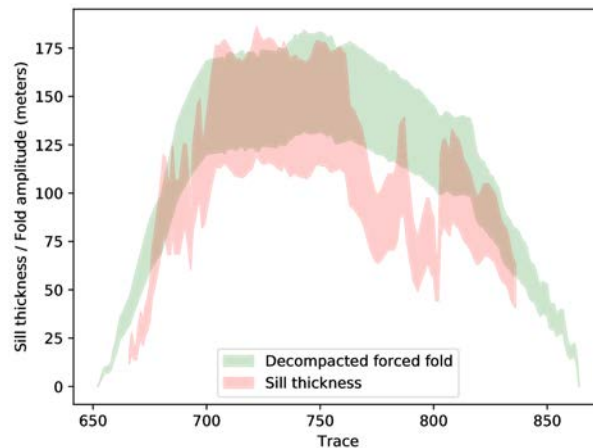


FIGURE 4.27: Resolution-1 forward model, comparing modelled forced fold amplitude to sill thickness. Overlap of the ranges for the majority of the fold gives support to the model of the forced fold amplitude / sill thickness discrepancy being compaction related.

As figure 4.27 shows, the modelled ranges predominantly overlap the sill thickness measured from the seismic profile, which shows strong evidence that the majority of the discrepancy in fold amplitude to sill thickness can be explained by post-emplacement modification of the fold amplitude by compaction. The sill thickness does not go to zero at the edges, due to the sill tips going below the seismic tuning thickness.

4.3.2.2 Inverse problem

The relative importance of decompaction parameters are then investigated by using an inversion approach. A sensible estimate for the thickness of the sill is specified, and then grid search optimisation is used to test the different parameter importance.

First, sill thickness is specified. The depth conversion approach works for the sedimentary section, as data was available for all of the shallow section. However, while the well penetrated the top of the sill, it reached total depth (TD) before exiting the sill. Therefore the depth to the base of the sill, and consequently the sill thickness, must be calculated. A compressional wave velocity log can be estimated from a sonic log by taking reciprocal, and converting from ft to m. However doing so results in velocities within the sill as low as 4300 ms^{-1} , which are not sensible ranges for the velocity of sills (Smallwood and Maresh, 2002). Speculatively, possibly the sill was well jointed and hence drilling mud invasion lowered the measured sonic velocity. Due to this, a velocity of 6000 ms^{-1} - the modal velocity from Smallwood and Maresh (2002) - was used for depth converting the sills.

The effects of decompaction parameter choices on the forced fold amplitude after decompaction were then tested. Values of ϕ of 0.25 to 0.7, and values of λ of 1.4 to 3.7, after Slater and Christie (1980). The goodness of model fit is measured as the root mean square (RMS) misfit, defined as:

$$RMS \text{ misfit} = \sqrt{\left(\frac{1}{n}\right) \sum_{i=0}^n (T_i - A_i)^2} \quad (4.4)$$

Where n is the number of points sampled along the fold, T_i is the sill thickness as a point along it's profile, and A_i is the fold amplitude at a corresponding point above T_i . Figure 4.28 shows the results of this. The optimum parameters are found to be $\phi_0 = 0.38$ and $\lambda = 3.2$. The solution trough is closer to horizontal than to diagonal, showing a greater importance of initial porosity than of decompaction length scale. Figure 4.29 shows the results of decompacting the fold with these parameters.

4.3.2.3 Inversion of matrix velocities

These parameter values can be further checked by creating a theoretical porosity curve from them, and applying different matrix velocities to the Raymer-Hunt-Gardner model (equation 4.3) to find the best fitting curve to the theoretical. This gives us a matrix velocity of $69 \text{ } \mu\text{s ft}^{-1}$. Carmichael (1982) give the range of matrix velocities of shale to

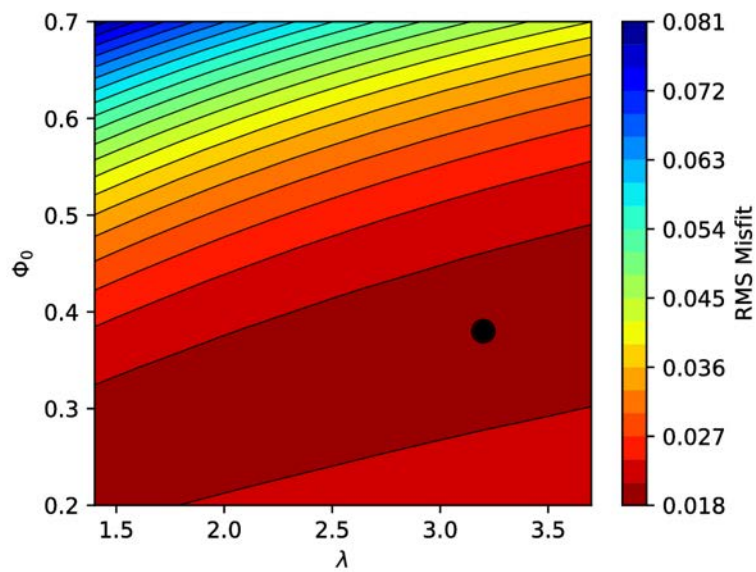


FIGURE 4.28: Parameter sweep of decompaction parameters for forced fold/sill thickness RMS misfit minimization. Black points show the optimum parameters.

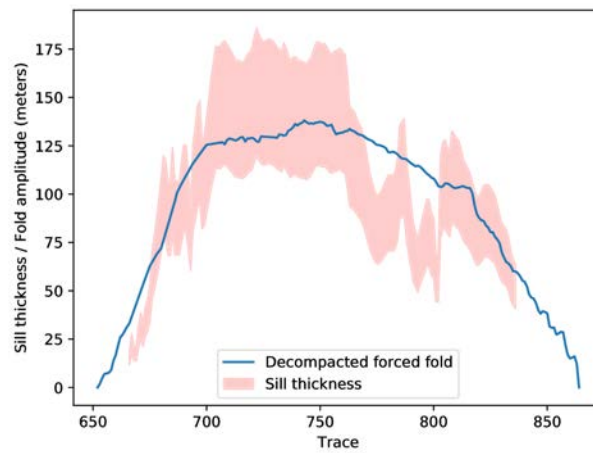


FIGURE 4.29: Best fitting inversion model for the Resolution fold-sill pair

be from 62.5 to 169 $\mu\text{s ft}^{-1}$, and of sandstone to be from 52 to 58.9 $\mu\text{s ft}^{-1}$. The value derived is in good agreement with the mudlogging report and wireline log records, which shows a mainly shale rich section with some thin sandstones.

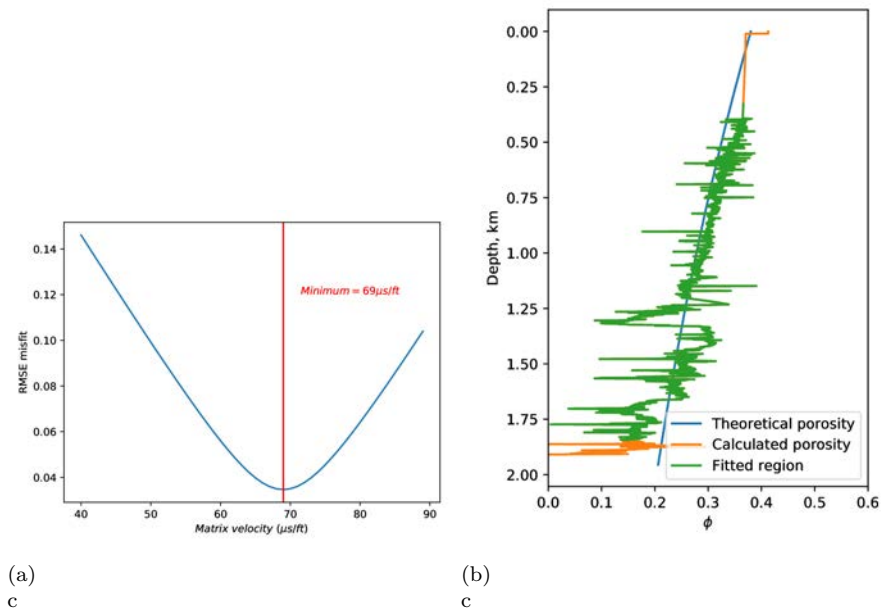


FIGURE 4.30: Left panel: misfit curve for inversion of matrix velocity from sonic logs in the Resolution-1 well. Right panel: Porosity log using the inverted matrix velocities.

4.4 Discussion

Forced folds accommodate the volume increase from injecting a volume of magma into the sediment pile. In some cases, particularly in the shallowest regions of sedimentary basins, forced folds have been observed where the amplitude of the forced fold is close to the thickness of the sill. Only a single example of a forced fold has been described that has greater amplitude than the sill which forms it (Reeves et al., 2018). We show an example in section 4.2.1 of a very shallowly buried fold which we also found to have greater thickness than it's underlying sill. However this single example notwithstanding, almost all folds studied here exhibited a discrepancy between the amplitude of the forced fold and the thickness of the sill, where the forced fold was lower amplitude than expected given the thickness of the sill. Section 4.2.1 explains a method for forward modelling the amplitude of the fold after compaction which shows good results for correcting the observed amplitude. The effectiveness of the correction gives weight to the model of compaction modifying the forced fold amplitude after emplacement. Figure 4.31 shows a diagram summarising the model. In panel 1, detrital sediments are deposited, likely underwater at a basin floor. This leads to sediments near the basin floor being unlithified,

uncompacted and likely of very high porosity. In panel 2 an igneous sill intrudes and cools, likely over the scale of a few tens of years. Once cool, it has close to zero porosity, meaning there is no porosity to collapse during later burial. In panel 3, sedimentation continues. The weight of the continuously deposited sediment causes porosity in the underlying sediment to collapse, giving the familiar basinal porosity depth trends (e.g. [Sclater and Christie, 1980](#)). At the present day this leads to the observed differences in the amplitude of the forced fold and the thickness of the sill.

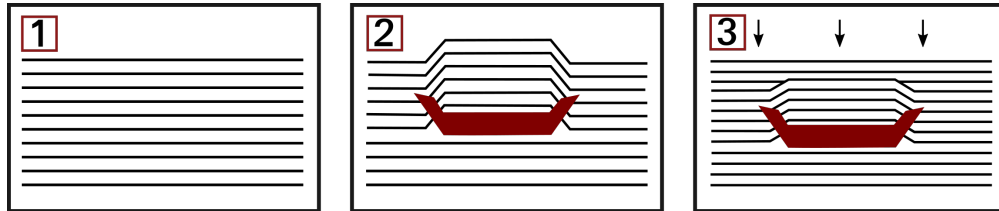


FIGURE 4.31: Summary of compaction model for the forced fold amplitude / sill thickness discrepancy. 1. Sediments are deposited, but as yet are not compacted or lithified. 2. a igneous sill intrudes by deforming the overburden into a forced fold. The sill cools and solidifies. 3. Sediment is continuously deposited, compacting the underlying sediment. The whole sediment pile compacts, leading to the amplitude of the forced fold being reduced.

The results of section 4.2.2 shows that decompacting the forced fold minimises the forced fold amplitude/sill thickness discrepancy in all bar one example. However, many of the sills show small scale variations that the compaction model does not account for. Inspection of the seismic does not show clear erosional features on the folds, which leaves mechanisms such as plastic host rock behaviour, imaging problems related to the 2D seismic data and unimaged sills as potential explanations. While the compaction model explains the majority of the shape and amplitude of the forced fold, smaller scale variation still exists which is not explained by the model alone.

The results of this chapter link with the work in Chapter 3 in a number of ways. First, both the results of section 3.5 and in this chapter imply that for many of the shallowly emplaced sills studied, the overburden has little to no elastic strength — i.e. low young's modulus. In section 3.5, the best fitting models to sill data were not the models which were based around the assumption of an isotropic host rock, but were the models which incorporated an overlying elastic plate. The data in figures 4.21, 4.22 and 4.27 shows this, as the wavelength of the fold is very similar to the diameter of the sill in almost all cases, and the wavelength of the fold will increase with increasing elastic strength. Seismic images such as figure 4.1 also support this anecdotally, as when seismic imaging is good, a large number of faults can often be seen in the forced fold, and an elastic plate with a large number of thoroughgoing discontinuities is unlikely to have much elastic strength.

4.5 Summary

In this chapter the observation that for most forced fold – sill pairs, the amplitude of the fold is generally less than the thickness of the sill. This was termed the forced fold amplitude–thickness discrepancy. Examples of this in the literature were shown, along with new data. A hypothesis was suggested that instead of the more exotic current models to explain the discrepancy, normal post emplacement burial related compaction might be responsible. The effect of burial was forward modelled by decompaction and backstripping procedures. For the modelled examples twelve out of fourteen folds were corrected to within sensible ranges with the backstripping procedure. The Resolution fold was then introduced as a case study offshore New Zealand. The same forward modelling procedure was then used to test the burial related compaction hypothesis, as well as an inversion procedure using available well logs. Both yielded results in support of the burial related compaction hypothesis. It is hence suggested that the forced fold amplitude – thickness discrepancy is likely due to post emplacement burial related compaction.

Chapter 5

Does the Opal A–CT transition in Rockall document the influence of sills on fluid flow?

In this chapter a chemical reaction boundary is investigated as a proxy for the influence of sills on basinal fluid flow. Here, the focus is on the presence of an opal A–CT transition, which when first identified by the author was hypothesised to show the influence of sills on fluid flow *sensu lato* [Rateau et al. \(2013\)](#). This work concludes that there is no evidence of a relationship between individual underlying sills and the overlying opal A–CT transitions *sensu stricto* [Rateau et al. \(2013\)](#). However, the opal A–CT transition may instead represent a fossilized convective planform driven by the thermal energy of multiple sills underneath. This work represents the first recognition of a seismically imaged opal A–CT transition in the North Rockall Basin, shows a new morphology of an opal A–CT transition unreported thus far in the literature, and shows the first example of a seismically imaged convective planform fossilized in a diagenetic boundary.

5.1 Introduction

Opal A–CT transitions are common features in sedimentary basins (e.g. [Davies and Cartwright, 2002](#); [Davies and Clark, 2006b](#); [Dralus, 2013](#); [Ireland et al., 2010a](#); [Kameda et al., 2017](#); [Wrona et al., 2017](#)). Opal A is a primary depositional pseudomorph of quartz composed mainly of radiolaria skeletons, sponge spicules and diatom frustules ([Ireland et al., 2011](#)). This creates a disordered structure which can be recognised in rock samples using X-ray diffraction data (e.g. [Kuramoto et al., 1992](#)). With burial, depositional opal A transforms into opal CT. Opal CT refers to the minerals Cristobalite and Tridymite,

which form by the dissolution and re-precipitation of opal A. Opal CT is the lithology containing these two low temperature pseudomorphs of quartz, where some degree of recrystallisation has occurred leading to a higher density rock. Due to this increase in density, opal A to opal CT boundaries commonly have a high reflection coefficient and therefore show up as a high amplitude reflection on seismic data, with a polarity which indicates an increase in acoustic impedance. With continued burial of opal CT, further transformation takes place leading to the formation of microcrystalline quartz and chert as the rock is fully recrystallised. This boundary, however, is less commonly imaged on seismic data due to the reflection being deeper, and the changes in acoustic properties not being as great as for the opal A to opal CT transition.

A number of factors influence the location and depth of Opal A–CT transitions in the subsurface. The most important of which is the presence of enough radiolaria skeletons, sponge spicules or diatom frustules to create an opal A to begin with. After that, the main controls on the reaction are temperature (Dralus, 2013), pressure, grain size and pore water chemistry (Isaacs, 1982; Kastner and Gieskes, 1983; Kastner et al., 1977), among other factors. Geological controls have been responsible for variations in the above factors to result in complex morphologies of the opal A–CT boundary, including complex polygonal patterns, changes in depth with sediment loading, priming of mass transport systems, and a variety of self-similar scale independent patterns (Davies and Cartwright, 2002; Davies and Clark, 2006a; Davies et al., 2006; Ireland et al., 2010b, 2011). However, at no point have opal A–CT transitions yet been found fossilizing a snapshot of a convective planform.

5.2 Reflector A in Rockall

The Northeast Rockall Basin is introduced in Chapter 1. Interpretation of sills in the Rockall 3D seismic volume (see Chapter 3 and 4) included interpretation of the high amplitude reflector A (Figure 5.1a), which was mapped throughout the seismic volume. The coincidence of obvious convex up morphologies with some sill tips led to the author forming the early hypothesis of reflector A being some sort of a diagenetic boundary, the morphology of which was being controlled by fluid flow focused by the underlying sills *à la* Rateau et al. (2013) (Figure 5.1b, also see section 6).

To investigate the origins of reflector A, two 3D seismic volumes and a single 2D seismic line was used. The first 3D seismic volume is the T38 survey (see Hansen and Cartwright, 2006a), which has a bin spacing of 25 m. It is not mentioned in Chapter 2 as the seismic processing on the version available to the author images very few sills, so the survey was only used to confirm that reflector A was present in this area (survey 1 on figure 5.2).

Figures/ch4_capture1.png

FIGURE 5.1: Seismic inline 20690 from the Rockall 3D seismic survey, and interpretation. Reflector A is shown in bright green. Black arrows show a possible fluid flow mechanism after [Rateau et al. \(2013\)](#). [Redacted]

The second (and main) 3D seismic volume used in this section is the Rockall 3D survey, which is described in section 2.3.1 (survey 2 on figure 5.2). The 2D seismic line used was the WG152DOGA1000002A012 line from the UK Oil and Gas Authority (UK OGA) survey, which is part of the OGA survey (see Chapter 2) (survey 3 on figure 5.2). Well control for the interpretation was from wells 164/27-1 and 164/28-1, for which full log suites and well completion reports were available. Unfortunately, the interval of interest was not logged, leading to difficulty in initially identifying what reflector A represents.

Figure 5.3 shows a seismic section from the Rockall 3D survey, while figure 5.5 shows the stratigraphy of the basin. Within the Horda package, a high amplitude reflector can be seen, interpreted in green. The reflector shows prominent topographic highs and lows, with varying wavelengths and amplitudes. Reflector A is positive polarity, indicating an increase in acoustic impedance, and can be seen to crosscut stratigraphy between the top Horda and top Balder horizons. Due to this discordance with other strata, one possibility is that it could be a seismic artefact. This is relatively easy to rule out. Figure 5.4 shows a region where all three seismic surveys overlap. The same reflector can be seen to crosscut stratigraphy in the same place on all three seismic surveys, despite different acquisition and processing parameters. Thus, the chance of it being a seismic artefact is extremely small.

Figure 5.6 shows a map of reflector A interpreted across the different seismic surveys. The horizon shows prominent domes and depressions of around 0.15 seconds from peak to trough, but in extreme cases close to 0.4 seconds. This represents an amplitude of around 200 m. The domes are spaced around 2–4 km apart. There is an overall trend of high in the southeast and low in the northwest, which represents the regional dip of strata in the area.

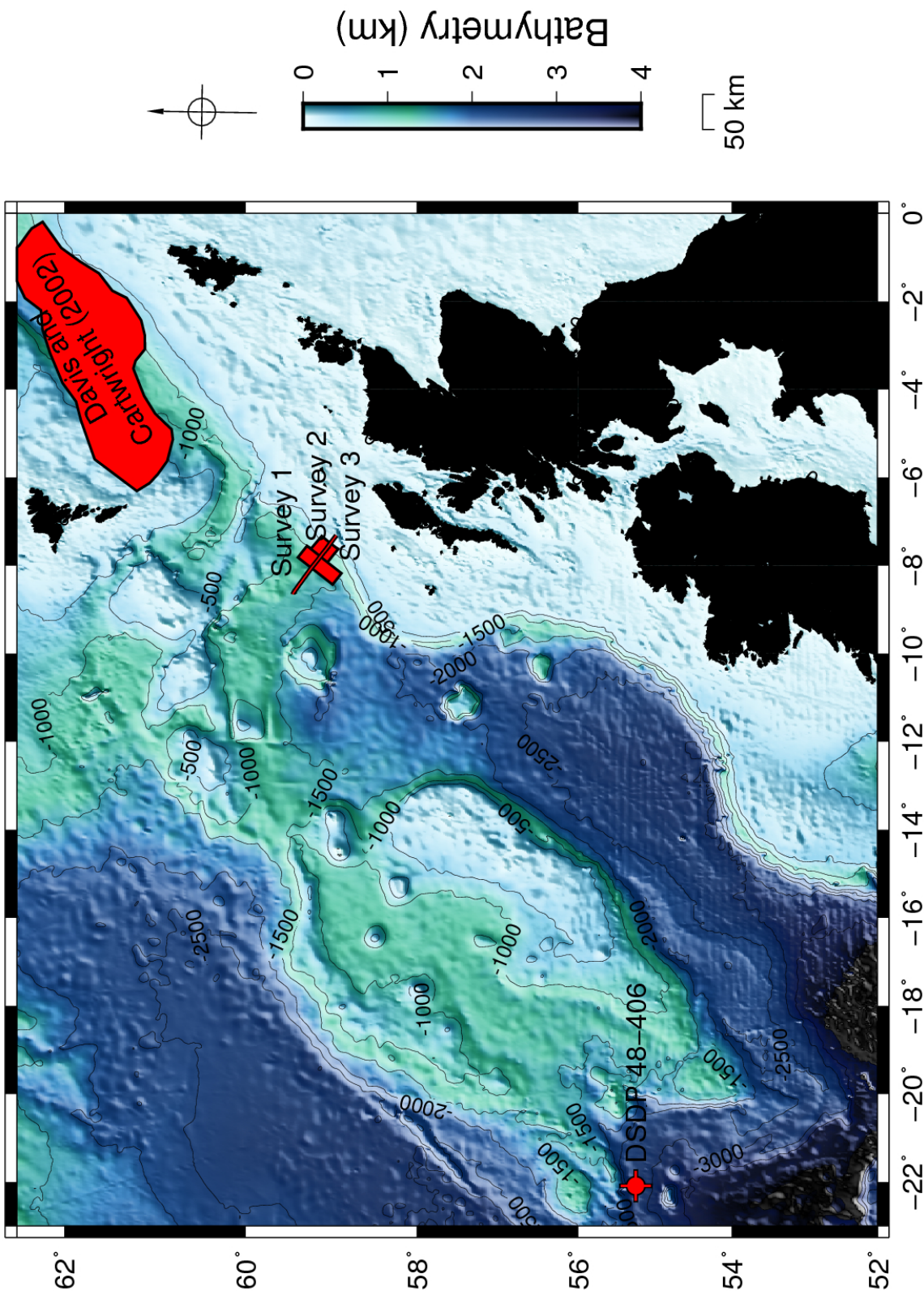


FIGURE 5.2: Map showing the three surveys where reflector A was mapped in the North Rockall basin. See text for details.

Figures/ch4_first_opal_fig.png

FIGURE 5.3: Seismic inline 20670 from the Rockall 3D survey, showing the interpreted stratigraphy of the basin. [Redacted]

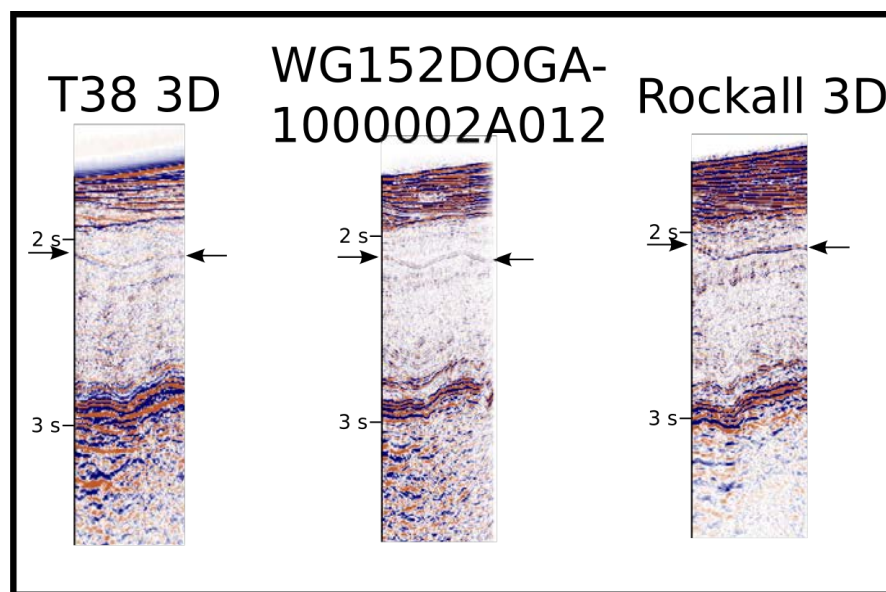


FIGURE 5.4: The same section on three different seismic surveys, showing that reflector A (delimited by arrows) is unlikely to be a seismic artefact. Reflector A is present on three different seismic surveys collected over a 20 year time span, with different seismic acquisition and processing for each survey.

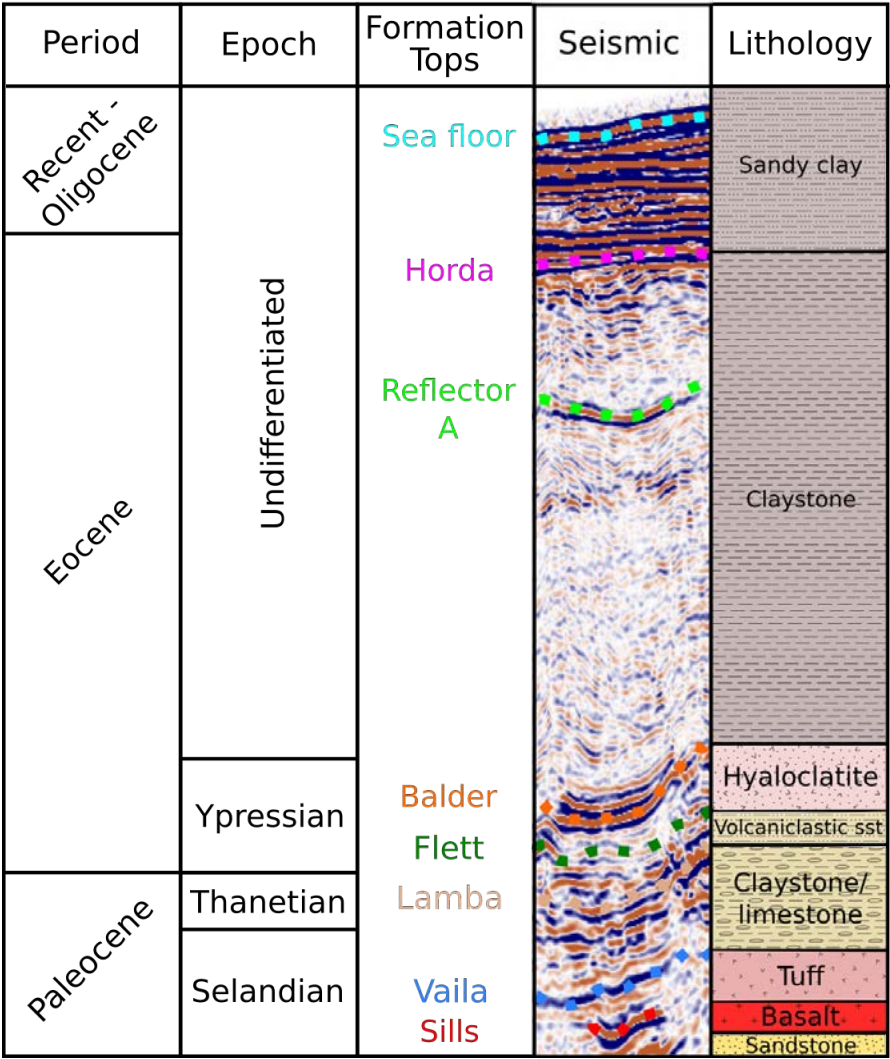


FIGURE 5.5: Stratigraphic column for NE Rockall, showing context for reflector A. Bulk lithology based on well 164/28-1.

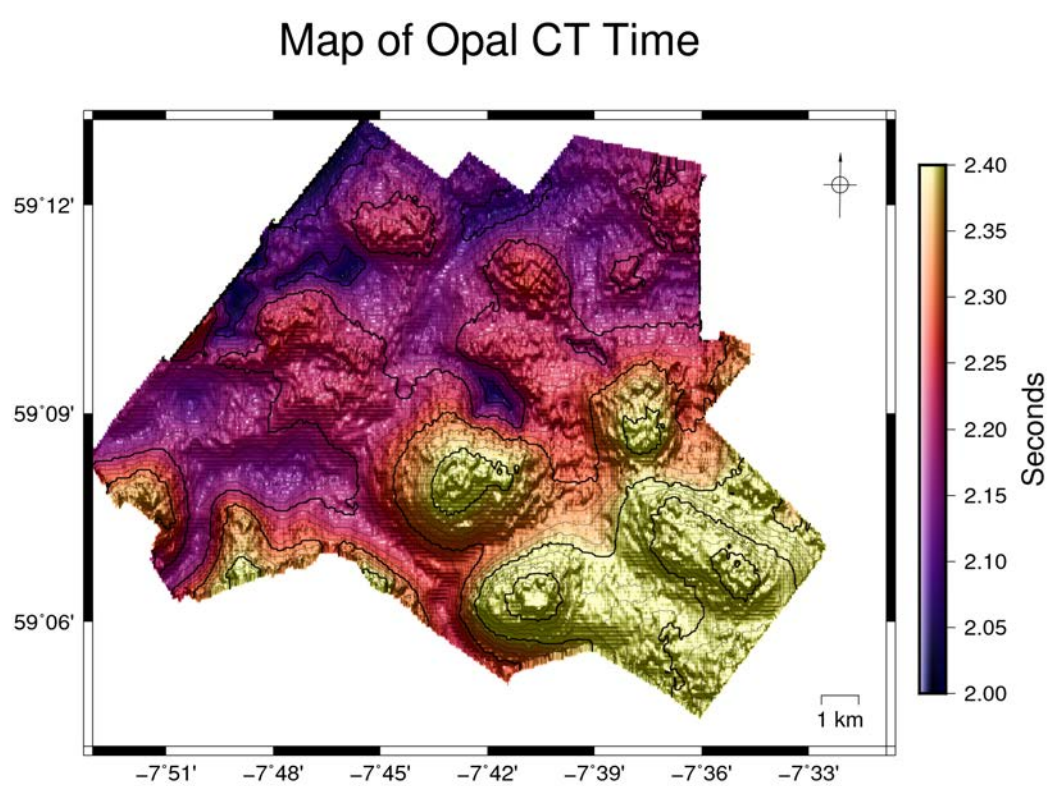


FIGURE 5.6: Time map of reflector A across the Rockall 3D seismic survey.

5.3 Is Reflector A an opal A–CT transition?

As is common in the petroleum industry, the shallow section of the wells which penetrate reflector A in the NE Rockall Trough were not logged. Due to this, it is difficult to unequivocally say what reflector A corresponds to. Given the observations that the reflector roughly parallels the seafloor but locally cross-cuts stratigraphy, a diagenetic boundary seems possible. Two types of diagenetic boundaries are commonly imaged in seismic reflection data: opal A–CT transitions and methane hydrates. These reflectors are commonly referred to as bottom simulating reflectors (BSRs) as they roughly parallel the seafloor. Reflector A in the NE Rockall basin is concluded to be an opal A–CT reflection, based on the following six arguments:

1. [Davies and Cartwright \(2002\)](#), [Ireland et al. \(2010a\)](#) and [Neagu et al. \(2010\)](#) describe seismic reflections from opal A–CT transitions where the opal transition is confirmed by well data. All reflections are high amplitude and have polarities indicating an increase in acoustic impedance. All reflections crosscut stratigraphy and roughly parallel the seafloor. Figures 5.1 and 5.3 show these factors to be satisfied for reflector A in Rockall. The observed positive polarity argues for an opal A–CT transition over other possible bottom simulating reflectors (BSRs) such as methane hydrates, which have a negative polarity.
2. The location of the study area is directly between two sites where an opal A–CT transition has been proven in well or borehole data (well 214/4-1 in the FSB ([Davies and Cartwright, 2002](#)), and DSDP leg 48 site 406 on the Southern Rockall Plateau). Notably, in the FSB the opal A–CT boundary is seismically imageable.
3. [Davies and Cartwright \(2007\)](#) and [Ireland et al. \(2011\)](#) show amplitude maps of opal CT reflectors, with rings of high and low amplitudes inside some structures comprising the opal CT reflection. Figure 5.7 is an amplitude extraction map of reflector A in NE Rockall, where hot colours indicate high amplitudes and cold colours indicate low amplitudes. Note the concentric ring structures that characterise many of the swells. Interestingly, the structures in [Davies and Cartwright \(2007\)](#) and [Ireland et al. \(2011\)](#) are not domes and swells as these are in Rockall, but instead are within polygonal structures which are not unlike a honeycomb structure. The gross morphology of reflector A in NE Rockall and the opal A–CT boundaries described in [Davies and Cartwright \(2007\)](#) and [Ireland et al. \(2011\)](#) are different, but the amplitude rings in both are probably caused by the same mechanism of tuning effects where the opal A–CT cuts other reflections, giving weight to the diagenetic boundary hypothesis.
4. There is evidence that the transition represents a boundary between a more and a less dense rock, based on the high amplitude and positive polarity of the reflector.

Map of Opal CT Amplitude

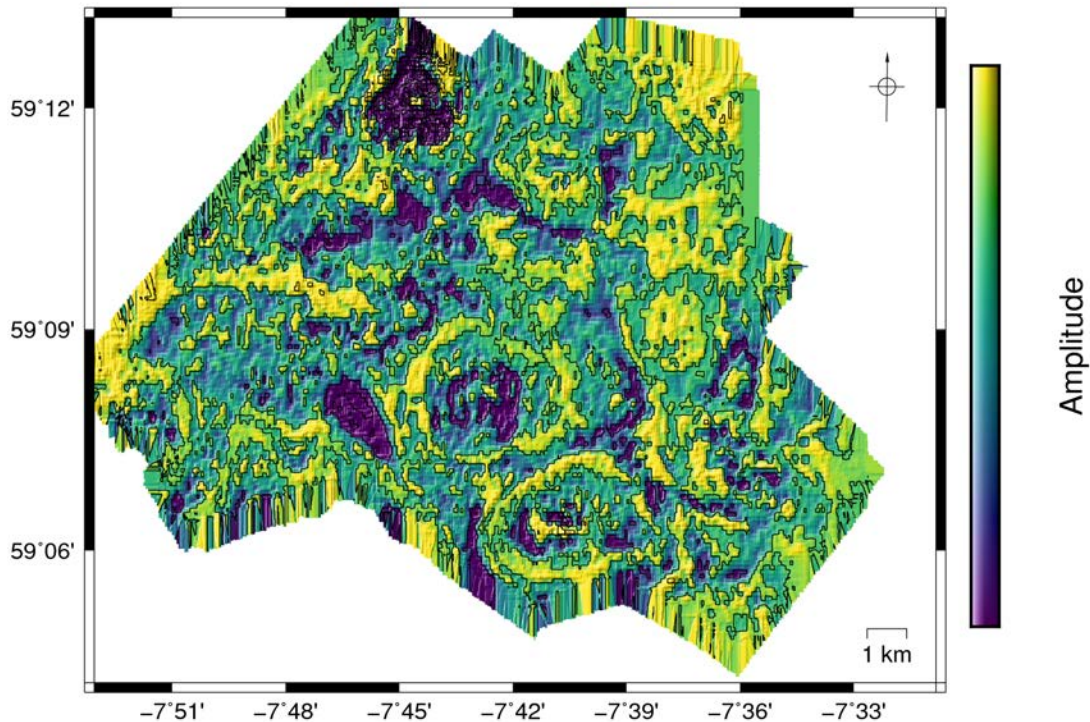


FIGURE 5.7: Map of reflector A across one of the 3D seismic surveys, with colours representing seismic amplitude.

Figure 5.8 shows a multipanel plot showing the correspondence between the time and amplitude maps shown previously, when they are co-blended with a similarity attribute. In this context, co-blended refers to that the two maps have been combined together by using the similarity attribute to apply dark and light shading to the colour scale, to give a map showing two seismic attributes. These maps show that the faults picked out by the similarity attribute have a pattern corresponding to many small concentric faults, with fewer small radial faults, which are most concentrated above the steepest dipping parts of the opal A–CT boundary. This may be expected above differential compaction structures, such as salt or igneous bodies. As the transformation from opal A to opal CT involves porosity loss and an increase in density it may be expected that the overlying rock may compact differently, which would lead to minor faulting above the topographic highs as figure 5.8 shows.

5. The DSDP drill core on leg 48, hole 406 encountered opal CT in Early Eocene strata. This is found in the same depth range as reflector A on the Rockall 3D survey, and has similar expected seismic characteristics compared to a synthetic seismogram. This site had poor recovery of core in the lower parts of the hole, but did have enough to be studied by Kagami (1979). Kagami (1979) show evidence from xray diffraction, which

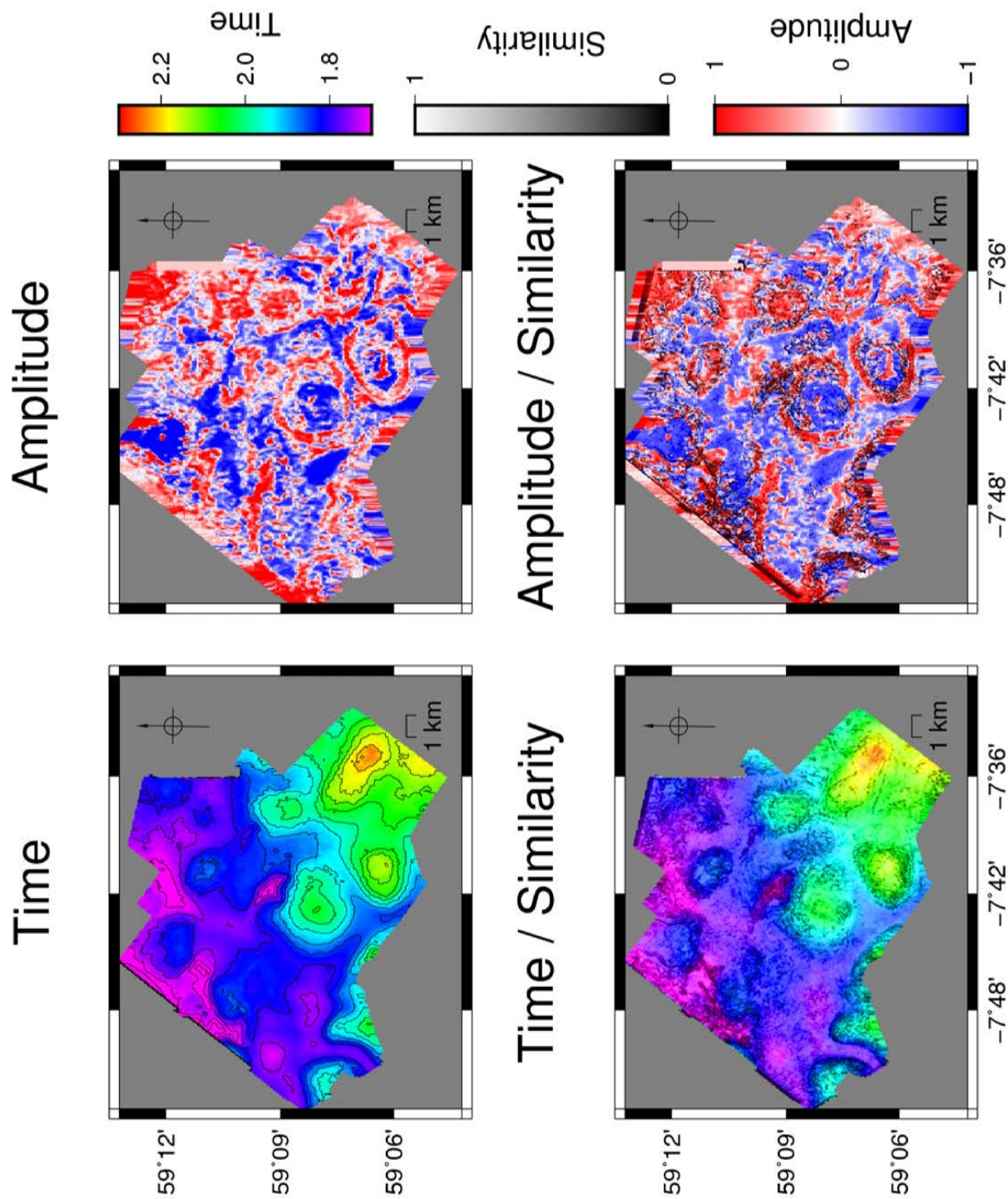


FIGURE 5.8: Maps of Reflector A. Clockwise from top left: Time structure map, Amplitude (time) map, Time-Semblance co-blend map, Amplitude-Semblance co-blended map.

shows change from opal A to opal CT at around 680 meters in hole 406. Figure 5.9 shows wireline well logs for DSDP borehole 406. The zone where opal CT was found by Kagami (1979) is marked. Kagami (1979) suggests that the opal CT transition is not a single sharp boundary, but either is gradational, or is a zone of multiple alternations of opal A and opal CT. This DSDP well is 900+ km from the study area, so direct seismic correlation between the two sites is not possible. However, Morewood et al. (2004) briefly mention a reflector in the central Rockall Trough that they believe may be an opal A–CT transition. This transition is also found in the depth range of reflector A, so this opal transition may be connected to reflector A in NE Rockall. The final panel of figure 5.9 shows a synthetic seismogram. This was created by finding the acoustic impedance ai :

$$ai = \rho V_p \quad (5.1)$$

Where ρ is the density and V_p is the p-wave velocity. From this, the reflection coefficient (RC) is found as the derivative of this, such that:

$$RC = \frac{d}{dz} ai \quad (5.2)$$

This was then convolved with a ricker wavelet with a peak frequency of 25 Hz. The synthetic seismogram shows that, as observed in the NE Rockall seismic survey, the opal CT is expected to be a positive polarity high amplitude reflection. However it shows that at the location of DSDP hole 406 a zone of several high amplitude reflections is expected, corresponding to a number of changes in acoustic impedance within the zone of opal CT recovery. It is difficult to say what this corresponds to geologically, but multiple authors (e.g. Behl, 1999) have reported the opal CT to be a zone rather than a sharp boundary, and this may be the case in hole 406.

Figure 5.10 shows a map of the depth below the seafloor of reflector A in the NE Rockall 3D seismic survey. As can be seen from the values on the horizon and from the inset histogram, the range of depths that reflector A is found in does encompass the depth where an opal CT transition was found in DSDP leg 87, hole 406 (Figure 5.9).

To summarise point 5, the opal A–CT transition DSDP borehole 406 occupies the same depth range as reflector A in NE Rockall, and although the the Rockall 3D survey and DSDP borehole 406 cannot be directly correlated, synthetic seismic models of DSDP borehole 406 has similar seismic characteristics to reflector A in NE Rockall.

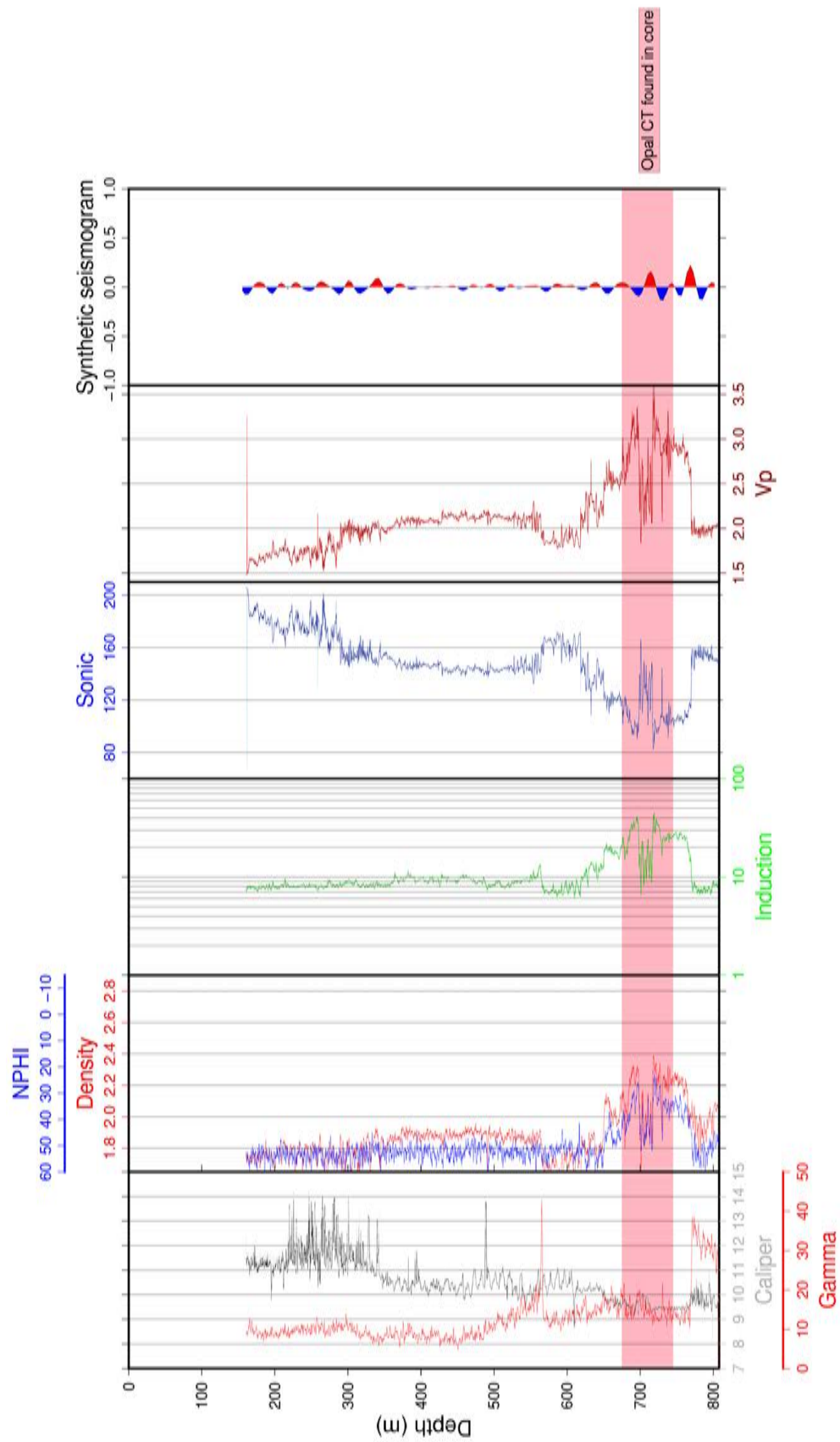


FIGURE 5.9: DSDP leg 48 hole 406 well logs, showing signatures which may imply an opal CT boundary. Zone where opal CT is found in cores is marked in red.

Depth below seafloor of Opal CT

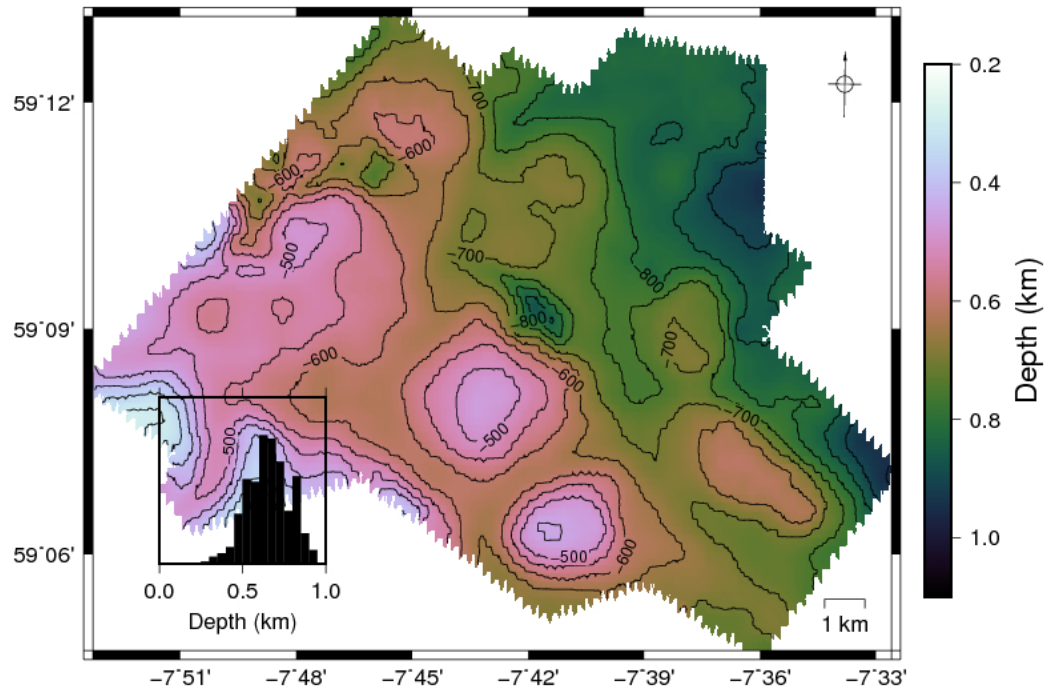


FIGURE 5.10: Map of depth below seafloor of reflector A in the NE Rockall seismic survey. Depth conversion used velocity information from well 164/27-1. Inset shows histogram of the depths.

6. Reflector A is not related to postdepositional folding or draping to give it its topography. This is easily shown by an isopack map between reflector A and the underlying Balder horizon (figure 5.11), which shows significant thickness variations between the two horizons. Assuming constant sedimentation rate across the area of the Rockall 3D survey, if the topography on reflector A was due to folding or draping only figure 5.11 would be expected to show almost no thickness variation.

Based on the six previous pieces of evidence, it is most likely that reflector A is an opal A–CT transition.

Isopack Opal A–CT to Balder

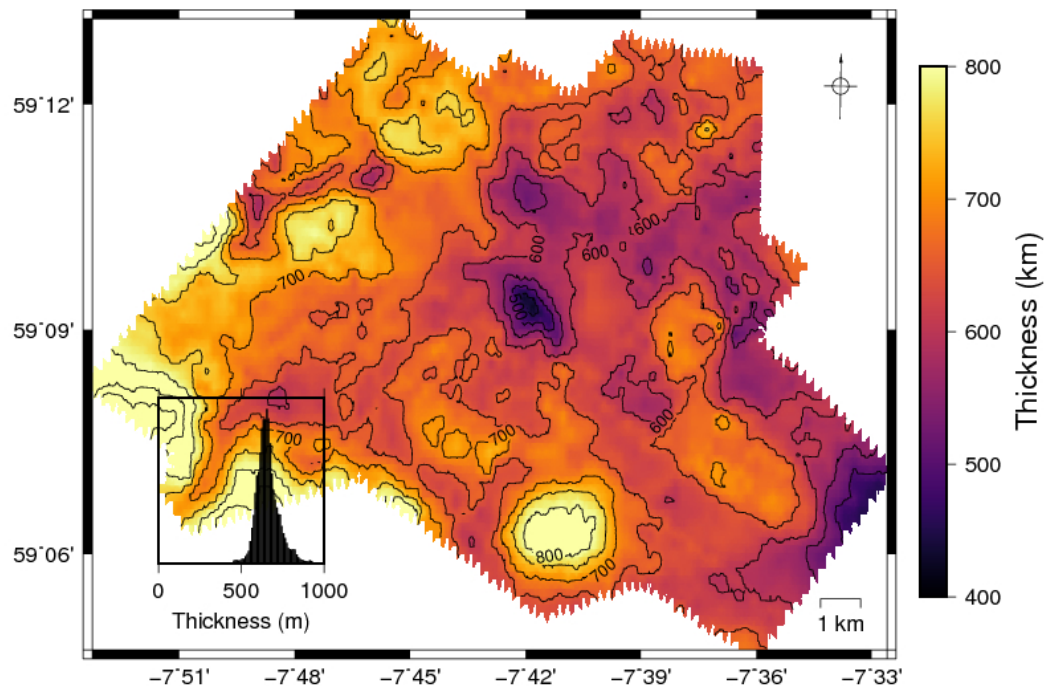


FIGURE 5.11: Reflector A to underlying Balder isopach.

5.4 Evidence for opal A–CT fossilisation

Having established reflector A to likely be an opal A to CT transition, a couple of observations needed to be explained. These observations lead to the opal A–CT transition in NE Rockall being classified as a fossilised opal A–CT transition (Davies and Cartwright, 2002).

- Much of the opal A–CT transition appears to be 600 m below the seafloor or deeper, and exists up to 1 km below the seafloor (figure 5.12).
- The opal A–CT parallels the top of the Horda formation more than it parallels the present day seafloor — the majority of the transition lies only 150 m below the top Horda, and is no deeper than 372 m below (figures 5.13 and 5.14).

The main control on opal A–CT transition formation is temperature (Davies and Cartwright, 2002; Dralus, 2013; Kastner et al., 1977), which is the main reason that opal transitions commonly subparallel the seafloor to form BSRs. However the opal transition is clearly not subparallel to the seafloor in NE Rockall (figure 5.10), having almost a kilometre of relief compared to the seafloor depth. The opal transition parallels the Horda formation top much more closely, having on average only ~ 150 m difference between the transition

and the top Horda reflection. These two observations would imply that the opal A-CT transition may be fossilised in NE Rockall.

Isopack Sea floor to Balder

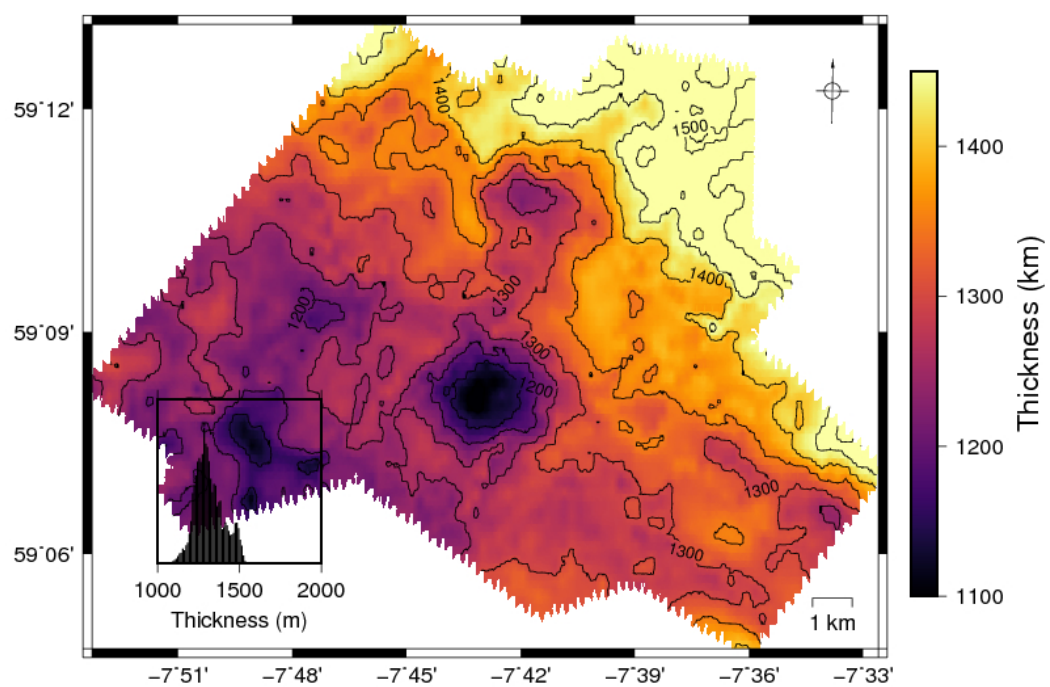


FIGURE 5.12: Sea floor to Balder isopack

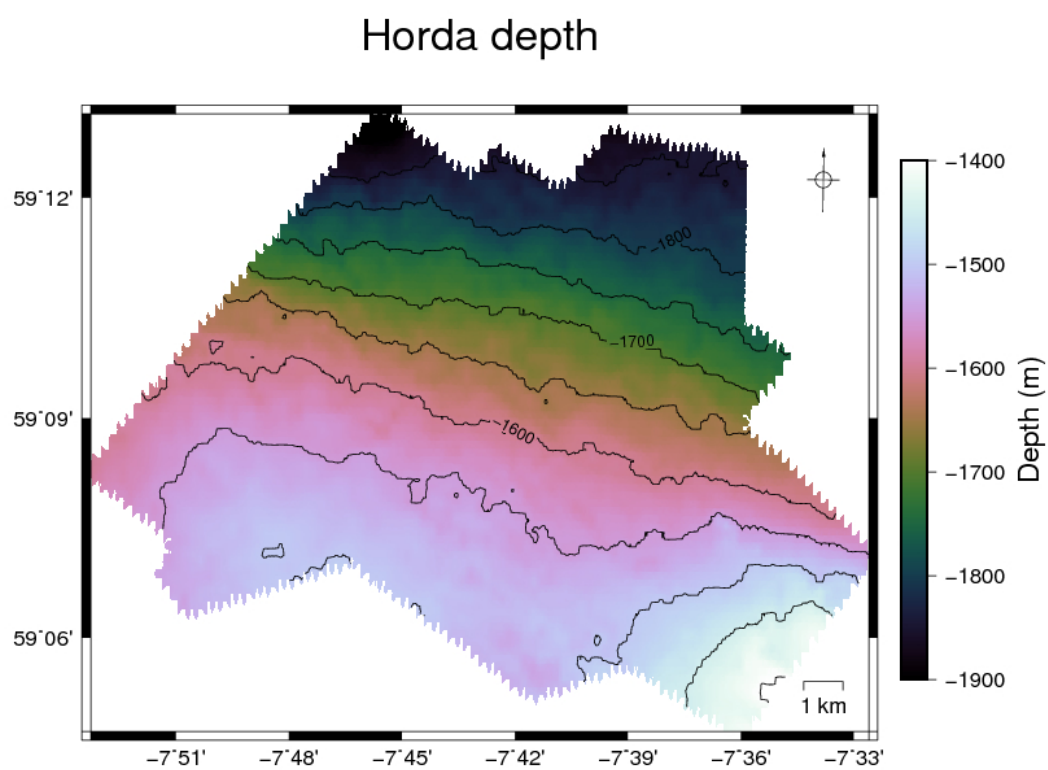


FIGURE 5.13: The depth below sea level of the top Horda horizon, interpreted on the Rockall 3D seismic survey.

Isopack Horda to reflector A

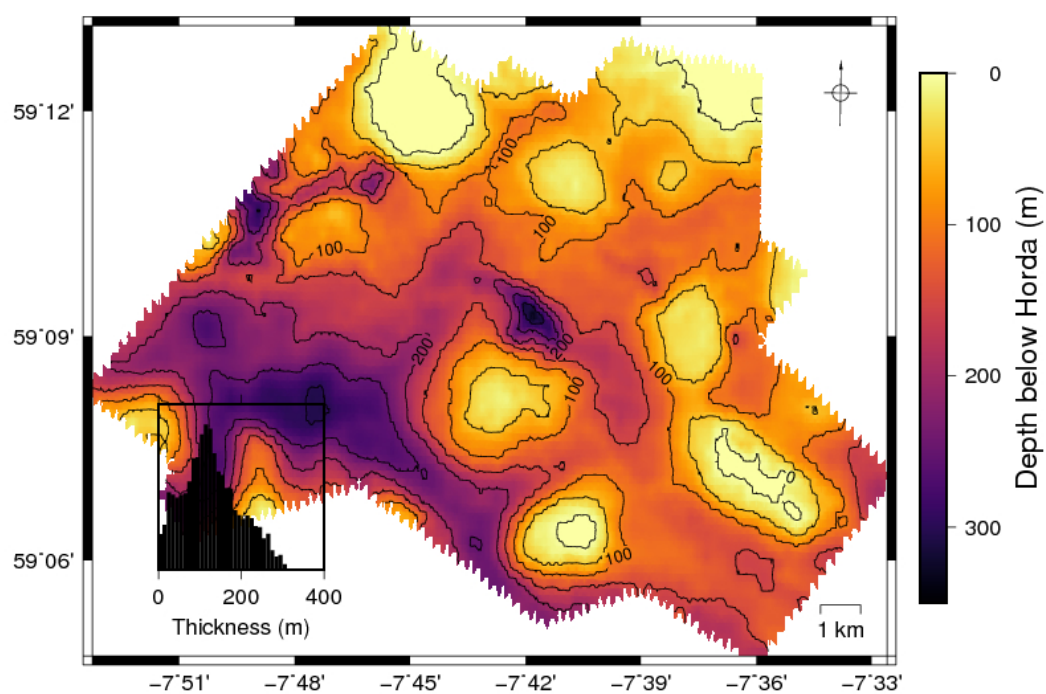


FIGURE 5.14: Isopack map showing distance between the top Horda horizon and reflector A

5.5 Relation to sills

Having established reflector A to likely be a fossilized opal A to CT transition the relation to underlying sills was then investigated, based on the apparent spatial relationship of highs in topography on the opal A–CT and sill tips *à la* figure 5.1. First, each sill was interpreted in the volume based on standard seismic stratigraphic principles (e.g. Hansen et al., 2004; Thomson, 2007). These sills were then exported as individual files and their outlines overlain on the opal A–CT topography to form figure 5.15. According to the model of Rateau et al. (2013), the shallowest sills should have the greatest effect on focusing fluid to shallower levels in most sill complex configurations, so we may expect to see areas of enhanced fluid flow around the edges of these. Furthermore, section 3.3.1 shows that the majority of sills in the FSB and Rockall Basins are saucer shaped, transgressive or inclined, which would give clear directions of fluid focusing, so the data used here should be directly applicable to the Rateau et al. (2013) model. However, figure 5.15 shows no obvious correlation between sills and the opal A–CT topography. There are examples where the opal boundary displays relative highs overlying the middle of sills, near the edges, and far away. In other words, there is no obvious correlation.

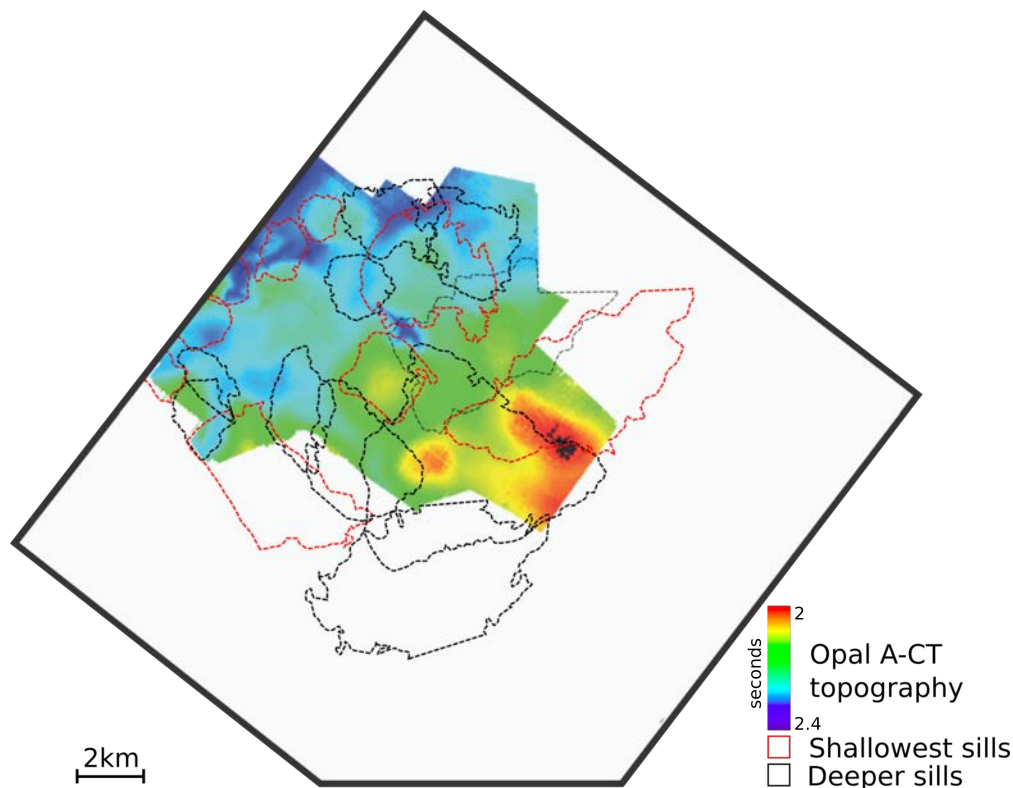


FIGURE 5.15: Topography of the opal A–CT boundary, with underlying sill outlines. The shallowest level of sills are coloured red. Under the model of Rateau et al. (2013), the highs should correlate with the edges of the shallowest sills or the outermost sills. This does not appear to be the case.

5.6 Towards a model for the Rockall opal A–CT transition

Turning the attention to the topography and planform of the opal A–CT transition, the morphology could be described as a series of convex-up domes with low areas between them. This looks similar to a convective planform system (figure 5.16). Many of these domes form some sort of an interlocking egg box like shape, leading to many of the domes being somewhat hexagonal. Many of the junctions between domes look close to trilete, with angles of $\sim 120^\circ$ being common. This is a common planform for a convection system formed between a hot basal layer and a cool upper layer with a fluid in between. The convection system is characterised by hot upwelling plumes of fluid being balanced by cool downwelling sheets of fluid. This can be observed over multiple length scales, from centimetre scale (e.g. a lava lamp) to thousands of kilometres (e.g. mantle convection, see figure and caption of figure 5.16).

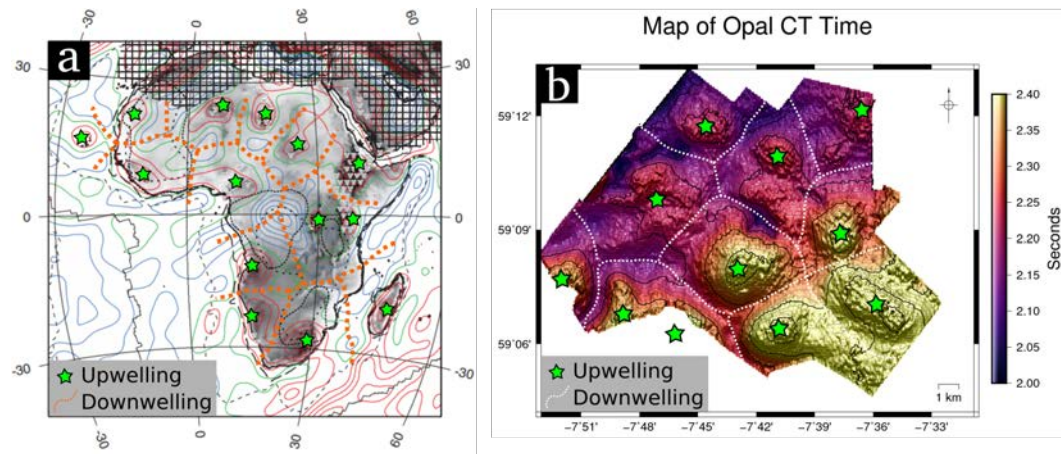


FIGURE 5.16: Similarity between the topography on the opal A–CT and a convective planform. a. Jones et al.’s (2012) figure 1a, showing the long wavelength gravity anomaly over Africa as a proxy for the mantle convective planform, modified to show sites of upwelling (green stars) and downwelling (orange dotted lines). b. Time structure map of the opal A–CT boundary in Rockall, with sites of upwelling (green stars) and downwelling (white dotted lines).

The Paleocene – Eocene sills may have acted together as a hot basal layer. This section will show evidence that many overlapping, closely spaced sills intruded over a short timescale, may act as a single hot, laterally extensive layer. Sequence stratigraphic evidence of a lack of erosional unconformities, and lithological evidence of the predominance of deep marine shales in nearby wells, indicates that the study area in NE Rockall has been submarine throughout the Cenozoic. This means the Eocene sedimentary sequences were sandwiched between the cool upper surface of the seafloor and the hot basal layer of intruded sills. Given that the opal A–CT transition likely represents close to an isothermal boundary, the observed topography could therefore be a function of the lateral variation in geothermal gradients induced by the convective system.

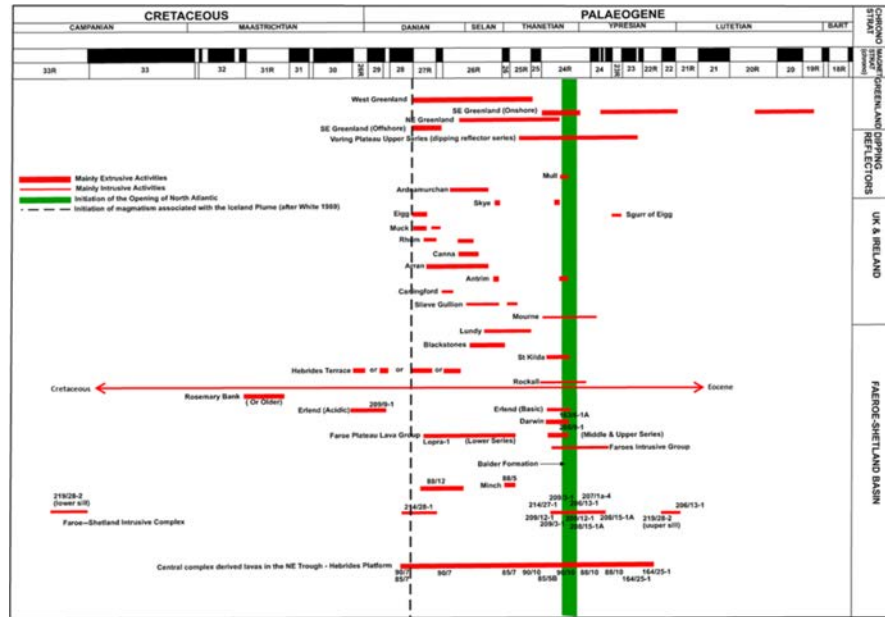


FIGURE 5.17: Radiometric derived ages for intrusion and extrusive magmatism in the NAIP, after Egbeni et al. (2014b). The dominant period of volcanic activity stretches from the mid Danian to the late Thanetian, a period of around 4 Ma.

From such observation the natural question is did the sills in NE Rockall intrude close together enough in time to be considered a single hot basal layer? This question can be studied by calculating intrusion repeat times in two separate ways. First, the time period of sill intrusion can be compared with the number of sills in the LIP. Secondly, the reciprocal of the sill area density can be compared with the plume area flux.

The repeat time T_r for sill intrusion can first be estimated by

$$T_r = \frac{S_n}{T_{si}} \quad (5.3)$$

where S_n is the number of sills in the province, and T_{si} is the time period for sill intrusion. T_{si} can be estimated by looking at radiometric dates (figure 5.17), which gives an estimate of 4 Ma. However in practise this will likely be the upper bound for the intrusion event, because the scatter in radiometric ages likely inflates this time period.

An intrusion time period of 4 Ma represents intrusion across the whole igneous province rather than just the NE Rockall basin, therefore to estimate the province repeat time of intrusion this should be divided by the number of sills present in the whole province. The number of sills in the NAIP is estimated in section 7.1.2. The number of sills in the NAIP is estimated to be 19,695, which is expected to be a lower bound, as it's calculation

is based on the number of sills observed on seismic data uncorrected for subseismic sills. Dividing 4 Ma by 19,695 gives a repeat time of around 51 years.

A different method of estimating the repeat time for sills is to use the equation

$$T_r = \frac{1}{\rho_s Q} \quad (5.4)$$

where ρ_s is the sill area density, and Q is the mantle plume area flux. Sill area density was estimated in section 3.4.1, and range from around 0.01 to 0.04 sills/km. Mantle plume area flux has been estimated by a number of authors (e.g. Rudge et al., 2008; Stucky de Quay et al., 2017). Here, a value of $4.6 \text{ km}^2 \text{ yr}^{-1}$ is used, which is found by modifying Stucky de Quay et al.’s (2017) estimate by aspect ratio of the the elliptical plume head model (MacLennan and Jones, 2006; Nisbet et al., 2009; Saunders et al., 2007). Using these values, equation 5.4 gives a repeat time of $\sim 10 \text{ yr}$. Using flux values for a circular plume head, or using Rudge et al.’s (2008) flux estimates, yields repeat times on the order of 5 – 50 years. Compared to the time scales to cool an intrusion — which we calculate as typically on the scale of thousands to tens of thousands of years (equations in section 7.3) — this is easily quick enough for the intruded sills to cool akin to a single hot basal layer.

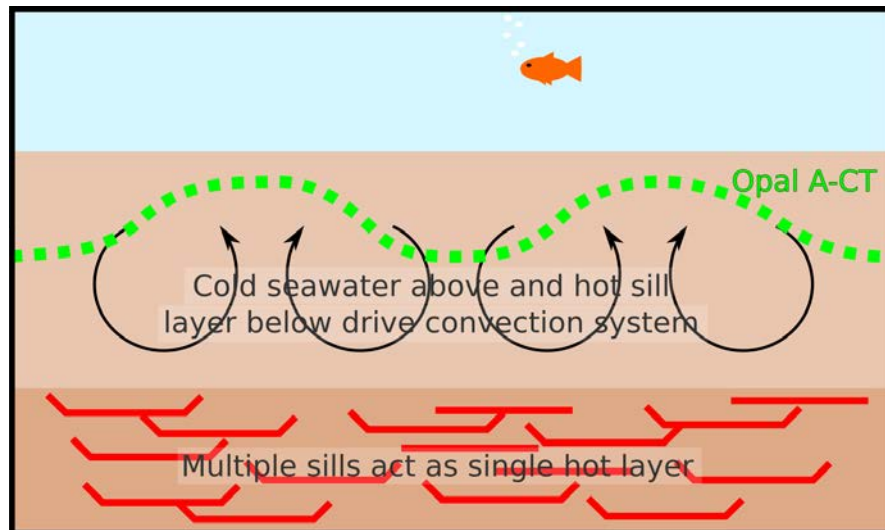


FIGURE 5.18: Conceptual model for the formation of topography on opal A–CT boundary in Rockall. Many sills intrude close together spatially in a short period of time, leading to the intruded stratigraphic sequence heating up. This layer stays hot through much of the Eocene, driving a convective system of pore fluids. During this time, opal rich sediments are deposited, and the opal A–CT boundary develops topography as a result of the perturbations in lateral geothermal gradients caused by the convective system.

There are few published studies with which to compare this model of opal A–CT formation with, however, some studies have been published which shed further insight. The

preceding section showed how intrusion rates across a province are high enough that sills are expected to intrude while the preceding intruded sill is still hot. The combined effect is expected to be large if thermal aureoles overlap. [Aarnes et al. \(2010\)](#) shows compilations of how thermal aureoles can be significantly wider than their sills (note, the compilation also shows that aureoles can be smaller than their sills), while [Annen \(2017\)](#) explains how the variation in aureole thicknesses can be a function of natural variation in thermal transfer rates between the magma and the host rock. Should this be the case in Rockall, this would serve to make the combined effect of multiple intrusions greater.

In relation to the large scale fluid convection proposed to be changing basin isotherms in Rockall, only two papers have so far studied convective flow around sills. [Wang and Manga \(2015\)](#) models the convective influence on the thermal properties of host rocks for a range of permeabilities using vitrinite reflectance as a tracer. Length scales of convection cells are on the order of a few tens of metres, which is almost two orders of magnitude smaller than the 1.5 – 2 km cells the opal boundary would require. However, convection is a naturally time dependent process, and [Wang and Manga \(2015\)](#) only presents results at a single unspecified time step in their model run.

[Iyer et al. \(2013\)](#) do similar modelling to [Wang and Manga \(2015\)](#), but show the importance of the time dimension. Similar to [Wang and Manga \(2015\)](#), lateral temperature gradients change on the tens to hundreds of meters scale in response to small scale convection cells. However, as the model run progresses cells merge to giving temperature contours with regular wavelengths at the kilometer scale, in good agreement with the scales observed for the Rockall opal boundary.

5.7 Opal A–CT kinetic parameterization

In the previous section it was argued that there was no evidence that the topography on the opal A–CT boundary in Rockall is related to the underlying sill tips. It was then suggested that instead of topography on the opal A–CT transition being related to individual sill tips, it may instead be the result of many sills acting as a single hot basal layer to drive a convection system.

One way to further investigate this convection hypothesis, is to model where the opal A–CT transition is expected to be in depth, and compare the transition's topography to this model. Such a model requires deriving the chemical kinetics for the opal A to opal CT reaction. Chemical kinetics describe how experimental conditions control the rate of a chemical reaction. Determination of chemical kinetics normally involves running multiple experiments for different combinations of parameters, to relate changes in

those parameters to changes in reaction rate. The most common parameters controlling the rate of a reaction are concentration, temperature, pressure, surface area, and the presence of a catalyst. In the case of opal A to opal CT transformation the dominant control is thought to be temperature (Dralus, 2013; Ernst and Calvert, 1969; Huang, 2003).

To make a kinetic parameterization for the opal A–CT transition, a global database of 83 opal A–CT measurements from well and borehole data was compiled. These observations mostly comprise DSDP, ODP and IODP records rather than purely seismic observations, and as such these observations are not subject to any bias due to misinterpretation of seismic reflectors not related to an opal transition (see appendix C). Data was collected on the depth of the opal transition, the age of the host sediments and the temperature at the boundaries, if this was recorded in the original studies. Average sedimentation rate was calculated between the present day and the age of the sediments at the current opal A to CT transition. The data collected is summarised in figure 5.19 for data less than 1 km below the seafloor.

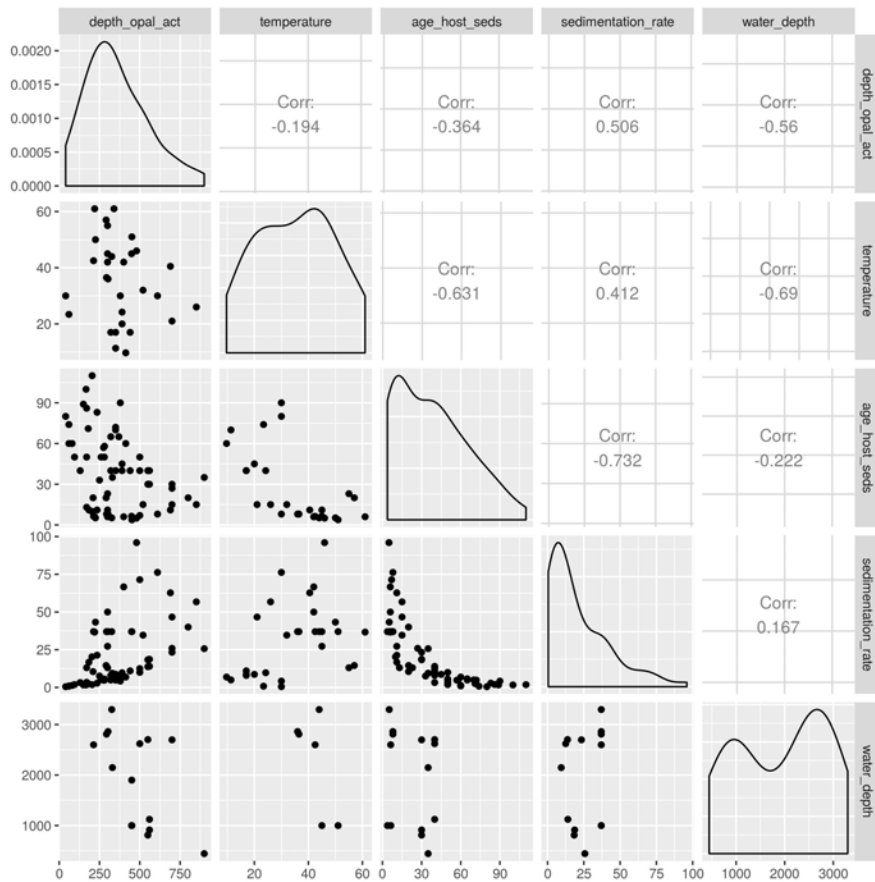


FIGURE 5.19: Scatter plot matrix for opal A–CT transitions less than 1 km deep. Plots on the lower left are scatter plots, the middle diagonal shows density polygons, and the upper right shows the Pearson correlation coefficient. See text for discussion.

The data have been truncated below 1 km because deeper than this the opal A to CT transitions are generally considered to be anomalous, often described as “fossilised” or inactive (e.g. [Davies and Cartwright, 2002](#)), and this would cause problems in deriving a kinetic model. Figure 5.19 shows that the modal depth of A–CT transition is 271 m below the seafloor. The histogram of the ages of host sediments shows that the opal A–CT transition is most likely to be found in young sediments, as would be expected for an active boundary. This helps to give confidence that most of the data points are active transitions. Water depth and temperature both comprise small sample sizes, so should be interpreted with caution. Positive correlation between the sedimentation rate and the depth of the opal A–CT is interesting as it implies that high sedimentation rates can bury active opal A–CT boundaries.

The observations from the opal A–CT database was then compared with the only two published kinetic models for the opal CT–quartz transition (figure 5.20). It is necessary to compare to an opal CT–quartz model rather than an opal A–CT model as no kinetic models for the opal A–CT transition have been published. Comparison of the opal A–CT data with the predictions of the opal CT–quartz models can be done because opal A–CT and opal CT–quartz boundaries — where both are observed — are commonly only a few tens of meters apart. Thus the depths of the opal A–CT data were increased by a constant 25 m to model an equivalent opal CT–quartz boundary for each opal A–CT observation (figure 5.20a).

Comparison of the geological observations with the laboratory kinetic models can be achieved with the key observation that the age of a sedimentary package is a function of depth and sedimentation rate. Due to this, the depth of the opal A–CT transition may be considered the time of reaction. Instead of considering a single area, the whole world is considered as one opal A to CT transition. In this reference frame, the range of depths that the opal A–CT transition is found at around the world is equivalent to the thickness of the reaction zone. This implies that the shallowest depth of observation of an opal A to CT transition is the start of the reaction, i.e. everywhere on earth shallower than the shallowest observed depth is only ever opal A. Similarly, the deepest observed depth of the opal A to CT transition is the end of the reaction zone, i.e. everywhere on earth deeper than the deepest observed occurrence will only be opal CT or microcrystalline quartz. With these assumptions, the normalised cumulative frequency graph of opal CT occurrence is a proxy for reaction progress, going from 0% to 100%, where 0% would indicate no reaction yet (e.g. everything shallower than that observation is still opal A) and 100% would indicate all opal A has converted to opal CT (i.e. everything deeper than the final occurrence is opal CT or microcrystalline quartz).

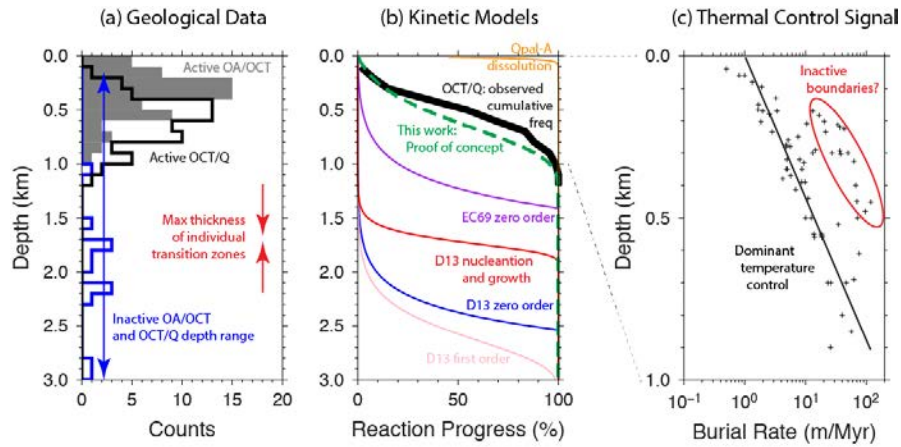
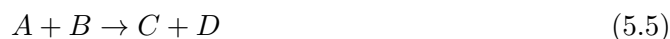


FIGURE 5.20: Comparison of data with published model results for opal CT-quartz kinetic parameterization. a) shows measured opal A to CT transition depths in DSDP, ODP and IODP wells around the world (grey bars), and modelled opal CT to quartz depths (white fill). Inactive opal A to CT depths are in blue. b) shows cumulative frequency plots of the active opal A to CT transitions, along with best fitting kinetic parameterization, and published models. Of the published models, EC69 refers to [Ernst and Calvert \(1969\)](#), while D13 refers to [Dralus \(2013\)](#). c) shows the importance of burial rate and depth — an indicator of a strong thermal control on the reaction.

Figure 5.20b shows the results of comparing the laboratory kinetic models with the geological observations of worldwide opal A–CT transitions. Figure 5.20b also shows the results of the kinetic parameterization we obtain by inversion of the worldwide dataset, which is described in subsequent paragraphs. As can be seen from figure 5.20b, none of the published parameterizations model geological observations well. The three models of [Dralus \(2013\)](#) predict opal CT–quartz transitions up to three kilometres depth, entirely at odds with geological observations, which indicate the deepest observations to lie around 1.1 km depth (with the exception of fossilised / inactive boundaries). Of the models by [Dralus \(2013\)](#), the logistic like shape of the nucleation and growth model appears to be the most similar to the shape of the geological observations. The model of [Ernst and Calvert \(1969\)](#) comes closest to geological observations in terms of depth, but predicts much of the observed boundaries to be around 750 m deeper than they are.

Due to this mismatch in the predictions of laboratory kinetic parameterizations and geological observations, a new kinetic model for the opal CT–quartz transition was found by inverting the worldwide opal A–CT data. Chemical kinetic parameters are normally found in three steps. First, a rate law is chosen to represent the reaction. This is normally found from running multiple experiments changing a single variable (e.g. concentration of one reactant, or temperature) and measuring the changes in concentration of a reactant or product with time. Secondly, a rate constant is found from the experimental runs where temperature is varied only. Thirdly, the constants A (the frequency factor) and E_a (activation energy) are found from further experiment runs.

To illustrate this, consider the following hypothetical chemical reaction:



Where A and B are reactants, and C and D are products. The reaction rate r can be expressed:

$$r = -\frac{\Delta[A]}{\Delta t} = -\frac{\Delta[B]}{\Delta t} = \frac{\Delta[C]}{\Delta t} = \frac{\Delta[D]}{\Delta t} \quad (5.6)$$

Where t is the time. Note the negative sign indicating that reactants are used up. This is defined by a rate law:

$$r = k[A]^x[B]^y \quad (5.7)$$

Where k is the rate constant, and x and y are the rate orders with respect to that reactant (Note that the units of k depend on the rate law, see table 5.1). The overall order of the reaction is found as the sum of the exponents ($x + y$, in the above example). The most common reaction orders are 0th, 1st and 2nd order reactions, although higher order reactions do exist.

TABLE 5.1: Rate constant units for different reaction orders

	Rate law	Units
0th order reaction	$r = k[A]^0$	mol s^{-1}
1st order reaction	$r = k[A]^1$	s^{-1}
2nd order reaction	$r = k[A]^2$	$\text{mol}^{-1} \text{s}^{-1}$

An easier way to visualise this is by considering how the rate constant controls the change in concentration with time, which gives the differential equation:

$$\frac{\delta[A]}{\delta t} = -k[A] \quad (5.8)$$

for the 1st order case, or

$$\frac{\delta[A]}{\delta t} = -k \quad (5.9)$$

for the 0th order case.

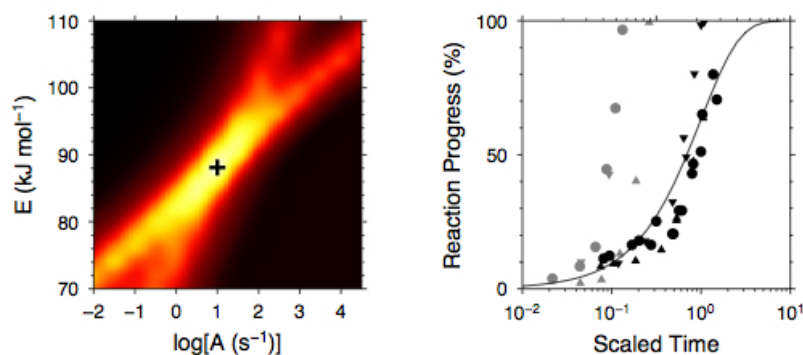


FIGURE 5.21: Inversion results for opal A-CT kinetic parameterization, model created by Jones, SM. Left panel is RMS misfit for frequency factor and activation energy. Right hand panel is best fit parameterization to all data.

Finally, the frequency factor A and the activation energy E need to be found from the Arrhenius equation:

$$k = A \exp\left(\frac{-E_a}{RT}\right) \quad (5.10)$$

Where R is the gas constant. More conveniently, the Arrhenius equation can be rewritten

$$\ln(k) = \ln(A) - \ln\left(\frac{E_a}{RT}\right) \quad (5.11)$$

which has the form $y = mx + c$, the equation of a straight line. Thus, A and E_a can be found by fitting a linear regression model of $\ln(k)$ against $\ln(1/t)$.

For this study, however, access to lab equipment and samples was not possible. Instead the standard method outlined in this section was modified, and worldwide data for opal A-CT depths were inverted to find the best fitting reaction parameters, using techniques similar to those used in section 4.3.2.2. A parameter sweep for frequency factor A between 10^{-4}s^{-1} and 10^{10}s^{-1} , and activation energy E between 70 kJ mol^{-1} and 110 kJ mol^{-1} was undertaken. The reaction is approximated as a first order reaction, based on the results of Dralus (2013). The profile of the conversion from opal A to opal CT is predicted from equation 5.8 and 5.10 and then normalised, and the RMS misfit between the predicted profile and the cumulative distribution of opal A-CT depths worldwide is found. The RMS misfit is also found between the normalized opal CT to quartz transition parameters of Ernst and Calvert (1969) and Dralus (2013) for comparison. Figures 5.20 and 5.21 show the results of this method.

Figure 5.21 shows there are a range of values of frequency factor and activation energy that result in a good fit to the data, with similar trade offs between the logarithm of the frequency factor and the activation energy. Figure 5.20 shows the results to be a good fit to much of the data, and indeed better than the laboratory results of Dralus (2013) and Ernst and Calvert (1969).

These results can be used to predict the opal A–CT transition depth for different geothermal gradients and sedimentation rates, assuming constant sedimentation rate and geothermal gradients. Figure 5.23 shows the result of modelling this, done by Jones, SM. In this model the relationship between the age of sediments at the depth of the opal transition, and the depth to the opal CT – Quartz transition is shown for different geothermal gradients. This model is made by combining equation 3.9 and 5.10, and was solved using a finite difference scheme. Parameters for equation 5.10 were taken from the new kinetic parameterization ($A = 10$, $E = 88100$, $n = 2.45$ and R (the universal gas constant) $= 8.314$), while equation 3.9 used values of $\phi_0 = 0.6$ and $\lambda = 2$ — appropriate values for fine grained sediments such as diatomites. Each model assumes a constant geothermal gradient and sedimentation rate, the latter calculated as the average rate from the Eocene to the present day. The opal transition depth can be seen to be strongly dependent on sedimentation rate, especially at lower geothermal gradients. Sedimentation rates in the NE Rockall basin have varied over time (figure 5.22). However, the area we are looking at covers only a few tens of square kilometres, and thus has the same sedimentation rate across the whole area, so this cannot be the cause of the opal A–CT topography. The depths on figure 5.14, combined with the age of the Horda formation would therefore indicate geothermal gradient to be 70°C km^{-1} or greater. This is much higher than the present day gradient of $\sim 40^\circ\text{C km}^{-1}$ in the FSB, and thus may well be consistent with a model of a hot basal layer of sills cooling through the Eocene. The swells on the opal A–CT transition can be seen in figure 5.10 to have amplitudes of around 150m. Figure 5.23 indicates that this would require lateral temperature gradients of $10 - 20^\circ\text{C}$ to achieve, giving an idea of the lateral temperature gradients from the convective system, should the convective planform model describe the system in the NE Rockall basin at that time.

Direct examination of the vertical seismic profiles does not shed further light on the mechanism for such temperature variations beyond the modelling shown here. There is no clear spatial association with areas of postrift faults (e.g. polygonal faults) which could be responsible for delivering deep basinal fluids to shallower stratigraphic levels. No obvious fluid escape pipes or chimneys can be seen (Huuse et al., 2010). No sand lenses or mass transport complexes correlate with the topography. The simplest explanation is that the sills in NE Rockall intruded in a geologically short period of time, much shorter than the timescale of sill cooling, and this provided thermal energy to drive a convection

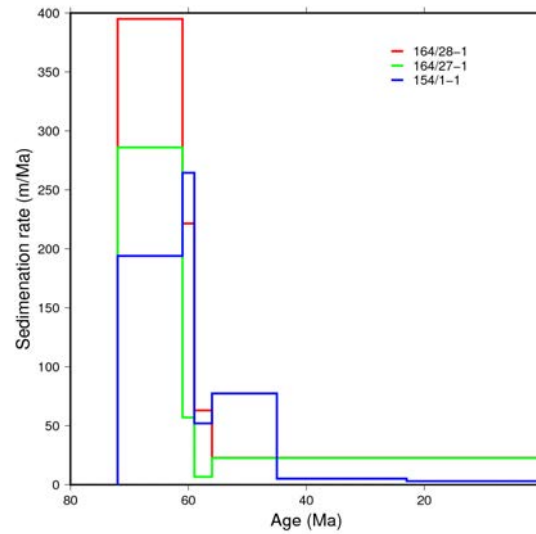


FIGURE 5.22: Sedimentation rate for the three closest wells to the opal A–CT boundary in NE Rockall.

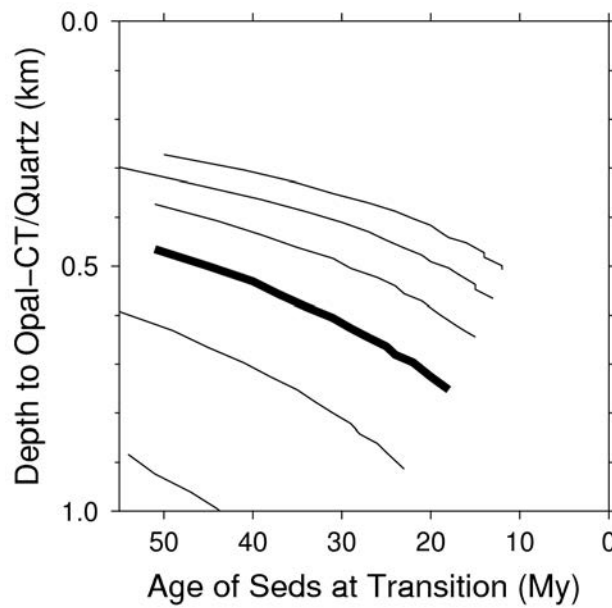


FIGURE 5.23: Model based predictions for the depth of the opal transition for different geotherms and burial rates, by Jones SM. Different lines correspond to different geothermal gradients ranging from $70^{\circ} \text{ km}^{-1}$ (top line) to $20^{\circ} \text{ km}^{-1}$ (bottom line) in steps of $10^{\circ} \text{ km}^{-1}$. bold line is $40^{\circ} \text{ km}^{-1}$, the present day geothermal gradient in the Faeroe-Shetland basin.

system. The exact details of how this can have happened is, however, unknown. This is left as an open question for future research.

5.8 Summary

In this section an unusual seismic reflection — reflection A — was mapped and described. Evidence was shown for it being unlikely to be a seismic artifact due to its presence on multiple seismic surveys. Evidence was then presented for it being due to an opal A–CT transition on NE Rockall. A hypothesis was then presented suggesting the transition to be due to warm water convection systems existing long after sill intrusion. A global database of open A–CT measurements was presented, along with a new methodology for inverting observations to fit kinetic models to the worldwide data. Kinetic models support higher geothermal gradients over the stratigraphic highs on the opal A–CT transition, giving weight to the hypothesis.

Chapter 6

The influence of sills on hydrocarbon migration and fluid flow

6.1 Introduction

Chapter 5 described how an opal A–CT transition was initially interpreted as being due to focused fluid flow due to igneous intrusions. In the case of that opal A–CT transition, it was hypothesized that the driver was not individual sills, but the thermal energy of many sills working together to drive a convection system. This thermal convection system will naturally have operated while the sills were hot, but stopped operating once the sills cooled. This chapter continues analysis of how sills may focus fluid around sedimentary basins, but via a different mechanism long after the sills have cooled. If intrusions can focus fluid flow in sedimentary basins, they may have a significant influence on hydrocarbon trapping and migration in basins hosting intrusions ([Rateau et al., 2013](#)). However, the basin wide significance of intrusion-controlled fluid flow has not been tested. In this chapter a statistical analysis is presented of oil and gas shows in boreholes associated with igneous sills in seismic reflection and well data from the North Rockall, Faeroe-Shetland and Judd basins, offshore north-west Scotland. It is found that there is no statistically significant relationship between the presence or absence of shows in wells near the edges of sills compared with sills away from sill edges. This result suggests either that sills play no significant role in focusing fluid flow (and therefore controlling hydrocarbon accumulations) at the basin scale, or that the effect is not detected at the resolution of the datasets. Demonstration of a clear link between sills and hydrocarbon migration would be an important tool in hydrocarbon exploration, since

sills are easily imaged on seismic reflection data, and thus migration pathways would be clearly mappable.

[Rateau et al. \(2013\)](#) suggest two mechanisms which could lead to focused fluid flow around sills, and fluid focusing at sill tips. In the first mechanism, fluids are focused by the baffling effect of the aureole of reduced inter-granular permeability around a sill. Such baffling could lead to fluids travelling preferentially through the sediments around the sill and its aureole, leading to an effect envisaged to be like an upside down dripping umbrella (figure 6.1a). In the second mechanism, fluids are focused preferentially through the network of columnar joints inside the sill, or fractures in the aureole. The fracture permeability due to the columnar joints is argued to be greater than the permeability of the host rock unaffected by intrusion, and fluids hence migrate through columnar joints to the shallowest point of the sill or aureole before resuming migration through sediments and away from the sill (figure 6.1b). Both mechanisms lead to enhanced fluid flow around the sill tip. The force driving the fluid flow is either buoyancy or gross rock volume loss due to compaction. If the driving force is buoyancy (due to fluids being gas or oil) then the mass loss due to convection is balanced by the displacement of pore water. If the driving force is related to compaction, no fluid balance is required as mass loss is balanced by volume loss of the host material. Henceforth, this general prediction that results from either mechanism is referred to as the “sill-focused fluid flow model”.

The sill-focused fluid flow model is challenging to test because a sill can both reduce intergranular porosity by thermal effects in its aureole, or increase porosity by fracturing. Fresh basaltic and doleritic sills have a largely impermeable matrix. However, sills also commonly contain a dense and connected fracture network arising from contractional cooling related columnar joints, which form secondary porosity and permeability (e.g. [Grossenbacher and McDuffie, 1995](#)). During and after intrusion, host sediment porosity and permeability can be lost due to thermal and compactional effects ([Aarnes et al., 2010](#)). Conversely, secondary fracture porosity and permeability in the host rocks are often increased due to formation of a fracture network in response to thermal stresses acting on the sediments ([Senger et al., 2015b](#)). The key problem is that the relative importance of each factor is unknown. In this chapter the sill-focused fluid flow model is tested quantitatively, and an attempt is made to shed light on whether the overall effect of sills on fluid flow is statistically significant at the basin scale.

An important point to make relates to the findings of the previous chapter, which suggested a model of thermally driven convection cells around a sill. As it is thermally driven, such a convection system would be suggested to be transient, while the fluid flow model outlined in [Rateau et al. \(2013\)](#) is not thermally driven and is thus essentially

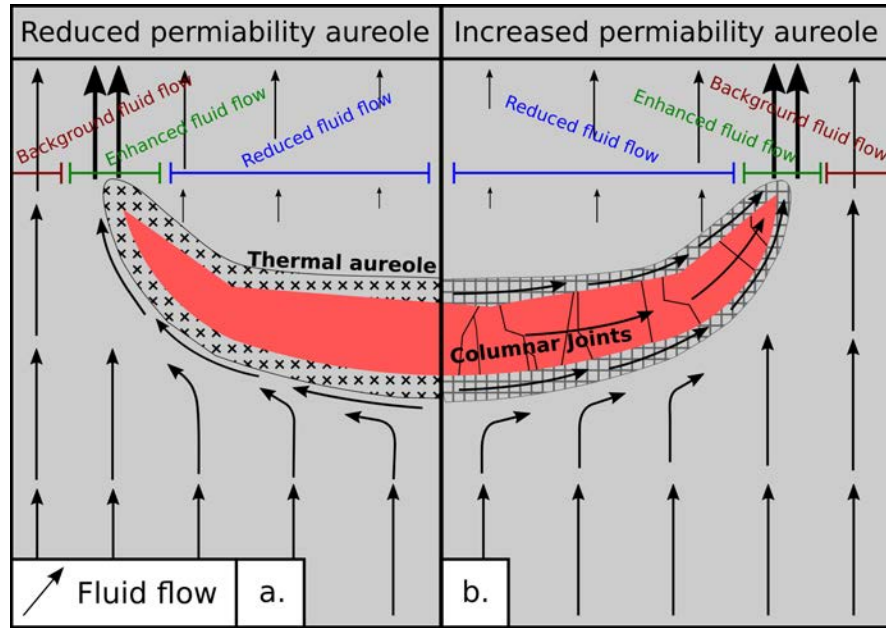


FIGURE 6.1: Schematic diagram showing the two potential modes of the sill-focused fluid flow model. a shows one possible mechanism, that the thermal aureole induces compaction and cementation in the host rock, decreasing porosity and permeability in the surrounding sediments and thus focusing fluid through sediments just outside of the aureole. b represents that the opposite can also occur, that the sill can cause development of a fracture network in the host rock, which may be higher permeability than the surrounding sediments and hence focus fluid flow.

constant. The aim of this chapter is to test the importance of the sill focused fluid flow model of [Rateau et al. \(2013\)](#) against all other mechanisms of fluid flow in the basin, and therefore the transient convection systems described in the previous chapter just become another factor in the class of all other mechanisms.

6.2 Data and methods

6.2.1 Seismic data

This chapter uses three different seismic reflection datasets: the UK Oil and Gas Authority (OGA) North Rockall 2D seismic survey, the Rockall 3D seismic dataset, and the Judd basin 3D seismic dataset (see chapter 2 and figure 6.2). Sills were interpreted on seismic data based on the criteria outlined in Chapter 3. In addition to the sills interpreted, it is expected that a proportion of sills will have been missed in interpretation, as some sills in volcanic basins are too thin to be imaged seismically ([Smallwood and Maresh, 2002](#)). No attempt is made to correct for these sills because they cannot be easily mapped, and therefore they cannot be a useful exploration tool.

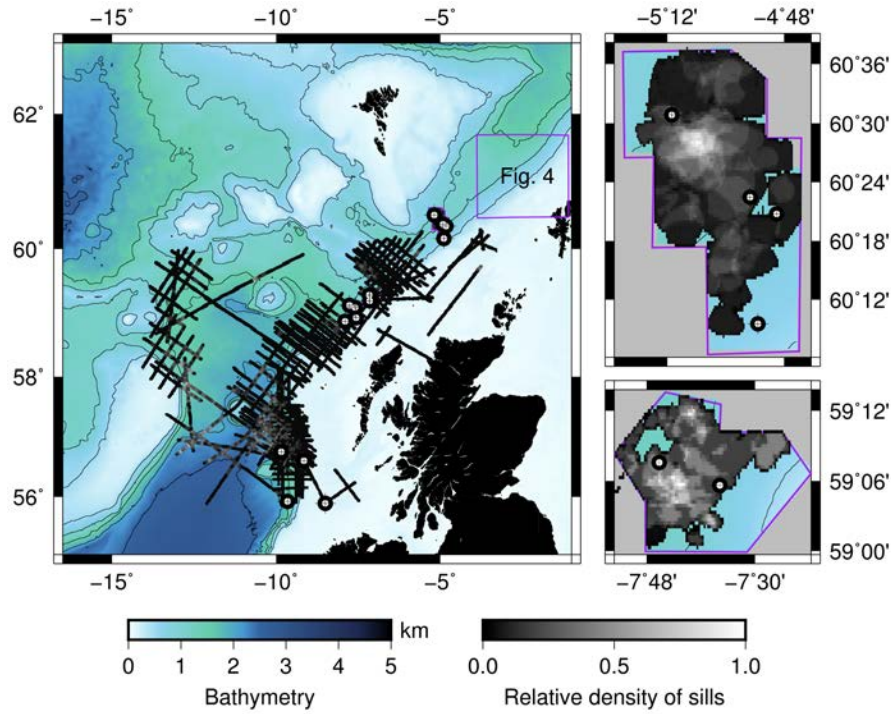


FIGURE 6.2: Panel A shows all three datasets, the 2D OGA seismic data set, and the NE Rockall and Judd basin 3D seismic datasets. Panel B shows the Judd 3D dataset, while Panel C shows the NE Rockall 3D dataset. Bathymetry is ETOPO1 satellite derived bathymetry ([Amante, 2009](#)).

On the two 3D seismic datasets, the horizontal footprint of each sill was interpreted and mapped directly. On the 2D seismic datasets sills were projected to either side of the seismic line assuming a circular planform, such that the length of sill on the seismic line represents the lower bound for the diameter of the sill, while the other 2D seismic lines around the sill constrain a polygon representing the upper bound (see discussions in section 3.2.2). At worst this affects five data points, the maximum possible error of which is 3 km around well 164/27-1. However, these five possible erroneous points are insignificant as a change in their classification is not enough to change the conclusions of this chapter. Commercial data within the study area of Flett basin studied by [Rateau et al. \(2013\)](#) was not available to the author due to confidentiality agreements, therefore sill interpretations within the Flett basin were used exclusively from maps published [Rateau et al. \(2013\)](#).

6.2.2 Well data

Well data was used to form a proxy for fluid flow by classifying each well into the cases of no shows, or shows/hydrocarbon discovery — based on the classification by [Rateau et al. \(2013\)](#), but introducing considerably more statistical rigour. A show or a hydrocarbon discovery indicates that petroliferous fluid had flowed into the drilled sequence from

deeper source rock sequences, while a lack of shows indicates no fluid has flowed into the drilled sequence.

Well logs in the Faeroe-Shetland basin were not available for analysis. However, the UK Oil and Gas Authority (OGA) make available the locations and status (e.g. no shows, discovery, etc.) of all wells on the UK continental shelf. Well locations and status were downloaded from the OGA databank, and added as shapefiles to QGIS open source GIS software. Ten wells which were within the bounds of maps from [Rateau et al. \(2013\)](#) but which were not on these maps already, were added to QGIS. Maps from [Rateau et al. \(2013\)](#) were imported into and georeferenced in QGIS, and checked for accuracy by matching the position of wells on the digitized maps with the positions of the wells loaded from shapefiles. The distances from wells to the edges of sill polygons from [Rateau et al.'s \(2013\)](#) maps were then measured and recorded to the nearest kilometre (figure 6.3).

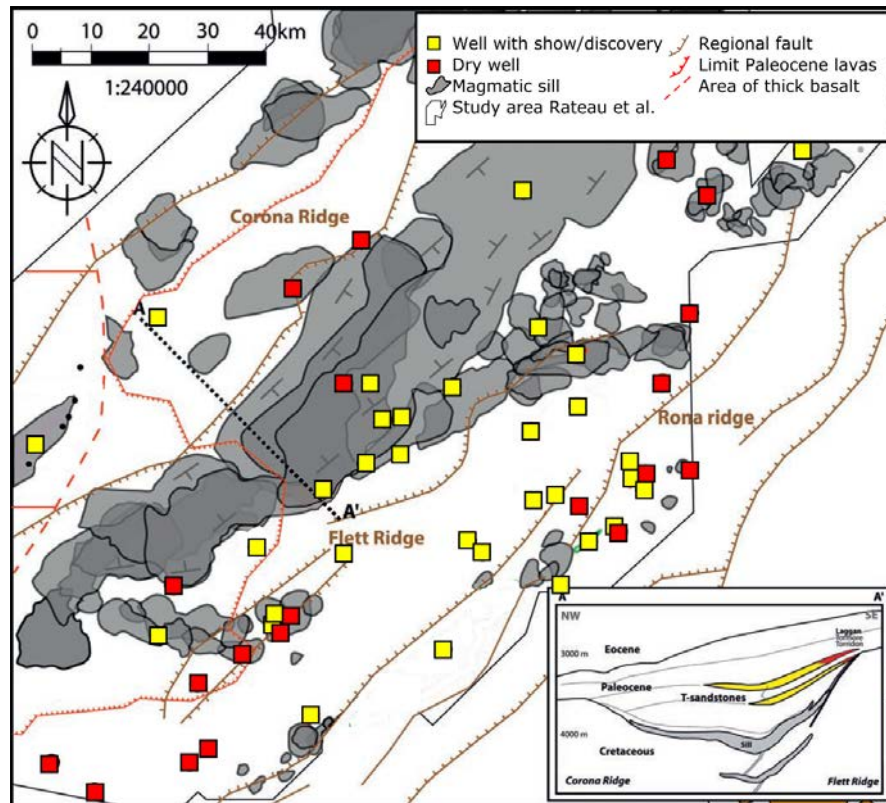


FIGURE 6.3: Locations of sills and major structural features in the Faeroe-Shetland Basin, and the presence/absence of shows in exploration wells. Modified after [Rateau et al., 2013](#)

Within the Judd 3D seismic dataset, OGA 2D seismic dataset and Rockall 3D seismic dataset, full well data and wireline logs were available. The same procedure was followed as for data extracted from [Rateau et al.'s \(2013\)](#) maps. Well data was loaded into IHS Kingdom Suite version 8.8, and the distance to the nearest interpreted sill was measured

within Kingdom, and recorded to the nearest kilometre along with the classification of no shows, or shows/hydrocarbon discovery (figure 6.4).

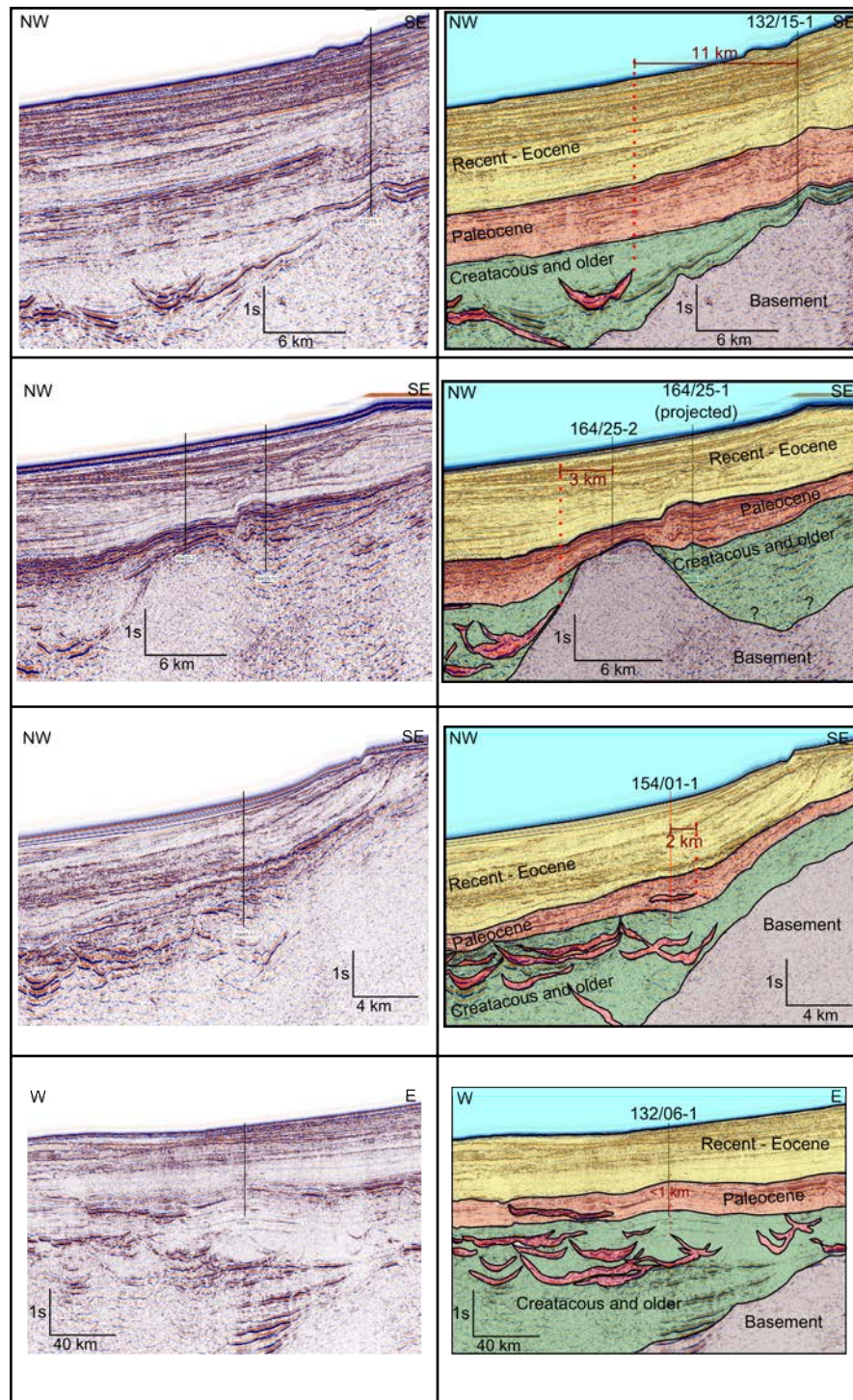


FIGURE 6.4: A selection of seismic data and interpretations from the OGA Rockall survey. Measurements from the well to the nearest sill edge are given in red.

The points and measurements made from wells and sill polygons or interpretations was then tested statistically. Statistical testing relies on the assumption of a random sample. Petroleum explorationists do not know whether a sequence will contain hydrocarbons

before any project is drilled, but all are drilled in locations considered to be likely to hold hydrocarbons. The exploration wells that make up the sample studied in this chapter can therefore be considered a random sample of areas in the subsurface likely to have a hydrocarbon accumulation. However, once a discovery has been made, further wells are drilled to appraise the discovery, and thus can no longer be considered a random sample as the appraisal wells are, in essence, resampling the same discovery. For this reason, from any gas or oil field in the study area only a single well is counted and further appraisal wells are ignored. Figure 6.3 shows the Faeroe-Shetland basin with appraisal and development wells removed, leaving a single well with shows representing any one oil or gas field.

For wells not underlain by sills, the distance measured is from the well to the nearest sill edge. For wells underlain by multiple sills, measurements were made to the nearest sill tip of the shallowest sill. These sills would affect fluid flow most in the vicinity of the well if there were no vertical dykes affecting fluid flow in between the sills (see figure 6.5) and if there were no large continuous impermeable sills near the base of the sill complex (which seismic data does not indicate for the studied basins (Rateau et al., 2013)). This relies on the assumption that all drilled reservoirs are shallower than the sills, which is the case in all datasets analysed here. Clearly, whether or not the majority of fluid will be focused to sill tips depends on the network of connections between sills and their feeders. For example, if the feeders were vertical dykes extending from the tip of each sill in figure 6.5, then the flow path would be different and the appropriate sill tip would always simply be the edge of the sill complex as a whole. In practise, it is never going to be possible to know the network connectivity of the sill-dyke network. The justification for measuring to the *nearest* sill tip therefore comes from the concept and testing as a usable exploration model. In actuality this does not have a major effect on the statistical testing outlined in this chapter for the study area datasets, as both the OGA dataset and the Rateau et al. (2013) dataset have wells at the edge of the sill complex anyway, thus minimising the role of unseen vertical dykes as a potential confounding factor.

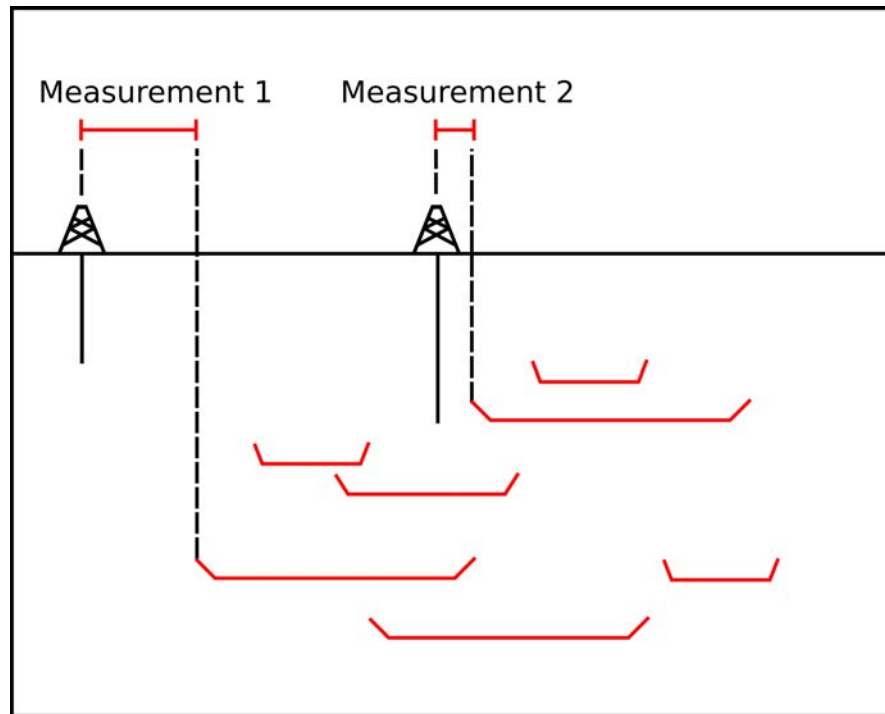


FIGURE 6.5: Schematic showing measurements made on the various datasets. Measurement 1 shows a well outside of the sill complex, where the measurement to the nearest sill equates to measuring to the edge of the sill complex. Measurement 2 is for a well in the middle of the sill complex. In this situation the measurement is made to the nearest sill tip which is not overlain by another sill vertically above. This method works for all sill complexes with randomly distributed, similar diameter sills without intervening dikes, as shown in this figure. However the method breaks down where large diameter, regionally extensive sills exist at depth, which would focus fluid to the edge of the sill complex and leave all other sills in a migration “shadow zone”. However, for the study datasets this should not introduce errors, as all wells happen to be drilled near the edge of the sill complex anyway.

6.2.3 Statistical analysis

A “show” counts as any observation of hydrocarbons in the well, cuttings, or sidewall cores. Three methods were used to search for correlation between wells being closer to sills equating to a greater chance of observing shows or discoveries, as predicted by the sill-focused fluid flow model. First, the distributions of the subsets of wells with shows and no-shows were examined with regard to distance from sills. Secondly, statistical hypothesis testing was used to test for the importance of distance between the well and the sill. Thirdly, Monte Carlo models were used to show what behaviour should be expected in the data if the sill-focused fluid flow model is assumed to work.

To examine their distributions with regards to distance from the nearest sill edge, the wells and their corresponding nearest-sill measurements were split into subsets of shows (including discoveries) and no-shows. Histograms and box and whisker plots were then made of the data to examine and compare how the distributions vary between the two

subsets. Qualitatively, a significant separation between the distributions of no-shows verses shows and discoveries would be seen as evidence for the sill focused fluid flow model, while significant overlap of the histograms would count as evidence against.

The second method used was designed to check whether sills only affect fluid flow in a certain area around them. If sills only affect fluid flow in a very localised area, it is possible that looking at all the data at once, as per the first method of examining distributions, may not show such an effect, because other data obscures the effect. To combat this possibility, within each subset of wells with shows and no-shows, wells were further split into being “close” to the edge of the nearest sill tip or “not close” to the edge of the nearest sill tip. This split was defined by a threshold value, and this threshold value was varied systematically from 0 km to 10 km. For example, for a threshold value of 1 km, any well within one kilometre of a sill was defined as “close”, and the rest were defined as “not close”. If the sill-focused fluid flow model works, then a statistically significant difference should be seen in the proportions of shows and discoveries to no-shows “close” to the sill, versus the proportions of shows and discoveries to no-shows “not close” to the sill. This testing was done with a Pearson Chi-squared test of independence in R statistical software. The null hypothesis is set as that sills have no effect on fluid flow, and therefore that the proportions of shows to no-shows “close” to the sill edge will be very the same or very similar to the proportion of shows to no-shows ‘not close’ to the sill edge. The Chi-squared test is to reject the null hypothesis if the calculated χ^2 test statistic exceeds the theoretical value of χ^2 by a 95 % confidence level. This process of testing all possible values of what is defined as “close” to a sill allowed us to remove bias in what was defined as close enough to a sill edge to affect fluid flow. Other factors, such as distance from faults or potential carrier beds, are not controlled prior to hypothesis testing, as the hypothesis to test is that sills have no influence on fluid focusing when compared with background fluid flow, which includes these factors.

The third and final method used to study the sill-focused fluid flow model is Monte Carlo modelling. The sill-focused fluid flow model states that fluid flow is increased in the vicinity of the edges of sills. This can be formalised as that the probability of observing a show increases as the sill edge is approached, should all other factors be equal. The Monte Carlo model was designed by specifying four categories as follows: A_{mo} as wells “close” to a sill edge with shows, B_{mo} as wells “close” to a sill edge without shows, C_{mo} as wells “not close” to a sill edge with shows, and D_{mo} as wells “not close” to a sill edge without shows. Subscript “mo” indicates a modelled value. Several thousand simulated observations are then created representing hypothetical wells with wells varying between zero kilometres and ten kilometres from the edge of a hypothetical sill. Each well is randomly assigned the label of a show or no-show based on a set of defined probabilities, modelled with a binomial distribution. These probabilities are

denoted $P(A)$, $P(B)$, $P(C)$ and $P(D)$. $P(A)$ is varied from 1 to $P(C)$, and $P(C)$ is varied from 0.1 to 0.5. $P(B)$ and $P(D)$ are the complements of $P(A)$ and $P(C)$, respectively. A variety of different probability combinations are then modelled subject to the constraints that $P(A) \geq P(B)$, and $P(A) \geq P(C)$.

The sill-focused fluid flow model implies that wells “close” to sills have experienced enhanced fluid flow, and therefore there is a higher probability of observing shows. However, it is unknown what distance from a sill edge this effect might operate within — fluid flow cannot be increased infinitely far from a sill, therefore there has to be some distance τ from a sill edge beyond which the probabilities of a show are not influenced by the sill, i.e. are at the background level. In the theoretical model, a distance τ is set as the distance that a sill does affect the chance of observing a show, and model this change in probabilities as one of three functions: a step function, a linearly decreasing function and an exponentially decreasing function (figure 6.6). A stochastic simulation is then performed for probabilities. After each simulation, the same procedure as for the second method involving statistical hypothesis testing explained in chapter 6 are followed: T is defined as the threshold distance, where less than or equal to T is classified as “close” to a sill, classifying a well as A or B, while greater than T is classified as “not close” to a sill, and is classified as C or D. Note the lack of “mo” subscript, indicating this is the measured final stochastic quantity, rather than the input theoretical probability. The ratio $A/A+B / C/C+D$ is then defined, as a convenient metric allowing comparison of both the theoretical results of the stochastic simulation, and the well shows data from the Rockall, Judd and Faeore-Shetland Basins. The proportion $A/A+B / C/C+D$ is then calculated for each threshold distance split of the stochastic model output, therefore treating our simulation data as if the value τ is unknown. We expect the behaviour of $A/A+B / C/C+D$ to be approximately equal to 1 if there is no difference in probabilities between A:B and C:D (i.e. sills do not truly affect fluid flow), while we expect the behaviour of $A/A+B / C/C+D$ to deviate towards values greater than 1 the closer we get to the sill if sills do truly affect fluid flow.

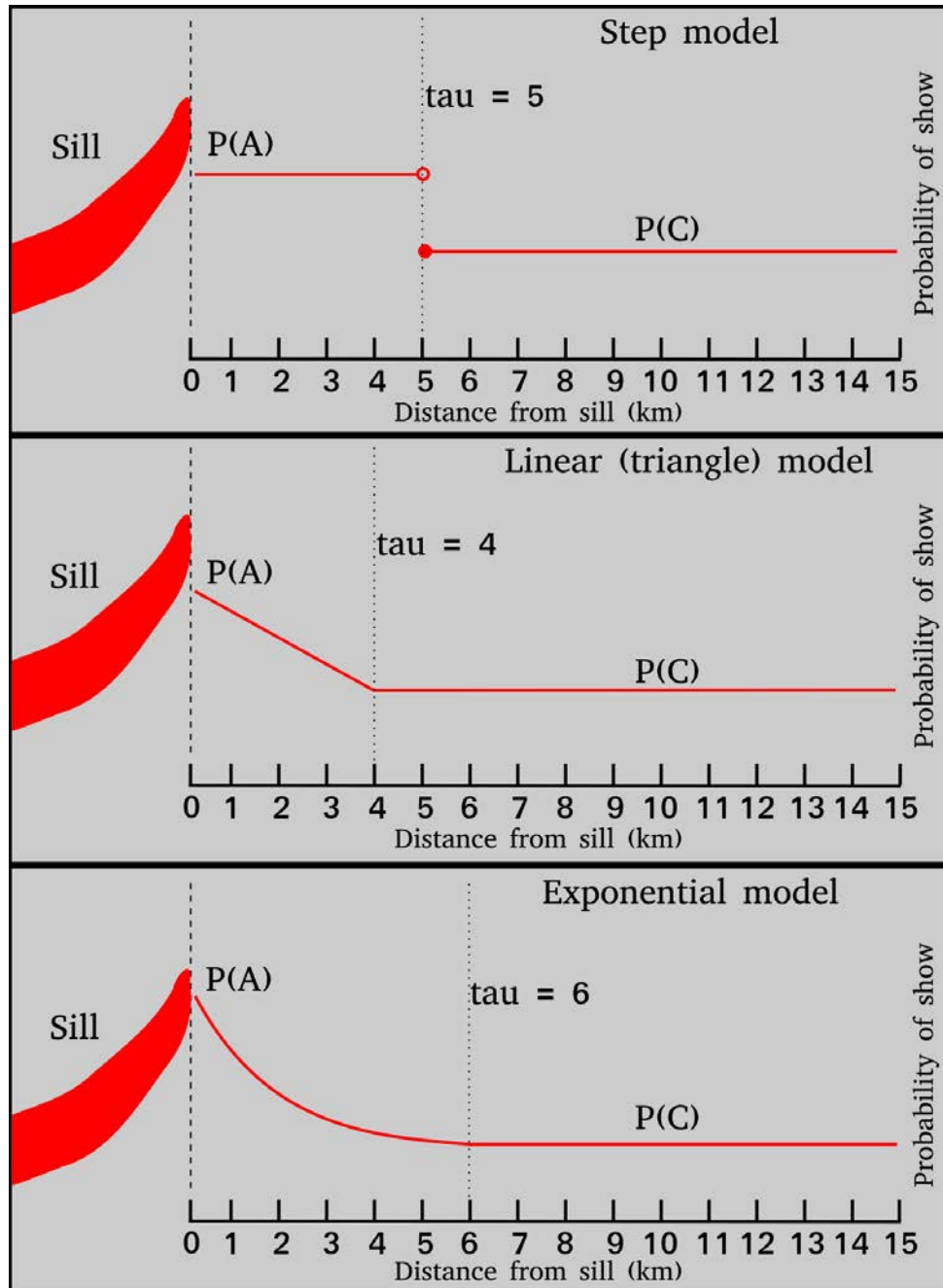


FIGURE 6.6: Model set up for Monte Carlo models. Note the lack of scales on the y axis — $P(A)$ and $P(C)$ were systematically varied throughout the modelling.

6.3 Results

6.3.1 Method 1 of 3: distribution analysis

The first method of analysis involves study of the distributions of shows and discoveries versus no-shows. Figure 6.7 shows histograms and box plots of the data. Both distributions show a strong right skew, and both distributions overlap almost entirely. Table 6.1 shows the descriptive statistics for the distributions. The mean of the shows data has been skewed slightly by the long tails of the distribution and outliers (shown as points on the box plots), but aside from that the summary statistics of both shows (and discoveries) and no-shows are very similar. The sill-focused fluid flow model states that there should be more shows or discoveries near sills than far away from sills. However, this data shows both samples to be very similar. This can be investigated formally with a two sample T test, which gives a p-value of 0.9347, showing further evidence of the samples being from the same population, which therefore implies that sills have no effect on observing a show.

TABLE 6.1: Summary statistics for the distances from wells with and without shows to the nearest sill edge

	Wells without shows	wells with shows
Mean	3.444	3.366
Median	2.000	2.000
Mode	0	0
Standard deviation	4.956	2.921
Lower Quartile	0.000	1.000
Upper Quartile	4.000	6.000
Skewness	2.327	1.003
Kurtosis	8.090	4.043
Number of samples	27	41

6.3.2 Method 2 of 3: statistics of “close” and “not close” subsets.

The second method of analysis further subdivides wells into being close to a sill, and not close to a sill. Figures 6.2 and 6.3 show the dataset. Hypothesis tests were carried out for all possible values of which wells were defined as “close” verses “not-close”, based on a threshold value. The Pearson chi-squared goodness of fit test is used to ascertain whether the proportions are large enough to reject the null hypothesis, or whether the observed variation is within believable error given the sizes of the samples. The data here is plotted only to a threshold distance of 6 km, as beyond this there are fewer than 5 data points classified as “not-close” to sill edges, which invalidates the Chi-squared hypothesis test. The black calculated points and the blue trend line in figure 6.8 can be

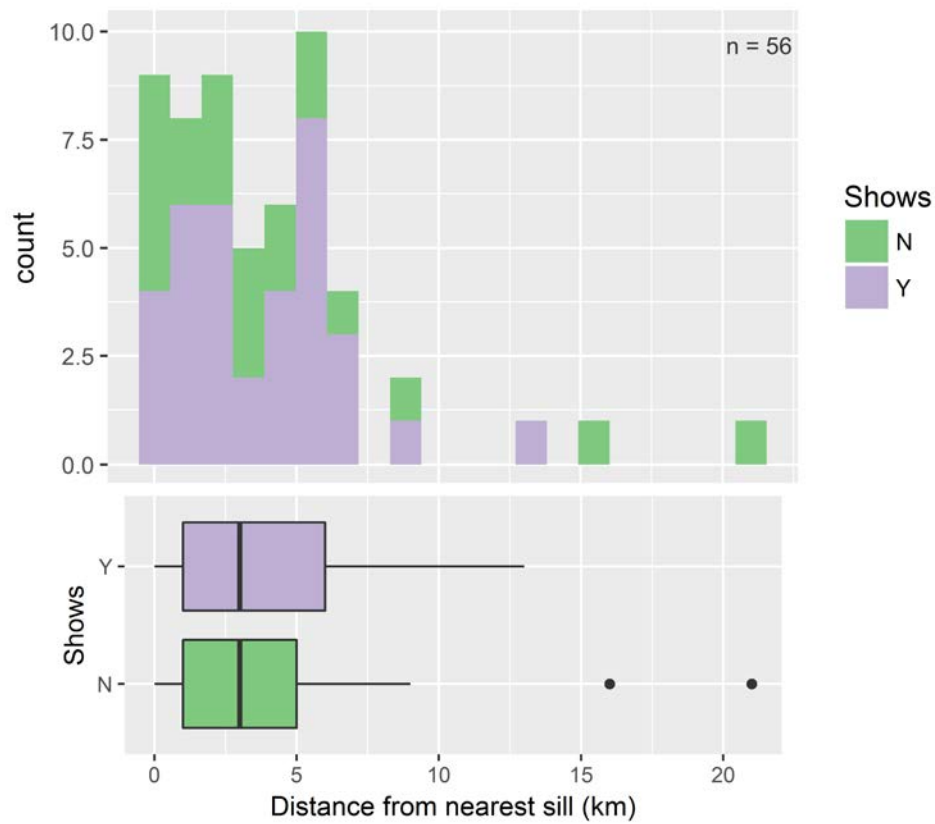


FIGURE 6.7: The distribution of distances from sill edges for wells with and without shows. Upper panel shows a histogram of wells with and without shows. The lower panel is a box and whisker plot of the same data, where the edges of the box show the lower and upper quartiles and the central line of the box shows the median. For detail on how to interpret box and whisker plots, see caption on figure 3.9.

seen to be consistently above the red line showing the 95% significance level. The black points never go below the red significance level, which shows that — irrespective of what is defined as a well “close” to a sill edge — there is no correlation between shows and a well being “close” to a sill tip.

6.3.3 Method 3 of 3: Monte Carlo modelling

Figure 6.9 shows data for the third method of analysis from all surveys plotted as open circles on top of a single run of the Monte Carlo model. The models show the expected behaviour of $A/(A+B) / C/(C+D)$ if there is a difference in proportions of shows to no-shows as a sill edge is approached, where A, B, C and D are defined in the methods section. As can be seen from figure 6.9, the trend of the models are that values of $A/(A+B) / C/(C+D)$ increases as τ is approached, as would be expected. Figure 6.9 shows that points most closely follow the line $A/(A+B) / C/(C+D) = 1$, the trend of no

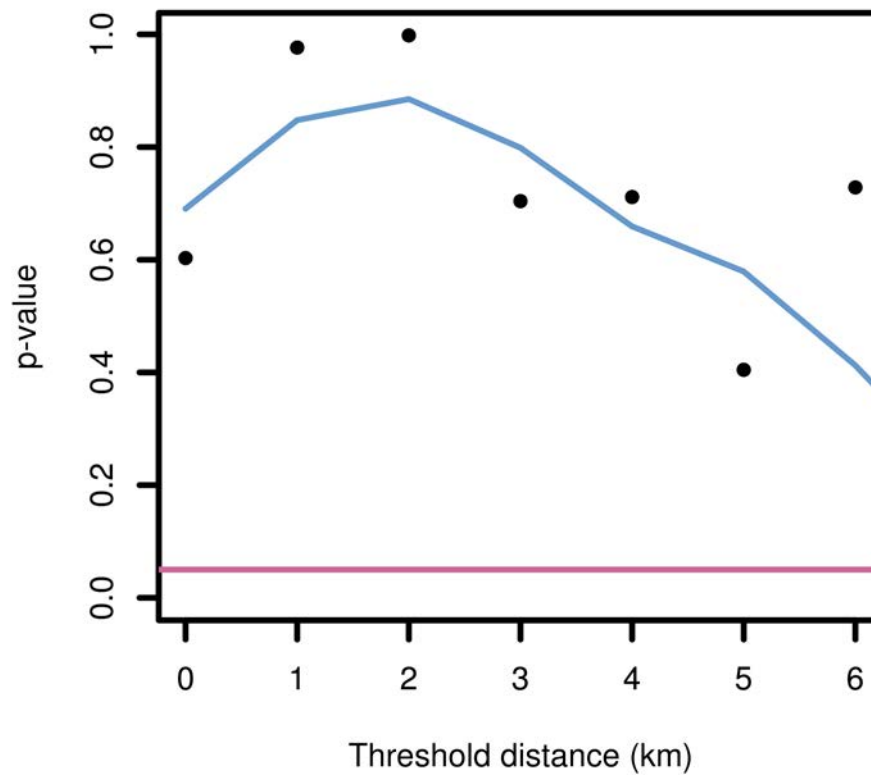


FIGURE 6.8: P-value as a function of the threshold value used to define a sill as close or not close to a sill edge. Black points are the calculated p-values. Blue line is a loess smooth trend line of the black points. Red line is the significance level of 0.05. If black points are below the red line, they are statistically significant and therefore there is a relationship between the chance of observing a show in a well and the distance from the sill. If the points are above the red line, the set of wells “close” to sills are statistically indistinguishable from the set of wells “not close” to sills, which would imply no effect of sills on the chance of observing a show in a well.

relation; i.e. that sills do not affect fluid flow. Beyond a threshold of 6 km points are not plotted due to a very small number of points being used in the calculations, meaning the denominator tends to zero and is hence undefined. All other parts of the model which have a change in probability of observing a show with distance display the property of increasing as the threshold distance is approached. The real data do not display such behaviour at any distance. Taking different sized samples of the data which make up the lines on the Monte Carlo model would be equivalent to having the same trend but with bigger and bigger error bars as the sample size gets smaller and smaller, analogous to the finite number of wells used in this chapter.

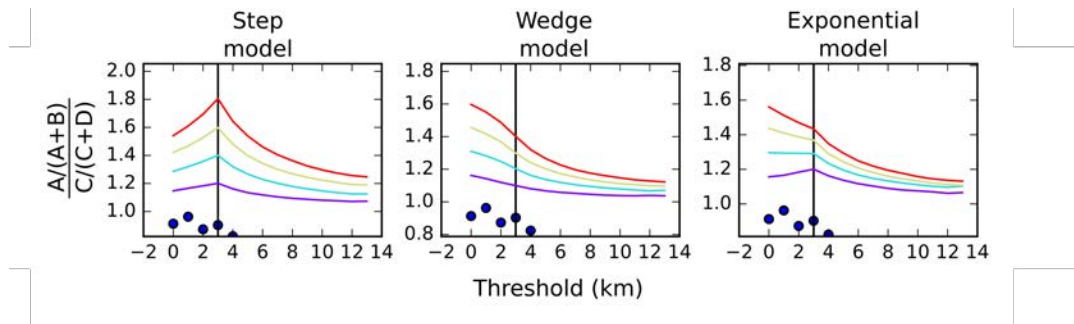


FIGURE 6.9: Monte Carlo models with real data plotted as points. Curves are Monte Carlo models, where $P(C)$ is held at 0.5, and red, yellow, blue and purple curves correspond to $P(A)$ s of 0.9, 0.8, 0.7 and 0.6 respectively. Model curves show that the bigger the difference in probability in observing a show in well “close” and “not close” to a sill, the larger the value of $\frac{A/(A+B)}{C/(C+D)}$. Points have values very close to 1, indicating no difference in proportions close to and far from sill edges.

6.4 Discussion

Three different methods have been used to show there is no statistical correlation between sills and shows in the study area, casting doubt of the use of the sill-focused fluid flow model in exploration. There are, however, a number of caveats to this analysis.

First, the findings of this chapter may seem at odds to observations of hydrocarbon shows and accumulations reservoirized in fractured sills, such as observed in the Nequen Basin, Argentina (e.g. [Rabbell et al., 2018](#); [Rodriguez Monreal et al., 2009](#); [Senger et al., 2015b](#); [Spacapan et al., 2018](#)). In fact, these observations are easily explained for the majority of cases, as sills containing shows or discoveries are almost always emplaced directly into source rocks. In such situations, some volume of hydrocarbons should be expected to be found within the sill, as the sill would likely represent the only permeable object in the source rock sequence; is in direct contact with the source rock on all sides; and would itself cause the hydrocarbon generation due to its thermal energy. It is noted that this is not guaranteed to be the case, it is still possible that hydrocarbons migrated into the sills long after intrusion, but the self-generation of hydrocarbons represents the simpler and probably more likely case. For example, [Rabbell et al. \(2018\)](#) describe sills currently producing oil in the Los Cavados field in the Nequen basin, and of the sills producing oil, all are emplaced into source rock sequences. Similarly, the gas producing intrusions in the Bohai Basin in China intrude coal seams ([Wang et al., 2012, 2013](#)). Of the well sticks shown in [Rateau et al. \(2013\)](#), all sills with shows can be seen to intrude shales. Thus the findings of this chapter can be summarised as sills appear to have no effect on migration *at the regional scale* — features such as carrier beds and faults likely have a much more significant effect on fluid flow and therefore overshadow any small effect of intrusions.

By expecting shows or discoveries in wells located near sill tips, it is assumed that petroliferous fluids were available to be focused by overlying sills towards the wells. However, the distribution of source rocks in the Rockall Basin is poorly understood due to lack of well penetration and seismic imaging issues through basalt. Therefore the assumption of source rocks being everywhere in the basin is not necessarily true. However, this same situation applies to most frontier exploration regions, and therefore is a situation which will commonly occur if using the sill-focused fluid flow model as an exploration tool.

Situations may exist where a sedimentary or structural feature exists in between a sill tip and a well which disrupts fluid flow. This could either increase the fluid flow to the well (e.g. focusing hydrocarbons from areas away from the sill towards the well) or decrease fluid flow (e.g. by diverting hydrocarbons away from the well). As this could have either a positive or negative effect on the likelihood of observing a show or discovery in a well this should not introduce a bias to these results.

Another caveat to this analysis is that the well data proxy (of shows (and discoveries) versus no-shows) may not be sensitive enough to pick up small fluid flow variations caused by sills. As detailed in section 6.2, data from the UK Oil and Gas Authority website was used in this analysis. This data does not give information on the age of the sequence in which the shows were found. The timing chart in [Rateau et al. \(2013\)](#) shows that phases of charge are expected during the Late Cretaceous, Paleocene-Eocene and Early Miocene. This means there is a possibility that shows in the Cretaceous section may have been included which were charged before sill intrusion, which could skew the hypothesis test either in favour of the sill-focused fluid flow model or away from it. However, this is only a potential issue for the ten wells added from the OGA data set. Removal of these wells and hypothesis testing on this subset still does not change any of the results in section 6.3.

The mapping of sills in a seismic data set is reliant on the seismic resolution. Results in section 3.2.1 showed that whether a sill was imaged is entirely dependent on seismic frequency content, and random noise content. A proportion of thin sills within the study area have not been resolved on seismic data. This is known as these sills were encountered in well data but not imaged on seismic data ([Rateau et al., 2013](#)). Modelling results in figures 3.7 and 3.8 indicate these sills are likely on the scale of tens of centimeters or less, which matches with well data. It is difficult to see how such thin sills could be the sills most responsible for focusing fluid, while the statistical testing in this chapter indicates large, thick sills do not have a discernible effect on fluid flow at the basin scale. Nevertheless, this is a further factor which may explain the lack of correlation the analysis finds. However, mapping sills as an exploration tool would not be a useful for

exploration if it relied on sub seismic sills, so this is not viewed as a major problem for this analysis.

The main difficulties for the analysis are quality of the input data in the form of seismic data of high enough quality to map small sills, and the sample size of number of wells. An interesting question may be whether more or better data would be likely to change the outcomes of this analysis. Whether it does or does not will depend on the size of the effect of sills on the probability of observing a show or a discovery. If the effect of sills on fluid flow is small then adding many more wells may change the conclusion of this chapter, but it would be questionable whether this would be worthwhile if there is hardly any effect on fluid flow anyway. However, if the data is available it would be interesting to redo the work in this chapter in other petroleum systems hosting intrusions, to find whether these results generalise to other basins.

A final discussion point may be the question of how many wells would there need to be in the basin before researchers could definitively observe sills to be having an effect? Or put another way, how many more wells would need to be drilled in the FSB before exploration managers could see a statistically significant difference between wells near sills verses far away from sills, and therefore will mapping sills ever be a useful petroleum exploration tool for visualising migration pathways? The study of how large a sample size would need to be to detect an effect of a certain size is named “power” in statistics. Figure 6.10 shows this calculation for the Chi Squared test used in this chapter. Cohen (1992) classifies effect sizes as small, medium or large. For the Chi squared test, this corresponds to differences in proportions of 0.1, 0.3 and 0.5. We want to model the whole range of possible values, and hence use boundaries equally between these values of 0.2 and 0.4 to delimit regions of small, medium and large effect sizes. Figure 6.10 shows modelling results for the sample size (in this case, the number of wells) needed to observe a specific effect size (difference in probability between a show and no show). Figure 6.10 shows that sills do not have a “large effect” on fluid flow at the basin scale — if sills did have a “large effect” it would have been discernable based on the well sample size presented in this chapter. If sills have a “small effect” on fluid flow at the basin scale, proximity to a sill will never be a practical exploration tool in frontier basins. Figure 6.10 shows that sills may be a practical exploration tool if sills have a “medium effect” size, and this would be a valid target for future research as more wells are drilled in the FSB and Rockall Basin.

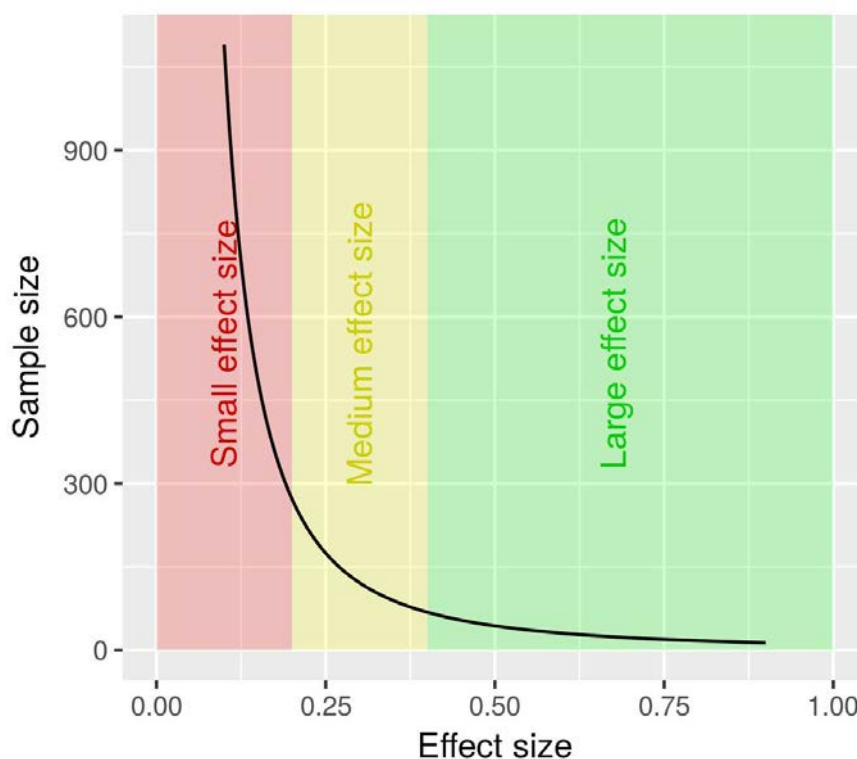


FIGURE 6.10: The sample size needed to observe different effect sizes, assuming the standard (in the statistical literature) power values of 0.8 and significance level of 0.05. In the case of this chapter, effect size corresponds to the increase in likelihood of observing a show, and the sample size is the number of wells in the basin before the effect could be observed.

6.5 The importance of sills in petroliferous basins

The work presented in this section shows valuable insights for understanding the importance of igneous intrusions in basins undergoing hydrocarbon exploration, which is now summarised as the conceptual model in figure 6.11. In figure 6.11, sills in sedimentary basins can be envisaged to result in one of four scenarios. In the “sill influence likely” scenario, a sill is emplaced directly into a reservoir sequence. In this scenario, the potential for the sill to influence fluid flow is likely. In this case thermal energy from the sill is likely to decrease porosity in the thermal aureole (e.g. Wang and Song, 2012), and may crack oil to gas if the reservoir has already been charged. If the sill acts as a baffle or barrier to flow the sill could cause reservoir compartmentalisation, requiring extra wells to exploit the structure, and pressure hazards while drilling (Zoback, 2010). If the sill has higher permeability than the surrounding reservoir sequence, the sill draining faster than the rest of the reservoir could cause early water cut, causing exploitation of the reservoir to be more costly. If the sill propagates through or beyond the reservoir, there is a possibility of top seal breach (e.g. Cartwright et al., 2007).

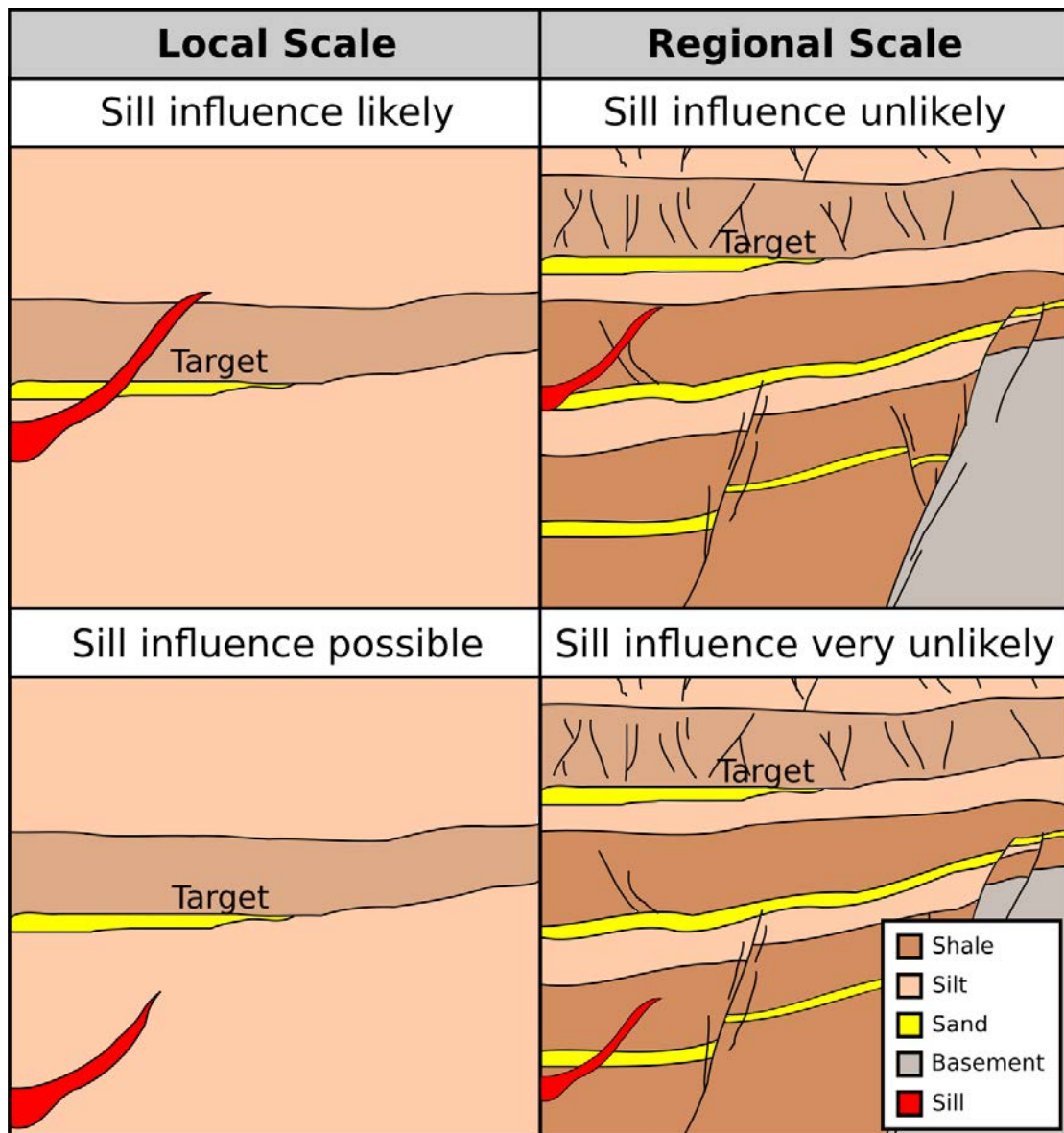


FIGURE 6.11: Conceptual model of how sills might influence fluid flow in sedimentary basins. The key factors are how close the sill is to the exploration target (labelled target), and whether other more permeable pathways (e.g. faults, carrier beds) exist in between. See text for discussion.

In the second scenario, labelled “sill influence possible”, a sill is intruded near a reservoir, and no other more permeable features lie close by or in between the sill and reservoir to influence fluid flow. In such a scenario it is possible that the sill focused fluid flow model works *sensu lato* [Rateau et al. \(2013\)](#). However, if the intervening shales between the sill and reservoir are impermeable there is no reason to suspect that the presence of a sill underneath undisturbed shales would necessarily lead to hydrocarbon charge.

However, the situation presented in the “sill influence possible” is uncommon, because most sedimentary basins contain a basin fill of variable amounts of sand, mud, carbonates and other materials, as well as faults, fractures and other structural features. Any of

these may be expected to have larger effects on fluid flow around a basin than a sill. The third scenario, labelled “sill influence unlikely” demonstrates this. Here a sill is emplaced close to a target reservoir sequence, however in between the sill and the reservoir is a permeable sandstone. In such a situation the more permeable sand bed may act as a carrier bed and transport hydrocarbons up-dip and away from the sill. And this situation only applies if hydrocarbons get to the level of the sill in the first place. In the case of the conceptual model, it is more likely that hydrocarbons would be transported through the faults and sandstones up-dip towards the edge of the basin and not necessarily get to the sill at all.

The final scenario, labelled “Sill influence very unlikely” represents the situation most akin to much of the FSB and Rockall Basins. In this scenario the sill or sills are well below the level of the target reservoir. In such a scenario, even if the sill acts to perfectly focus fluid, beyond the sill tip hydrocarbons would be expected to either be trapped within the sill, due to the sill being surrounded by shales, or if hydrocarbons were to travel vertically through the shales they would then be intercepted by the intervening sandstone carrier bed and be focused away from the target reservoir.

The overall message of this chapter is hence not that sills have no effect on fluid flow — in fact it is likely that direct intrusion of a sill into a reservoir sequence would have significant effects. Instead the message is that sills are highly unlikely to have an effect at the basin scale, due to the presence of other, higher permeability conduits and pathways which are more important in focusing fluid flow around a basin. This work then leads to the set of testable conceptual models outlined in figure 6.11 for future study. Questions arising include what distance must a sill be from a target reservoir before it becomes important? What bulk permeability range do sills occupy? And how can this be predicted pre-drill?

6.6 Summary

To summarise, basins containing voluminous igneous intrusions are difficult to explore because the igneous material hampers seismic imaging. Understanding the importance of igneous sills on fluid flow is important, because if they exert a control on fluid migration they may unlock resources in basins which have experienced igneous activity. Three seismic data sets, well data, and published data have been used to investigate the sill-focused fluid flow model. Three methods are used to show that there is no evidence for there being a difference in proportions of wells with and without shows near sills. This finding shows that mapping sills is unlikely to be an important exploration tool in frontier basins containing intrusions. Finally, power analysis shows that if sills do have

a small positive increase in the chances of observing a show, it is unlikely it will ever be found because of the practical constraints of needing many hundred wells to observe a statistically significant difference. This work therefore shows that there is no evidence that a sill intruded deep below or far away from a reservoir increases the chance of observing a hydrocarbon show. The research questions going forward then revolve around matching these results with observations of hydrocarbons being reservoired inside sills, and at what distance from a reservoir does a sill start to become an important consideration in the petroleum system. The take away message from this chapter therefore is that sills do have an effect on petroleum systems, but that there likely exists a certain distance within which sills are a major influence, and beyond which they are insignificant. The search for understanding this distance has the potential to be valuable in exploration if it can be understood.

Chapter 7

Discussion and Further Work

This thesis started by describing the current state of understanding of the magmatic plumbing system in Chapter 1. In Chapter 3, a database of sill measurements was described, and used to test models of sill intrusion. Chapter 4, and 6 then studied the effects of sills on the petroleum system, while Chapter 5 described a study which started as an analysis of a potential new indicator of sill-focused fluid flow, but results showed that this may not be the case. Each of the previous four chapters have already contained discussion on the results presented within them. In this chapter, the separate chapters are drawn together; wider implications for different research topics are explored; and topics of future research are outlined.

7.1 Large Igneous Province plumbing systems

7.1.1 Magma pressure implications

Getting a true distribution for emplacement depth of sills in sedimentary basins is extremely difficult and may never be truly possible. Due to the nature of seismic data, sills deep within sedimentary basins are poorly imaged, and if their signal is below the background noise level of the seismic data the intrusions can be missed entirely. This makes the right hand side of the histograms in figure 3.27 unlikely to be a true representation of the emplacement depth population. However, this data is still enough to strongly dispute a number of published studies. Francis (1982) explain sill intrusion as occurring at a level of neutral buoyancy. Magma density is typically around 2650 kg m^{-3} (Bradley, 1965). As Smallwood and Maresh (2002) note, host sediments at emplacement depths in each basin are uniformly lower density than this at the present day (and by inference will only be of lower density at time of sill intrusion due to less burial related

compaction have occurred), so the neutral buoyancy level model is easy to rule out. Likewise, [Turcotte \(1991\)](#), [Lister \(1990\)](#), [Lister and Kerr \(1991\)](#) and [Rubin \(1995\)](#) all imply magma filled cracks stall at around the neutral buoyancy level in the lithosphere.

Both [Johnson and Pollard \(1973\)](#) and [Smallwood and Maresh \(2002\)](#) observed the disparity between the implications of the neutral buoyancy level model and the observations of sills emplaced at shallow level in sedimentary basins, and proposed a pressure support based model instead. Their models imply that sills emplaced at shallow level must still be connected to the magma chamber at depth to give the pressures required for high level intrusion. The requirement for pressure support raises further questions when considering the data presented in this thesis. First, many sills are demonstrably in contact with other sills and therefore potentially have been fed by other sills. However, equally many sills are clearly isolated from other sills, and therefore must have fed directly by a dyke. This implies the wide emplacement distribution represents multiple separate intrusion events, otherwise sills would be expected to be very clustered with depth. Does this observation imply multiple magma chambers at different depths to allow the width of the emplacement depth histogram ([Figure 3.27](#))? This may be a question that geochemistry can shed the most light on. An alternative possibility is that this observation represents a single magma chamber, but with varying overpressures from different volumes of magma recharge, or from internal magma chamber processes. Regardless of the exact cause of magma pressure variations, the fact that sills must be connected at depth to a magma chamber leads to the exciting possibility of using sills as a new method of predicting the magnitude of magma chamber pressures, and ranges of variations of magma chamber pressures.

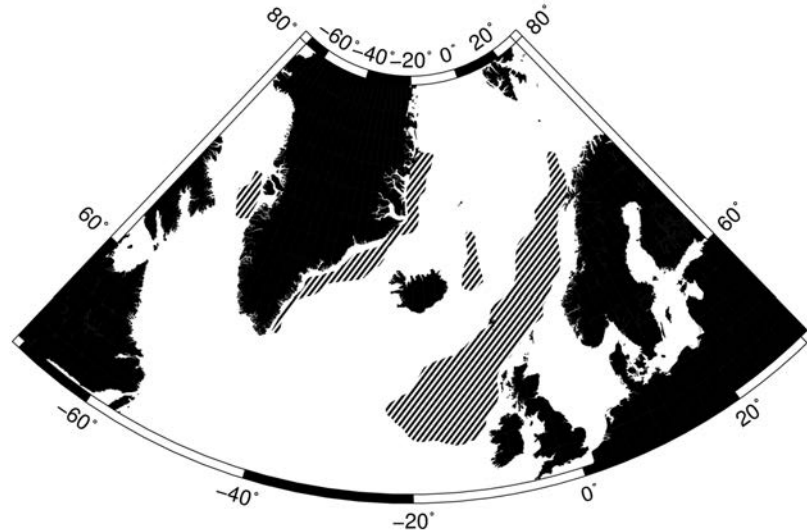
7.1.2 Volumetric implications

The volume of large igneous provinces is poorly understood, due to dense sampling of data being close to impossible in all LIPs. The importance of the shallow intrusive component of LIPs is entirely unknown, having had no estimates of the volume of the shallow igneous system published. The Parana LIP in South America and the NAIP LIP are probably the best candidate LIPs to get accurate estimates of volumes of, because of their large amounts of exposure and youth / lack of deep sedimentary cover, respectively.

[Eldholm and Grue \(1994\)](#) published estimates of the volume of the NAIP, split into the extrusive and lower crustal components. There are many ways to compare the volume of the shallow igneous system to [Eldholm and Grue's \(1994\)](#). Here a very simple method is used to obtain an estimate. The total volume of sills within a LIP can be defined as

$$V_{total} = SA \cdot SD_{ave} \cdot \pi r_{ave}^2 \cdot Ts_{ave} \quad (7.1)$$

where V_{total} is the total volume of all sills in the sill province, SA is the area of crust intruded by sills, SD_{ave} is the sill area density (in *sills* km⁻¹), r_{ave} is the average sill radius and Ts_{ave} is the mean sill thickness. Most of these values can be obtained from this work, with the exception of the area of intruded crust. Figure 7.1 shows the areas thought to be most likely to contain intruded crust, modified after White and McKenzie (1989), Eldholm and Grue (1994), Geissler et al. (2017) and Horni et al. (2017). These areas combined come to a total of 1.313×10^6 km². This is very similar to the area of extrusive basalt in Eldholm and Grue (1994). This is because, while sill intrusion extends over a wider area than extrusive sequences, sills are likely to intrude sedimentary basins much more readily than oceanic crust. It appears the extra area of sill intrusion interpreted in figure 7.1 is similar to the area of Eldholm and Grue's (1994) extrusive polygons over oceanic crust. An average representative sill area density from figure 3.36 is 0.015 sills km⁻¹. Multiplying 1.313×10^6 km² by 0.015 sills km⁻¹ gives an estimate of the number of sills in the NAIP of 19,695. Similarly, an average sill radius of 4.95 km is used, after results in section 3.3. An average sill thickness was taken as 20 m (chosen arbitrarily, but with reference to section 3.3.3). Plugging these values into equation 7.1 yields an answer of 30 340 km³, close to two orders of magnitude smaller than the extrusive and lower crustal volumes estimated by Eldholm and Grue (1994). However, results from White et al. (2008) indicate that the underplated volume may actually be lower crustal sills, which would significantly reduce the volume of the underplated magmatic material. Our back of the envelope estimates here indicate the shallow intrusive component is volumetrically minor compared with the other LIP components. However, there have not been more recent estimates of the volume of different components of the NAIP, and a reappraisal of volumes with respect to some of the new data that has been published recently (Funck et al., 2016a,b, e.g.) may be a useful future research direction.



NAIP sill presence

FIGURE 7.1: Polygons of sill extent, modified after [White and Mckenzie \(1989\)](#), [El-dholm and Grue \(1994\)](#), [Geissler et al. \(2017\)](#) and [Horni et al. \(2017\)](#). Projection is Albers conic equal-area projection.

7.2 Emplacement mechanisms of sills

There are a number of different emplacement models for sills, and some of these models predict different sill shapes (e.g. [Malthe-Sørenssen et al., 2004](#); [Schofield et al., 2010](#)). The overlap in ranges of sill diameter split by sill shape might imply that most of the sills measured in our dataset were emplaced by similar processes, rather than a multitude of different models for differently shaped sills.

Summary statistics for various sill dimensions in different basins were then applied to test different sill emplacement models. First, generic models for a crack in an infinite elastic medium were examined. These models were found to fit very poorly with the measured sill data. It was then shown that models involving flexure of an overlying plate fit the data more satisfactorily. The analysis of the flexural plate model, however, was hampered by lack of elastic parameter knowledge for the individual basins and how these elastic parameters vary with depth. For this reason, a wide range of sensible parameters were forward modelled to observe whether the predicted ranges overlapped the data. In the vast majority of cases, they did. Future work could involve narrowing down the parameter ranges for specific basins to further test models, or potentially using an inverse modelling scheme to find the optimum parameterization of the models to the data.

In section 3.5.5 sill measurements were applied to the order of magnitude models of [Lister \(1990\)](#) and [Lister and Kerr \(1991\)](#), which have been used by recent authors such as [Kavanagh et al. \(2006\)](#) and [Menand \(2011\)](#). The work in this thesis found that the models of [Lister \(1990\)](#) and [Lister and Kerr \(1991\)](#) underpredicted the thickness of the measured intrusions, often by orders of magnitude. The same results were found in testing models by [Rubin \(1995\)](#) and [Gonnermann and Taisne \(2015\)](#) in section 3.5.4, which also underpredicted sill thickness. Both of these sets of models are based on the assumptions of an infinite homogeneous elastic solid intruded by a magma filled crack. However, in Chapter 3 it was concluded that the data may be the subject of sampling bias, as only sills which have a clear reflection at the top and base can have their thickness measured, and therefore used for models involving sill thickness. These are normally among the shallowest and thickest sills in a basin. Chapter 3 shows that these categorically do not fit the linear elastic fracture mechanics (LEFM) models based around the assumption of an infinite elastic solid. However, deeper in sedimentary basins magma filled cracks may not “feel” the influence of the free surface and would likely be intruding into more consolidated rock. The host rocks may therefore deform in a manner more applicable to the LEFM model. The analysis in this thesis cannot therefore rule out the possibility that deeper sills do fit the LEFM generic crack models in [Rubin \(1995\)](#) and [Gonnermann and Taisne \(2015\)](#). However, the fact that the results in section 3.5.5 do fit within modelled ranges for [Pollard \(1973\)](#)’s elastic plate model suggests that the dominant process for intrusion at the depth of a few hundred metres up to a kilometre is still well modelled by a magma filled crack, albeit a magma filled crack where the mechanics are governed by an overlying elastic plate. This argues against the conceptual model of [Schofield et al. \(2010\)](#) and [Schofield et al. \(2012\)](#), whose fluidization mechanism represents a type of plastic / ductile deformation to emplace intrusions shallower than 2 km depth. It also argues against recent papers (e.g. [Haug et al., 2017](#); [Schmiedel et al., 2017](#); [Spacapan et al., 2017](#)) and models of a viscous indenter style intrusion mechanism, an inherently plastic process. Future work with this dataset and the methods used in this thesis could be a good approach to test these new models against real data.

The modelling and observations outlined thus far leads to an intrusion scheme as follows. Sills are known to intrude sedimentary basins, both in the deep reaches of basins (e.g. [Cartwright and Hansen, 2006](#); [Eide et al., 2017b](#); [Hutton, 2009](#)); in the shallow regions (e.g. [Hansen et al., 2004](#); [Smallwood and Maresh, 2002](#); [Thomson, 2004](#)); and in the very shallow regions (e.g. [Miles and Cartwright, 2010](#); [Trude et al., 2003b](#)). Sills are also known to intrude to the lower and middle crust ([White et al., 2008](#)). While direct observation of the dimensions of deep sills is currently difficult — leading to few datapoints — studies such as by [Eide et al. \(2017b\)](#) suggest that longer and thinner sills may exist at depth. This may fit better with models such as [Lister \(1990\)](#), [Lister and](#)

Kerr (1991) and Rubin (1995), as logically, deeper intrusions are less likely to feel the influence of the free surface, and thus the model assumption of an infinite elastic solid is less invalidated. Closer to the surface the Pollard (1973) model better approximates sill intrusion, as the sill begins to feel the influence of the free surface. Under what conditions this applies (i.e. at what depth is “close” enough to the free surface for the intruding sill to “feel” the free surface) is up for debate and constitutes a future research question. Finally, in the very shallowest sediments, magma can intrude more like a lava flow, forming hybrid flow sills of the type interpreted by Miles and Cartwright (2010).

7.2.1 Magma fingers and smaller scale structures

Beyond the idea of sills emplacing as a magma filled crack rather than a fluidization driven mechanism, there is the question of small scale magmatic structures, that this thesis has not examined in detail. Some models of sill emplacement advocate the idea of the front edge of the advancing sill propagating as a series of breakouts, termed “magma fingers”. Pollard et al. (1975) explained the observations of finger like terminations in the Shonkin Sag laccolith as due to the local stress field, while Schofield et al. (2010) explained magma finger initiation and propagation as diagnostic of plastic emplacement processes such as fluidization of host rock. The work in this thesis showed that models involving a magma filled crack with an overlying elastic plate fitted sill intrusion well. Models based around the propagation of magma fingers as breakouts from a crack subject to a stress field would be closer to the assumptions made in models tested in section 3.5.5, while fluidization would fit less well with the model assumptions tested in section 3.5.5. Again, the fact that the observations do fit with models of sill emplacement with an overlying elastic plate would tend to favour Pollard et al.’s (1975) interpretation, while Schofield et al.’s (2010) would seem less likely.

7.3 Forced folds as hydrocarbon traps

In Chapter 3 it was shown that models which incorporated an overlying elastic plate fitted the seismically observed sills best. Chapter 4 focused on the deformation of the overlying rock mass, and specifically on the contention that the amplitude of a forced fold often does not appear to match the thickness of the sill causing it (Jackson et al., 2013; Magee et al., 2013a). A number of examples of forced folds where both the forced fold and the thickness of the sill were analysed in this thesis. The vast majority of the discrepancy between the sill and forced fold could be explained by compaction processes modifying the fold as the basin subsides and is filled. The effects cited in Hansen and Cartwright (2006a), Jackson et al. (2013) and Magee et al. (2013a), who discuss erosion,

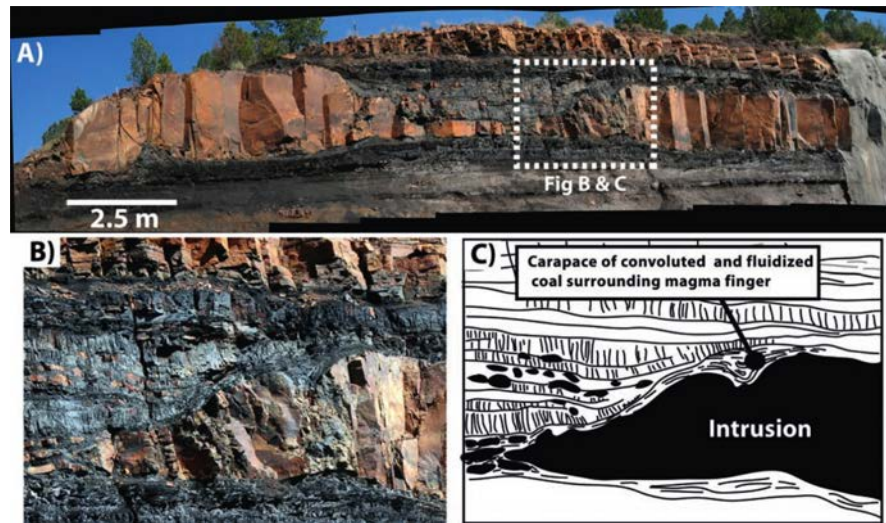


FIGURE 7.2: Schofield et al.'s (2012) figure 9, showing a sill intruding without deforming its overburden, at least at the scale of the field outcrop.

imaging problems, plastic host rock behaviour and other mechanisms as candidates to explain the observations are not disputed by this work — these are likely factors in modifying the host rock. The best example of this is in figure 9 of Schofield et al. (2012), who clearly show an intruding sill which has not deformed its overburden, due to the weak coals the sill has intruded behaving in a ductile fashion (figure 7.2). However, this is likely not the normal state of affairs for sills intruding sedimentary basins; sandstones and lithified shales do not normally flow. In the context of the volume of a sedimentary basin, weak coals and unlithified shales are expected to be the exception rather than the rule. Indeed during a recent field trip to the Isle of Skye, only a handful of examples (~ 7) of host rock fluidisation were observed around the sixty one sills observed, and this fluidisation (in the form of pepperites) occurred at the centimetre scale, nothing like the metre scale fluidization seen in the Raton basin coal beds in Schofield et al. (2012). Furthermore, in figure 7.2 the palaeoseabed cannot be seen. There is clearly ductile deformation at the metre scale around the sill, but this does not necessarily mean the palaeoseabed did not deform into a forced fold at the larger scale anyway. Indeed, in the rare examples of outcrops which exposes large amounts of strata above an intruding sills can be observed (e.g. Eide et al., 2017b) deformation does appear to always be taken up above the sill even if there are thickness variations along the profile of the sill. It is therefore contended that these aforementioned factors are not as common as implied by Schofield et al. (2012), and where they are present constitute a minor effect on the amplitude of the fold, while compaction is the major effect.

This work has a number of implications for forced folds as traps. Firstly, further study of the compaction of forced folds may highlight folds which do appear to be compacting normally, versus folds which do not appear to be compacting normally. Some authors

(e.g. [Holford et al., 2013](#); [Senger et al., 2017](#)) have expressed concern about potential reservoir degradation around igneous intrusions. This has been documented in a number of field studies (e.g. [Ahmed, 2002](#); [Ledevin et al., 2012](#); [Mckinley et al., 2001](#); [Senger et al., 2014](#)). However, these observations have only been shown to apply close to a sill, and the observed effects decrease away from the sill. What counts as “close” to the sill depends on how thick the sill is, the sill’s temperature, the magma flux and the thermal conductivity of the sediments, which in combination control the thermal aureole size. In practice the principal control is the sill thickness. This is because the sills studied in this thesis are predominantly basaltic and the sediments are predominantly siliclastic, limiting the temperature and thermal conductivity of the materials. The diagenetic effects observed depend on the lithology of the host sediments, the chemistry of pore waters and presumably the addition of any volatiles from the intruding magma. The most important factors controlling diagenetic effects on host sediments are the petrology of the host sediment and the chemistry of the pore waters. For example, [Mckinley et al. \(2001\)](#) found dissolution of calcite, saponite (a type of smectite), haematite and talc approaching the margins of a 2 m wide dyke in Northern Ireland, and precipitation and growth of bundles of acicular actinolite amphibole minerals in pore throats. However, crucially both the porosity and permeability of the host Sherwood Sandstone was largely unaltered as there was no volume change between the dissolved and reprecipitated minerals. In contrast, [George \(1993\)](#) found porosity dropped from around 5% to almost 0% within 10 meters of a 30 meter thick dyke in the Midland Valley of Scotland. This involved a strong increase in the amount of quartz overgrowths and secondary illite and chlorite development, which formed pore filling authigenic mineral growths. [Senger et al. \(2017\)](#) report on sills intruding reservoir sequences in the Faeroe-Shetland basin which do not appear to have abnormal porosity trends, although they do display lower than expected permeabilities. As [Mckinley et al. \(2001\)](#) note, while the onset of many diagenetic effects can be predicted, in the case of reservoir quality there is an interest in the abnormal diagenetic effects such as may be expected around intrusions, and need to be able to predict reservoir quality pre-drill rather than post-drill. The aforementioned studies by [Mckinley et al. \(2001\)](#), [George \(1993\)](#) and [Senger et al. \(2017\)](#) may in the future form starting points to parameterize predictive models of diagenetic effects around intrusions. In particular, the thermodynamic modelling of [Mckinley et al. \(2001\)](#) indicated that temperature is the controlling factor for the location of diagenetic changes. Conductive cooling of intrusions is now well understood (e.g. see review in [Turcotte and Schubert, 2014](#)) and well parameterized. For example the thermal conduction is described by the differential equation

$$\frac{\delta T}{\delta t} = \kappa \frac{\delta^2 T}{\delta x^2} \quad (7.2)$$

where T is temperature, t is time, x is distance and κ is the thermal diffusivity, defined by

$$\kappa = \frac{k}{\rho C_p} \quad (7.3)$$

where k is thermal conductivity, ρ is the density and C_p is the specific heat capacity. For the 1D case, this has an analytical solution such that

$$T(x, t) = T_0 + \frac{\Delta T}{2} \left(\operatorname{erf} \frac{a-x}{\sqrt{4\kappa t}} + \operatorname{erf} \frac{a+x}{\sqrt{4\kappa t}} \right) \quad (7.4)$$

where a is the half thickness of the intrusion, T_0 is the initial temperature and erf is the error function. This equation neglects the latent heat of crystallisation. The equation is not solvable analytically if latent heat is included, so the normal way to include it is by increasing the starting temperature to an “effective temperature”. This gives more realistic values in the host rock, at the expense of temperatures which are too high in the centre of the intrusion. The effective temperature is defined as

$$\Delta T = T_m + \frac{L}{C_p} - T_0 \quad (7.5)$$

where T_m is the temperature of the magma and L is the latent heat of crystallisation. Figure 7.3 shows an example of a model showing the change in temperature with time as an intrusion cools. If chemical models — such as those in [Mckinley et al. \(2001\)](#) — can be found for the petrography of different reservoirs, combining such thermal models with seismic images allows the possibility of predicting reservoir diagenetic effects pre-drill. As world hydrocarbon reserves decline this may form an economically important avenue of future research for the petroleum systems in UK sectors of the Hatton Basin, Rockall Basin and FSB.

A different concern for exploitation of forced fold traps is structural deformation. [Hansen and Cartwright \(2006a\)](#) and [Magee et al. \(2017\)](#) have examined and noted moderate degrees of faulting within forced folds, which could cause reservoir compartmentalisation if the faults are sealing. A number of 3D seismic attributes can be useful for this. For example, fig 7.4 shows the interpretation of the top Balder formation over one of the forced folds in the Rockall 3D survey. The panels show maps of time, amplitude, trace envelope, similarity, instantaneous dip and maximum curvature. Each panel has contours from the time map overlayed in grey. The time map shows the structure and 4-way dip closed nature of the fold. Amplitude shows faults more clearly, while trace

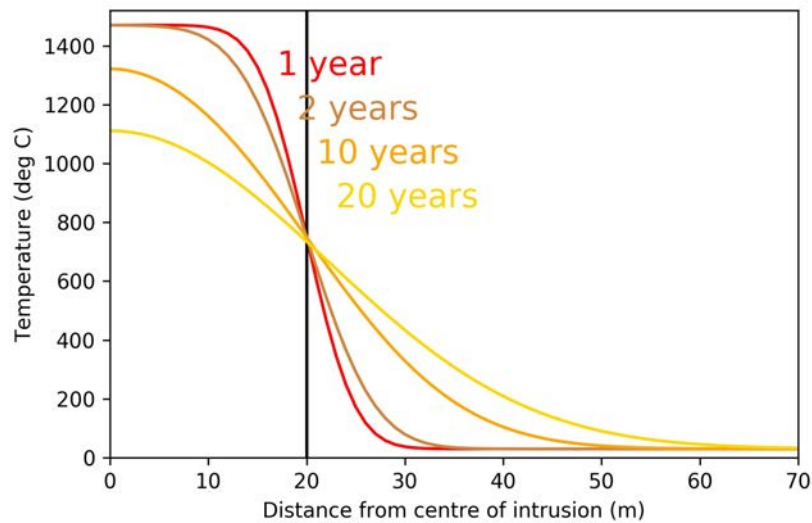


FIGURE 7.3: Model of a conductively cooling intrusion with latent heat, from equation 7.4. Parameters are $a = 20$ m, $T_m = 1200$, $T_0 = 30$, $C_p = 1480$ J K⁻¹, $\rho = 2830$ kg m⁻³, $k = 1$ m² s⁻¹ and $L = 4e5$ J kg⁻¹. A future research target may be relating such temperature models to zones of diagenetic alteration inside thermal aureoles, to predict aureole fluid flow properties.

envelope shows a slight increase in the number of faults imaged and a clearer idea of where amplitude changes do and do not correlate with fault bounded areas. Similarity shows a major improvement in the number of faults clearly imaged, while instantaneous dip makes more details visible in the larger faults while showing the smaller faults less clearly. For fault identification, maximum curvature shows the largest number of faults and arguably the greatest detail. However, these maps only show the seismically observable deformation. Wilson et al. (2016a) shows that compaction bands/granulation seams can be associated with emplacement of sills into sandstones. This is hypothesised to have a serious effect on permeability, as compaction bands act as baffles to fluid flow across them. Models of deformation of a forced fold such as Pollard's (1973) figure 15 (figure 3.24) can predict high strain zones for an ideal case. However, in reality sills are not expected to be an ideal magma filled crack, and therefore the overlying forced fold is not expected to be ideal either. For a non-ideal forced fold, a finite element style model would allow geometries to be modelled more closely to find high strain zones (e.g. Barnett and Gudmundsson, 2014). Following this, field studies may allow parameterization to convert estimates of strain into estimates of compaction band / sub-seismic fault density. This constitutes a possible piece of future work to de-risk these forced folds as potentially producible hydrocarbon traps.

The discussion started with an academic question of why the amplitude of a forced fold does not seem to match the thickness of the sill which formed it. It was then

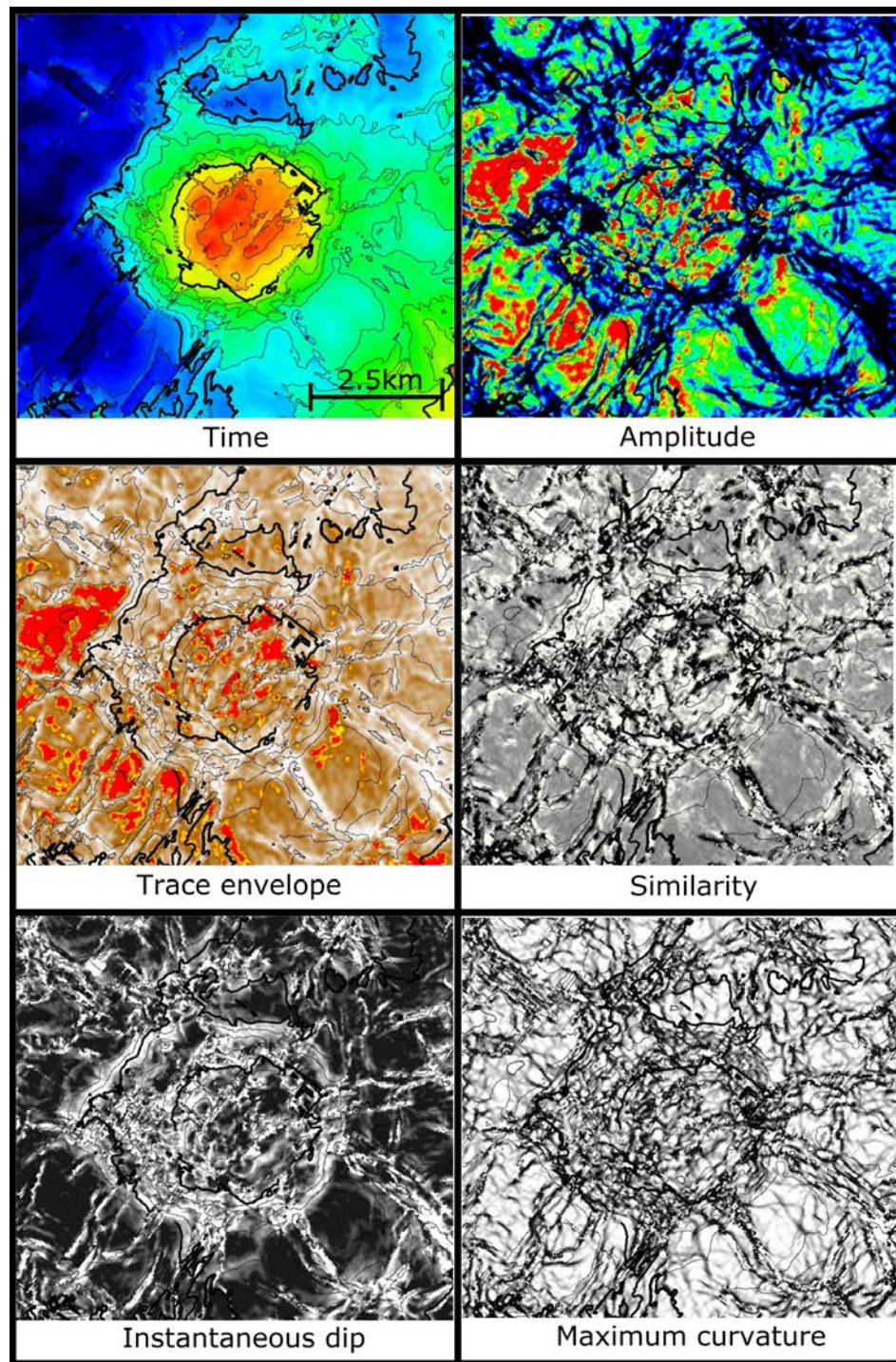


FIGURE 7.4: Forced fold horizon (top Balder) in the Rockall 3D dataset. Field of view is the same in each image.

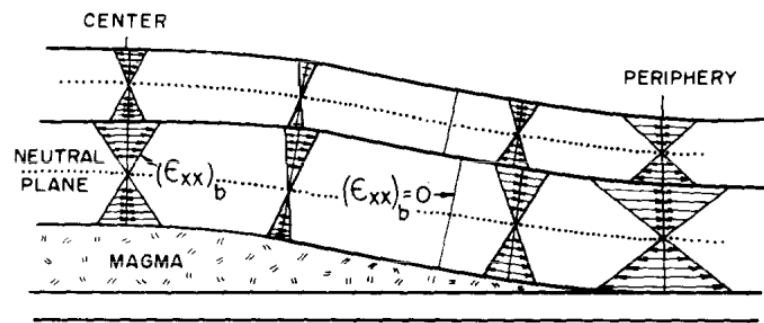


FIGURE 7.5: Pollard's (1973) figure 15, showing vectors visualising the calculated deformation in an ideal forced fold.

shown that decompacting the fold resulted in improving the match between the fold amplitude and the sill thickness. From this it can be inferred that 1. The majority of the amplitude/thickness discrepancy is due to compaction, and 2. the folds are compacting normally; if the folds were compacting abnormally then decompacting them would not make them fit the sills. This implies a lack of anomalous diagenetic effects on the majority of the fold's sediment, and therefore has positive implications for these structures as potential hydrocarbon bearing traps.

7.3.1 Influence of sills on fluid flow

In Chapter 6, analysis of the sill-focused fluid flow model of Rateau et al. (2013) was continued to try to shed further light on its potential use. First, the data in Rateau et al. (2013) were reanalysed, and no statistically significant influence of sills based on the data in the original paper was found. Secondly, a set of forward models was made for different theoretical fluid flow profiles at the end of a sill, and this was compared with real data. No correspondence between the ideal models and the observed data was found. It was concluded that based on the dataset and the data in the original study, there is no evidence for the sill-focused fluid flow model.

The implications for hydrocarbon exploration in such basins is clear. It is not disputed that igneous intrusion can have local effects on fluid flow. For example, dykes have been found to influence ground water flow in Ethiopia (Mège and Rango, 2010), Sudan (Babiker and Gudmundsson, 2004), India (Chandra et al., 2006; Perrin et al., 2011; Satpathy and Kanungo, 1976) and Northern Ireland (Comte et al., 2017). Furthermore sills have been observed to directly influence groundwater from in South Africa (Chevallier et al., 2001). Many of these observations are likely controlled by the relative balance

of amount and orientation of fracture sets in the intrusions, which controls permeability and permeability anisotropy in them (Senger et al., 2015a). Note, however, that these studies all involve an intrusion intruding into an aquifer. In the context of Rateau et al.’s (2013) study this would be equivalent to the sills directly intruding the reservoir. Based on the afore-cited studies (plus other studies, e.g. Cartwright et al., 2007), it is suspected that sill intrusion into a reservoir would have a major and important effect on the fluid flow within the reservoir. Figure 7.6 shows an open access seismic image of the Dooish discovery in the Irish sector of Rockall. A sill is clearly imaged intruding the side of the tilted fault block structure. This may have one of three effects: retarding fluid flow, making a negligible difference to fluid flow, or increasing fluid flow. Geologically, retarding fluid flow would make it a side seal, potentially making the discovery viable. However, given that the overlying sequences are mudstones, if this is the case it is unlikely a crucial part of the trapping mechanism. Having a negligible difference on fluid flow would imply that the fracture permeability is similar to the fracture and intergranular permeability of the reservoir sequences, and it should then therefore be included in the reservoir volumetrics. If the fracture permeability of the intrusion is greater than the permeability of the reservoir sequences, the then sill may represent possible early water cut in developing the reservoir; a potential hazard for economic extraction. Production data from the reservoir would be the only want to quantitatively answer the question of which of these three situations is the case at depth, and would lead to valuable insight for many other prospects in the volcanic basins and margins worldwide.

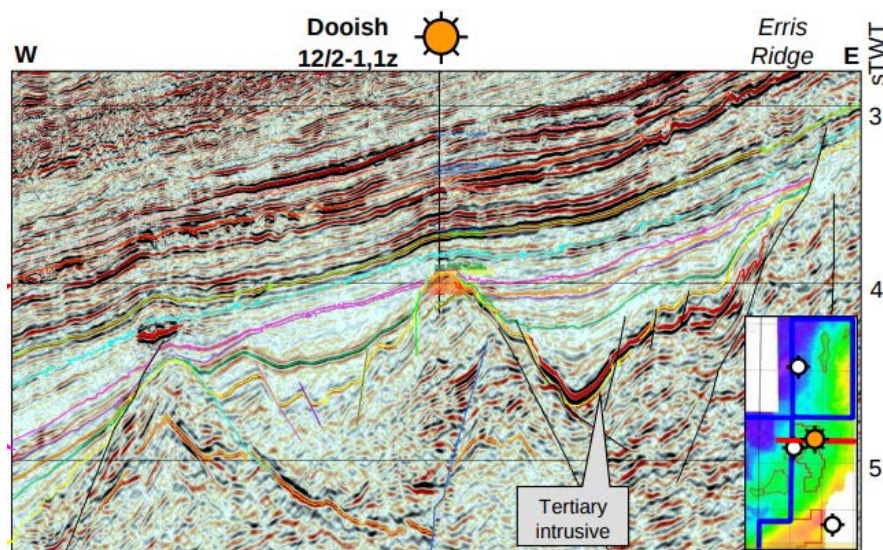


FIGURE 7.6: Seismic line of the Dooish discovery, showing a sill (labelled “Tertiary intrusive”) climbing the flank of the structure. Other seismic lines show the sill to transgress almost to the top of the structure. Accessed on the 22/12/2017 from http://www.serica-energy.com/downloads/farmouts/Serica_Rockall_APPEX2013_Presentation_March2013.pdf

To return to the analysis of Rateau et al. (2013)’s study, the sills are not intruded

directly into a groundwater aquifer or a petroleum reservoir, but are intruded several kilometres below reservoir level, into varying combinations of sand and shales. The results show that statistically, the presence of these sills and the distance from them cannot be distinguished from the shows data. In geological context, this is interpreted to indicate that the effects of faults and carrier beds is significantly more important to regional scale fluid flow and hydrocarbon migration than the effects of the sills. Future work on this may be very important for exploration in LIPs. Sills and igneous intrusions are relatively easy to image and therefore map on seismic data (with the exception of dykes), and thus if they represent a major migration path, mapping them could be a vitally useful tool for exploration. For this reason further study of the model in other basins where there are both a number of intrusions, and a number of wells would be a good idea. As detailed in section 6.4, there could be a number of reasons that a negative result was obtained: there could truly be no effect on fluid flow above background; some wells could have shows which were not identified as they were not cored; the effect on fluid flow could be extremely small and thus many more wells would be required to observe the effect; source rock may not be present under all wells representing a confounding factor; and other potential reasons. The easiest and most reliable way to continue study of this would be to repeat that study methodology with other datasets. Good candidates for this could be the Vøring, Møre, North Porcupine, Barrents or Carnarvon basins, all of which have both good well coverage and intrusion to allow further testing of the model. An easy future goal would be to undertake studies on the porosity and permeability of the sills and dykes, to parameterize the potential effects on fluid flow of each. Surprisingly, little work on this has been done. There would always be difficulties with applying surface based measurements and parameterization to deep basins, but it would certainly be worthwhile to try.

7.4 Sills outside sedimentary basins — magmatic margins and oceanic crust

This thesis has been concerned primarily with sills found in sedimentary basins, and specifically with the dimensions, implications and effect on the surrounding subsurface environment. However sedimentary basins are not the only place sills are found. (White et al., 2008) showed evidence for lower crustal sills making up at least part of the high velocity lower crustal bodies found on the Faeroe-Shetland magma rich continental margin (figure 7.7). From White et al.'s (2008) figure 2, these sills appear to have diameters in the region of 10 km although, as section 3.2 showed, this measurement should be considered unreliable because of the 2D line intersection problem. An apparent diameter of 10 km is within the ranges of data examined in Chapter 3, but it is not sensible to try

to upscale measurements from a single seismic line to the province scale. More densely spaced seismic data is not available over any ocean-continent transitions on volcanic margins that the author knows of, as the oceanward extent of these margins is rarely prospective for hydrocarbons. However, should such data become available, the same techniques developed in sections 3.4.1 (missing sills test), 3.2 (2D – 3D correction) and 3.3.3 (sill thickness prediction from sill diameter) could be used to study sills imaged on such seismic lines, which would allow estimation of the volume of lower crustal magmatic intrusion in LIPs.

Sills also form axial melt lenses in oceanic spreading centres. Such sills are difficult to image using geophysical methods, but a number of studies have focused on resolving and measuring them. For example, (Kent et al., 2000) found up to 6 km diameter sill with a transgressive shape and a raggedy outline at the East Pacific Rise, while (Singh et al., 2006) found a ~ 4.5 km sill along a different section of the East Pacific Rise. (Canales et al., 2009) also found a 2.4 km diameter sill at the Juan de Fuca ridge. These sparse observations all place oceanic axial melt lens sills within the same measurement ranges as the sills described in Chapter 3. This could imply that similar processes are emplacing sills in sedimentary basins and at oceanic spreading centres, however the sill diameter alone is not good evidence for the emplacement processes. Section 3.5.5 showed that the thickness profile is required to discern between brittle and ductile modes of emplacement, and the axial melt sills imaged at spreading centres are all below seismic tuning thickness and hence thickness profile cannot be measured. On the other hand, the similarity in sill diameters between oceanic and sedimentary realms might mean that similar size magma batches are generated in both environments. While the sill diameter observations hint at such possible relationships, significantly more work needs to be done before any conclusions can be drawn.

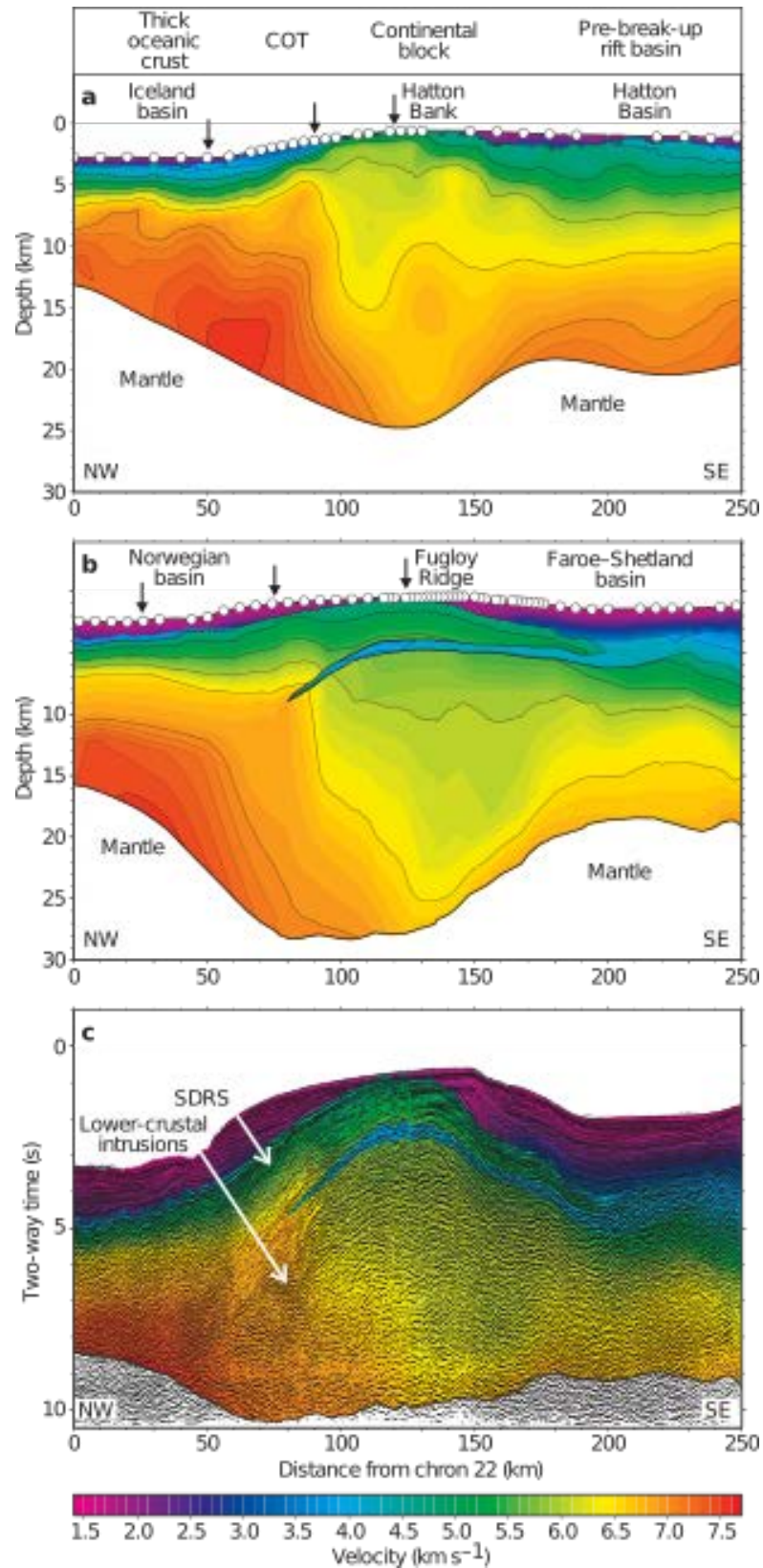


FIGURE 7.7: [White et al.'s \(2008\)](#) figure 2, showing wide angle data from the Hatton margin (a), the Faeroe-Shetland margin (b) and seismic reflection data with an overlaid velocity model from the Faeroe-Shetland margin (c). For full caption, see [White et al. \(2008\)](#).

7.5 Towards an integrated understanding of opal A-CT transitions

Focused fluid flow can often be observed on seismic data as seismic amplitude anomalies, pipes and chimneys (e.g. [Cartwright et al., 2007](#)) and such focused fluid flow structures can constitute an exploration risk. However, these structures can also be an indirect hydrocarbon indicator, as they imply overpressure in the basin system, which can be driven by hydrocarbon generation. In the Rockall 3D dataset, such features were not observed. However, a high amplitude undulating seismic reflector — termed reflector A — was observed. The early hypothesis was that this was a diagenetic boundary of some sort, and that the undulations may represent undulations in the basin's isotherms. The first thing to rule out is that the reflection is a seismic artefact. This is relatively easy to rule out, as it can be observed on three separate seismic surveys, acquired and processed by different contractors. Furthermore, coherent seismic noise needs some sort of a source. The most common type of coherent noise is a water bottom multiple, which is caused by the seafloor and hence the noise has the same shape as the seafloor. Similarly, peg-leg and interbed multiples have the same shape as the reflectors they reflect off. There is no obvious candidate for something with a similar geometry to the opal A-CT transition to cause such noise. Secondly, it was argued that reflector A is an opal A – Opal CT reflection, based on its seismic characteristics, as well as the re-discovery of a drilled opal A-CT boundary in Southern Rockall. Therefore a previously unrecognised opal A-CT transition in the NE Rockall basin is recognised and mapped.

The opal A-CT boundary has an unusual pattern of domes and depressions. It was initially speculated - in the absence of any other obviously spatially varying feature — that the lateral extent of sills may be affecting the isothermal boundaries of the basin, possibly via the fluid flow mechanisms of [Rateau et al. \(2013\)](#). However, when plotting the opal CT's domes over polygons of sill perimeter, there seems to be no obvious correlation with sills edges, which would be expected with [Rateau et al. \(2013\)](#)'s model. This left the problem of what was causing the domes and depressions. A large scale survey of the literature and of IODP / DSDP boreholes was undertaken, with the goal of creating a model of the opal transition. A kinetic reaction model was found using grid search based inversion techniques. This model was found to fit well, but raises additional questions about the temperature structure of Northeast Rockall. Future work will focus around testing the model further in basins with better well control.

The recognition of an opal A-CT boundary in NE Rockall is interesting, as it can form a petroleum trapping mechanism ([Dralus, 2013](#), e.g.). The Monterey formation San Joaquin basin in California, USA has a number of fields trapped and reservoired in

opaline sediments. The Rose and North Shafter fields are trapped under opal CT and reservoired in microcrystalline quartz, where there is commonly an increase in permeability associated with volume loss at the opal CT – microcrystalline quartz transition, forming the trapping mechanism. Figure 7.8 shows this conceptually.

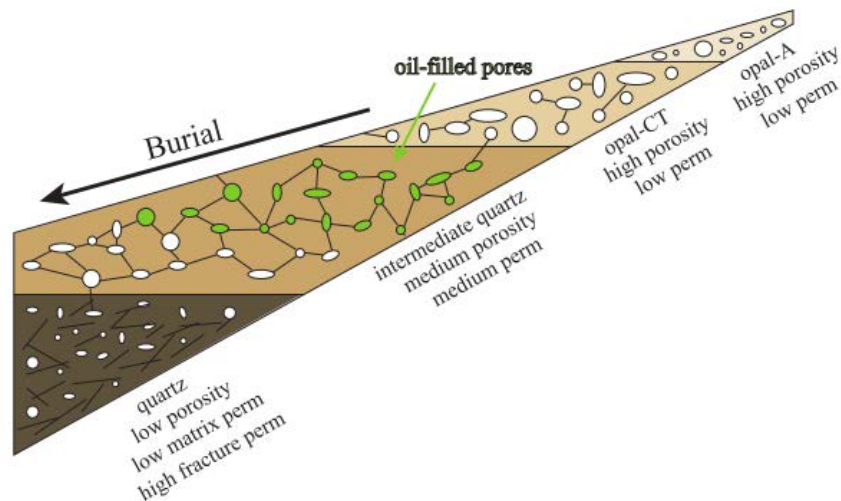


FIGURE 7.8: Figure 3.1 from Dralus (2013), showing the trapping mechanism (via permeability decrease) for the opal transition play in the San Joaquin basin, USA.

Fields trapped under opal transitions in the San Joaquin basin are generally found in stratigraphic pinch outs, of which there is certainly no shortage of in the Rockall basin. The work in Chapter 5 identified an opal A to opal CT transition, and by extension it can be assumed an opal CT to quartz transition likely exists, even if it is not imaged on seismic data. Therefore this play may have potential in the Rockall basin. However, current oil prices it is unlikely that an opal A-CT play would be explored for, even if it was possible.

Being undrilled, this would be a high risk play, in a basin with unproven source rock extent, thus making this unlikely to be explored in the current climate. the opal transition also has implications for other plays in the basin. One of the main potential plays constitutes Tertiary basin floor fans. If it is assumed that the opal CT to microcrystalline quartz transition exists in the Rockall basin, then this has implications for seal integrity for Tertiary fans. The formation of microcrystalline quartz involves an increase in fracture permeability, thus forming the reservoir sequences in the Monterey formation. If this is happening deeper in the Horda formation in Rockall, it could compromise top seals for the Eocene basin floor fans. For example, figure 7.9 shows an isolated basin floor channel and fan complex in the NE Rockall 3D dataset. If this was considered a viable prospect, it would need to be sealed by the compaction drape overlying it. However, if this has been compromised by an increase in permeability due to opal transformations, fluids would have the chance to escape up-dip.

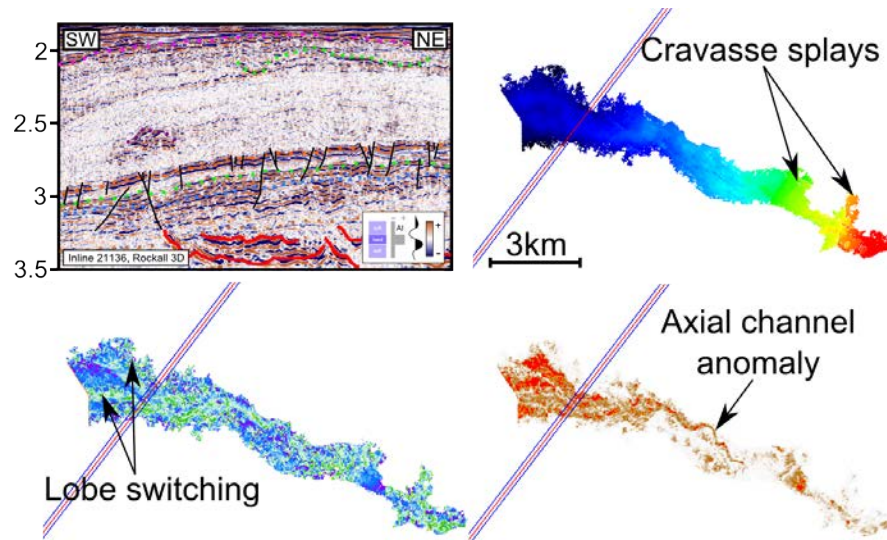


FIGURE 7.9: Basin floor fan play in NE Rockall. Upper left is seismic section in TWT. Horizons from top are Horda (pink), opal A-CT (green), basin floor fan (purple), Balder (orange), Flett (green), Lambda (brown), Vaila (blue), Cretaceous undifferentiated (beige) (see figure 5.5 for stratigraphy). Upper right is time structure map of the basin floor fan horizon. Lower left is dominant frequency, and lower right is Envelope. Blue and red line shows the seismic line.

Future work on this could focus around why there is an opal A to opal CT transition imaged in North East Rockall. The fact that the boundary exists elsewhere but is not imaged could indicate that the opal content of the sediments is higher in NE Rockall than elsewhere in the Rockall basin. If this is the case it implies higher productivity of opal constituents (e.g. diatoms, radiolaria and other silicious organisms) in the Eocene – Oligocene. Whether this is the case, and the reason behind this, could be an interesting topic of research for future palaeoecology and palaeoclimatic studies in Rockall.

Chapter 8

Conclusions

The findings of this thesis have been numerous. The main findings are presented here in list form:

- Lateral resolution is unlikely to often be a problem to sill measurements; given average tapers of a few degrees over the scale of kilometres, errors in measurement due to the sill tips being unimaged typically represent less than 1%.
- The differences in measurement between 2D and 3D seismic data are significant. Assuming a roughly circular sill, the diameter sample means from 2D seismic data typically represent between 0.75 and 0.9 of the true value.
- Sill shape is found to vary widely between basins.
- Saucer shaped sills are the most common sill shape by a significant margin in almost all basins.
- Sill diameter varies between basins, and this variation is statistically significant between almost all basins. We hypothesise this is due mainly to different magma generation rates and volumes; as well as different stress states and different basinal fills, between basins.
- Sill diameter varies far less between sill shapes than it does between different basins. The difference in mean sill diameters between several sills shapes is not statistically significant.
- There is no evidence in this dataset for fractal or power law behaviour in the sill diameters.
- Sill thickness is difficult to sample and measure in a statistically sensible way. This is because the main two methods of sampling sill thickness — well data and seismic data — both suffer from resolution issues.

- Linear relationships do appear to exist between sill thickness and sill diameter, giving rise to a statistical method for predicting sill thickness when a sill is below tuning thickness.
- There is no evidence for fractal or power law behaviour in the sill thickness data.
- Transgressive height is found to vary greatly between basins.
- Sill emplacement depth varies the least of the measurements between basins. However, this measurement is biased to the shallowest sills (as shallow sills inhibit imaging deeper sills), thus this may not be a real effect.
- Different basins are found to have different sill area-densities.
- In the NAIP, sill area densities are found to vary systematically with distance from the Iceland mantle plume, and with basin water depth. This is suggested to show the influence of decompression melting of a hot patch of plume material encountering pre-thinned crust.
- Igneous sill and dyke intrusion models of [Lister \(1990\)](#) and [Lister and Kerr \(1991\)](#) are found to be a poor fit to the sill data presented in Chapter 3.
- The standard LEFM model [Rubin](#) (e.g. [1995](#)) was also found to be a poor fit to the sill data. It was hypothesized that the poor fit may be due to the sill measured in this being emplaced shallowly, leading to model assumptions about host rock elasticity and isotropy being violated.
- The model of [Johnson and Pollard \(1973\)](#) was found to be a far better fit to the data. It is hypothesized that this is due to the incorporation of an elastic plate into the model, thus removing the assumption of host rock isotropy.
- The forced fold amplitude – thickness discrepancy is shown to be removed in twelve out of fourteen cases by taking account of post emplacement burial related compaction.
- An opal A–CT transition is shown to exist in the NE Rockall Basin.
- This opal transition displays a morphology which is possibly new in the literature.
- The morphology is suggested to be due to warm water pore fluid convection systems due to the sills acting as a single hot layer.
- A worldwide database of opal A–CT transition depths is assembled, and it is shown that inverting the data to get a kinetic model outperforms laboratory kinetic parameterizations.
- The kinetic parameterization suggests that high, but realistic, lateral geothermal gradient changes may be responsible for the topography on the Rockall opal A–CT transition.
- It is shown that the data presented in [Rateau et al. \(2013\)](#) does not support the sill focused fluid flow hypothesis.
- A further statistical test for the [Rateau et al. \(2013\)](#) model was presented to test different distances of influence for sills. No distance was found to be statistically

significant in terms of increasing the proportion of shows or discoveries vs a lack of shows.

- The number of wells required to observe a small effect size means that this statistical methodology will likely never observe this, as many hundreds of petroleum exploration wells would be required to give a large enough sample. A medium effect size could be observed by this test, and the existence of a large effect size can effectively be ruled out as it should have been observed with this sample.
- Given the observation of oil and gas reservoirs in some sills, sills must at some scale affect fluid flow systems. A conceptual model was therefore advanced marrying this information with the information of no observed regional affect. It is suggested that if the sill is close to the target then the sill may well have influenced the fluid flow systems. However, at the regional scale other fluid flow systems (e.g. carrier and their beds, and fault and fracture systems) may well lie inbetween the sill and the target, and their effect will be larger than that of the sill.
- The volume of magma in the intrusive sill complex in the NAIP is estimated using parameters from this thesis. It is found to be significantly smaller than the volume of the extrusive and the underplated components.

Appendix A

Sills database

The sills database is a large spreadsheet of several thousand measurements. It is too large to be reproduced as an appendix, but is available for free online at

<https://doi.org/10.6084/m9.figshare.6126974.v1>

where it is licensed by Creative Commons 4.0 license. A second tab on the main spreadsheet, named "clean data" exists, where a cleaned version of the sills database ready for analysis in statistical programs such as R or python.

Appendix B

Sill thickness database (well data)

[illegible]

[illegible]

[illegible]

[illegible]

[illegible]

Source or well name	Basin name	Thickness (m)	Aureole thickness (m)	Lithology
Schofield et al., (2015)	FSB	10		
Schofield et al., (2015)	FSB	10		
Schofield et al., (2015)	FSB	15		
Schofield et al., (2015)	FSB	15		
Schofield et al., (2015)	FSB	15		
Schofield et al., (2015)	FSB	15		
Schofield et al., (2015)	FSB	15		
Schofield et al., (2015)	FSB	15		
Schofield et al., (2015)	FSB	15		
Schofield et al., (2015)	FSB	15		
Schofield et al., (2015)	FSB	15		
Schofield et al., (2015)	FSB	15		
Schofield et al., (2015)	FSB	15		
Schofield et al., (2015)	FSB	15		
Schofield et al., (2015)	FSB	15		
Schofield et al., (2015)	FSB	20		
Schofield et al., (2015)	FSB	20		
Schofield et al., (2015)	FSB	20		
Schofield et al., (2015)	FSB	20		

Source or well name	Basin name	Thickness (m)	Aureole thickness (m)	Lithology
Schofield et al., (2015)	FSB	25		
Schofield et al., (2015)	FSB	25		
Schofield et al., (2015)	FSB	25		
Schofield et al., (2015)	FSB	25		
Schofield et al., (2015)	FSB	25		
Schofield et al., (2015)	FSB	25		
Schofield et al., (2015)	FSB	30		
Schofield et al., (2015)	FSB	30		
Schofield et al., (2015)	FSB	30		
Schofield et al., (2015)	FSB	35		
Schofield et al., (2015)	FSB	35		
Schofield et al., (2015)	FSB	40		
Schofield et al., (2015)	FSB	40		
Schofield et al., (2015)	FSB	40		
Schofield et al., (2015)	FSB	45		
Schofield et al., (2015)	FSB	45		
Schofield et al., (2015)	FSB	45		
Schofield et al., (2015)	FSB	45		
Schofield et al., (2015)	FSB	45		

Source or well name	Basin name	Thickness (m)	Aureole thickness (m)	Lithology
Schofield et al., (2015)	FSB	50		
Schofield et al., (2015)	FSB	50		
Schofield et al., (2015)	FSB	50		
Schofield et al., (2015)	FSB	50		
Schofield et al., (2015)	FSB	55		
Schofield et al., (2015)	FSB	55		
Schofield et al., (2015)	FSB	55		
Schofield et al., (2015)	FSB	60		
Schofield et al., (2015)	FSB	65		
Schofield et al., (2015)	FSB	90		
Schofield et al., (2015)	FSB	95		
Schofield et al., (2015)	FSB	105		
Schofield et al., (2015)	FSB	110		
Schofield et al., (2015)	FSB	110		
Barker and Bone (1995)	Buchan Rift	2.2	0.11	Limestone
Brown et al. (1994)	Karoo	50	75	Limestone
Cooper et al. (2007)	Raton	1.1	1.21	Coal
Drits et al. (2007)	Greenland	40	30	Mudstone
Fjeldskaar et al. (2008)	Voring basin	118.5	177.75	Mudstone

Source or well name	Basin name	Thickness (m)	Aureole thickness (m)	Lithology
Galushkin (1997)		50	50	Mudstone
George (1992)	Midland Valley	3.5	2.45	Mudstone
Grocke et al. (2009)	Ferrar	1.35	1.35	Coal
Meyers and Simoneit (1999)	Colorado	1.5	0.9	Coal
Othman et al. (2001)	Gunnedah Basin	15.58		Mudstone
Othman et al. (2001)	Gunnedah Basin	2.93		Mudstone
Othman et al. (2001)	Gunnedah Basin	1.3		Mudstone
Othman et al. (2001)	Gunnedah Basin	0.4		Mudstone
Othman et al. (2001)	Gunnedah Basin	0.88		Mudstone
Othman et al. (2001)	Gunnedah Basin	1.24		Mudstone
Othman et al. (2001)	Gunnedah Basin	2.18		Mudstone
Perregaard and Schiener (1979)	Greenland	4.5	2.25	Mudstone
Peters et al. (1983)	Cape Verde Rise	5	3	Mudstone
Raymond and Murchison (1988)	Midland Valley	145	300	Mudstone
Raymond and Murchison (1988)	Midland Valley	120	202	Mudstone
Raymond and Murchison (1988)	Midland Valley	100	242	Mudstone
Raymond and Murchison (1988)	Midland Valley	6		Mudstone
Raymond and Murchison (1988)	Midland Valley	65		Mudstone
Raymond and Murchison (1988)	Midland Valley	10		Mudstone

Source or well name	Basin name	Thickness (m)	Aureole thickness (m)	Lithology
Raymond and Murchison (1988)	Midland Valley	20		Mudstone
Raymond and Murchison (1988)	Midland Valley	15		Mudstone
Raymond and Murchison (1988)	Midland Valley	6		Mudstone
Raymond and Murchison (1988)	Midland Valley	3		Mudstone
Raymond and Murchison (1988)	Midland Valley	3		Mudstone
Raymond and Murchison (1988)	Midland Valley	40		Mudstone
Santos et al. (2009)	Parana Basin	13	11.7	Limestone
Saxby and Stephenson (1987)	Rundle	3	1.5	Mudstone
Simoneit et al. (1978, 1981)	Eastern Atlantic	0.2		Mudstone
Simoneit et al. (1978, 1981)	Eastern Atlantic	0.7		
Simoneit et al. (1978, 1981)	Eastern Atlantic	15		
Svensen et al. (2007)	Karoo	80	24	Mudstone
Sweeney and Burnham (1990)		10.4	10.4	Mudstone
Zhu et al. (2007)	Jiyang	50	10	Mudstone
Peace et al. (2017)	Newfoundland	10.3		Mudstone
6004/16-1z	FSB	10		Sandstone
132/15-1	Rockall	15		Limestone
132/15-1	Rockall	10		Mudstone
132/15-1	Rockall	2		Mudstone

Source or well name	Basin name	Thickness (m)	Aureole thickness (m)	Lithology
132/15-1	Rockall	2		Mudstone
132/15-1	Rockall	5		Mudstone
132/15-1	Rockall	2		Mudstone
132/15-1	Rockall	7		Mudstone
132/15-1	Rockall	20		Mudstone
132/15-1	Rockall	12		Sandstone
154/01-1	Rockall	70		Mudstone
164/25-2	Rockall	70		Sandstone
164/25-2	Rockall	45		Mudstone
164/25-2	Rockall	15		Mudstone
164/25-2	Rockall	30		Mudstone
164/25-2	Rockall	10		Mudstone
164/25-2	Rockall	5		Mudstone

Appendix C

Opal A-CT database

Location	Basin name	Depth opal A-CT	Temperature	Age host sed	Water depth
Location	Basin name	Depth opal A-CT	Temperature	Age host sed	Water depth
	South Korea Plateau	450			1900
Site 794	Japan sea	293.5	36.5	8	2811
site 795	Japan sea	326	44	5.2	3298
Site 796	Japan sea	213	42.5	6.3	2600
Site 797	Japan sea	303	36	8	2862
Site 798	Japan sea	451	51	3.8	1000
Site 799	Japan sea	449	45	6.4	1000
6505/10-1	Voring Basin	1700	29	7	684
6406/1-2	Voring Basin	2200	70	7	383
6404/1-1	Voring Basin	1700	70	7	344
6403/6-1	Voring Basin	2800	21	7	1721
6405/7-1	Voring Basin	2140	37	7	1242
6403/10-1	Voring Basin	2900	21	7	1717
6404/11-1	Voring Basin	3000	42	7	1495
6405/10-1	Voring Basin	2118	49	7	928
6305/1-1	Voring Basin	1886	44	7	840
6302/6-1	Voring Basin	1500	62	7	1261
6305/4-1	Voring Basin			7	1004

Location	Basin name	Depth opal A-CT	Temperature	Age host sed	Water depth
6305/7-1	Voring Basin			7	857
6506/3-1	Voring Basin			7	341
6506/11-1	Voring Basin			7	246
6506/6-1	Voring Basin			7	434
6605/8-1	Voring Basin			7	838
6305/8-1	Voring Basin			7	837
6305/8-1	Voring Basin			7	837
	Voring Basin	291	57	20	
6704/12-1	Voring Basin - Gjallar Ridge	1745		7	1352
6305/5-1	More Basin - Ormen Lange	1910		7	886
ODP 150 902	New Jersey, USA	550		30	811
ODP 150 903	New Jersey, USA	900		35	444
ODP 150 904	New Jersey, USA	560		40	1123
ODP 150 905	New Jersey, USA	700		30	2698
ODP 150 906	New Jersey, USA	560		30	913
ODP 189 1170	Southern Ocean	550		40	2703
ODP 189 1171	Southern Ocean	330		35	2148
ODP 189 1172	Southern Ocean	500		40	2622
ODP 113 696	Antarctica, South Orkney	520	32	15	

Location	Basin name	Depth opal A-CT	Temperature	Age host sed	Water depth
ODP 113 695	Antarctica, South Orkney	690	40.5	11	
ODP 105 647	Labrador Sea	250		33	
ODP 198 1207					
DSDP leg 95 605	Baltimore Canyon Trough	350	17	40	
DSDP leg 95 612	Baltimore Canyon Trough	320	17	40	
DSDP leg 95 613	Baltimore Canyon Trough	440	17	40	
DSDP leg 47 site 397	North-west Africa	800		20	
ODP 201 1225					
ODP 113 689					
ODP 138 site 847					
214/4-1	FSB	700		27	
leg 61 site 462	Marshall islands	390	20	45	
DSDP leg 5 - 9					
DSDP leg 16 - 21					
DSDP 26?					
DSDP leg 30 - 33					
DSDP leg 35					
DSDP 38					
DSDP leg 63 site 471	Baja, California	170		13	

Location	Basin name	Depth opal A-CT	Temperature	Age host sed	Water depth
467		500		7	
468		184		11	
469		235		11	
473		203		10	
OCS CAL 78-164 No. 1		1001			
DSDP leg 62 site 463	Hess rise	60		60	
464		80		60	
465		235		83	
466		170		86	
DSDP 80 site 548	Goban Spur, NE Atlantic	390	24.2	40	
549		350	11.33	70	
550		413	9.7	60	
551		150		89	
ODP 121 Site 752B	Broken Ridge, Australia	281		58	
IODP 323 U1341	Bering Sea	122			
ODP leg 127 and 128 Site 799	Japan Basin	400	42	6	
797	Japan Basin	300	42	6	
796	Japan Basin	220	61	6	
798	Japan Basin	480	46	5	

Location	Basin name	Depth opal A-CT	Temperature	Age host sed	Water depth
794	Japan Basin	300	45	11	
795	Japan Basin	340	61		
ODP leg 188 Site 1165	Antarctica	610	30	8	
ODP leg 104 Site 643	Norwegian Sea	300	55	23	
DSDP 69 site 504	Costa Rica rift	225	50	5.2	
DSDP leg 56 site 436	NE Honshu, Japan	379	30	90	
DSDP 41 site 370		210		20	
DSDP 41 site 369		350		72	
DSDP 41 site 368		370		65	
DSDP 41 site 367		320		65	
DSDP 43 site 384	North Atlantic Basin	95		50	
DSDP 43 site 385	North Atlantic Basin	170		50	
DSDP 43 site 386	North Atlantic Basin	500		50	
DSDP 43 site 387	North Atlantic Basin	260		50	
ODP 119 site 738	Southern Indian Ocean	130		40	
ODP 119 site 737	Southern Indian Ocean	555		30	
ODP 108 site 661	Eastern equatorial Atlantic	180		71	
ODP 115 site 707		280		50	
DSDP 57 Site 438		700	21	15	

Location	Basin name	Depth opal A-CT	Temperature	Age host seds	Water depth
DSDP 57 Site 439	West Pacific	851	26	15	
ODP 129 site 800		40	30	80	
ODP 129 site 801		60	23.4	74	
ODP 129 site 802		275		57	
Site 766		166.5		100	
Site 261		204		110	

Bibliography

- Ingrid Aarnes, Henrik Svensen, James AD Connolly, and Yuri Y Podladchikov. How contact metamorphism can trigger global climate changes: Modeling gas generation around igneous sills in sedimentary basins. *Geochimica et Cosmochimica Acta*, 74(24): 7179–7195, 2010.
- Ingrid Aarnes, Kirsten Fristad, Sverre Planke, and Henrik Svensen. The impact of host-rock composition on devolatilization of sedimentary rocks during contact metamorphism around mafic sheet intrusions. *Geochemistry, Geophysics, Geosystems*, 12(10):n/a–n/a, oct 2011. ISSN 15252027. doi: 10.1029/2011GC003636.
- Wolela Ahmed. Effects of heat-flow and hydrothermal fluids from volcanic intrusions on authigenic mineralization in sandstone formations. *Bulletin of the Chemical Society of Ethiopia*, 16(1):37–52, 2002. ISSN 10113924.
- Giulia Airoidi, James D Muirhead, James D L White, and Julie Rowland. Emplacement of magma at shallow depth: insights from field relationships at Allan Hills, south Victoria Land, East Antarctica. *Antarctic Science*, 23(03):281–296, 2011. doi: 10.1017/S0954102011000095.
- Philip A Allen and John R Allen. *Basin analysis: Principles and application to petroleum play assessment*. John Wiley & Sons, 2013.
- Christopher Amante. Etopo1 1 arc-minute global relief model: procedures, data sources and analysis. <http://www.ngdc.noaa.gov/mgg/global/global.html>, 2009.
- Catherine Annen. Implications of incremental emplacement of magma bodies for magma differentiation, thermal aureole dimensions and plutonism–volcanism relationships. *Tectonophysics*, 500(1):3–10, 2011.
- Catherine Annen. Factors Affecting the Thickness of Thermal Aureoles. *Frontiers in Earth Science*, 5(October):1–13, 2017. doi: 10.3389/feart.2017.00082.
- Mohamed Babiker and Agust Gudmundsson. The effects of dykes and faults on groundwater flow in an arid land: The Red Sea Hills, Sudan. *Journal of Hydrology*, 297(1-4): 256–273, 2004. ISSN 00221694. doi: 10.1016/j.jhydrol.2004.04.018.

- Gregor T Baechle, Ralf J Weger, Gregor P Eberli, Jose L Massaferro, and Yue-Feng Sun. Changes of shear moduli in carbonate rocks: Implications for gassmann applicability. *The Leading Edge*, 24(5):507–510, 2005.
- Zoe A. Barnett and Agust Gudmundsson. Numerical modelling of dykes deflected into sills to form a magma chamber. *Journal of Volcanology and Geothermal Research*, 281:1–11, 2014. ISSN 03770273. doi: 10.1016/j.jvolgeores.2014.05.018.
- Richard J Behl. Since Bramlette (1946): The Miocene Monterey Formation of California revisited. *Geological Society of America Special Papers*, 338(1946):301–313, 1999. ISSN 00721077. doi: 10.1130/0-8137-2338-8.301.
- A N Bishop and G D Abbott. Vitrinite reflectance and molecular geochemistry of Jurassic sediments: the influence of heating by Tertiary dykes (northwest Scotland). *Organic Geochemistry*, 22(1):165–177, 1995. doi: 10.1016/0146-6380(95)90015-2.
- David PG Bond and Stephen E Grasby. On the causes of mass extinctions. *Palaeogeography, Palaeoclimatology, Palaeoecology*, 478:3–29, 2017.
- S Bonvalot, G Balmino, A Briais, M Kuhn, A Peyrefitte, N Vales, R Biancale, G Galba, F Reinquin, and M Sarrailh. World gravity map. commission for the geological map of the world. eds. Technical report, BGI-CGMW-CNES-IRD, Paris, 2012.
- Gabriel J Bowen, Timothy J Bralower, Margareth L Delaney, Gerald R Dickens, Daniel C Kelly, Paul L Koch, Lee R Kump, Jin Meng, Lisa C Sloan, Ellen Thomas, et al. Eocene hyperthermal event offers insight into greenhouse warming. *Eos, Transactions American Geophysical Union*, 87(17):165–169, 2006.
- J Bradley. Intrusion of major dolerite sills. *Transactions Of The Royal Society Of New Zealand-Geology*, 3(4):27, 1965.
- AR Brown. *Interpretation of three-dimensional seismic data*. Society of Exploration Geophysicists and American Association of Petroleum Geologists, 2011.
- Scott E Bryan and Richard E Ernst. Revised definition of Large Igneous Provinces (LIPs). *Earth-Science Reviews*, 86(1-4):175–202, 2008. doi: 10.1016/j.earscirev.2007.08.008.
- S. D. Burgess, J. D. Muirhead, and S. A. Bowring. Initial pulse of Siberian Traps sills as the trigger of the end-Permian mass extinction. *Nature Communications*, 8(1):1–4, 2017. ISSN 20411723. doi: 10.1038/s41467-017-00083-9.
- J. Pablo Canales, Mladen R. Nedimovi, Graham M. Kent, Suzanne M. Carbotte, and Robert S. Detrick. Seismic reflection images of a near-axis melt sill within the lower

- crust at the Juan de Fuca ridge. *Nature*, 460(7251):89–93, 2009. ISSN 00280836. doi: 10.1038/nature08095.
- Robert S Carmichael. *CRC handbook of physical properties of Rocks*. CRC Press. Inc., 1982.
- J. Cartwright. The impact of 3D seismic data on the understanding of compaction, fluid flow and diagenesis in sedimentary basins. *Journal of the Geological Society*, 164(5): 881–893, 2007. ISSN 0016-7649. doi: 10.1144/0016-76492006-143.
- Joseph Cartwright and Dorte Mller Hansen. Magma transport through the crust via interconnected sill complexes. *GEOLOGY*, 34(11):929–932, 2006. doi: 10.1130/G22758A.1.
- Joseph Cartwright, Mads Huuse, and Andrew Aplin. Seal bypass systems. *AAPG Bulletin*, 91(8):1141–1166, 2007. doi: 10.1306/04090705181.
- Jonathan M Castro, Benoit Cordonnier, C Ian Schipper, Hugh Tuffen, Tobias S Baumann, and Yves Feisel. Rapid laccolith intrusion driven by explosive volcanic eruption. *Nature communications*, 7:13585, 2016.
- Subash Chandra, V. A. Rao, N. S. Krishnamurthy, S. Dutta, and Shakeel Ahmed. Erratum: Integrated studies for characterization of lineaments used to locate groundwater potential zones in a hard rock region of Karnataka, India (Hydrogeology Journal (2006) (767-776) 10.1007/s10040-005-0480-3)). *Hydrogeology Journal*, 14(6):1042–1051, 2006. ISSN 14312174. doi: 10.1007/s10040-006-0097-1.
- L Chevallier, M Goedhart, and A.C Woodford. The Influences of Dolerite Sill and Ring Complexes on the Occurrence of Groundwater in Karoo Fractured Aquifers: A Morpho-Tectonic Approach, 2001.
- Jacob Cohen. A power primer. *Psychological bulletin*, 112(1):155, 1992.
- J.-C. Comte, C. Wilson, U. Ofterdinger, and A. González-Quirós. Effect of volcanic dykes on coastal groundwater flow and saltwater intrusion: A field-scale multiphysics approach and parameter evaluation. *Water Resources Research*, 53(3):2171–2198, mar 2017. ISSN 00431397. doi: 10.1002/2016WR019480.
- MP Coward, JF Dewey, M Hempton, and J Holroyd. Tectonic evolution. *The Millennium Atlas: Petroleum Geology of the Central and Northern North Sea*. Geological Society, London, pages 17–33, 2003.
- Alison C Cullen, H Christopher Frey, and Christopher H Frey. *Probabilistic techniques in exposure assessment: a handbook for dealing with variability and uncertainty in models and inputs*. Springer Science & Business Media, 1999.

- Luca D'Auria, Susi Pepe, Raffaele Castaldo, Flora Giudicepietro, Giovanni Macedonio, Patrizia Ricciolino, Pietro Tizzani, Francesco Casu, Riccardo Lanari, Mariarosaria Manzo, Marcello Martini, Eugenio Sansosti, and Ivana Zinno. Magma injection beneath the urban area of Naples: a new mechanism for the 2012-2013 volcanic unrest at Campi Flegrei caldera. *Scientific reports*, 5(April):13100, 2015. ISSN 2045-2322. doi: 10.1038/srep13100.
- JHFL Davies, Andréa Marzoli, H Bertrand, N Youbi, M Ernesto, and Urs Schaltegger. End-triassic mass extinction started by intrusive camp activity. *Nature communications*, 8:15596, 2017.
- R J Davies and J Cartwright. A fossilized Opal A to Opal C/T transformation on the northeast Atlantic margin: support for a significantly elevated Palaeogeothermal gradient during the Neogene? *Basin Research*, 14(4):467486, 2002.
- Richard J Davies and Joseph A Cartwright. Kilometer-scale chemical reaction boundary patterns and deformation in sedimentary rocks. *Earth and Planetary Science Letters*, 262(1):125–137, 2007.
- Richard J. Davies and Ian R. Clark. Submarine slope failure primed and triggered by silica and its diagenesis. *Basin Research*, 18(3):339–350, sep 2006a. ISSN 13652117. doi: 10.1111/j.1365-2117.2006.00297.x.
- Richard J Davies and Ian R Clark. Submarine slope failure primed and triggered by silica and its diagenesis: Submarine slope failure due to silica diagenesis. *Basin Research*, 18(3):339–350, 2006b. doi: 10.1111/j.1365-2117.2006.00297.x.
- Richard J Davies, Mads Huuse, Philip Hirst, Joseph Cartwright, and Yuesuo Yang. Giant clastic intrusions primed by silica diagenesis. *GEOLOGY*, 34(11):917, 2006. doi: 10.1130/G22937A.1.
- Michiel O. De Kock, Nicolas J. Beukes, Elijah O. Adeniyi, Doug Cole, Annette E. Götz, Claire Geel, and Frantz Gerard Ossa. Deflating the shale gas potential of South Africa's Main Karoo basin. *South African Journal of Science*, 113(9-10):18DUMMY, 2017. ISSN 19967489. doi: 10.17159/sajs.2017/20160331.
- Kevin Dean, Kevin McLachlan, and Alan Chambers. Rifting and the development of the faeroe-shetland basin. In *Geological Society, London, Petroleum Geology Conference series*, volume 5, pages 533–544. Geological Society of London, 1999.
- A G Doré and E R Lundin. Cenozoic compressional structures on the NE Atlantic margin; nature, origin and potential significance for hydrocarbon exploration. *Petroleum Geoscience*, 2(4):299311, 1996.

- Danica Dralus. *Chemical Interactions Between Silicates and Their Pore Fluids: How They Affect Rock Physics Properties from Atomic to Reservoir Scales*. PhD thesis, Stanford University, 2013.
- AL Du Toit. The karoo dolerites of south africa: A study of hypabyssal injection. *Geological Society of South Africa Transactions*, 23, 1920.
- T. Dunkley Jones, H. R. Manners, M. Hoggett, S. Kirtland Turner, T. Westerhold, M. J. Leng, R. D. Pancost, A. Ridgwell, L. Alegret, R. Duller, and S. T. Grimes. Orbital forcing of terrestrial hydrology, weathering and carbon sequestration during the palaeocene-eocene thermal maximum. *Climate of the Past Discussions*, 2017:1–22, 2017. doi: 10.5194/cp-2017-131.
- S Egbeni, K McClay, J Jian-kui Fu, and D Bruce. Influence of igneous sills on Paleocene turbidite deposition in the Faroe-Shetland Basin: a case study in Flett and Muckle sub-basin and its implication for hydrocarbon exploration. *Geological Society, London, Special Publications*, 397(1):33–57, 2014a. doi: 10.1144/SP397.8.
- Sylvester Egbeni, Ken McClay, Jack Jian-kui Fu, and Duncan Bruce. Influence of igneous sills on paleocene turbidite deposition in the faroe–shetland basin: a case study in flett and muckle sub-basin and its implication for hydrocarbon exploration. *Geological Society, London, Special Publications*, 397(1):33–57, 2014b.
- C. H. Eide, N. Schofield, I. Lecomte, S. J. Buckley, and J. A Howell. Seismic Interpretation of Sill-Complexes in Sedimentary Basins : The 'Sub-Sill Imaging Problem'. *Journal of the Geological Society*, 175(3), 2017a. doi: <http://doi.org/10.1144/jgs2017-096>.
- Christian Haug Eide, Nick Schofield, Dougal A Jerram, and John A Howell. Basin-scale architecture of deeply emplaced sill complexes: Jameson land, east greenland. *Journal of the Geological Society*, 174(1):23–40, 2017b.
- Olav Eldholm and Kjersti Grue. North Atlantic volcanic margins : Dimensions and production rates a volume of flood basalts a mean eruption rate of the basalts were emplaced within volume in a mean crustal accretion rate. *Journal of Geophysical Research*, 99(B2):2955–2968, 1994. ISSN 2156-2202. doi: 10.1029/93JB02879.
- John Encarnación, Thomas H. Fleming, David H. Elliot, and Hugh V. Eales. Synchronous emplacement of Ferrar and Karoo dolerites and the early breakup of Gondwana. *GEOLOGY*, 24(6):535–538, 1996. ISSN 00917613. doi: 10.1130/0091-7613(1996)024<0535:SEOFK>2.3.CO;2.
- Richard E Ernst and Nasrddine Youbi. How large igneous provinces affect global climate, sometimes cause mass extinctions, and represent natural markers in the geological record. *Palaeogeography, Palaeoclimatology, Palaeoecology*, 478:30–52, 2017.

- W G Ernst and Stephen E. Calvert. An experimental study of the recrystallization of porcelanite and its bearing on the origin of some bedded cherts. *American Jour*, 267-A:114–133, 1969.
- NF Exon, BU Haq, and U Von Rad. Exmouth plateau revisited: scientific drilling and geological framework. In *Proceedings of the Ocean Drilling Program, Scientific Results*, volume 122, pages 3–20, 1992.
- Karina Fernandes. *Irish sills of the North Atlantic Igneous Province : seismic imaging observations and implications for climate change*. PhD thesis, Trinity College Dublin, 2011.
- W Fjeldskaar, HM Helset, H Johansen, I Grunnaleite, and I Horstad. Thermal modelling of magmatic intrusions in the Gjallar Ridge, Norwegian Sea: implications for vitrinite reflectance and hydrocarbon maturation. *Basin Research*, 20(1):143–159, 2008.
- E. H. Francis. Magma and sediment-I Emplacement mechanism of late Carboniferous tholeiite sills in northern Britain: President’s anniversary address 1981. *Journal of the Geological Society*, 139(1):1–20, feb 1982. ISSN 0016-7649. doi: 10.1144/gsjgs.139.1.0001.
- Thomas Funck, Gmundur Erlendsson, Wolfram H Geissler, Sofie Gradmann, Geoffrey S Kimbell, Kenneth Mcdermott, and U N I K Petersen. A review of the NE Atlantic conjugate margins based on seismic refraction data. *Geological Society, London, Special Publications*, 447:171–205, 2016a. doi: 10.1144/SP447.9.
- Thomas Funck, Wolfram H Geissler, Geoffrey S Kimbell, Sofie Gradmann, Kenneth M C Dermott, and Unik Petersen. Moho and basement depth in the NE Atlantic Ocean based on seismic refraction data and receiver functions. *Geological Society, London, Special Publications*, 447:207–231, 2016b.
- Olivier Galland, Sverre Planke, Else Ragnhild Neumann, and Anders Malthes-Sørensen. Experimental modelling of shallow magma emplacement: Application to saucer-shaped intrusions. *Earth and Planetary Science Letters*, 277(3-4):373–383, 2009. ISSN 0012821X. doi: 10.1016/j.epsl.2008.11.003.
- Wolfram H. Geissler, Carmen Gaina, John R. Hopper, Thomas Funck, Anett Blischke, Uni Arting, Jim á Horni, Gwenn Péron-Pinvidic, and Mansour M. Abdelmalak. Seismic volcanostratigraphy of the NE Greenland continental margin. *Geological Society, London, Special Publications*, 447(1):149–170, 2017. ISSN 0305-8719. doi: 10.1144/SP447.11.

- S C George. Black Sandstones in the midland valley of Scotland: thermally metamorphosed hydrocarbon reservoirs? *Transactions of the Royal Society of Edinburgh: Earth Sciences*, 84:61–72, 1993. ISSN 14737116. doi: doi:10.1017/S0263593300005927.
- H Gercek. Poisson's ratio values for rocks. *International Journal of Rock Mechanics and Mining Sciences*, 44(1):1–13, 2007.
- F G F Gibb and R Kanaris-Sotiriou. The geochemistry and origin of the Faeroe-Shetland sill complex. *Geological Society, London, Special Publications*, 39(1):241–252, 1988.
- Grove Karl Gilbert. *Report on the Geology of the Henry Mountains*. US Government Printing Office, 1877.
- Jon Gluyas and Richard Swarbrick. *Petroleum geoscience*. John Wiley & Sons, 2013.
- H Gonnermann and B Taisne. Magma transport in dikes. *The Encyclopedia of Volcanoes*,, pages 215–224, 2015.
- N. R. Goult. Emplacement mechanism of the Great Whin and Midland Valley dolerite sills. *Journal of the Geological Society*, 162(6):1047–1056, dec 2005. ISSN 0016-7649. doi: 10.1144/0016-764904-141.
- N.R. Goult and N. Schofield. Implications of simple flexure theory for the formation of saucer-shaped sills. *Journal of Structural Geology*, 30(7):812–817, jul 2008. ISSN 01918141. doi: 10.1016/j.jsg.2008.04.002.
- Kenneth A Grossenbacher and Stephen M McDuffie. Conductive cooling of lava: columnar joint diameter and stria width as functions of cooling rate and thermal gradient. *Journal of volcanology and geothermal research*, 69(1-2):95–103, 1995.
- A Gudmundsson and I F Lotveit. Sills as fractured hydrocarbon reservoirs: examples and models. *Geological Society, London, Special Publications*, 374(1):251–271, 2014. doi: 10.1144/SP374.5.
- Dorthe Moller Hansen. *3D seismic characterisation of igneous sill complexes in sedimentary basins: North-East Atlantic Margin*. PhD thesis, Cardiff University, 2004.
- Dorthe Mller Hansen. The morphology of intrusion-related vent structures and their implications for constraining the timing of intrusive events along the NE Atlantic margin. *Journal of the Geological Society*, 163(5):789–800, 2006. doi: 10.1144/0016-76492004-167.
- Dorthe Mller Hansen and Joseph Cartwright. The three-dimensional geometry and growth of forced folds above saucer-shaped igneous sills. *Journal of Structural Geology*, 28(8):1520–1535, 2006a. doi: 10.1016/j.jsg.2006.04.004.

- Dorthe Mller Hansen and Joseph Cartwright. Saucer-shaped sill with lobate morphology revealed by 3D seismic data: implications for resolving a shallow-level sill emplacement mechanism. *Journal of the Geological Society*, 163(3):509523, 2006b.
- Dothe Mller Hansen, Joseph A Cartwright, and David Thomas. 3D Seismic Analysis of the Geometry of Igneous Sills and Sill Junction Relationships. *Geological Society, London, Memoirs*, 29(1):199–208, 2004. doi: 10.1144/GSL.MEM.2004.029.01.19.
- Øystein Thordén Haug, Olivier Galland, Pauline Souloumiac, Alban Souche, Frank Guldstrand, and Tobias Schmiedel. Inelastic damage as a mechanical precursor for the emplacement of saucer-shaped intrusions. *GEOLOGY*, 45(12), 2017. doi: 10.1130/G39361.1.
- Stefanie Hautmann, Joachim Gottsmann, R Stephen J Sparks, Antonio Costa, Oleg Melnik, and Barry Voight. Modelling ground deformation caused by oscillating overpressure in a dyke conduit at soufrière hills volcano, montserrat. *Tectonophysics*, 471(1):87–95, 2009.
- Thea H Heimdal, Henrik H Svensen, Jahandar Ramezani, Karthik Iyer, Egberto Pereira, René Rodrigues, Morgan T Jones, and Sara Callegaro. Large-scale sill emplacement in brazil as a trigger for the end-triassic crisis. *Scientific reports*, 8(1):141, 2018.
- Timothy J. Henstock, Andrew W. Woods, and Robert S. White. The accretion of oceanic crust by episodic sill intrusion. *Journal of Geophysical Research*, 98:4143, 1993. ISSN 0148-0227. doi: 10.1029/92JB02661.
- S. P. Holford, N. Schofield, C. A. L. Jackson, C. Magee, P. F. Green, and I. R. Duddy. Impacts of igneous intrusions on source and reservoir potential in prospective sedimentary basins along the western Australian continental margin. In *West Australian Basins Symposium 1821 August 2013*, 2013.
- Jim á Horni, John R. Hopper, Anett Blischke, Wolfram H. Geisler, Margaret Stewart, Kenneth McDermott, Maria Judge, Ögmundur Erlendsson, and Uni Árting. Regional distribution of volcanism within the North Atlantic Igneous Province. *Geological Society, London, Special Publications*, 447(1):SP447.18, 2017. ISSN 0305-8719. doi: 10.1144/SP447.18.
- Wuu-Liang Huang. The nucleation and growth of polycrystalline quartz: Pressure effect from 0.05 to 3 GPa. *European Journal of Mineralogy*, 15(5):843–853, 2003. ISSN 09351221. doi: 10.1127/0935-1221/2003/0015-0843.
- H E Huppert. Propagation of two-dimensional and axisymmetric viscous gravity currents over a rigid horizontal surface. *Journal of Fluid Mechanics*, 121:43–58, 1982. ISSN

- 0022-1120. doi: 10.1017/S0022112089001448. URL <http://journals.cambridge.org/production/action/cjoGetFulltext?fulltextid=389693>.
- D H W Hutton. Insights into magmatism in volcanic margins: bridge structures and a new mechanism of basic sill emplacement - Theron Mountains, Antarctica. *Petroleum Geoscience*, 15(3):269–278, 2009. ISSN 1354-0793. doi: 10.1144/1354-079309-841.
- Mads Huuse, Christopher A.L. Jackson, Pieter Van Rensbergen, Richard J. Davies, Peter B. Flemings, and Richard J. Dixon. Subsurface sediment remobilization and fluid flow in sedimentary basins: An overview. *Basin Research*, 22(4):342–360, 2010. ISSN 0950091X. doi: 10.1111/j.1365-2117.2010.00488.x.
- RD Hyndman. Poisson’s ratio in the oceanic crusta review. *Tectonophysics*, 59(1): 321–333, 1979.
- M T Ireland, N R Goulty, and R J Davies. Influence of pore water chemistry on silica diagenesis: evidence from the interaction of diagenetic reaction zones with polygonal fault systems. *Journal of the Geological Society*, 167(2):273–279, 2010a. doi: 10.1144/0016-76492009-049.
- Mark T Ireland, Neil R Goulty, and Richard J Davies. Influence of pore water chemistry on silica diagenesis: evidence from the interaction of diagenetic reaction zones with polygonal fault systems. *Journal of the Geological Society*, 167(2):273–279, 2010b.
- Mark T Ireland, Richard J Davies, Neil R Goulty, and Daniel Carruthers. Structure of a silica diagenetic transformation zone: the Gjallar Ridge, offshore Norway: Silica diagenetic transformation zone offshore Norway. *Sedimentology*, 58(2):424–441, 2011. doi: 10.1111/j.1365-3091.2010.01170.x.
- Caroline M. Isaacs. Porosity Reduction During Diagenesis of Monterey Formation, Santa Barbara, California. *AAPG Bulletin*, 65, 1981. ISSN 0149-1423. doi: 10.1306/2F919F0D-16CE-11D7-8645000102C1865D.
- Caroline M Isaacs. Influence of rock composition on kinetics of silica phase changes in the Monterey Formation, Santa Barbara area, California. *GEOLOGY*, 10(6):304, 1982. doi: 10.1130/0091-7613(1982)10<304:IORCOK>2.0.CO;2.
- Karthik Iyer, Lars Rüpke, and Christophe Y. Galerne. Modeling fluid flow in sedimentary basins with sill intrusions: Implications for hydrothermal venting and climate change. *Geochemistry, Geophysics, Geosystems*, 14(12):5244–5262, 2013. ISSN 15252027. doi: 10.1002/2013GC005012.
- C A.-L. Jackson, N Schofield, and B Golenkov. Geometry and controls on the development of igneous sill-related forced folds: A 2-D seismic reflection case study from

- offshore southern Australia. *Geological Society of America Bulletin*, 125(11-12):1874–1890, 2013. doi: 10.1130/B30833.1.
- Bjorn Jamtveit, Henrik Svensen, Y. Y Podladchikov, and Sverre Planke. Hydrothermal vent complexes associated with sill intrusions in sedimentary basins. *Geological Society, London, Special Publications*, 234(1):233–241, 2004. ISSN 0305-8719. doi: 10.1144/GSL.SP.2004.234.01.15.
- Bjørn Jamtveit, Fernando Corfu, Yuri Y. Podladchikov, Alexander G. Polozov, Sverre Planke, Norbert Schmidbauer, and Henrik Svensen. Siberian gas venting and the end-Permian environmental crisis. *Earth and Planetary Science Letters*, 277(3-4):490–500, 2008. ISSN 0012821X. doi: 10.1016/j.epsl.2008.11.015. URL <http://dx.doi.org/10.1016/j.epsl.2008.11.015>.
- Dougal A. Jerram and Scott E. Bryan. Plumbing Systems of Shallow Level Intrusive Complexes. In *Advances in Volcanology*, pages 1–14. Springer, 2015. doi: 10.1007/11157_2015.8.
- Arvid M Johnson and David D Pollard. Mechanics of growth of some laccolithic intrusions in the Henry mountains, Utah, I: field observations, Gilbert’s model, physical properties and flow of the magma. *Tectonophysics*, 18(3-4):261309, 1973.
- Stephen M Jones, Bryan Lovell, and Alistair G Crosby. Comparison of modern and geological observations of dynamic support from mantle convection. *Journal of the Geological Society*, 169(6):745–758, 2012.
- H Kagami. Transformation of opaline silica in sediments from bay of biscay and rockall bank. *Initial Reports of Deep Sea Drilling Project*, 48:757–764, 1979.
- Jun Kameda, Atsushi Okamoto, Kiminori Sato, Koichiro Fujimoto, Asuka Yamaguchi, and Gaku Kimura. Opal-CT in chert beneath the toe of the Tohoku margin and its influence on the seismic aseismic transition in subduction zones. *Geophysical Research Letters*, 44(2):687–693, 2017. ISSN 19448007. doi: 10.1002/2016GL071784.
- M Kastner and J M Gieskes. Opal-A to opal-CT transformation: a kinetic study. *Developments in Sedimentology*, 36:211—227, 1983.
- Miriam Kastner, JB Keene, and JM Gieskes. Diagenesis of siliceous ooze. chemical controls on the rate of opal-a to opal-ct transformationan experimental study. *Geochimica et Cosmochimica Acta*, 41(8):1041–1059, 1977.
- J. L. Kavanagh, D. Boutelier, and A. R. Cruden. The mechanics of sill inception, propagation and growth: Experimental evidence for rapid reduction in magmatic overpressure. *Earth and Planetary Science Letters*, 421:117–128, 2015. ISSN 0012821X.

- doi: 10.1016/j.epsl.2015.03.038. URL <http://dx.doi.org/10.1016/j.epsl.2015.03.038>.
- Janine L Kavanagh, Thierry Menand, and R Stephen J Sparks. An experimental investigation of sill formation and propagation in layered elastic media. *Earth and Planetary Science Letters*, 245(3-4):799–813, 2006. doi: 10.1016/j.epsl.2006.03.025.
- Janine L. Kavanagh, Samantha Engwell, and Simon Martin. A review of analogue and numerical modelling in volcanology. *Solid Earth Discussions*, pages 1–80, 2017. ISSN 1869-9537. doi: 10.5194/se-2017-40. URL <https://www.solid-earth-discuss.net/se-2017-40/>.
- Janine L. Kavanagh, Alec J. Burns, Suraya Hilmi Hazim, Elliot P. Wood, Simon A. Martin, Sam Hignett, and David J.C. Dennis. Challenging dyke ascent models using novel laboratory experiments: Implications for reinterpreting evidence of magma ascent and volcanism. *Journal of Volcanology and Geothermal Research*, 354:87–101, 2018. ISSN 03770273. doi: 10.1016/j.jvolgeores.2018.01.002.
- G M Kent, S C Singh, A J Harding, M C Sinha, J A Orcutt, P J Barton, R S White, S Bazin, R W Hobbs, C H Tong, and J W Pye. Evidence from three-dimensional seismic reflectivity images for enhanced melt supply beneath mid-ocean-ridge discontinuities. *Nature*, 406(August):614–618, 2000.
- S. D. Killops, R. A. Cook, R. Sykes, and J. P. Boudou. Petroleum potential and oil-source correlation in the Great South and Canterbury Basins. *New Zealand Journal of Geology and Geophysics*, 40(4):405–423, dec 1997. ISSN 0028-8306. doi: 10.1080/00288306.1997.9514773.
- Michael Krumbholz, Christoph F Hieronymus, Steffi Burchardt, Valentin R Troll, David C Tanner, and Nadine Friese. Weibull-distributed dyke thickness reflects probabilistic character of host-rock strength. *Nature Communications*, 5, 2014. ISSN 2041-1723. doi: 10.1038/ncomms4272. URL <https://www.nature.com/articles/ncomms4272.pdf><http://www.nature.com/doifinder/10.1038/ncomms4272>.
- S Kuramoto, K Tamaki, M G Langseth, D C Nobes, H Tokuyama, K A Pisciotto, and A Taira. Can Opal-A/Opal-CT BSR Be An Indicator Of The Thermal Structure Of The Yamato Basin, Japan Sea? *Age*, 794(36.5):365, 1992.
- Shigekazu Kusumoto, Nobuo Geshi, and Agust Gudmundsson. Aspect ratios and magma overpressures of non-feeder dikes observed in the miyake-jima volcano (japan), and fracture toughness of its upper part. *Geophysical Research Letters*, 40(6):1065–1068, 2013.

- MG Laird and JD Bradshaw. The break-up of a long-term relationship: the cretaceous separation of new zealand from gondwana. *Gondwana Research*, 7(1):273–286, 2004.
- M Ledevin, N Arndt, M R Cooper, G Earls, P Lyle, C Aubourg, and E Lewin. Intrusion history of the Portrush Sill, County Antrim, Northern Ireland: evidence for rapid emplacement and high-temperature contact metamorphism. *Geological Magazine*, 149(1):67–79, 2012. ISSN 0016-7568. doi: 10.1017/s0016756811000537.
- J. H. Ligtenberg. Detection of Fluid migration pathways in seismic data: Implications for fault seal analysis. *Basin Research*, 17(1):141–153, mar 2005. ISSN 0950091X. doi: 10.1111/j.1365-2117.2005.00258.x.
- John R. Lister. Buoyancy-driven fluid fracture: similarity solutions for the horizontal and vertical propagation of fluid-filled cracks. *Journal of Fluid Mechanics*, 217(-1): 213, 1990. ISSN 0022-1120. doi: 10.1017/S0022112090000696.
- JR Lister and RC Kerr. Fluid-Mechanical Models of Crack Propagation and Their Application to Magma Transport in Dykes. *Journal of Geophysical Research*, 96: 10,049–10,077, 1991. ISSN 0148-0227. doi: 10.1029/91JB00600.
- Hongbo Lu, Craig S Fulthorpe, and Paul Mann. Three-dimensional architecture of shelf-building sediment drifts in the offshore canterbury basin, new zealand. *Marine Geology*, 193(1):19–47, 2003.
- J MacDonald, G Backé, R King, S Holford, and R Hillis. Geomechanical modelling of fault reactivation in the ceduna sub-basin, bight basin, australia. *Geological Society, London, Special Publications*, 367(1):71–89, 2012.
- John MacLennan and Stephen M Jones. Regional uplift, gas hydrate dissociation and the origins of the paleocene–eocene thermal maximum. *Earth and Planetary Science Letters*, 245(1-2):65–80, 2006.
- C Magee, C A.-L. Jackson, and N Schofield. Diachronous sub-volcanic intrusion along deep-water margins: insights from the Irish Rockall Basin. *Basin Research*, 26(1): 85–105, 2014a. doi: 10.1111/bre.12044.
- Craig Magee, Freddie Briggs, and Christopher AL Jackson. Lithological controls on igneous intrusion-induced ground deformation. *Journal of the Geological Society*, 170(6):853–856, 2013a.
- Craig Magee, Christopher A.-L Jackson, and Nick Schofield. The influence of normal fault geometry on igneous sill emplacement and morphology. *GEOLOGY*, 41(4):406–410, 2013b. ISSN 00917613. doi: 10.1130/G33824.1.

- Craig Magee, Kenneth G McDermott, Carl TE Stevenson, and Christopher A.L. Jackson. Influence of crystallised igneous intrusions on fault nucleation and reactivation during continental extension. *Journal of Structural Geology*, 62:183–193, 2014b. ISSN 01918141. doi: 10.1016/j.jsg.2014.02.003.
- Craig Magee, Shivani M. Maharaj, Thilo Wrona, and Christopher A L Jackson. Controls on the expression of igneous intrusions in seismic reflection data. *Geosphere*, 11(4): 1024–1041, aug 2015. ISSN 1553040X. doi: 10.1130/GES01150.1.
- Craig Magee, James D Muirhead, Alex Karvelas, Simon P Holford, Christopher A L Jackson, Ian D Bastow, Nick Schofield, Carl T E Stevenson, Charlotte McLean, William McCarthy, and Olga Shtukert. Lateral magma flow in mafic sill complexes. *Geosphere*, page GES01256.1, 2016. doi: 10.1130/GES01256.1.
- Craig Magee, I.D. Ian D. Bastow, Benjamin van Wyk B.W. de Vries, Christopher A.L. C.A. Jackson, Rachel Hetherington, Miruts Hagos, and Murray Hoggett. Structure and dynamics of surface uplift induced by incremental sill emplacement. *GEOL- OGY*, 45(5), 2017. ISSN 19432682. doi: 10.1130/G38839.1.
- A Malthe-Sørenssen, S Planke, H Svensen, and B Jamtveit. Formation of saucer-shaped sills. *Physical Geology of High-Level Magmatic Systems. Geological Society, London, Special Publications*, 234:215–227, 2004.
- J. Maresh, R. S. White, R. W. Hobbs, and J. R. Smallwood. Seismic attenuation of Atlantic margin basalts: Observations and modeling. *Geophysics*, 71(6):B211–B221, 2006. ISSN 00168033. doi: 10.1190/1.2335875.
- Milena Marjanović, Suzanne M. Carbotte, Helene Carton, Mladen R. Nedimović, John C. Mutter, and Juan Pablo Canales. A multi-sill magma plumbing system beneath the axis of the East Pacific Rise. *Nature Geoscience*, 7(11):825–829, 2014. ISSN 17520908. doi: 10.1038/ngeo2272.
- L Mathieu, B. van Wyk de Vries, Eoghan P Holohan, and Valentin R Troll. Dykes, cups, saucers and sills: Analogue experiments on magma intrusion into brittle rocks. *Earth and Planetary Science Letters*, 271(1-4):1–13, 2008. ISSN 0012821X. doi: 10.1016/j.epsl.2008.02.020.
- Kenneth McClay, Nicola Scarselli, and Sukonmeth Jitmahantakul. *Igneous Intrusions in the Carnarvon Basin, NW Shelf, Australia*. APPEA, 8 2013.
- Dan McKenzie. The variation of temperature with time and hydrocarbon maturation in sedimentary basins formed by extension. *Earth and Planetary Science Letters*, 55 (1):8798, 1981.

- Dan Mckenzie, Peter G Ford, Fang Liu, and Gordon H Pettengill. Pancakelike Domes on Venus. *Journal of Geophysical Research E: Planets*, 97(E10):15,967–15,976, 1992. ISSN 2156-2202. doi: 10.1029/92JE01349.
- Jennifer M. Mckinley, Richard H. Worden, and Alastair H. Ruffell. Contact Diagenesis: the Effect of an Intrusion on Reservoir Quality in the Triassic Sherwood Sandstone Group, Northern Ireland. *Journal of Sedimentary Research*, 71(3):484–495, 2001. ISSN 1527-1404. doi: 10.1306/2dc40957-0e47-11d7-8643000102c1865d.
- Daniel Mège and Tewodros Rango. Permanent groundwater storage in basaltic dyke fractures and termite mound viability. *Journal of African Earth Sciences*, 57(1-2): 127–142, 2010. ISSN 1464343X. doi: 10.1016/j.jafrearsci.2009.07.014.
- Thierry Menand. The mechanics and dynamics of sills in layered elastic rocks and their implications for the growth of laccoliths and other igneous complexes. *Earth and Planetary Science Letters*, 267(1):93–99, 2008.
- Thierry Menand. Physical controls and depth of emplacement of igneous bodies: A review. *Tectonophysics*, 500(1-4):11–19, 2011. doi: 10.1016/j.tecto.2009.10.016.
- I Metcalfe. Gondwana dispersion and asian accretion: tectonic and palaeogeographic evolution of eastern tethys. *Journal of Asian Earth Sciences*, 66:1–33, 2013.
- Andrew Miles and Joseph Cartwright. Hybrid flow sills: A new mode of igneous sheet intrusion. *GEOLOGY*, 38(4):343–346, apr 2010. ISSN 00917613. doi: 10.1130/G30414.1.
- Nigel C. Morewood, P. M. Shannon, and G. D. Mackenzie. Seismic stratigraphy of the southern Rockall Basin: A comparison between wide-angle seismic and normal incidence reflection data. *Marine and Petroleum Geology*, 21(9):1149–1163, 2004. ISSN 02648172. doi: 10.1016/j.marpetgeo.2004.07.006.
- Raluca Cristina Neagu, Joseph Cartwright, Richard Davies, and Lars Jensen. Fossilisation of a silica diagenesis reaction front on the mid-Norwegian margin. *Marine and Petroleum Geology*, 27(10):2141–2155, dec 2010. ISSN 02648172. doi: 10.1016/j.marpetgeo.2010.09.003.
- E. G. Nisbet, S. M. Jones, J. MacLennan, G. Eagles, J. Moed, N. Warwick, S. Bekki, P. Braesicke, J. A. Pyle, and C. M.R. Fowler. Kick-starting ancient warming. *Nature Geoscience*, 2(3):156–159, 2009. ISSN 17520894. doi: 10.1038/ngeo454.
- MS Norvick and MA Smith. Mapping the plate tectonic reconstruction of southern and southeastern australia and implications for petroleum systems. *The APPEA Journal*, 41(1):15–35, 2001.

- J F Nye. The mechanics of glacier flow. *Journal of Glaciology*, 2(January):82–93, 1952. ISSN 00221430. doi: 10.3198/1952JoG2-12-82-93.
- Ross Parnell-Turner, Nicky White, Tim Henstock, Bramley Murton, John MacLennan, and Stephen M Jones. A continuous 55-million-year record of transient mantle plume activity beneath iceland. *Nature Geoscience*, 7(12):914, 2014.
- Luigi Passarelli, Eleonora Rivalta, and Ashley Shuler. Dike intrusions during rifting episodes obey scaling relationships similar to earthquakes. *Scientific reports*, 4:3886, 2014.
- Jerome Perrin, Shakeel Ahmed, and Daniel Hunkeler. The effects of geological heterogeneities and piezometric fluctuations on groundwater flow and chemistry in a hard-rock aquifer, southern India. *Hydrogeology Journal*, 19(6):1189–1201, 2011. ISSN 14312174. doi: 10.1007/s10040-011-0745-y.
- G. Pickering, J.M. Bull, and D.J. Sanderson. Sampling power-law distributions. *Tectonophysics*, 248(1-2):1–20, 1995. ISSN 00401951. doi: 10.1016/0040-1951(95)00030-Q.
- S Planke, T Rasmussen, SS Rey, and R Myklebust. Seismic characteristics and distribution of volcanic intrusions and hydrothermal vent complexes in the vøring and møre basins. In *Geological Society, London, Petroleum Geology Conference series*, volume 6, pages 833–844. Geological Society of London, 2005.
- David D Pollard. Derivation and evaluation of a mechanical model for sheet intrusions. *Tectonophysics*, 19(3):233269, 1973.
- David D. Pollard, Otto H. Muller, and David R. Dockstader. The form and growth of fingered sheet intrusions. *Bulletin of the Geological Society of America*, 86(3):351–363, 1975. ISSN 00167606. doi: 10.1130/0016-7606(1975)86(351:TFAGOF)2.0.CO;2.
- Stéphane Polteau, Adriano Mazzini, Olivier Galland, Sverre Planke, and Anders Malthe-Sørenssen. Saucer-shaped intrusions: Occurrences, emplacement and implications. *Earth and Planetary Science Letters*, 266(1-2):195–204, feb 2008. ISSN 0012821X. doi: 10.1016/j.epsl.2007.11.015.
- Ole Rabbal, Olivier Galland, Karen Mair, Isabelle Lecomte, Kim Senger, Juan Bautista Spacapan, and Rene Manceda. From field analogues to realistic seismic modelling: a case study of an oil-producing andesitic sill complex in the Neuquén Basin, Argentina. *Journal of the Geological Society*, pages jgs2017–116, mar 2018. ISSN 0016-7649. doi: 10.1144/jgs2017-116. URL <http://jgs.lyellcollection.org/lookup/doi/10.1144/jgs2017-116>.

- Rmi Rateau, Nick Schofield, and Michael Smith. The potential role of igneous intrusions on hydrocarbon migration, West of Shetland. *Petroleum Geoscience*, 19(3):259272, 2013.
- A C Raymond and D G Murchison. The relationship between organic maturation, the widths of thermal aureoles and the thicknesses of sills in the Midland Valley of Scotland and Northern England. *Journal of the Geological Society*, 148(2):215218, 1991.
- Jennifer Reeves, Craig Magee, and Christopher Aiden-Lee Jackson. Unravelling intrusion-induced forced fold kinematics and ground deformation using 3d seismic reflection data. *Volcanica*, 2017.
- Jennifer Reeves, Craig Magee, and Christopher A-l Jackson. Unravelling intrusion-induced forced fold kinematics and ground deformation using 3D seismic reflection data. *Volcanica*, 1(1):1–17, 2018.
- P. Reynolds, S. Holford, N. Schofield, and A. Ross. The shallow depth emplacement of mafic intrusions on a magma-poor rifted margin: An example from the Bight Basin, southern Australia. *Marine and Petroleum Geology*, 88:605–616, dec 2017. ISSN 02648172. doi: 10.1016/j.marpetgeo.2017.09.008.
- J. A. Richardson, C. B. Connor, P. H. Wetmore, L. J. Connor, and E. A. Gallant. Role of sills in the development of volcanic fields: Insights from lidar mapping surveys of the San Rafael Swell, Utah. *Geology*, 43(11):1023–1026, 2015. ISSN 19432682. doi: 10.1130/G37094.1.
- Malcolm H Rider. *The geological interpretation of well logs*. 1986.
- F Rodriguez Monreal, H J Villar, R Baudino, D Delpino, and S Zencich. Modeling an atypical petroleum system: A case study of hydrocarbon generation, migration and accumulation related to igneous intrusions in the Neuquen Basin, Argentina. *Marine and Petroleum Geology*, 26(4):590–605, 2009. doi: 10.1016/j.marpetgeo.2009.01.005.
- Allan M Rubin. Propagation of magma-filled cracks. *Annual Review of Earth and Planetary Sciences*, 23(1):287–336, 1995.
- John F. Rudge, Max E. Shaw Champion, Nicky White, Dan McKenzie, and Bryan Lovell. A plume model of transient diachronous uplift at the Earth’s surface. *Earth and Planetary Science Letters*, 267(1-2):146–160, 2008. ISSN 0012821X. doi: 10.1016/j.epsl.2007.11.040.
- B. N. Satpathy and D. N. Kanungo. Groundwater Exploration in Hard Rock Terrain. a Case History. *Geophysical Prospecting*, 24(4):725–736, 1976. ISSN 13652478. doi: 10.1111/j.1365-2478.1976.tb01569.x.

- AD Saunders, JG Fitton, AC Kerr, MJ Norry, and RW Kent. The north atlantic igneous province. *Large igneous provinces: Continental, oceanic, and planetary flood volcanism*, pages 45–93, 1997.
- AD Saunders, SM Jones, LA Morgan, KLM Pierce, M Widdowson, and YG Xu. Regional uplift associated with continental large igneous provinces: The roles of mantle plumes and the lithosphere. *Chemical Geology*, 241(3-4):282–318, 2007.
- J. Scheibert, O. Galland, and A. Hafver. Inelastic deformation during sill and laccolith emplacement: Insights from an analytic elastoplastic model. *Journal of Geophysical Research: Solid Earth*, 122(2):923–945, 2017. ISSN 21699356. doi: 10.1002/2016JB013754.
- Tobias Schmiedel, Sigurd Kjoberg, Sverre Planke, Craig Magee, Olivier Galland, Nick Schofield, Christopher A.-L. Jackson, and Dougal A. Jerram. Mechanisms of overburden deformation associated with the emplacement of the Tulipan sill, mid-Norwegian margin. *Interpretation*, 5(3):1–15, 2017. ISSN 2324-8858. doi: 10.1190/INT-2016-0155.1.
- Nick Schofield, Carl Stevenson, and Tim Reston. Magma fingers and host rock fluidization in the emplacement of sills. *Geology*, 38(1):63–66, 2010.
- Nick Schofield, Simon Holford, John Millett, David Brown, David Jolley, Simon R. Passey, Dave Muirhead, Clayton Grove, Craig Magee, Joanne Murray, Malcolm Hole, Christopher A.L. Jackson, and Carl Stevenson. Regional magma plumbing and emplacement mechanisms of the Faroe-Shetland Sill Complex: implications for magma transport and petroleum systems within sedimentary basins. *Basin Research*, 29(1): 41–63, 2017. ISSN 13652117. doi: 10.1111/bre.12164.
- Nick J. Schofield, David J. Brown, Craig Magee, and Carl T. Stevenson. Sill morphology and comparison of brittle and non-brittle emplacement mechanisms. *Journal of the Geological Society*, 169(2), 2012.
- John G Sclater and P A F Christie. Continental stretching: an explanation of the post-mid-Cretaceous subsidence of the central North Sea basin. *Journal of Geophysical Research*, 85(B7):37113739, 1980.
- Kim Senger, Sverre Planke, Stephane Polteau, Kei Ogata, Henrik Svensen, Kim Senger, Kim Senger, Sverre Planke, and Henrik Svensen. Sill emplacement and contact metamorphism in a siliciclastic reservoir on Svalbard, Arctic Norway. *Norsk Geologisk Tidsskrift*, 94(2-3):155–169, 2014. ISSN 0029196X.
- Kim Senger, Simon J. Buckley, Luc Chevallier, Åke Fagereng, Olivier Galland, Tobias H. Kurz, Kei Ogata, Sverre Planke, and Jan Tveranger. Fracturing of doleritic intrusions

- and associated contact zones: Implications for fluid flow in volcanic basins. *Journal of African Earth Sciences*, 102:70–85, 2015a. ISSN 18791956. doi: 10.1016/j.jafrearsci.2014.10.019.
- Kim Senger, Simon J Buckley, Luc Chevallier, ke Fagereng, Olivier Galland, Tobias H Kurz, Kei Ogata, Sverre Planke, and Jan Tveranger. Fracturing of doleritic intrusions and associated contact zones: Implications for fluid flow in volcanic basins. *Journal of African Earth Sciences*, 102:70–85, 2015b. doi: 10.1016/j.jafrearsci.2014.10.019.
- Kim Senger, John Millett, Sverre Planke, Kei Ogata, Christian Haug Eide, Marte Festøy, Olivier Galland, and Dougal A. Jerram. Effects of igneous intrusions on the petroleum system: a review. *First Break*, 35(6):47–56, 2017. ISSN 1365-2397. doi: 10.3997/1365-2397.2017011.
- F. Shaw, M. H. Worthington, R. S. White, M. S. Andersen, and U. K. Petersen. Seismic attenuation in Faroe Islands basalts. *Geophysical Prospecting*, 56(1):5–20, 2008. ISSN 00168025. doi: 10.1111/j.1365-2478.2007.00665.x.
- Freysteinn Sigmundsson, Sigrún Hreinsdóttir, Andrew Hooper, Thóra Árnadóttir, Rikke Pedersen, Matthew J. Roberts, Níels Óskarsson, Amandine Auriac, Judicael Decriem, Páll Einarsson, Halldór Geirsson, Martin Hensch, Benedikt G. Ófeigsson, Erik Sturkell, Hjörleifur Sveinbjörnsson, and Kurt L. Feigl. Intrusion triggering of the 2010 Eyjafjallajökull explosive eruption. *Nature*, 468(7322):426–430, 2010. ISSN 0028-0836. doi: 10.1038/nature09558.
- R. (Robert) Simm and M. (Michael) Bacon. *Seismic amplitude : an interpreter's handbook*. Cambridge University Press, 2014. ISBN 9781107011502.
- S. C. Singh, A. J. Harding, G. M. Kent, M. C. Sinha, V. Combier, S. Bazin, C. H. Tong, J. W. Pye, P. J. Barton, R. W. Hobbs, R. S. White, and J. A. Orcutt. Seismic reflection images of the Moho underlying melt sills at the East Pacific Rise. *Nature*, 442(7100):287–290, 2006. ISSN 14764687. doi: 10.1038/nature04939.
- J R Smallwood. Back-stripped 3D seismic data: A new tool applied to testing sill emplacement models. *Petroleum Geoscience*, 15(3):259–268, 2009. doi: 10.1144/1354-079309-844.
- John R Smallwood and Jenny Maresh. The properties, morphology and distribution of igneous sills: modelling, borehole data and 3D seismic from the Faroe-Shetland area. *Geological Society, London, Special Publications*, 197(1):271306, 2002.
- RMH Smith. A review of stratigraphy and sedimentary environments of the karoo basin of south africa. *Journal of African Earth Sciences (and the Middle East)*, 10(1-2): 117–137, 1990.

- J. B. Spacapan, J. O. Palma, O. Galland, R. Manceda, E. Rocha, A. D'Odorico, and H. A. Leanza. Thermal impact of igneous sill-complexes on organic-rich formations and implications for petroleum systems: A case study in the northern Neuquén Basin, Argentina. *Marine and Petroleum Geology*, 91(August 2017):519–531, 2018. ISSN 02648172. doi: 10.1016/j.marpetgeo.2018.01.018. URL <https://doi.org/10.1016/j.marpetgeo.2018.01.018>.
- Juán B Spacapan, Olivier Galland, Héctor A Leanza, and Sverre Planke. Igneous sill and finger emplacement mechanism in shale-dominated formation: a field study at Cuesta del Chihuido, Neuquén Basin, Argentina. *Journal of the Geological Society*, 174(2013):422–433, 2017. ISSN 00167649. doi: 10.1144/jgs2016-056.
- D. A. Spence and D. L. Turcotte. Magma-driven propagation of cracks. *Journal of Geophysical Research: Solid Earth*, 90(B1):575–580, jan 1985. ISSN 01480227. doi: 10.1029/JB090iB01p00575.
- G. Stucky de Quay, G. G. Roberts, J. S. Watson, and C. A.-L. Jackson. Incipient mantle plume evolution: Constraints from ancient landscapes buried beneath the North Sea. *Geochemistry, Geophysics, Geosystems*, 18(3):973–993, mar 2017. ISSN 15252027. doi: 10.1002/2016GC006769. URL <http://doi.wiley.com/10.1002/2016GC006769>.
- Henrik Svensen, Sverre Planke, Anders Malthes-Sørensen, Bjørn Jamtveit, Reidun Myklebust, Torfinn Rasmussen Eidem, and Sebastian S Rey. Release of methane from a volcanic basin as a mechanism for initial Eocene global warming. *Nature*, 429(6991): 542–545, 2004. doi: 10.1038/nature02566.
- Henrik Svensen, Bjørn Jamtveit, Sverre Planke, and Luc Chevallier. Structure and evolution of hydrothermal vent complexes in the Karoo Basin, South Africa. *Journal of the Geological Society*, 163(4):671682, 2006.
- Henrik Svensen, Fernando Corfu, Stéphane Polteau, Øyvind Hammer, and Sverre Planke. Rapid magma emplacement in the Karoo Large Igneous Province. *Earth and Planetary Science Letters*, 325-326:1–9, apr 2012a. ISSN 0012821X. doi: 10.1016/j.epsl.2012.01.015.
- Henrik Svensen, Fernando Corfu, Stéphane Polteau, Øyvind Hammer, and Sverre Planke. Rapid magma emplacement in the Karoo Large Igneous Province. *Earth and Planetary Science Letters*, 325-326:1–9, 2012b. doi: 10.1016/j.epsl.2012.01.015.
- B Tapley, J Ries, S Bettadpur, D Chambers, M Cheng, F Condi, B Gunter, Z Kang, P Nagel, R Pastor, et al. Ggm02—an improved earth gravity field model from grace. *Journal of Geodesy*, 79(8):467–478, 2005.

- J. Tarasewicz, R. S. White, B. Brandsdóttir, and C. M. Schoonman. Seismogenic magma intrusion before the 2010 eruption of Eyjafjallajökull volcano, Iceland. *Geophysical Journal International*, 198(2):906–921, 2014. ISSN 1365246X. doi: 10.1093/gji/ggu169.
- M P Tate, C D Dodd, and N T Grant. The Northeast Rockall Basin and its significance in the evolution of the Rockall-Faeroes/East Greenland rift system. In *Geological Society, London, Petroleum Geology Conference series*, volume 5, page 391406. Geological Society of London, 1999.
- Michael Tate, N White, and John-Joe Conroy. Lithospheric extension and magmatism in the Porcupine Basin west of Ireland. *Journal of Geophysical Research*, 98(B8):13905, 1993. ISSN 0148-0227. doi: 10.1029/93JB00890.
- K Thomson. Extrusive and intrusive magmatism in the North Rockall Trough. In *Geological Society, London, Petroleum Geology Conference series*, volume 6, page 16211630. Geological Society of London, 2005a.
- Ken Thomson. Sill complex geometry and internal architecture: a 3D seismic perspective. *Geological Society, London, Special Publications*, 234(1):229232, 2004.
- Ken Thomson. Volcanic features of the north rockall trough: application of visualisation techniques on 3d seismic reflection data. *Bulletin of Volcanology*, 67(2):116–128, 2005b.
- Ken Thomson. Determining magma flow in sills, dykes and laccoliths and their implications for sill emplacement mechanisms. *Bulletin of Volcanology*, 70(2):183–201, 2007. doi: 10.1007/s00445-007-0131-8.
- Ken Thomson and Nick Schofield. Lithological and structural controls on the emplacement and morphology of sills in sedimentary basins. *Geological Society, London, Special Publications*, 302(1):31–44, 2008. doi: 10.1144/SP302.3.
- JM Totterdell and AA Krassay. The role of shale deformation and growth faulting in the late cretaceous evolution of the bight basin, offshore southern australia. *Geological Society, London, Special Publications*, 216(1):429–442, 2003.
- James Trude, Joseph Cartwright, Richard J Davies, and John Smallwood. New technique for dating igneous sills. *GEOLOGY*, 31(9):813, 2003a. doi: 10.1130/G19559.1.
- James Trude, Joseph Cartwright, Richard J Davies, and John Smallwood. New technique for dating igneous sills. *Geology*, 31(9):813–816, 2003b.
- D. L. Turcotte. Fractals in geology: what are they and what are they good for?, 1991. ISSN 10525173.

- Donald Turcotte and Gerald Schubert. *Geodynamics*. Cambridge University Press, 2014.
- JD Turner and RA Scrutton. Subsidence patterns in western margin basins: evidence from the faeroe-shetland basin. In *Geological Society, London, Petroleum Geology Conference series*, volume 4, pages 975–983. Geological Society of London, 1993.
- RJ Walker, D Healy, TM Kawanzaruwa, KA Wright, RW England, KJW McCaffrey, AA Bubeck, TL Stephens, NJC Farrell, and TG Blenkinsop. Igneous sills as a record of horizontal shortening: The san rafael subvolcanic field, utah. *GSA Bulletin*, 129(9-10):1052–1070, 2017.
- Dayong Wang and Michael Manga. Organic matter maturation in the contact aureole of an igneous sill as a tracer of hydrothermal convection. *Journal of Geophysical Research: Solid Earth*, 120(6):4102–4112, 2015.
- Dayong Wang and Yongchen Song. Influence of different boiling points of pore water around an igneous sill on the thermal evolution of the contact aureole. *International Journal of Coal Geology*, 104:1–8, 2012. doi: 10.1016/j.coal.2012.08.009.
- Kai Wang, Xiancai Lu, Meng Chen, Yemu Ma, Kuiyuan Liu, Lianqi Liu, Xiaozhao Li, and Wenxuan Hu. Numerical modelling of the hydrocarbon generation of Tertiary source rocks intruded by doleritic sills in the Zhanhua depression, Bohai Bay Basin, China. *Basin Research*, 24(2):234–247, 2012. ISSN 0950091X. doi: 10.1111/j.1365-2117.2011.00518.x.
- Liang Wang, Yuan ping Cheng, Chao Xu, Feng hua An, Kan Jin, and Xiao lei Zhang. The controlling effect of thick-hard igneous rock on pressure relief gas drainage and dynamic disasters in outburst coal seams. *Natural Hazards*, 66(2):1221–1241, 2013. ISSN 0921030X. doi: 10.1007/s11069-012-0547-0.
- Paul Wessel, Walter HF Smith, Remko Scharroo, Joaquim Luis, and Florian Wobbe. Generic mapping tools: improved version released. *Eos, Transactions American Geophysical Union*, 94(45):409–410, 2013.
- Nicky White, Bryan Lovell, and others. Measuring the pulse of a plume with the sedimentary record. *Nature*, 387(6636):888891, 1997.
- Robert White and Dan Mckenzie. Magmatism at Rift Zones: The Generation of Volcanic Continental Margins. *Journal Of Geophysical Research*, 94(B6):76857729, 1989.
- RS White, LK Smith, AW Roberts, PAF Christie, NJ Kusznir, AM Roberts, D Healy, R Spitzer, A Chappell, JD Eccles, et al. Lower-crustal intrusion on the north atlantic continental margin. *Nature*, 452(7186):460–464, 2008.

- M. B. Widess. How Thin Is A Thin Bed? *GEOPHYSICS*, 38(6):1176–1180, dec 1973. ISSN 0016-8033. doi: 10.1190/1.1440403.
- Paul B Wignall. Large igneous provinces and mass extinctions. *Earth-science reviews*, 53(1):1–33, 2001.
- Penelope I R Wilson, Ken J W McCaffrey, Robert W Wilson, Ian Jarvis, and Robert E Holdsworth. Deformation structures associated with the Trachyte Mesa intrusion, Henry Mountains, Utah: Implications for sill and laccolith emplacement mechanisms. *Journal of Structural Geology*, 87:30–46, 2016a. doi: 10.1016/j.jsg.2016.04.001.
- Penelope I R Wilson, Ken J W McCaffrey, Robert W Wilson, Ian Jarvis, and Robert E Holdsworth. Deformation structures associated with the Trachyte Mesa intrusion, Henry Mountains, Utah: Implications for sill and laccolith emplacement mechanisms. *Journal of Structural Geology*, 87:30–46, 2016b. doi: 10.1016/j.jsg.2016.04.001.
- Thilo Wrona, Kevin G Taylor, Christopher A-L Jackson, Mads Huuse, Jens Najorka, and Indranil Pan. Impact of silica diagenesis on the porosity of fine-grained strata: An analysis of cenozoic mudstones from the north sea. *Geochemistry, Geophysics, Geosystems*, 18(4):1537–1549, 2017.
- J. Zachos. Trends, Rhythms, and Aberrations in Global Climate 65 Ma to Present. *Science*, 292(5517):686–693, apr 2001. ISSN 00368075. doi: 10.1126/science.1059412.
- James C Zachos, Gerald R Dickens, and Richard E Zeebe. An early cenozoic perspective on greenhouse warming and carbon-cycle dynamics. *Nature*, 451(7176):279, 2008.
- Mark D Zoback. *Reservoir geomechanics*. Cambridge University Press, 2010.